Asymptotic limit analysis for numerical models of atmospheric frontogenesis

by

Abeed Richard Visram

Department of Aeronautics
Imperial College London

Submitted for the degree of Doctor of Philosophy

June 2014

Abstract

Accurate prediction of the future state of the atmosphere is important throughout society, ranging from the weather forecast in a few days time to modelling the effects of a changing climate over decades and generations. The equations which govern how the atmosphere evolves have long been known; these are the Navier-Stokes equations, the laws of thermodynamics and the equation of state. Unfortunately the nonlinearity of the equations prohibits analytic solutions, so simplified models of particular flow phenomena have historically been, and continue to be, used alongside numerical models of the full equations.

In this thesis, the two-dimensional Eady model of shear-driven frontogenesis (the creation of atmospheric fronts) was used to investigate how errors made in a localised region can affect the global solution. Atmospheric fronts are the boundary of two different air masses, typically characterised by a sharp change in air temperature and wind direction. This occurs across a small length of $\mathcal{O}\,(10\text{ km})$, whereas the extent of the front itself can be $\mathcal{O}\,(1000\text{ km})$. Fronts are a prominent feature of mid-latitude weather systems and, despite their narrow width, are part of the large-scale, global solution. Any errors made locally in the treatment of fronts will therefore affect the global solution.

This thesis uses the convergence of the Euler equations to the semigeostrophic equations, a simplified model which is representative of the large-scale flow, including fronts. The Euler equations were solved numerically using current operational techniques. It was shown that highly predictable solutions could be obtained, and the theoretical convergence rate maintained, even with the presence of near-discontinuous solutions given by intense fronts.

Numerical solutions with successively increased resolution showed that the potential vorticity, which is a fundamental quantity in determining the large-scale, balanced flow, approached the semigeostrophic limit solution. Regions of negative potential vorticity, indicative of local areas of instability, were reduced at high resolution. In all cases, the width of the front reduced to the grid-scale.

While qualitative features of the limit solution were reproduced, a stark contrast in amplitude was found. The results of this thesis were approximately half in amplitude of the limit solution. Some attempts were made at increasing the intensity of the front through spatial- and temporal-averaging. A scheme was proposed that conserves the potential vorticity within the Eady model.

Declaration

I certify that the work presented in this thesis is the result of my own research, and where the work of other people has been included it has been fully acknowledged and referenced.

A. R. Visram, June 2014

Acknowledgements

First and foremost I would like to thank Colin and Mike for their supervision over the last three and a half years. Without their guidance, support and discussions none of this would have been possible.

In my time at Imperial I have been lucky enough to meet lots of amazing people. For fear of forgetting someone I would just like to say thanks to the occupants of E256; past, present and honorary. The tea breaks, poker nights, debates and cake Fridays made it the friendliest place one could ever hope to work in.

To my family; Amir, Margaret, Amy, Nadia and Sarah. Your love, encouragement and patience over these years never failed to pick me up when I needed it most. I love you all.

Dedication

To my parents.

Contents

Nomenclature

Abbreviations

KE	Kinetic energy
APE	Available potential energy
PE	Potential energy
IGW	Inertia gravity waves
LANS	Lagrangian-averaged Navier-Stokes
NWP	Numerical weather prediction
PV	Potential vorticity
QG	Quasigeostrophic
QM	Quasi-monotone
RMS	Root mean square
SG	Semigeostrophic
SIE	Semi-implicit Eulerian
SI	Semi-implicit
SISL	Semi-implicit semi-Lagrangian
SIVIE	Semi-implicit vector invariant Eulerian
SL	Semi-Lagrangian

Constants

α	Lagrangian-averaging lengthscale
ϑ	Semi-implicit time centering parameter
ϑ_T	Semi-Lagrangian trajectory time centering parameter

ϑ_E	Eulerian advecting velocity time centering parameter
β	Rescaling parameter
Ω	Domain
$\partial\Omega$	Boundary
c_p	Specific heat capacity at constant pressure
c_v	Specific heat capacity at constant volume
f	Coriolis parameter
g	Gravitational acceleration
N	Buoyancy frequency
ν	Kinematic viscosity
κ	Thermal conductivity
p_0	Reference pressure
R	Ideal gas constant
Λ	Velocity shear
θ_0	Reference potential temperature

Nondimensionalnumbers

Bu	Burger number, $^{NH}/_{fL}$
δ	Domain aspect ratio, $^{H}/_{L}$
Fr	Froude number, $^{U}/_{NH}$
Ri	Richardson number, $^{N^2}/_{\Lambda^2}$
Ro	Rossby number, $^{U}/_{fL}$
Ro_L	Lagrangian Rossby number, $\left\lvert\frac{D\mathbf{u}}{Dt}\right\rvert / \lvert f\mathbf{u}\rvert$

Scalars

E	Energy
p	Pressure
Π	Exner pressure, $\left(\frac{p}{p_0}\right)^{R/c_p}$

ϕ Geopotential

q Potential vorticity

ρ Density

ψ Streamfunction

T Temperature

θ Potential temperature, $T\left(\frac{p_0}{p}\right)^{R/c_p}$

χ Arbitrary passive tracer

u Component of velocity in the x-direction

v Component of velocity in the y-direction

w Component of velocity in the z-direction

Vectors

$\hat{\mathbf{n}}$ Unit normal

$\mathbf{r}$ Position

$\mathbf{x}$ Cartesian position

$\boldsymbol{\Omega}$ Rotation

$\mathbf{a}$ Semi-Lagrangian displacement

$\mathbf{u}$ Velocity

ζ Vorticity

Derivatives & integrals

C Material circuit

S Surface enclosed by material circuit C

∂_χ Partial derivative with respect to χ, i.e. $\frac{\partial}{\partial \chi}$

$\mathrm{d}\mathbf{r}$ Infinitesimal line element of C

$\mathrm{d}\mathbf{s}$ Infinitesimal area element of S

D_t Material derivative, $\partial_t + \mathbf{u} \cdot \nabla$

Γ Circulation, $\oint_C \mathbf{u} \cdot \mathrm{d}\mathbf{r}$

Discrete variables

Δt	Time-step
Δx	Grid spacing in the x-direction
Δz	Grid spacing in the z-direction
i	Index in the x-direction
j	Index in the z-direction
k	Iteration index
n	Timelevel index

Symbols & notation

$[\chi]_d$	Evaluation at the departure point
$\overline{\chi}$	Constant background value
χ_g	Geostrophic value
$\nabla\chi$	Gradient
$\nabla \cdot \chi$	Divergence
$\nabla \times \chi$	Curl
$\chi^{\perp}$	Perpendicular component

List of Figures

List of Tables

Chapter 1

Introduction

In all things of nature there is something of the marvelous.

Aristotle

Contents

1.1 Motivation

Accurate prediction of the state of the atmosphere at some time in the future is of great importance for all aspects of society. Short range forecasts, on the scale of a few days to a few weeks, are vital in ensuring that adequate precautions can be taken in the event of extreme weather events. Figure 1.1 shows the surface analysis chart and corresponding rain radar of an intense cold front during November 2012 which led to severe flooding and disruption over much of the United Kingdom.

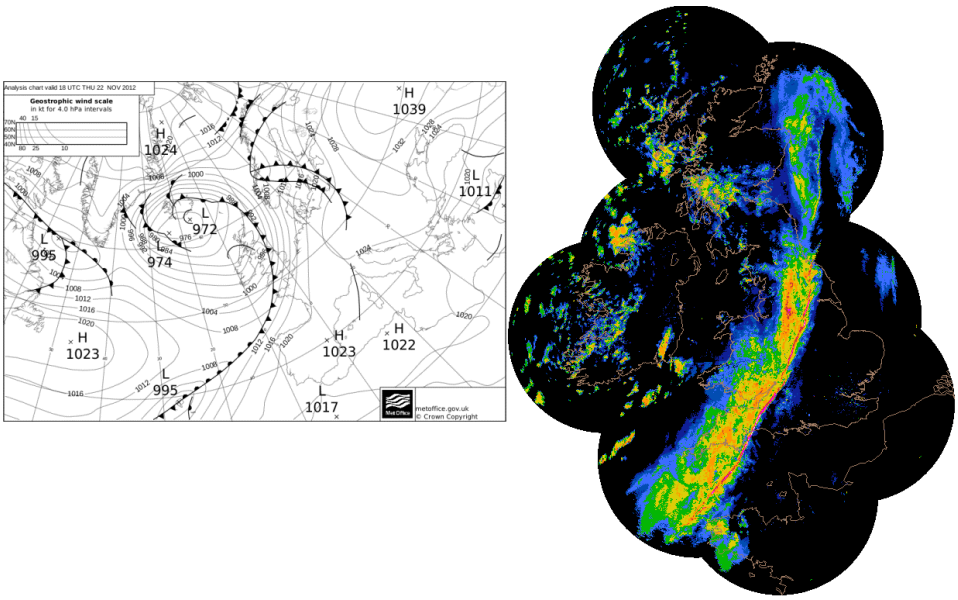

Figure 1.1: *Synoptic chart from November 2012, in which an intense cold front moved over the United Kingdom and brought extreme levels of rain, as shown in the satellite rain radar image on the right.* © *Crown Copyright, UK Met Office*[1].

Medium range forecasts, from a few weeks up to several months and seasonal variation, can help businesses in strategic planning or farmers in choice of crops for best yield. At the longer term, on climatic time scales of years and longer, it is imperative that the effects of a changing climate can be modelled, giving governments and policy makers the most useful information available.

It is an open question how predictable the atmosphere is. Whilst the large scale forecasts have improved, as shown over the last 30 years in Figure 1.2, the details at smaller scales remain difficult to predict, such as the intensity and position of the narrow band of heavy rain shown in Figure 1.1. Perfect deterministic predictability is clearly impossible, but extending the range of predictability, through reducing initial condition and model errors, is an achievable objective.

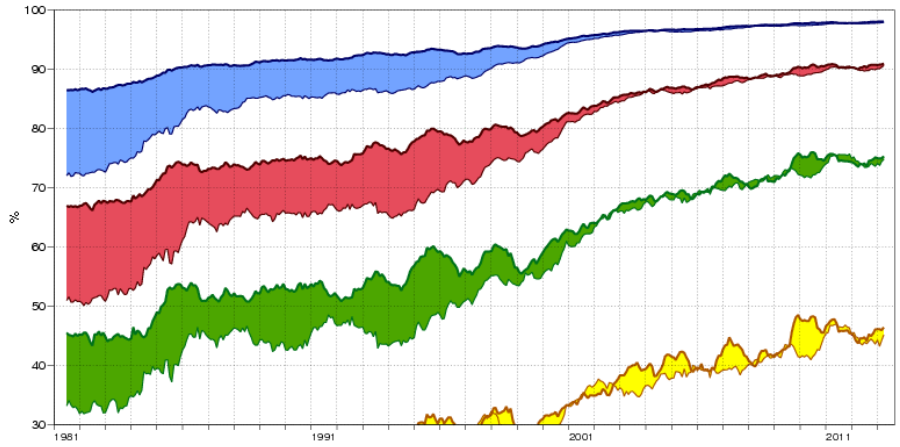

Figure 1.2: *Anomaly correlation of* 500 mb *geopotential height for the European Centre for Medium-Range Weather Forecasts over the last 30 years at day 3 (blue), 5 (red), 7 (green) and 10 (yellow). Original image taken from ECMWF*[2].

Improving the predictability window, a limit at which the short range weather forecast is no longer useful, is the subject of much international research, such as the World Meteorological Organization's THORPEX project (Shapiro and Thorpe, 2004; Szunyogh et al., 2008). This thesis uses the bottom-up approach of THORPEX (2010); by using simplified or idealised models and detailed diagnostic techniques it is hoped that further improvements in extending the predictability window, as well as improved statistics for longer term forecasts, are possible.

1.2 Introduction

The dynamics of the atmosphere are governed by the Navier-Stokes equations for fluid motion and the laws of thermodynamics. The atmosphere exhibits a rich variety of phenomena, from tropical cyclones to thunderstorms, that are contained within the mathematical simplicity and elegance of a system of nonlinear partial differential equations, (Houghton, 2002; Cushman-Roisin and Beckers, 2011).

Unfortunately, although the equations of motion are known, it is not possible to solve them analytically. In a three-dimensional turbulent fluid energy cascades to ever smaller spatial and temporal scales, down to that at which viscous dissipation takes over. To be able to simulate this numerically without any approximations would require a grid resolution of $\mathcal{O}(1\text{ mm})$, (Gill, 1982). Compared to the UK Met Office's current global model, which runs with a resolution at mid-latitudes of 25 km, the increase in grid resolution, and hence computational cost and power usage, required would be 30

orders of magnitude and beyond the limit of computer technology for the foreseeable future.

Since it is not feasible to solve the equations at the smallest required scales it is necessary to average the equations, and then solve the averaged equations (Cullen and Brown, 2009). The equations are averaged in both space and time, where the effects of unresolved processes, i.e. those occurring below the averaging scale, are accounted for either implicitly within the numerical method or explicitly through the use of an additional sub-grid model. It is important that the averaging procedure be consistent with the original equations, so that as the averaging scale reduces down to the minimum required physical scale the solutions of the averaged equations converge to the physical solutions.

It has been accepted for a long time that the weather forecast, as a solution to the averaged equations, tends to show characteristics of chaos, as captured succinctly and eloquently in the title of Lorenz (1972)'s note, widely referred to as the "butterfly effect". An illustration of the difficulties faced in predicting chaotic systems is shown in Figure 1.3, in which the same system can exhibit both good and bad predictability.

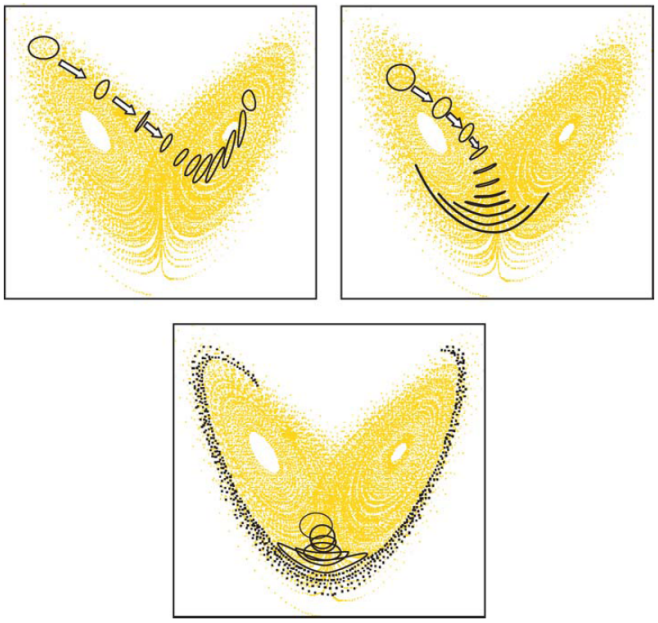

Figure 1.3: *Illustration of different simulation ensembles of the Lorenz (1963) model, taken from Palmer et al. (2005).*

In chaotic systems two similar initial states can quickly diverge, leading to very different outcomes. There are two main sources of error that can give rise to these divergent trajectories: initial condition error and model

error. Irrespective of the source of error the implication for a chaotic system is clear; whilst it might be possible to delay this divergence, ultimately there is a finite window of predictability, and hence useful forecasts (Lorenz, 1969).

The upper limit of predictability of the atmosphere was estimated to be around two weeks by Lorenz (1965) using a simplified model. This is greater than the currently accepted range of about five days for single deterministic forecasts, e.g. Figure 1.2. Reducing the errors, then, should lead to an increased window of predictability, (Kalnay, 2003). In numerical weather prediction (NWP) the initial condition error is reduced through improvements in the availability and coverage of observations, such as increased satellite and aircraft coverage, more accurate measuring equipment and through more sophisticated data assimilation techniques, (Kalnay, 2003).

The model error, which is the source of error covered in this thesis, can be harder to quantify. Increased resolution, higher order numerical methods and better sub-grid models have been among the methods used to reduce model error and improve predictability and forecast skill, e.g. (Cullen et al., 1997; Davies et al., 2005). These improvements have generally increased the fidelity of the model, so that small scale features are better resolved, (Kalnay, 2003). This thesis investigates the model error on the *large scale* solution, which is generally thought to be well resolved. Despite their narrow width, fronts are part of the large scale dynamics, and are a prominent feature of extra tropical weather systems. Thus any errors made in fronts, even if they are fairly localised, can affect the large scale behaviour of the solution as well, (Cullen, 2007a).

The justification for fronts being part of the large scale flow can be considered from a scale analysis. The large scale flow of the atmosphere is close to geostrophic balance, in which acceleration due to pressure equals that due to rotation. The appropriateness of this assumption can be measured by the Rossby number, $\mathrm{Ro} = U/fL$, where U is a horizontal velocity, f is the Coriolis parameter and L is a horizontal length scale, which is the ratio of inertial to rotational motion. At $\mathrm{Ro} \ll 1$ the motion is dominated by rotation, corresponding to slowly evolving large scale solutions. For synoptic scale motion including mid-latitude fronts, a representative Rossby number is $\mathrm{Ro} \approx 0.1$.

Whilst the dynamics are large on a horizontal scale the majority of moisture in the atmosphere, and hence weather systems, is contained within the troposphere which is bounded in the vertical by the tropopause at approximately 10 km. Based on a scale analysis using the continuity equation one would expect $W/U = H/L$, where H and W are representative vertical length and velocity scales. The troposphere is strongly stratified, which in the case of stable stratification inhibits the vertical motion so that $W/U < H/L$. The combined effects of stratification and rotation increase the anisotropy in the dynamics of the atmosphere; at times the motion appears to be close to two dimensional, as illustrated in Figure 1.4.

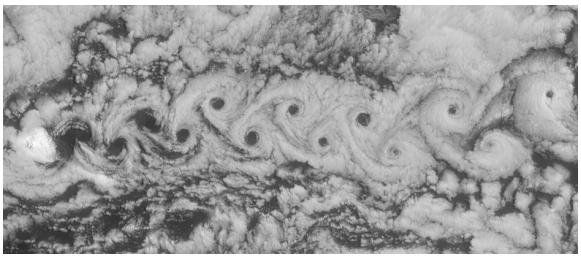

Figure 1.4: *Classical von Kármán vortex street captured off an island in the north Atlantic Ocean, as shown through the downwind cloud patterns. Original image taken from NASA Earth Observatory*[3].

Although Figure 1.4 resembles the classic vortex street it should be noted that they are at smaller scale than the weather systems shown in Figure 1.1. The geostrophic assumption is suitable in the context of the large scale pressure systems, but not for the small scale features which can arise through mechanisms such as shear and convective instabilities, (Cushman-Roisin and Beckers, 2011).

The features of the large scale flow can be well modelled by *balanced models*. Examples of balanced models include the quasigeostrophic (QG) and semigeostrophic (SG) approximations, which are based on a series expansion and require the Rossby number to be small. In the QG approximation both the momentum and trajectories are replaced with their geostrophic component, whereas in the SG approximation only the momentum is. The quasigeostrophic approximation is restricted in its range of validity, since ageostrophic motion often becomes comparable to geostrophic, whilst the semigeostrophic approximation permits a rich range of solutions, including fronts (Hoskins and Bretherton, 1972).

Unfortunately the imposition of geostrophic balance at all scales is not appropriate; the results given by such models are not realistic. Whilst not used for the forecast itself, balanced models are often used in the context of data assimilation. Creating a balanced initialisation is important for numerical weather prediction (NWP) to avoid spuriously large accelerations from unsuitable initial conditions, (Kalnay, 2003).

Operational forecasting uses the "full" equations: the compressible Navier-Stokes equations, with the first law of thermodynamics and equation of state for an ideal gas, e.g. (Davies et al., 2005). These are solved in space-time averaged models, as previously discussed. Numerical schemes have been developed which ensure that the results from these averaged models stay as close to geostrophic balance as they should, such as through the use of semi-implicit time-stepping, (Cullen, 2007a).

It is necessary to make sure that the mathematical and numerical models are suited to capturing the phenomena of interest. Short range NWP

requires accurate simulation of motion from the planetary and synoptic scale, $\mathcal{O}(1000\text{ km})$, down to the mesoscale, $\mathcal{O}(10\text{ km})$ and below, as well as timescales varying from several days down to fluctuations and gusts at minutes and below.

One approach to investigate the effects of the model error, both in terms of the averaging but also referring to the mathematical model itself, is through the use of *asymptotic convergence*. Asymptotic convergence takes a "full" model, for which it is not possible to calculate analytic solutions, and a "reduced" model, which is the limit of the full model as some parameter(s) go to zero and for which it is possible to calculate analytic solutions. A sequence of solutions to the *full* model is carried out in the limit of a vanishing, but still finite, small parameter. This sequence of solutions from the full model is then compared with the "true" solution from the reduced model. The error, such as the deviation from the reduced model solutions, is measured, and ensured that it reduces at the theoretical rate. Thus, numerical solutions from the full model can be validated against the (analytic) solutions from the reduced model, in the regime in which the reduced model is valid. This then validates the mathematical model and numerical method, so that solutions can be trusted in the appropriate parameter regime, (Cullen, 2007a).

The accurate simulation of the two extremes mentioned above, the large scale slowly evolving features down to small scale fast processes, presents the challenge to NWP and means that there are several limits that solutions from the full equations should reproduce, each with their own requirements. A summary of results, primarily using the UK Met Office's Unified Model, are discussed below.

Solutions from the rotating shallow water equations have been validated against two distinct limits for large scale flow by comparing with solutions from the semigeostrophic equations and the incompressible equations in Cullen (2007a, 2000). In Cullen (2007a), the use of asymptotic convergence was able to show how an inappropriate choice of discretisation could violate the convergence in the asymptotic limit.

At the other end of the spectrum the anelastic equations have been used in Cullen (2007a) to validate small scale flow over a ridge, in which the approximation of hydrostatic balance is no longer appropriate, using solutions from the fully compressible equations. Other examples of asymptotic convergence have been shown for a discontinuous solution (Cullen, 2008), large scale flow with topography (Cullen, 2007b) and for growing baroclinic waves (Cullen, 2006).

As well as quantitative convergence studies the procedure can be used to learn more about marginally resolved processes, in that they occur at the averaging scale, such as convection. The "hypohydrostatic" model has been used to investigate the large scale flow (Garner et al., 2007) and convection statistics (Pauluis et al., 2006) in climate models. Whilst there is no limit

solution as in the previous examples, it is beneficial in the development of better sub-grid models and physical parameterisations.

The results outlined above give a useful insight as to why it *is* possible to skillfully forecast the weather, despite the potential limitation of using the averaged equations which cannot be solved properly. The Unified Model performs well in both the large and small scale regimes. In the large scale it shows a good degree of predictability. These results are *a posteriori*, but justifies the rationale in using asymptotic convergence as a method of assessing current models and influencing future development without the need to go to the full atmospheric system.

Mid-latitude weather systems are highly anisotropic; this can be seen through the effect of the jet streams, which are thin, high speed wind structures, and the prevalence of weather fronts, which are air mass boundaries, in the atmosphere, (Cushman-Roisin and Beckers, 2011). Idealised vertical cross sections through fronts are shown in Figure 1.5, whilst the horizontal anisotropy can be seen in Figure 1.1.

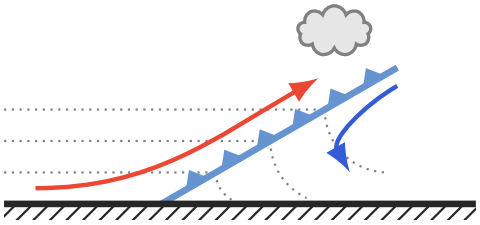

Figure 1.5: *Idealised vertical slice cross section through a surface cold front.*

Mid-latitude weather systems typically have two very different characteristic scales when viewed from an *Eulerian* frame; the length is on the synoptic scale, or even planetary scale in the case of the jet streams, whilst the width is on the mesoscale and below. In a *Lagrangian* frame, fronts have a long time scale despite their small width, (Hoskins, 1975, 1982). They provide a mechanism by which motion on the large scale can induce motion on the small scale.

Fronts are found in the ocean as well as the atmosphere. Oceanic fronts, just like their atmospheric counterparts, are boundaries between two distinct fluid masses. Along with changes in velocity a front can be observed through sharp changes in temperature or the salinity. Oceanic fronts are important in the energy balance of the global ocean circulation, (Ferrari, 2011).

The choice of reference frame can have an impact on the ability to simulate these flow phenomena in a numerical model. In an Eulerian frame the equations determine the evolution in time for a fixed spatial volume whilst a Lagrangian frame moves with a volume of fluid itself. Lagrangian methods are appealing from a physical perspective, in which atmospheric motions appear to be characterisable into different air masses, and are naturally suited

to the description of fronts. Lagrangian methods are problematic from a computational perspective, in which cells can rapidly become distorted. In general, for practical and reliable methods the Eulerian approach is used, (Ritchie et al., 1995; Davies et al., 2005).

The boundaries of air masses, when viewed in an Eulerian frame, appear to change abruptly, whilst fluid motion in general can exhibit (near) discontinuous behaviour. Although the Navier-Stokes equations do not have true discontinuities they permit solutions with steep gradients that vary over the viscous length scale. This is problematic for a numerical method that is incapable of resolving down to that scale. In the rest of this thesis the term "discontinuities" will refer to these steep gradients that effectively appear as discontinuities to a numerical method, whilst "true discontinuities" will be reserved for the precise mathematical definition. In fluid mechanics only two types of discontinuities may exist; a *shock*, in which fluid properties such as pressure and density vary rapidly over a short spatial scale, and a *contact discontinuity* which represents a boundary between two fluid masses, and between which there is no transport.

A disadvantage of the Eulerian approach is in simulating moving contact discontinuities such as fronts. A Lagrangian model would be able to model this as the boundary between two cells, which are themselves able to move and evolve, whereas an Eulerian model must diffuse this boundary, either explicitly or implicitly, to the minimum resolvable scale on the grid.

For correct results from a numerical method it is necessary to have a method that is consistent and convergent. Consistency is the requirement that the discrete differential equation correctly approximates the continuous differential equation and convergence is whether the solution from the discrete differential equation correctly reproduces the continuous solution in the limit as the spatial and temporal grid spacings go to zero. Consistency and convergence are related to the stability of a numerical scheme through the Lax equivalence theorem, which states that if a scheme is consistent and stable then it converges to the solution of the continuous differential equation, (Lax and Richtmyer, 1956). For a finite difference scheme to a linear problem it is sufficient to show that a scheme is stable and consistent to ensure that the solution is convergent, but for more complex problems the convergence is not assured, (Durran, 2010).

For nonlinear partial differential equations the Lax equivalence theorem is no longer sufficient to ensure convergence. Instead, it is necessary to have a proof that solutions exist, in either a classical or *weak* Eulerian or Lagrangian sense. Weak solutions satisfy the original equations in an integral form when multiplied with a smooth test function, as opposed to classical solutions satisfying the differential form. The use of weak solutions is required in situations in which the solution is discontinuous, where gradients are not defined, such as for shocks. It then becomes necessary to ensure that the numerical method converges to a weak solution, (LeVeque, 1992).

The convergence of a numerical scheme to a weak solution can be achieved by solving the governing equations in conservation form, in which the time derivative is coupled to spatial derivatives through spatial fluxes over a fixed control volume. Non-differentiable weak solutions, though, are not necessarily unique. In this case it is necessary to enforce an additional requirement that the solution be *physically correct*. The physically correct solution can be found by enforcing physical requirements that are not explicit in the equations themselves, such as that the solution be entropy non-decreasing or through measures on the solution such as the total variation be non-increasing, (LeVeque, 1992; Durran, 2010).

This, then, raises an interesting question for atmospheric fronts, as to whether or not an Eulerian numerical method can converge to a weak solution which only exists in a Lagrangian sense. Cullen and Feldman (2006) showed that for the Eady model weak Lagrangian solutions exist, whilst weak Eulerian solutions may not.

In this thesis an idealised model of the generation of fronts, or *frontogenesis*, will be studied which was given in the pioneering work on baroclinic instability by Eady (1949). The Eady model, which is covered in detail in Chapter 4, provides a suitable model to carry out the asymptotic convergence analysis outlined above. It is sufficiently complex to allow the formation of fronts but also simple enough so that approximations are analytically tractable, (Eady, 1949; Hoskins and Bretherton, 1972).

The approximations used for the limit solution are common in the solution of large scale atmospheric dynamics, that of hydrostatic and geostrophic balance together with the geostrophic momentum approximation, giving the semigeostrophic Eady equations. The semigeostrophic Eady equations have been shown to have weak Lagrangian solutions (Cullen and Feldman, 2006), in the sense that the equations apply when averaged locally over fluid parcels. Robust numerical results using the geometric method, an inviscid fully Lagrangian model, have been shown in (Cullen et al., 2007). It is not known if weak Eulerian solutions exist. The solution to the semigeostrophic Eady problem forms a true discontinuity in finite time (Hoskins and Bretherton, 1972), but it is not known whether this also occurs for the Euler Eady equations.

Numerical solutions to the semigeostrophic Eady problem using a Lagrangian numerical method have shown the solutions to be quasi periodic and highly predictable for long time scales, (Cullen and Roulstone, 1993b; Cullen, 2006), whilst Eulerian solutions to the standard Eady problem have shown strong sensitivity to small variations of the model parameters (Nakamura and Held, 1989).

By using the asymptotic convergence framework in the limit of vanishing Rossby number in the Eady model it is hoped that improvements in the large scale predictability can be achieved, which in turn can help to improve NWP forecasts and climate simulations.

1.3 Research objectives

The aims of this thesis follow from the discrepancy between results for the Eady problem using fixed grid, or Eulerian, methods and Lagrangian methods. In particular, this thesis will be centred around the following research questions:

① Is it possible to maintain a balanced solution despite the presence of a discontinuity?

② Can the long term predictability of solutions to the Euler Eady problem be improved to show robust quasi-periodic lifecycles similar to those observed in the semigeostrophic Eady problem?

③ Do numerical solutions to the inviscid Euler Eady problem converge to inviscid semigeostrophic Eady solutions?

This thesis will show strong evidence that the first two of these points can be achieved. The third point is a lot harder to answer definitively; several aspects of the solution properties show the expected behaviour in convergence, but there remains a large difference in amplitude between Eulerian and Lagrangian solutions.

1.4 Thesis outline

The rest of this thesis is structured as follows.

In Chapter 2 an overview of the use of vertical slice models of frontogenesis is given. The governing equations, along with the equations of the balanced semigeostrophic model, are presented in vertical slice configuration. An overview of general analytic and numerical results to slice models are discussed, with particular focus on the properties of solutions to the Eady model.

In Chapter 3 the discretisations and numerical methods are developed, based on current operational techniques representative of the Unified Model. Several validation tests are carried out to ensure that the implemented methods reproduce established results.

The Eady model is covered in detail in Chapter 4, with particular reference to the problem description in terms of initial and boundary conditions. The process of the asymptotic convergence framework is explained, and the effects on the relevant dynamical quantities is shown.

Chapter 5 presents the main findings of this thesis. High resolution experiments, and the use of conservative methods, show Eulerian solutions to the Eady problem to be highly predictable, answering the first research objective. The asymptotic convergence process is used to show that geostrophically balanced solutions can be achieved after frontal collapse, answering the second research objective.

The domain integrated potential vorticity is analysed to show that the solutions are approaching a non-negative state, as enforced in the limit solution and attempting to answer the third research objective. Finally, systematic errors made within the advection step are identified as being responsible for the degradation of the predictability of the solution at long times seen at low resolution.

Chapter 6 considers some numerical techniques that could potentially reduce the errors found in the preceding chapter, and discusses some of the provisional results found using these methods. Finally, Chapter 7 offers some conclusions, and discusses the implications and limitations of the results presented in this thesis.

The results of Chapters 4 and 5 have been presented in Visram et al. (2014), but are extended and discussed to a greater extent in this thesis.

Chapter 2

Vertical slice models of fronts

Contrary to popular opinion, mathematics is about simplifying life, not complicating it.

B. Mandelbrot (2004)

Contents

2.1 Use of slice models

Whilst there are several mechanisms that contribute to the formation of atmospheric fronts, two main mechanisms have been the focus of much attention (Hoskins and Bretherton, 1972), hereafter HB72. These are horizontal deformation, in which there is simultaneous expansion in one direction and contract in the other, and vertical shear, in which horizontal contraction balances vertical motion. In reality a combination of both of these effects, and others mentioned in HB72, will cause frontogenesis, but to learn more about the basic dynamical processes involved it is necessary to study them in isolation.

Both of the deformation and shear fronts exhibit similar characteristics, and can be analysed using similar models. One of the main simplifications involved is that although the real dynamics are three-dimensional, the frontogenesis mechanism can be studied using a two-dimensional vertical slice model, but with different background states corresponding to the mechanism of interest. This corresponds to a solution of the three-dimensional equations, in which any variations normal to the vertical slice are zero. The vertical slice Eady model is a solution of the full three-dimensional equations corresponding to no variation in the y-direction (Hoskins and West, 1979; Hoskins, 1982), see Figure 2.1 for a schematic of the coordinate system. The other main simplification is that frontogenesis can be well modelled by the semigeostrophic equations.

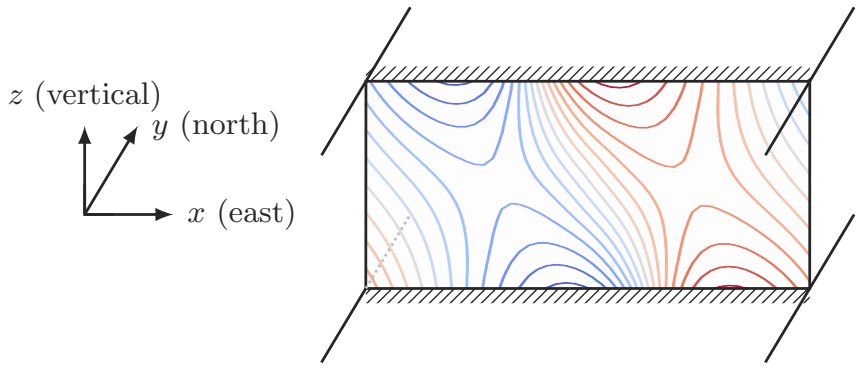

Figure 2.1: *Schematic of the vertical slice coordinate system, together with the positive directions.*

Whilst the dynamical considerations allow one to simplify frontogenesis down to a slice model, it is insightful to carry out *a posteriori* analyses to justify the assumptions made at the start. The following section will compare real observations of fronts and associated circulations with theoretical models, before the rest of the chapter goes on to discuss the equations and solutions.

2.1.1 Comparison with real fronts

There are several features commonly seen in an idealised model of a surface cold front; a narrow band of cyclonic vertical vorticity separating two along-front jets close to the surface, a region of isotherms packed close together along the ground indicating the change in air temperature, and a thermally direct circulation pattern of warm air rising ahead and cold air sinking below the front, (Hoskins and Bretherton, 1972).

These features have often been found in observations. Ogura and Portis (1982) studied a cold front over North America and found good agreement with the model front, in particular with attributing the vertical circulation in triggering severe thunderstorms. In Blumen (1980) the results of the HB72 model were compared with early observational results from Sanders (1955), which showed evidence of a strong rising jet ahead of the front, which was not shown in HB72.

The vertical circulation around a front has been well studied. Eliassen (1962), building on the work of Sawyer (1956) and Eliassen (1959), showed how the circulation around a front could be obtained from the Sawyer-Eliassen equation. The circulation calculated from the Sawyer-Eliassen equation was consistent with the conversion of available potential energy through rising warm and sinking cold air masses. The circulation was found to act against the horizontal convergence leading to the strengthening of the frontal zone, suggesting the nonlinear effects might become significant in the formation of a discontinuity. As will be discussed later, see Section 2.4.2, the formation of a true discontinuity in the semigeostrophic equations is one of the key, and unfortunately problematic, features of idealised models of fronts.

A consequence of the circulation is that the front appears as a material surface separating two air masses, i.e. a contact discontinuity as described in the Introduction. Blumen (1980) found that the real front acted as a material surface, whilst Ogura and Portis (1982) found that a small amount of moist warm air was able to cross the band of maximum cyclonic vorticity. This seems acceptable, considering that in reality there are numerous complicating factors compared to the clean dynamics of an idealised model.

One aspect commonly observed close to real fronts that is not exhibited in balanced models is that of gravity waves, (Knippertz et al., 2010). These gravity waves show evidence of seasonal variation, being stronger in winter when baroclinic activity is increased, as well as strong wave activity causing perturbations in temperature and wind of up to six times that of the background variability, see review of Plougonven and Zhang (2014) and observations of Fritts and Nastrom (1992).

The generation of gravity waves supported the observations of narrow cloud bands above and ahead of fronts being correlated with areas of extreme weather such as thunderstorms and tornadoes, (Ley and Peltier, 1978; Gall

et al., 1988). The waves themselves are typically high frequency with periods $\mathcal{O}(1\text{ h})$ and wavelengths in the range of 10 to 100 km, with amplitudes up to 10 mb which is sufficient to have an effect on precipitation and convection (Plougonven and Zhang, 2014).

As well as having an effect in the immediate area around them, fronts have been shown to have a non-negligible contribution to global circulation. Blumen (1990b) investigated the dissipation in energy and enstrophy in the frontal zone, and showed that fronts make a non-negligible contribution to the global dissipation, being two orders of magnitude larger than that of clear air turbulence. These values were from viscous semigeostrophic solutions, such that other ageostrophic effects such as breaking gravity waves have not been accounted for, and so the real value is potentially higher. The dissipation, or lack of in an inviscid model, associated with fronts is significant in affecting the large scale dynamics.

The differences between warm and cold fronts was examined in Hoskins and Heckley (1981), using the three-dimensional Eady wave. By using the deformation model and comparing with slices from the three-dimensional Eady wave, the stronger gradients in temperature with a cold front and weaker gradients with a warm front were shown. The generation of fronts was later classified into a type (A) primary cold front with secondary warm front or type (B) primary warm front, (Hoskins, 1982).

The differences observed in cold and warm fronts is also apparent in the growth of baroclinic waves. The semigeostrophic equations provided further insight into the development of large scale planetary and cyclone waves. Solutions from the semigeostrophic equations showed "tight lows and broad highs" which were in agreement with observations, whereas solutions using the quasigeostrophic equations were symmetric with regard to high and low pressure systems (Hoskins, 1976).

2.2 Governing equations

In this section the various approximations that are used in deriving the equations of motion for the slice model will be explained. Most of the approximations that are made are common to geophysical fluid dynamics and are suitable to the phenomena of interest.

The use of the two-dimensional vertical slice configuration in this thesis is motivated by the desire to reproduce the challenging dynamics of a near discontinuity in a simplified model. Whilst there are well documented test cases for more complex flow features, such as the Jablonowski and Williamson (2006) experiment for an unstable baroclinic wave on the sphere, the non-smooth solutions associated with frontogenesis are inherently difficult to model. A detailed study is much easier in a two-dimensional model, and with less computational requirements.

2.2.1 Basic equations

Following standard fluid dynamics, e.g. Batchelor (1967); Pedlosky (1987), the first equation is the conservation of mass, or the continuity equation

$$\frac{\partial \rho}{\partial t} + \nabla \cdot (\rho \mathbf{u}) = 0, \tag{2.1}$$

$$\frac{D\rho}{Dt} + \rho \nabla \cdot \mathbf{u} = 0, \tag{2.2}$$

where ρ is the fluid density, $\nabla = (\partial_x, \partial_y, \partial_z)$ is the three-dimensional gradient operator, and $\mathbf{u} = (u, v, w)$ is the three-dimensional velocity vector field. The second form of the equation makes use of the Lagrangian or material derivative

$$\frac{D}{Dt} = \frac{\partial}{\partial t} + \mathbf{u} \cdot \nabla.$$

In the rest of this thesis the notation

$$\frac{\partial}{\partial \chi}(\cdot) = \partial_\chi (\cdot) = (\cdot)_\chi,$$

will be used interchangeably where there is no ambiguity, to represent the partial derivative of a variable or expression $(\cdot)$ with respect to the variable χ.

The balance of momentum is given by Newton's second law as

$$\rho \frac{D\mathbf{u}}{Dt} = -\nabla p + \rho \nabla \Phi + \mathbf{F}, \tag{2.3}$$

where p is the pressure, Φ represents conservative forcing terms, those that can be written as the gradient of a potential, and $\mathbf{F}$ are the non-conservative forces such as viscous dissipation. The above equations are the Navier-Stokes equations, but they require additional equations to be solvable.

The ideal gas law

$$p = \rho R T, \tag{2.4}$$

relates the temperature T to the pressure and density through the ideal gas constant R.

The conservation of energy, given by the first law of thermodynamics, is written in terms of the temperature as

$$c_v \frac{DT}{Dt} = \kappa \nabla^2 T + Q + \frac{RT}{\rho} \frac{D\rho}{Dt}, \tag{2.5}$$

where κ is the thermal conductivity, c_v is the specific heat capacity at constant volume and Q is a source term of the rate of heat applied.

Rotation

The equations of motion outlined in the previous section are for an *inertial* frame, one moving at a constant velocity, whilst for atmospheric fluid dynamics it will be necessary to consider a *rotating* frame.

The justification for requiring the equations of motion in a rotating frame will be covered in a later section, but for now it suffices to check that rotation will be significant. The ratio of the rotational to the inertial timescale is given by the Rossby number

$$\mathrm{Ro} = \frac{U}{2\Omega L},$$

where U and L are representative velocity and length scales and Ω is the rate of rotation. For rotational effects to dominate inertial effects $\mathrm{Ro} \ll 1$ is required. For large scale motion in the atmosphere typical values of these are

$$U = 10 \text{ m s}^{-1}, \quad L = 1000 \text{ km}, \quad f = 10^{-4} \text{ s}^{-1},$$

where $f = 2\Omega \sin\theta$ is the Coriolis parameter, with θ the angle from the Equator, with a value given representative for mid-latitudes. Combining these values gives $\mathrm{Ro} = 0.1$, which meets the requirement of small Rossby number.

Velocities in the rotating and inertial frames can be linked through

$$\mathbf{u} = \mathbf{v} + \boldsymbol{\Omega} \times \mathbf{r}, \tag{2.6}$$

where $\mathbf{u}$ is the velocity in the inertial frame, $\mathbf{v}$ is the velocity in the rotating frame, $\boldsymbol{\Omega}$ is the rotational vector and $\mathbf{r}$ is the position vector. Using this and relating it back to the material derivative gives

$$\frac{D\mathbf{u}}{Dt} = \frac{D\mathbf{v}}{Dt} + 2\boldsymbol{\Omega} \times \mathbf{r} + \underbrace{\boldsymbol{\Omega} \times (\boldsymbol{\Omega} \times \mathbf{r})}_{①} + \underbrace{\frac{D\boldsymbol{\Omega}}{Dt} \times \mathbf{r}}_{②}. \tag{2.7}$$

The first of the terms can be shown to give

$$① = -\nabla \frac{|\boldsymbol{\Omega} \times \mathbf{r}|^2}{2},$$

which is the gradient of a potential, and so this will simply modify the conservative forcing term. For constant rotation the second term is zero. Combining the above, and using $\mathbf{u}$ to represent the velocity in the rotating frame from hereon, the Navier-Stokes equations become

$$\rho \left[\frac{D\mathbf{u}}{Dt} + 2\boldsymbol{\Omega} \times \mathbf{u} \right] = -\nabla p + \rho \nabla \Phi + \mathbf{F}. \tag{2.8}$$

Circulation & vorticity

The correct simulation of the large scale solution is dependent on maintaining the appropriate conservation properties of the governing equations. The Lagrangian conservation of potential vorticity was identified as one of these key properties in Cullen (2007a). The derivation using Stokes' theorem is covered below, and follows Pedlosky (1987).

Taking a material circuit C of the fluid, the definition of the circulation, Γ, is

$$\Gamma = \oint_C \mathbf{u} \cdot \mathrm{d}\mathbf{r}. \tag{2.9}$$

Using Stokes' theorem it is possible to write the circulation as

$$\Gamma = \int_S \zeta \cdot \mathrm{d}\mathbf{s} = \int_S \zeta \cdot \hat{\mathbf{n}} \, \mathrm{d}s, \tag{2.10}$$

where S is the surface enclosed by the material circuit C, $\hat{\mathbf{n}}$ is the unit normal and ζ is the vorticity vector defined as

$$\zeta = \nabla \times \mathbf{u}. \tag{2.11}$$

Taking the material time derivative gives

$$\frac{D\Gamma}{Dt} = \frac{D}{Dt} \oint_C \mathbf{u} \cdot \mathrm{d}\mathbf{r} = \oint_C \frac{D\mathbf{u}}{Dt} \cdot \mathrm{d}\mathbf{r} \; + \oint_C \mathbf{u} \cdot \frac{D\left(\mathrm{d}\mathbf{r}\right)}{Dt}, \tag{2.12}$$

where it can be shown that for the second term

$$\begin{aligned} \oint_C \mathbf{u} \cdot \frac{D\left(\mathrm{d}\mathbf{r}\right)}{Dt} &= \oint_C \mathbf{u} \cdot \left(\mathrm{d}\mathbf{r} \cdot \nabla\right) \mathbf{u}, \\ &= \oint_C \mathbf{u} \cdot \frac{\partial \mathbf{u}}{\partial s} \mathrm{d}s, \\ &= \oint_C \mathrm{d}\left(\frac{1}{2}\mathbf{u} \cdot \mathbf{u}\right) = 0, \end{aligned}$$

which is the integral around a closed loop of the gradient of a scalar, so that

$$\frac{D\Gamma}{Dt} = \oint_C \frac{D\mathbf{u}}{Dt} \cdot \mathrm{d}\mathbf{r}. \tag{2.13}$$

Substituting Equation (2.8) into Equation (2.13) gives

$$\frac{D\Gamma}{Dt} = \underbrace{-\oint_C \left(2\boldsymbol{\Omega} \times \mathbf{u}\right) \cdot \mathrm{d}\mathbf{r}}_{①} \underbrace{- \oint_C \frac{\nabla p}{\rho} \cdot \mathrm{d}\mathbf{r}}_{②} \underbrace{- \oint_C \frac{\mathbf{F}}{\rho} \cdot \mathrm{d}\mathbf{r}}_{③}. \tag{2.14}$$

The first term on the right-hand side of Equation (2.14) can be absorbed in the left hand side by considering the *absolute* circulation,

$$\Gamma_a = \Gamma + 2\boldsymbol{\Omega} S.$$

The second of these is the *baroclinicity* of the fluid

$$② = -\int_S \nabla \times \left(\frac{\nabla p}{\rho}\right) \cdot \hat{\mathbf{n}}\, \mathrm{d}s, \tag{2.15}$$

$$= \int_S \frac{\nabla \rho \times \nabla p}{\rho^2} \cdot \hat{\mathbf{n}}\, \mathrm{d}s, \tag{2.16}$$

where Stokes' theorem has been used to go from Equation (2.14) to (2.15). The third term is the contribution from external forces. Combining these gives Kelvin's circulation theorem for the absolute circulation

$$\frac{D\Gamma_a}{Dt} = \int_S \frac{\nabla \rho \times \nabla p}{\rho^2} \cdot \hat{\mathbf{n}}\, \mathrm{d}s + \oint_C \frac{\mathbf{F}}{\rho} \cdot \mathrm{d}\mathbf{r}. \tag{2.17}$$

Using the intrinsic relation between the circulation and vorticity and the continuity equation gives

$$\frac{D}{Dt}\left(\frac{\zeta_a}{\rho}\right) = \left(\frac{\zeta_a}{\rho} \cdot \nabla\right)\mathbf{u} + \nabla\rho \times \frac{\nabla p}{\rho^3} + \frac{1}{\rho}\left[\nabla \times \left(\frac{\mathbf{F}}{\rho}\right)\right]. \tag{2.18}$$

For a Lagrangian conserved property

$$\frac{D\chi}{Dt} = 0,$$

it is then possible to show (Pedlosky, 1987)

$$\frac{D}{Dt}\left(\frac{\zeta_a}{\rho} \cdot \nabla\chi\right) = \nabla\chi \cdot \left(\frac{\nabla\rho \times \nabla p}{\rho^3}\right) + \frac{\nabla\chi}{\rho} \cdot \left[\nabla \times \left(\frac{\mathbf{F}}{\rho}\right)\right]. \tag{2.19}$$

In the absence of any non-conservative forcing and for $\chi = \chi(\rho, p)$, Equation (2.19) implies a conservation law

$$\frac{Dq}{Dt} = 0, \tag{2.20}$$

for the quantity

$$q = \frac{1}{\rho}(\zeta + 2\boldsymbol{\Omega}) \cdot \nabla\chi, \tag{2.21}$$

which is the potential vorticity.

2.2.2 Approximations

The following approximations will be made to simplify the equations of motion, so as to make them more amenable for analysis in the rest of this thesis. Note that not all of the approximations are really suited for large scale flows, but their use is justified through previous work having used them successfully to investigate frontogenesis, e.g. (Hoskins and Bretherton, 1972; Hoskins, 1982).

It is beyond the scope of the present work to go into detail about the effects of the neglected processes, but a summary of the relevant results is given in Section 2.4.5, and the interested reader is referred to the references given there.

Inviscid

In this thesis the large scale motion, and hence fronts, will be modelled as essentially inviscid, in that no explicit diffusion terms will be included. Several conservation properties follow from the inviscid approximation, which are used in the long term solutions as discussed later in this chapter.

In the real atmosphere viscous effects will become significant at small scales, at which diffusion will dissipate energy cascaded from larger scales. This will alter the real dynamics, and viscous experiments have been carried out as described in Section 2.1.1, but for the purposes of this thesis the fundamental mechanism that will be investigated is inviscid.

Constant rotation

Whilst rotation will be important, as already mentioned based on the Rossby number, it is possible to simplify the form that this forcing term takes. Constant rotation is not appropriate for large scale flows, but it is suitable in the context of frontogenesis and its effect on the large scale flow. The axis of rotation of $\mathbf{\Omega}$ is assumed to be in the vertical, so that effects of rotation are purely in the horizontal. This then implies that terms arising from the rotation will be conservative and in the horizontal (x, y) plane.

Under these assumptions the Coriolis term becomes

$$2\mathbf{\Omega} \times \mathbf{u} = f\hat{\mathbf{z}} \times \mathbf{u},$$

where $f = 10^{-4}$ s^{-1} is the constant Coriolis parameter evaluated at the mid-latitude and $\hat{\mathbf{z}}$ is a unit vector in the z direction. This is commonly referred to as an f-plane approximation.

Cartesian coordinate system

The equations of motion for the full atmosphere should be solved in a curved coordinate system, taking the topography into account. In this thesis it will be sufficient to use the Cartesian coordinate system with flat surfaces. The x coordinate is aligned in the zonal direction, with eastwards positive; the y coordinate is aligned in the meridional direction, with northwards positive; the z direction is in the vertical, with upwards positive.

The z coordinate will be redefined using a function of pressure, as described in the following section, but z will still be referred to as "vertical". Using this coordinate system corresponds to taking a tangent plane at a point on the surface of the Earth, and discarding any effects of topography.

Adiabatic motion

All source terms in the conservation of energy will be ignored, so that the motion will be adiabatic. On the introduction of the potential temperature

$$\theta = T\left(\frac{p_0}{p}\right)^{R/c_p},$$

where p_0 is a reference pressure at sea level, the first law of thermodynamics implies a conservation law for the potential temperature as

$$\frac{D\theta}{Dt} = 0. \tag{2.22}$$

Incompressible Boussinesq

The vertical coordinate is replaced by a function of pressure following Hoskins and Bretherton (1972)

$$Z = \left[1 - \left(\frac{p}{p_0}\right)^{\gamma-1/\gamma}\right]\frac{\gamma}{\gamma-1}H_s; \quad H_s = \frac{p_0}{g\rho_0},$$

where H_s is referred to as the scale height. The coordinate Z is referred to as the pseudo-height and is linked to the physical height through

$$\theta \mathrm{d}Z = \theta_0 \mathrm{d}h,$$

so that the pseudo-height corresponds to physical height in an isentropic atmosphere, (White and Beare, 2005). The use of this vertical coordinate gives an incompressible form of the continuity equation as

$$\nabla \cdot (\rho \mathbf{u}) = 0. \tag{2.23}$$

For low speed flows, and for the density being a function of the potential temperature only and not dependent on pressure, it is possible to make the incompressible Boussinesq approximation, (Gill, 1982). The Boussinesq approximation assumes that density perturbations are small, so that it can be replaced by a constant value in the momentum equations, except where it is multiplied by gravity. This is summarised as

$$\rho = \rho_0 + \rho'; \quad \rho' \ll \rho_0; \quad \frac{g\rho'}{\rho_0} = \mathcal{O}(1).$$

This reduces the continuity equation to

$$\nabla \cdot \mathbf{u} = 0, \tag{2.24}$$

so that the velocity field $\mathbf{u}$ is divergence free.

The vertical acceleration term owing to the forcing is replaced in terms of the potential temperature, defined in the previous section, through the use of the buoyancy frequency, N,

$$N^2 = -\frac{g}{\rho_0}\frac{\mathrm{d}\rho}{\mathrm{d}z} = \frac{g}{\theta_0}\frac{\mathrm{d}\theta}{\mathrm{d}z},$$

where the primes have been dropped.

Finally the pressure and conservative forcing terms are replaced with the geopotential

$$\phi = \frac{p_0}{\rho_0} + \rho_0 g h, \tag{2.25}$$

and from hereon the vertical coordinate will be identified with the symbol z.

Whilst operational models use the fully compressible equations, the use of the incompressible Boussinesq equations is sufficient to study frontogenesis. In the real atmosphere the flow speed is small compared to the speed of sound, but density changes are not small over the entire atmosphere. The use of the incompressible Boussinesq equations is required so that solutions in the slice geometry correspond to three-dimensional solutions with no variation normal to the slice.

2.2.3 Summary

Summarising Sections 2.2.1 to 2.2.2 the three-dimensional, incompressible, Boussinesq, Euler equations are given by

$$\frac{D\mathbf{u}}{Dt} + f\hat{\mathbf{z}} \times \mathbf{u} = -\nabla\phi + \frac{g}{\theta_0}\theta\hat{\mathbf{z}}, \tag{2.26}$$

$$\frac{D\theta}{Dt} = 0, \tag{2.27}$$

$$\nabla \cdot \mathbf{u} = 0. \tag{2.28}$$

These are now the five equations for the five unknowns, $\mathbf{u}$, ϕ and θ, where the incompressibility condition has reduced the number of unknowns. Equations (2.26) to (2.28) require initial and boundary conditions to be complete. These are covered in depth for the vertical shear model in Section 4.4; briefly the boundary conditions are periodic in the horizontal and rigid lid in the vertical and the initial conditions correspond to a small amplitude perturbation with the structure of the fastest growing wave.

Combining the potential temperature with Equation (2.21) gives the Ertel potential vorticity as

$$q = \frac{1}{\rho}\left(\zeta + f\hat{\mathbf{z}}\right) \cdot \nabla\theta. \tag{2.29}$$

The system of Equations (2.26) to (2.28) conserve an energy integral given by

$$E_T = \rho_0 \int_\Omega \frac{1}{2} |\mathbf{u}|^2 - \frac{g}{\theta_0} \theta z \, \mathrm{d}V, \tag{2.30}$$

where the first term is the kinetic energy and the second the potential energy. The conservation of the energy and potential vorticity are vital for the long term evolution of the large-scale flow (Cullen, 2007a), and will be discussed in the context of the Eady model in Chapter 4.

As mentioned in section 2.1, there are two mechanisms to frontogenesis that have been well studied. In a modelling context they can both be covered from the same set of equations given above, but with different background states, (Snyder et al., 1993). In both cases apart from the background state in $\left(\overline{\mathbf{u}}, \overline{\theta}\right)$ all variables are independent of y.

$$\frac{D\mathbf{u}}{Dt} + \mathbf{u} \cdot \nabla \overline{\mathbf{u}} + f\hat{\mathbf{z}} \times \mathbf{u} = -\nabla\phi + \frac{g}{\theta_0}\theta\hat{\mathbf{z}}, \tag{2.31}$$

$$\frac{D\theta}{Dt} + \mathbf{u} \cdot \nabla \overline{\theta} = 0, \tag{2.32}$$

$$\nabla \cdot \mathbf{u} = 0, \tag{2.33}$$

where

$$\frac{D}{Dt} = \frac{\partial}{\partial t} + (\mathbf{u} + \overline{\mathbf{u}}) \cdot \nabla.$$

Note that in Equations (2.31) to (2.33) the background advective state has been explicitly stated, whereas in the rest of this thesis $\mathbf{u}$ will contain both the background state and the perturbation from it.

The deformation model corresponds to a contraction in the x-direction and expansion in the y-direction. This means that as the numerical experiments proceed the computational domain in (x, z) also contracts. The deformation model background state is given by

$$\overline{\mathbf{u}} = (-\alpha x, \alpha y, 0)\,; \quad \overline{\theta} = \frac{\theta_0}{g} N^2 z,$$

where $\alpha = \alpha(t)$ is the deformation rate.

A detailed account of the vertical shear (Eady model) equations are deferred to the problem specification in Chapter 4. The vertical shear model corresponds to a fixed temperature gradient in the y-direction, with the background state

$$\overline{\mathbf{u}} = (\Lambda z, 0, 0)\,; \quad \overline{\theta} = \frac{\theta_0}{g}\left(-f\Lambda y + N^2 z\right),$$

where Λ is the uniform vertical shear.

2.3 Balanced models

Before introducing the semigeostrophic equations the relevant nondimensional parameters are covered, as touched upon in the Introduction. The vertical slice model equations are nondimensionalised using the following scalings

$$u = Uu', \quad v = Vv', \quad w = Ww',$$

where U, V and W are characteristic velocities. The horizontal velocities are related through

$$\frac{U}{V} = \epsilon \ll 1,$$

which is the requirement of Hoskins and Bretherton (1972) to assume cross-front geostrophic balance. Note that whilst this suggests that the along-front wind, v, will be close to geostrophic balance, no such approximation can be made for the across-front wind, u.

In the vertical slice the characteristic lengths are given as

$$x = Lx', \quad z = Hz'.$$

The requirement of consistency with the continuity equation for the velocity and length scales within the slice suggests that the aspect ratio, δ, given by

$$\frac{H}{L} = \frac{W}{U} = \delta \ll 1,$$

is sufficiently small for hydrostatic balance to be a good approximation. In addition the scalings

$$t = Tt' = \frac{L}{U}t', \quad \phi = fLV\phi', \quad \theta = \theta_0 \frac{fLV}{gH}\theta'.$$

are consistent with the requirements of a hydrostatic and geostrophically balanced state. Using the above scalings gives

$$\frac{D}{Dt} = \frac{U}{L}\frac{D}{Dt'},$$

and the Rossby number

$$\mathrm{Ro} = \frac{U}{fL},$$

which is the ratio of the inertial to rotational velocities. For $\mathrm{Ro} \ll 1$ the flow is rotation dominated, whilst for $\mathrm{Ro} \gg 1$ the effects of rotation are minimal and the inertial motions are significant.

A more relevant parameter is the *Lagrangian* Rossby number

$$\mathrm{Ro}_L = \left|\frac{D\mathbf{u}}{Dt}\right| / \left|f\mathbf{u}\right|,$$

which measures the Lagrangian acceleration to rotation (Hoskins, 1975). The requirement of a small Lagrangian Rossby number is less strict than a small (Eulerian) Rossby number based on characteristic scales (Cullen, 2006), and is naturally associated with $U \ll V$. A small Lagrangian Rossby number implies that the direction of the trajectories changes slowly relative to the Coriolis parameter. At mid-latitudes this means that trajectories should change direction less than 45° in one day, which is a good approximation, (Cullen, 2007a).

There are other nondimensional parameters that are important for geophysical flows. For the deformation model the rate of deformation relative to the Coriolis is given by

$$\upsilon = \frac{\alpha}{f},$$

which for deformation to be slow relative to rotation requires that $\upsilon \ll 1$. For the shear model the Richardson number is the ratio of the buoyancy frequency to the shear

$$\mathrm{Ri} = \frac{N^2}{\Lambda^2},$$

where the vertical shear is given by

$$\overline{U} = \Lambda z, \quad \Lambda = -\frac{g}{f\theta_0}\frac{\partial \overline{\theta}}{\partial y}.$$

When the velocity shear is large relative to the stratification, $\mathrm{Ri} < 1/4$, the flow will suffer from shear instability, which violates the hydrostatic balance, (Chandrasekhar, 1961). Note that $N^2 \leq 0$ is a sufficient condition for shear instability, but this corresponds to the case of convective instability. Attention will be restricted to the case of stable stratification $N^2 > 0$ and large Richardson number $\mathrm{Ri} \gg 1$ so that shear and convective instabilities are not present in the basic flow.

The importance of stratification is better measured by the Froude number (Cushman-Roisin and Beckers, 2011), which is the ratio of flow velocity to gravity wave velocity given by

$$\mathrm{Fr} = \frac{U}{NH}.$$

The ratio of the Rossby number to the Froude number gives the Burger number

$$\mathrm{Bu} = \frac{\mathrm{Ro}}{\mathrm{Fr}} = \frac{NH}{fL}.$$

When $\mathrm{Bu} = \mathcal{O}(1)$ both the effects of rotation and stratification are important to the dynamics, and corresponds to the most efficient conversion of potential to kinetic energy. This then suggests that

$$\frac{f}{N} \approx \frac{H}{L} = \delta.$$

The smallness, and relative magnitude, of the above nondimensional parameters allows for approximations to be made: the geostrophic approximation is suitable when $\mathrm{Bu} < 1$ and the hydrostatic approximation is suitable when $\delta \ll 1$. The semigeostrophic equations, which have both the geostrophic and hydrostatic balance approximations, will be discussed in the next section.

2.3.1 Semigeostrophic equations

The semigeostrophic equations provide a simplified model in which to study frontogenesis. Starting from the Boussinesq equations in Section 2.2.3, the hydrostatic approximation is made. The hydrostatic approximation is common in geophysical flows, and for synoptic scale motion a typical aspect ratio is $\delta = 0.01$. This gives the equations as

$$\frac{Du}{Dt} - fv = -\frac{\partial \phi}{\partial x}, \tag{2.34}$$

$$\frac{Dv}{Dt} + fu = -\frac{\partial \phi}{\partial y}, \tag{2.35}$$

$$\frac{g}{\theta_0}\theta = \frac{\partial \phi}{\partial z}, \tag{2.36}$$

$$\frac{D\theta}{Dt} = 0, \tag{2.37}$$

$$\nabla \cdot \mathbf{u} = 0. \tag{2.38}$$

Using values representative of the large scale flow at mid-latitudes the Rossby number is typically $\mathrm{Ro} = \mathcal{O}(0.1)$, so that a series expansion is possible (Hoskins, 1975):

$$u = u_g + \mathcal{O}(\mathrm{Ro}); \quad u_g = -\frac{1}{f}\frac{\partial \phi}{\partial y}, \tag{2.39}$$

$$v = v_g + \mathcal{O}(\mathrm{Ro}); \quad v_g = \frac{1}{f}\frac{\partial \phi}{\partial x}, \tag{2.40}$$

where the subscript $(\cdot)_g$ corresponds to the geostrophic value. The use of the geostrophic momentum approximation (Hoskins, 1975) gives

$$\frac{Du_g}{Dt} - fv = -\frac{\partial \phi}{\partial x}, \tag{2.41}$$

$$\frac{Dv_g}{Dt} + fu = -\frac{\partial \phi}{\partial y}, \tag{2.42}$$

$$\frac{g}{\theta_0}\theta = \frac{\partial \phi}{\partial z}, \tag{2.43}$$

$$\frac{D\theta}{Dt} = 0, \tag{2.44}$$

$$\nabla \cdot \mathbf{u} = 0. \tag{2.45}$$

The system of Equations (2.41) to (2.45), together with Equations (2.39) and (2.40), are the semigeostrophic equations in physical space. Whilst the momentum has been approximated by its geostrophic value, which is valid for small Lagrangian Rossby number, the trajectories still use the full velocities, i.e.

$$\frac{D}{Dt} = \frac{\partial}{\partial t} + u\frac{\partial}{\partial x} + v\frac{\partial}{\partial y} + w\frac{\partial}{\partial z}.$$

Equations (2.41) to (2.45) give prognostic equations for the geostrophic velocities, whilst the full velocities are only defined diagnostically.

As written above the semigeostrophic equations are appropriate when $\mathrm{Ro} < \mathrm{Fr}$, or equivalently $\mathrm{Bu} < 1$. The benefits of the SG equations are given in Section 2.3.3, but first consideration is given to a change of coordinates.

2.3.2 Coordinate transformation

In this section two coordinate transformations are presented in the context of the semigeostrophic equations. The first is the geostrophic coordinate transformation, first presented in Hoskins and Bretherton (1972) in the vertical slice, and extended to three dimensions in Hoskins (1975). The second is the isentropic coordinate transformation, which uses the potential temperature as a vertical coordinate (Cullen, 2006).

The geostrophic transformation is advantageous in that it eliminates the nonlinearity in the tendency equations, and moves it to the transformation between the physical and dual space. The isentropic transformation is necessary in the proofs of existence of solutions to the semigeostrophic equations in dual space.

It is common to use the "semigeostrophic equations" to refer to the dynamical equations with the geostrophic momentum and hydrostatic approximation in both physical and dual space. In the rest of this thesis SG will refer to the equations in *physical* space, and where the coordinate transformation has been used, it will be explicitly noted as dual space.

Geostrophic coordinates

The geostrophic coordinate transformation of (Hoskins, 1975) corresponds to

$$(X, Y, Z, T) = \left(x + \frac{v_g}{f}, y - \frac{u_g}{f}, z, t\right), \tag{2.46}$$

where uppercase variables refer to the dual space whilst lower case correspond to physical space. The name "geostrophic coordinates" refers to the fact that they represent the positions air parcels would have if they were transported by the geostrophic velocity.

If the geopotential in dual space is transformed as

$$\varphi = \phi + \frac{1}{2}\left(u_g^2 + v_g^2\right), \tag{2.47}$$

then it can be shown, (Hoskins, 1975), that

$$\left(\frac{\partial\varphi}{\partial X}, \frac{\partial\varphi}{\partial Y}, \frac{\partial\varphi}{\partial Z}\right) = \left(\frac{\partial\phi}{\partial x}, \frac{\partial\phi}{\partial y}, \frac{\partial\phi}{\partial z}\right). \tag{2.48}$$

Equation (2.48) shows that gradients of the geopotential are preserved between the physical and geostrophic spaces, and so can be described as a "contact transformation", (Blumen, 1981).

Isentropic coordinates

The isentropic coordinate transformation is reviewed in Cullen (2006), and corresponds to

$$(X, Y, Z, T) = \left(x + \frac{v_g}{f}, y - \frac{u_g}{f}, \frac{g}{\theta_0 f^2}\theta, t\right), \tag{2.49}$$

where the vertical coordinate is now a function of the potential temperature, and the geopotential becomes

$$\varphi = \frac{1}{f^2}\phi + \frac{1}{2}\left(x^2 + y^2\right), \tag{2.50}$$

so that

$$(X, Y, Z) = \nabla\varphi. \tag{2.51}$$

This transformation gives solutions to the semigeostrophic equations, provided that φ is convex (Cullen, 2006, Definition 3.2).

If the dependency is switched so that coordinates in physical space become functions of dual space coordinates

$$\mathbf{x} = \left[x\left(X, Y, Z\right), y\left(X, Y, Z\right), z\left(X, Y, Z\right)\right],$$

then Cullen (2006, Theorem 3.5) can be used to explain the formation of discontinuities in physical space, which is discussed in Section 2.4.2. Briefly, the evolution in dual space, with domain Σ, corresponds to a free boundary problem as the evolution of u_g, v_g changes the original domain.

When mapping back to physical space, with domain Ω, only points on the convex hull of Σ can be mapped onto the physical boundary, $\partial\Omega$. In doing so parcels outside of Σ can be mapped onto an infinitesimal filament in Ω, i.e. the formation of a discontinuity. This is covered in Section 2.4.2 for the two-dimensional case; an illustration is given in Figure 2.2.

Solutions to the semigeostrophic equations have been shown to exist for arbitrarily large times. In particular, weak Lagrangian solutions in dual variables (Benamou and Brenier, 1998) and weak Lagrangian solutions in physical variables (Cullen and Feldman, 2006). The convergence of smooth solutions from the Boussinesq equations to solutions of the semigeostrophic equations has been shown formally in Brenier and Cullen (2009).

Numerical solutions to the SG equations have been obtained using a geometric model in dual space (Cullen, 2007a). The convergence of numerical solutions using this model to the analytic solutions has been given in Cullen et al. (2007). This is one of the main benefits in using the semigeostrophic equations in asymptotic convergence: the solutions have been shown to exist for long times whilst it is not known if the same is true for solutions of the Boussinesq equations.

2.3.3 Conservation properties

The semigeostrophic equations have the following Lagrangian conservation laws (Hoskins, 1975). The first is for the geostrophic potential vorticity

$$\frac{Dq_g}{Dt} = \frac{D}{Dt}\left(\zeta_g \cdot \nabla\theta\right) = 0, \tag{2.52}$$

where the geostrophic vorticity, ζ_g, is given by

$$\zeta_g = \nabla \times \mathbf{u}_g + f\hat{\mathbf{z}} + \frac{1}{f}\left(\frac{\partial\left(u_g, v_g\right)}{\partial\left(y, z\right)}, -\frac{\partial\left(u_g, v_g\right)}{\partial\left(x, z\right)}, \frac{\partial\left(u_g, v_g\right)}{\partial\left(x, y\right)}\right), \tag{2.53}$$

and the geostrophic velocity is

$$\mathbf{u}_g = \left(u_g, v_g, 0\right).$$

The second is for the energy

$$\frac{D}{Dt}\left(E_{ke}^g + E_{pe}\right) = 0,$$

where

$$E_{ke}^g = \frac{1}{2}\left(u_g^2 + v_g^2\right), \quad E_{pe} = -\frac{g}{\theta_0}\theta z,$$

are the geostrophic kinetic and potential energy, respectively. In addition, Hoskins (1975) states the conservation of potential temperature and the evolution equation for the geostrophic vorticity.

In the review of Cullen (2007a) the conservation properties, in particular the Lagrangian conservation of potential vorticity and energy, were highlighted as necessary for long term solutions. The analogue of the semigeostrophic and Boussinesq equations having similar conservation properties will be used later in this thesis to analyse the long term evolution. The application of asymptotic convergence in the Eady problem is covered in Chapter 4, with particular mention to the effects on the energy and potential vorticity (PV), whilst the results are presented in Chapter 5.

2.4 Survey of general results from slice models

As mentioned at the beginning of this chapter, there are two main mechanisms responsible for frontogenesis, both of which can be studied using the equations of motion given in the previous section. This section will summarise the key features of solutions of vertical slice models of fronts, using results from both mechanisms. The aspects of the frontal discontinuity, potential vorticity and Lagrangian dynamics and unbalanced motion will be discussed, all of which are key features of frontogenesis, irrespective of the underlying model. Solutions specific to the shear (Eady) model will be described in the next section.

Hoskins and Bretherton (1972) was a fundamental body of work on frontogenesis, including an analytic result for the Eady model in dual space. Hoskins and Bretherton used the assumption of cross-front geostrophic balance, building on earlier work by Sawyer (1956) and Eliassen (1959), which required that $\epsilon = {}^{U}/_{V} \ll 1$, i.e. the across-front velocity is negligible compared to the along-front velocity. Many of the results that follow, and in particular the development of semigeostrophic theory, were made possible in no small part by the results presented in Hoskins and Bretherton (1972).

2.4.1 Solution features

Early numerical experiments were carried out by Williams and Plotkin (1968) using the quasigeostrophic model, which suggested that fronts could form, provided that there was an initial variation in the potential temperature on the boundary. The QG model permits solutions in which a weak surface front is formed, but it does not show the same tendency to discontinuity found in the SG equations; once the ageostrophic motion becomes large in the QG model the underlying assumptions break down. Insights into the omitted ageostrophic effects were shown in Williams (1972) by comparing solutions from the linear and nonlinear primitive equations.

Experiments representative of frontogenesis on more realistic background state, as given by mesoscale perturbations on a smooth synoptic state, were investigated in Hoskins et al. (1984) and remarked in Davies and Muller (1988). A small perturbation of warm air ahead of the surface cold front could lead to an additional updraft ahead of the front, in good agreement with observations (see Section 2.1.1). Whilst these disturbances did modify the structure close to the surface, the large scale growth and structure of the baroclinic wave were little altered by them.

By considering perturbations in the deformation model HB72 noted that the inclusion of latent heat, as a source term in the potential temperature equation, increased the ageostrophic circulation and frontogenesis, whilst the inclusion of a vertical boundary layer had a frontolytic (reducing the strength of the front) effect. HB72 inferred that whilst mixing is not important in the

early stage of frontogenesis, once the gradients become large the Richardson number will become $\mathcal{O}(0.1)$ and so shear instability and mixing will influence the subsequent behaviour.

2.4.2 Frontal discontinuities

In HB72 the use of the SG equations in dual space, and the convergence from the induced ageostrophic circulation, showed that there was a tendency to form a discontinuity in finite time, owing to the map back to physical space becoming singular. The semigeostrophic PV was shown to satisfy an elliptic Monge-Ampère equation, which implied that the discontinuities could only form on the boundary. For a two layer model representing the tropopause the tendency to discontinuity was not found, owing to the fact that the free surface nature of the tropopause was sufficient to prevent the collapse occuring, (Hoskins and Bretherton, 1972). This is consistent with the semigeostrophic equations being unable to form fronts without boundaries, (Ambrosio et al., 2012).

In Cullen and Purser (1984) it was shown that weak solutions to the semigeostrophic equations that contained a frontal discontinuity existed, based on the Lagrangian form of the conservation laws. In addition, and as discussed in the next section, Cullen and Purser (1984) showed that there was no contradiction in Lagrangian conservation of potential vorticity which changed the Eulerian mean PV. The concept of the PV anomaly forming on the boundary was first proposed in Bretherton (1966), in which gradients in the potential temperature on the boundary could be interpreted as gradients of infinitesimal PV sheets just inside the domain. This mechanism of PV intrusion into the physical domain has been well accepted, (Nakamura and Held, 1989; Nakamura, 1994).

An informative interpretation of the formation of the discontinuity in physical space is shown in Figure 2.2. As the boundaries deform in dual space the convex hull is mapped back to physical space, (Cullen, 2006), and so two air parcels that were separate in dual space become adjacent in physical space.

In Koshyk and Cho (1992) the growth of the discontinuity in physical space suggests that Lagrangian deformation of the surface in dual space is key in being able to allow the front to increase intensity whilst remaining stationary in physical space. Koshyk and Cho note that the appropriate boundary conditions require that air parcels on the boundary in dual space remain on the boundary for all times, but, it is possible that the boundaries themselves can deform. Thus, while the front itself was shown to be a material surface, as supported by their plots of circulation in physical space, an interesting aspect of the further evolution is that parcels of air initially on the warm side could end up on the cold side of the front in physical space, due to the boundary deformation in dual space.

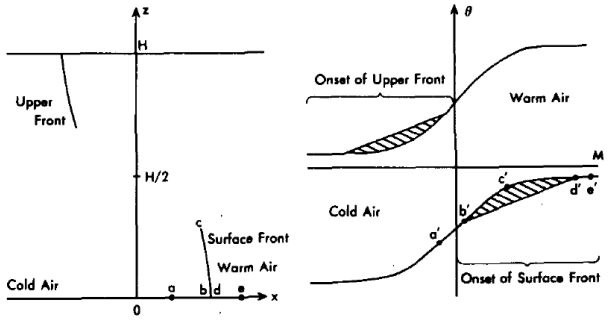

Figure 2.2: *Illustration of frontal discontinuity in physical* (x, z) *space (left) and gradient* $(v+fx, \theta)$ *space (right), taken from Cullen and Purser (1984). The shaded region in gradient (dual) space maps to the discontinuity in physical space.*

The front acts as a material surface in physical space, which has been supported by the agreement with observations in Section 2.1.1. Other experiments have found similar behaviour, for example using the viscous semi-geostrophic equations in physical space (Xu et al., 1998; Gu and Xu, 2000). Lagrangian experiments have been carried out by Garner et al. (1992), the results of which from a potential vorticity perspective will form the next section.

An alternative approach of investigating the tendency to discontinuity was found in the work of Blumen (1979), which showed that the meridional velocity equation could be manipulated to show it as a form of the viscous Burgers' equation. The inviscid Burgers' equation leads to non-unique solutions, whilst the viscous Burgers' equation supports shocks, where the effect of viscosity is to limit the scale reduction.

2.4.3 Potential vorticity dynamics

In Garner et al. (1992), hereafter G92, the PV dynamics were investigated using a three-layer Lagrangian model. The solutions of G92 showed that the frontogenesis evolution is strongly deformational, and that the interfaces between the layers of PV have a tendency to "roll up" into the domain.

It is interesting to compare the roll up shown in Figure 2.3 with the deformation in dual space shown in Figure 2.2. In the physical domain the rolling up manifests itself as a PV intrusion from the boundary, which in the limit should appear as an infinitesimal filament. In both examples the PV intrusion never becomes part of the circulation within the vertical slice since it is on the contact discontinuity.

Xu and Gu (2000) provided a very succinct description of the processes involved within the physical domain, from a geostrophic potential vorticity,

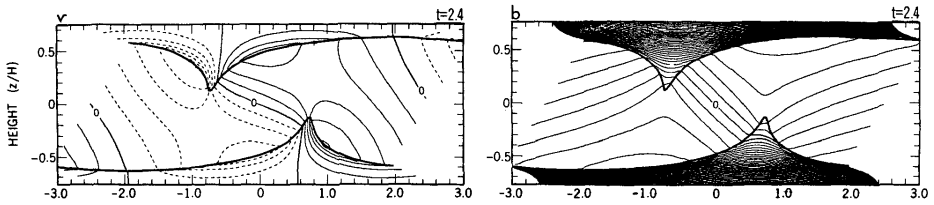

Figure 2.3: *Three layer fully Lagrangian model showing "rolling up" of the interface, meridional velocity field on the left and potential temperature on the right, taken from Garner et al. (1992).*

GPV, perspective. The GPV anomalies form first on the boundaries, but through diffusion explicitly included in the model a small amount of GPV is able to enter the interior. Once inside the GPV intrusion is advected further into the interior, owing to the induced circulation from the GPV, as well as further GPV being generated at the boundary as the front strengthens. The circulation reduces in the horizontal, leading to the two plumes coalescing into a single vertical column. This then tilts forward and causes the wave to recede, and generation of GPV at the boundaries stops. This analysis is very much consistent with other viscous results, e.g. (Nakamura and Held, 1989; Nakamura, 1994).

The effects of different boundary layer parameterisations on the geostrophic potential vorticity were discussed in Xu and Gu (2000). The no-slip case lead to a large negative GPV anomaly after the initial positive anomaly had formed, stopping the continued growth of the wave, whilst the behaviour of the free slip case was comparable to the inviscid results.

For the semigeostrophic equations the solution is determined entirely by the semigeostrophic PV in dual space, which is itself a Lagrangian conserved quantity, see Section 2.3.3. The PV intrusion in physical space is an artefact of the transformation from dual to physical space without being part of the solution, (Cullen, 2006). The semigeostrophic PV is conserved in physical space, as long as the integration does not include the frontal region.

In the Boussinesq incompressible model considered in this thesis the Lagrangian conservation of PV given by Equation (2.29) suggests an equivalent Eulerian conservation law,

$$\frac{\partial q}{\partial t} + \nabla \cdot (q\mathbf{u}) = 0. \tag{2.54}$$

This conservation law will be satisfied if solutions stay smooth. It is not known if the Boussinesq equations have smooth solutions at a front, but in practice the numerical solutions always collapse below the grid scale. Equation (2.54) is then violated because of the explicit or implicit numerical dissipation. This corresponds to the PV source which is present in the semigeostrophic solution.

Experiments comparing the evolution of a baroclinic wave using the nonlinear balance (NLB) model and the primitive equation (PE) model were shown in Ziemianski and Thorpe (2002). The early evolution of the waves were in very good agreement with each other, showing that in the early stages of development the PV is conserved by the PE model. Once the surface front reached an appreciable amplitude there was a marked difference in the two solutions, in which the PV intrusion was found in the PE model but clearly not in the NLB model, which enforced conservation of the PV. The intrusion was stated to be spurious, but, it is in fact quite consistent with the discussion outlined above.

The consideration of the PV dynamics in frontogenesis highlights why it is a challenging problem for Eulerian numerical methods. In the inviscid case the PV intrusion is never part of the flow, in that it represents the contact discontinuity. In an Eulerian numerical method it is not possible to stop the PV intrusion spuriously mixing, in that it will be resolved on a finite grid. Once this occurs the large scale solution is altered, with the implication that the long term predictability will deteriorate.

2.4.4 Unbalanced dynamics

Whilst sources of inertia gravity waves (IGWs) in geophysical fluid dynamics include topographical forcing from sharp terrain and an adjustment process to a geostrophically balanced state, the gravity waves observed in models of fronts fall into a different category. The review of Plougonven and Zhang (2014) provides a comprehensive account of IGWs in baroclinic jet/front systems. The generation of IGWs from a front is described as "spontaneous balance adjustment" to describe the continuous generation of IGWs from a predominantly balanced flow. Note that this is not the same as geostrophic adjustment since the emission is continuous not instantaneous, the imbalance does not decay, there is no simple final state that can be predicted in advance, and finally the waves do not propagate away (Plougonven and Zhang, 2014).

Ley and Peltier (1978) used the semigeostrophic model of HB72 to investigate the generation of IGWs. By calculating a secondary ageostrophic circulation, but which did not couple back into the model dynamics, they were able to identify a source of IGWs from the surface front, which were comparable in strength to observations.

Gall et al. (1987) used a nested nonhydrostatic model to look at whether there was an inviscid minimum scale on fronts. For the high horizontal resolution experiments the minimum scale was controlled by the vertical resolution; there was a linear relation between the vertical resolution and the final width, with no evidence of any natural limit. The reason for the vertical resolution controlling the width was attributed to the shallowness of the model front with the slope being 1/140. No evidence of "converged"

results, in the sense of further refinements would produce no smaller scales, were presented.

In Gall et al. (1988) the deformation front was used to investigate the generation of gravity waves, as seen earlier in Gall et al. (1987). The waves shown in G87 were not Kelvin-Helmholtz waves; although there were small areas where Ri $< 1/4$ these were not large enough to explain all the waves observed. Similarly, symmetric instability was ruled out owing to the model being adiabatic and inviscid. The vertical gravity waves above the front were described as "stationary, hydrostatic gravity waves forced by nongeostrophic and nonhydrostatic accelerations in the frontal zone", which suggests that they would not be captured by a SG model.

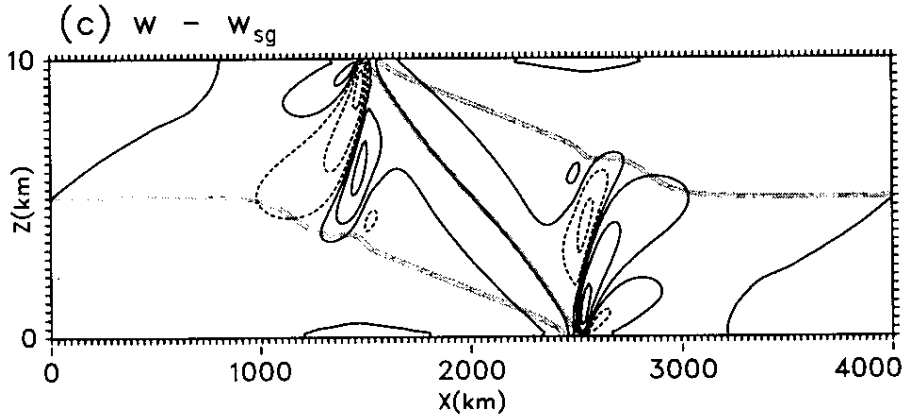

Figure 2.4: *Gravity wave jet originating from the surface fronts, taken from Snyder et al. (1993). Contours are at* $\pm 1, 3, 6$ cm s^{-1}.

An example of the gravity waves generated at fronts is shown in Figure 2.4, in which the Euler equations were integrated and compared with diagnostic semigeostrophic fields, showing the gravity wave jet in the vertical velocity (Snyder et al., 1993). The model was nonhydrostatic but almost identical results were found for hydrostatic integrations, suggesting that whilst not present in the SG solutions the Euler equations permit the generation of hydrostatic IGWs at fronts.

The observed and modelled IGWs are found for finite Rossby number, whilst in the SG limit there should not be any. The convergence between the Euler and semigeostrophic equations, see Section 2.3, suggests that the gravity wave activity should reduce as Ro $\to 0$, as will be shown in Chapter 5.

2.4.5 Physical parameterisation effects

In the final section results using modifications to the frontogenesis models are presented, to show the changes that the neglected physical processes have on the subsequent dynamics. In all cases the general features of the solutions are the same as previously discussed, unless explicitly stated.

In Knight and Hobbs (1988) experiments were carried out using the Eady model with moisture. The inclusion of moisture showed a banding structure of precipitation ahead of the front, in agreement with the observations of cold fronts in Section 2.1.1. The inclusion of moisture was also shown to increase the vertical circulation associated with a cold front by Ross and Orlanski (1978), as well as generated gravity waves which were suggested as being capable of influencing precipitation further afield.

The effect of diffusion, and in particular boundary layer parameterisations, has been noted previously. The effect of vertical diffusion is that the peak amplitude of the meridional jet is lifted off the surface, giving a more realistic front (Xu et al., 1998; Keyser and Anthes, 1982). The lifting of the jets corresponded to significant areas of negative PV in the domain, suggesting that it would not be consistent with a large scale flow with a conserved PV.

2.5 Shear induced frontogenesis solutions

In this section results specifically for the Eady model of frontogenesis through vertical shear are presented. The discussion extends the general solution features discussed in the preceding section. The full details of the problem specification, along with the relevant parameters and techniques used, is presented in Chapter 4.

As mentioned in the Introduction, the work of Eady (1949) used baroclinic instability to explain the growth of planetary and cyclone waves observed in mid-latitude weather systems. The mechanism of the instability was to exchange available potential energy, as provided by the poleward temperature gradient, into kinetic energy.

Eady solved the linearised, quasigeostrophic model in a vertical slice bounded by two rigid lids. Whilst the top boundary is artificial, it is the surface cold front that is of interest. The structure of the Eady wave is shown in Figure 2.5. Whilst most of the fields tilt backwards (Westwards) with height, the entropy tilts forwards; the resulting circulation pattern of rising warm and descending cold air clearly corresponding to a release of potential energy.

The linear Eady model has been very well studied in the literature, with textbooks such as Gill (1982) and Pedlosky (1987) containing detailed analyses. Although the nonlinear effects are required for the formation of a

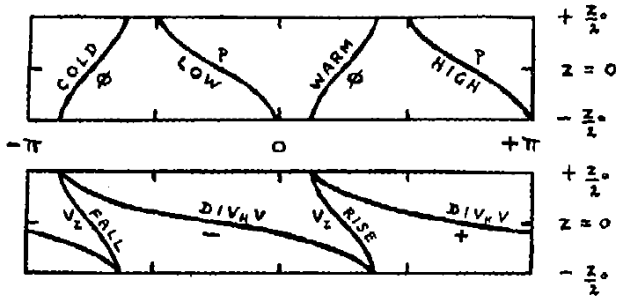

Figure 2.5: *Phase structure for pressure & entropy (top) and vertical velocity & horizontal divergence (bottom), taken from Eady (1949, Fig. 1a). The bottom plot shows the shape of the circulation within the vertical slice, whilst the top plot shows the temperature and pressure distribution.*

frontal discontinuity, Eady remarked that the idea of frontogenesis occurring through the dynamical processes was possible.

2.5.1 Edge waves

The solution to the Eady problem can be seen as the interaction of edge waves on the top and bottom surfaces. This has been covered in the literature, with Gill (1982, Section 13.3) providing a detailed account. In Figure 2.5 the growing mode keeps the same structure, such that the phase between the two waves is constant, during the linear stage of the growth.

A similar approach was used in Davies and Bishop (1994), in which the perturbations were modelled as edge waves in the thermal profile on the boundaries. The development of the long waves became phase locked, such that they appeared stationary, whilst the phase of short waves changed, either advancing or decreasing, until they reached the phase locking value.

The edge wave interpretation has also been remarked by Egger (2009), in which the Eady solutions correspond to a specific combination of sine and cosine modes. In Plougonven et al. (2005) the vertical shear model was coupled with a radiating upper boundary to show a coupling between balanced and unbalanced motion outside of geostrophic adjustment. Below the critical level the structure of the waves matched that of the Eady edge waves, whilst above they were gravity waves. Coexistence of balanced and unbalanced motion for atmospheric flows has been shown in the review of Vanneste (2013).

2.5.2 Evolution prior to collapse

Using a simplified two-layer model of baroclinic instability Williams (1965) was able to reproduce the qualitative features of a frontal region, including

the steep gradients in the along-front wind and the strong vertical updrafts. These were some of the first numerical experiments using the primitive equations to show that the ageostrophic effects neglected in quasigeostrophic theory were responsible for the tendency to discontinuity shown analytically later in Hoskins and Bretherton (1972).

These two-layer experiments were a precursor to further numerical results of Williams (1967) using the primitive equations. Increasing resolution did not stop the tendency of the front to collapse to the grid scale, supporting the tendency to discontinuity.

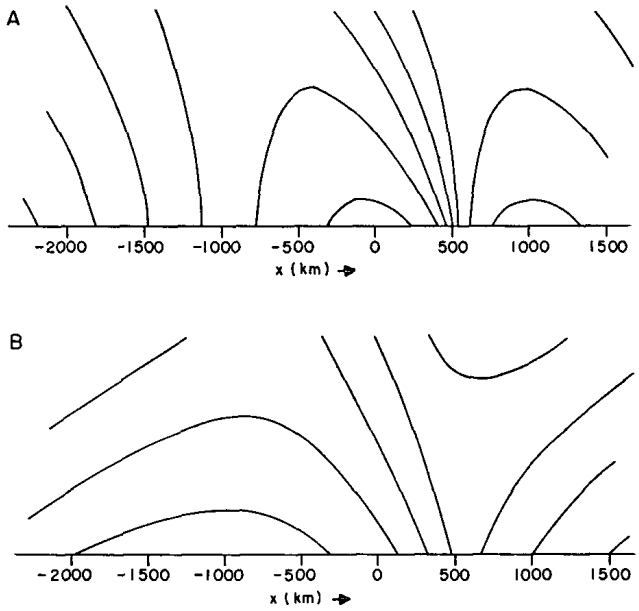

Figure 2.6: *Analytic frontal structure taken from Hoskins and Bretherton (1972), their Figure 11. (a) is the meridional wind with contours every* 15.2 m s^{-1} *and (b) is the potential temperature with contours every* 10.3 K.

The frontal structure, in terms of the meridional wind and the potential temperature, can be seen in Figure 2.6. HB72 found very good agreement between their numerical results and the analytic solution. No further numerical results were shown for later times, but it is apparent from Figure 2.6 that the contours are beginning to come together, for both fields, and the strength of the front is rapidly increasing.

In the context of the semigeostrophic model the term "frontal collapse" refers to the point at which the map from dual space becomes singular. In a numerical context on a fixed Eulerian grid the term refers to the time at which the front reduces to the grid scale. It is likely that whilst the early numerical results showed the correct features and behaviour at least part

of the spurious oscillations found in Williams (1967) are due to insufficient resolution.

One approach to circumvent this problem is to increase resolution where it is required. Integrations using a finite difference scheme combined with mesh adaptivity were presented in Budd et al. (2013). For meshes with the same number of elements the adaptive mesh was much more successful at capturing the nonlinear evolution of the growing Eady wave. In particular the results highlighted the consequence of the implicit numerical diffusion in the under resolved experiments in both the amplitude and structure of the wave.

Comparisons between solutions using the full and SG equations have also been used to investigate the ageostrophic dynamics. In Volkert and Bishop (1990) there was good agreement between analytic solutions from the SG model with numerical results using the full model. A strong vertical jet of IGWs could be observed in the times leading up to collapse, which was attributed to insufficient resolution, but later results, (Snyder et al., 1993), suggest that this was a genuine source of waves.

2.5.3 Post-collapse and predictability

The evolution of the Eady wave can be split up into several distinct phases. The initial growth is well described by the linear instability, and corresponds to an exponentially growing normal mode in physical space. Once the wave reaches a certain amplitude the nonlinear effects become significant, and the ageostrophic circulation accelerates the strengthening of the front, indicating the tendency to discontinuity. The behaviour post-collapse is harder to state definitively. It is dependent on several factors such as the numerical method, as well as the form and magnitude of any diffusion used. It is the behaviour near and following collapse that forms the discussion of the results in the current section.

The solution of the Eady problem quickly reduces to the grid scale. To be able to continue integrations using an Eulerian method past the point of frontal collapse it becomes necessary to restrict the generation of the smallest scales. In a numerical context this can be achieved through an additional diffusive term, which would limit the motion based on a viscous length scale. Experiments using the viscous Eady problem were carried out in Nakamura and Held (1989), hereafter NH89, for the hydrostatic primitive equations and for the semigeostrophic equations in Nakamura (1994), hereafter N94.

In NH89 it was shown that the large scale behaviour of the solution post-collapse was highly sensitive to the form and magnitude of the diffusion used. When looking at the large scale flow useful diagnostics can be extracted from the meridional velocity field, such as the maximum absolute value and the root mean square. The variation of the evolution of the maximum meridional velocity with the eddy viscosity is shown in Figure 2.7, and similar results

were found when the diffusion for the potential temperature was varied.

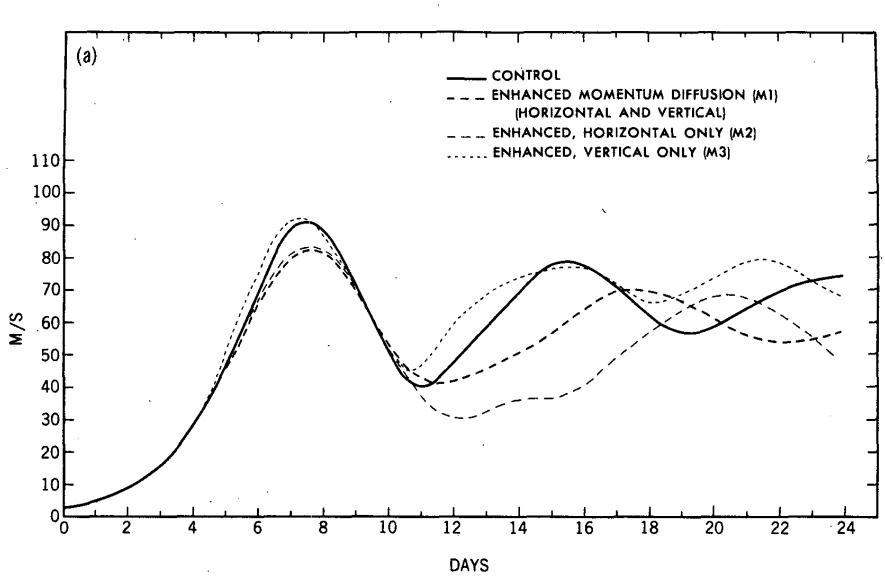

Figure 2.7: *Variation of evolution of maximum meridional wind with momentum diffusion, taken from Nakamura and Held (1989).*

Blumen (1990a) used momentum diffusion in a small region around the fronts in a semigeostrophic model to allow integrations to continue past collapse, and to attempt to maintain the inviscid dynamics away from the transition region. The results did not show the same periodic behaviour seen in NH89 or N94. Diffusion was highlighted as a key factor that determined whether a steady-state was reached, in which mixing and frontogenetic forcing balanced as shown in other models of fronts, (Orlanski and Ross, 1977), or whether the mixing would dominate and frontolytic effects would take over.

In a trio of papers by Xu et al. (1998); Xu and Gu (2000); Gu and Xu (2000) the viscous SG Eady model was investigated with various boundary layer parameterisations. The effect of the diffusion was to inhibit the growth, and to reduce the magnitude of any secondary lifecycles post-collapse.

One aspect that is important in the post-collapse behaviour is the treatment of unbalanced motion. After collapse the unbalanced motion becomes the same magnitude as the balanced dynamics, as shown in Snyder et al. (1993) and Figure 2.4. This suggests that accurate treatment of the IGWs is necessary for the correct long term evolution when solving the full equations.

From the results covered thus far it might be reasonable to assume that the post-collapse behaviour is not well defined. The results, though, share a common feature in that they are Eulerian, and so require some numerical

diffusion in order to continue the integrations. These results can be classified as viscous solutions, whilst the Eady wave is inviscid.

True inviscid results have been presented in Cullen and Roulstone (1993a); Cullen (2006, 2007a) by using a fully Lagrangian method. These results show a much larger amplitude, and highly predictable behaviour for several lifecycles after the initial front. The results are also very robust, being well resolved on a relatively coarse Lagrangian mesh despite the presence of the discontinuity, and showing near identical agreement in the post-collapse behaviour.

This, then, raises several important questions, as stated in the research objectives of Section 1.3. Firstly, whether it is possible to maintain a balanced solution post-collapse. Secondly, what is the effect of the unbalanced motion on the predictability. Finally, whether the Eulerian solutions of the incompressible Boussinesq equations converge to the inviscid Lagrangian semigeostrophic solutions.

2.6 Summary

In this chapter a general overview of vertical slice models of fronts has been presented. The use of the two-dimensional models is justified both *a priori*, through considering the equations of motion and the important terms, but also *a posteriori* by good agreement between results of the simplified models and observations of the real atmosphere.

The general equations of motion, complete with the approximations made to simplify the equations to the incompressible Boussinesq Euler equations were presented. The approximations, and the potential limitations they make, were discussed.

A balanced model, given by the semigeostrophic equations, was shown to be derivable from the Euler equations. This was subject to the requirement of small *Lagrangian* Rossby number, whilst the other important nondimensional parameters were also covered. Obtaining solutions to the semigeostrophic equations was shown to be made possible through the use of certain coordinate transformations.

General solutions to slice models of fronts were shown. The notable features included the Lagrangian evolution in dual space, the collapse down to a discontinuity in finite time, the front behaving as a material surface and the potential vorticity dynamics within the physical domain.

Results for the Eady model have been presented. In all cases the pre-collapse behaviour was almost identical, being well resolved even on a coarse Eulerian grid. The post-collapse evolution using Eulerian methods, though, showed a wide range of behaviour, whilst the inviscid Lagrangian results suggested that there should be baroclinic lifecycles which were not being observed.

Chapter 3

Discretisation methods for numerical weather prediction

It's always seemed like a big mystery how nature, seemingly so effortlessly, manages to produce so much that seems to us so complex. Well, I think we found its secret. It's just sampling what's out there in the computational universe.

S. Wolfram (2010)

Contents

In this chapter an overview of some numerical methods commonly used in weather prediction is presented. This is not meant to be an exhaustive review of the state of the art, but rather describe well-established techniques and their prevalence in operational centres around the world.

The UK Met Office Unified Model uses a semi-implicit semi-Lagrangian numerical method to solve the fully compressible equations of motion, with the same dynamical core used for both short range forecasts and climate simulations, (Davies et al., 2005). The European Centre for Medium-Range Weather Forecasts (ECMWF) uses a spectral model for wave propagation, combined with a semi-Lagrangian treatment of advection, (Ritchie et al., 1995).

The Weather Research and Forecasting model uses a combined implicit / explicit Eulerian dynamical core, with Runge-Kutta time-stepping coupled with high-order transport schemes, (Michalakes et al., 2004). Eulerian advection has been coupled with a semi-implicit time discretisation in the German Weather Service's GME model, (Majewski et al., 2002).

Alongside the dynamical cores there are also several choices for the grid. The latitude-longitude grid is often used, with both equispaced and Gaussian grids used. More isotropic grids, such as the icosahedral grid, that avoid the problem of clustering of grid points at the poles are also used (Staniforth and Thuburn, 2012).

No single method has widespread adoption. The topic of comparing and evaluating these dynamical cores has been the subject of much research; Lauritzen et al. (2010a) present an exhaustive comparison of many operational models following a workshop in 2008.

In the rest of this thesis the semi-implicit method coupled with semi-Lagrangian and Eulerian transport schemes using a finite-difference discretisation on a uniform grid will be used. Whilst this might be a narrow scope given the large range of models outlined above, the test cases and results presented in the later chapters will provide a framework to evaluate other numerical methods not considered.

3.1 Finite-difference discretisation

In this section a brief overview of the application of the finite-difference method in the context of vertical slice models is given. In the following sections the horizontal refers to the zonal and meridional directions, whilst the vertical refers to the modified vertical coordinate given in Section 2.2.2. The equations of motion are the Boussinesq equations, given by Equations (2.26) to (2.28).

3.1.1 Notation

A continuous variable, $\chi(x, y, t)$, is approximated by its value on a uniformly spaced grid and at finite intervals in time. Subscripts will refer to spatial indices, whilst superscript will refer to temporal index. Written explicitly in two-dimensions this gives

$$\chi^n_{i,j} = \chi(x_0 + i\Delta x, y_0 + j\Delta y, t_0 + n\Delta t).$$

This notation will be used interchangeably, with the former preferred for the description of the Eulerian methods and the latter for the semi-Lagrangian method.

Derivatives are approximated using two or more neighbouring points, in space or time, through a Taylor series expansion. The order of the approximation will refer to the leading order term in the truncation of the series, so that n^{th} order accurate in space corresponds to $\mathcal{O}(\Delta x^n)$, and similarly for accuracy in time, (Durran, 2010).

3.1.2 Horizontal grids

An overview of the horizontally staggered grids is shown in Figure 3.1. In this thesis the C-grid is chosen, as it is widely used in operational models. The C-grid does not suffer from any spurious modes, such as the "checkerboarding" in the A-grid (Acharya et al., 2007); it has good dispersion properties, (Cullen et al., 1997); and it is possible to create compact and stable second-order accurate centred differences in space, (Durran, 2010, Chapter 4).

The computational domain corresponding to a vertical slice with rigid lid boundary conditions is shown in Figure 3.2 for a C-grid staggering. For a right-handed coordinate system the positive y-direction is into the plane. The pseudo-control volumes are also highlighted in Figure 3.2. These are used in the Eulerian advection schemes described in Section 3.2.2.

3.1.3 Vertical grids

In addition to staggering the velocity components to avoid the pressure mode mentioned in the previous section, it is possible, and in fact desirable, to stagger the thermodynamic variable in the vertical. In this case the options are a Charney-Phillips grid, in which it is staggered by half a grid spacing to be collocated with the vertical component of velocity, or the Lorenz grid, in which it is collocated at the cell centres with the pressure-like variable.

In this thesis attention will be restricted solely to the Charney-Phillips grid. In particular for frontogenesis the Charney-Phillips grid was required for stability, (Cullen, 1989), as well as reducing the amount of spurious gravity waves from intense frontal regions, (Cullen et al., 1997).

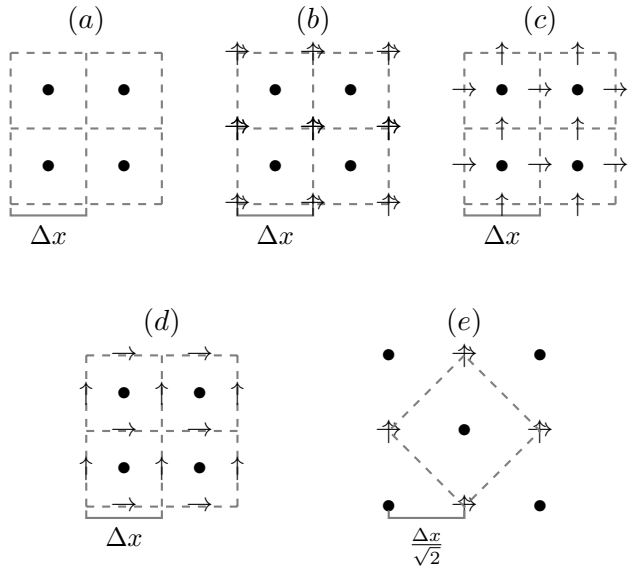

Figure 3.1: *Overview of the horizontal staggered grids, (Arakawa and Lamb, 1977), where velocity components are given with the arrows and cell centred variables are at the nodes. The A-grid velocity components are located at the cell centres. The label above the grid corresponds to the grid type, e.g. (a) corresponds to the A-grid.*

3.2 Advection schemes

In the following section several approaches for advection, or transport, schemes are discussed. The general form of the advection equation is given by

$$\frac{\partial \chi}{\partial t} + \mathcal{A}(\mathbf{u}, \chi) = 0, \tag{3.1}$$

where χ is an arbitrary passive tracer and $\mathcal{A}$ represents the advection terms. For incompressible flow, $\nabla \cdot \mathbf{u} = 0$, the advection equation can be written equivalently in conservative form

$$\frac{\partial \chi}{\partial t} + \nabla \cdot (\mathbf{u}\chi) = 0, \tag{3.2}$$

or in advective form

$$\frac{D\chi}{Dt} = \frac{\partial \chi}{\partial t} + (\mathbf{u} \cdot \nabla)\chi = 0, \tag{3.3}$$

where

$$\frac{D}{Dt} \equiv \frac{\partial}{\partial t} + (\mathbf{u} \cdot \nabla)$$

is the material, or Lagrangian, time derivative introduced in the previous chapter. Equation (3.3) can be derived from Equation (3.2) by expanding

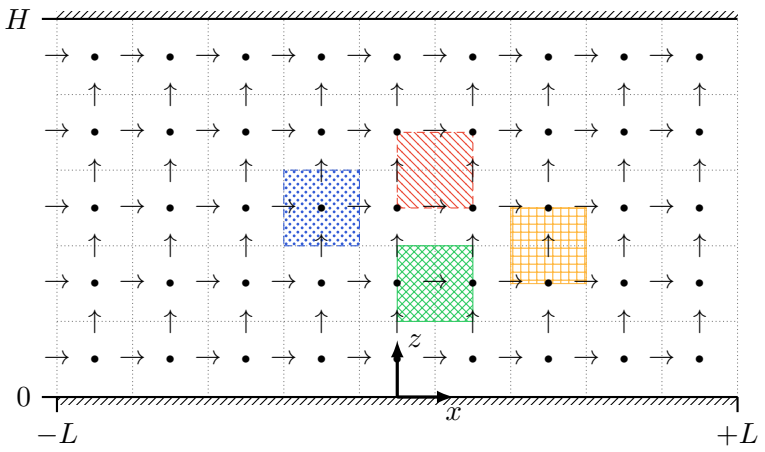

Figure 3.2: *Vertical domain using a staggered C-grid variable arrangement. Highlighted in dotted-blue is a primary grid cell, in which the divergence is calculated, and in dashed-red is a dual grid cell, in which the vorticity is calculated. In addition the cell formed around a horizontally staggered variable is given in green diagonal hatching whilst the corresponding vertically staggered cell is in orange hatching.*

out the divergence term and applying the incompressibility condition. In the following sections the semi-Lagrangian and Eulerian advection schemes will be described; the semi-Lagrangian scheme will discretise the advective form whilst the Eulerian schemes will discretise the conservative form.

3.2.1 Semi-Lagrangian

The semi-Lagrangian method carries out Lagrangian advection over a single timestep, subject to the constraint that the fluid always arrives at the fixed Eulerian grid, (Robert, 1981). For a thorough review of the semi-Lagrangian method the reader is referred to Staniforth and Côté (1991). The terminology and notation in this thesis follows that of Staniforth and Côté.

Attention is focused to the two time-level method, since it offers comparable accuracy and performance but with the benefit of reduced storage of previous values compared to the three time-level alternative, (Staniforth and Côté, 1991). For the idealised test cases covered in this work storage is not an issue, but in the context of operational NWP, and moving towards ever larger supercomputers, it is desirable to choose the most efficient methods in terms of data storage and communication.

The semi-Lagrangian method can be broken down into two steps. The first of which is tracing backwards over the trajectories that arrive at each of the grid points to find the departure points. The second step is then to evaluate the field at the foot of the trajectory, which gives the value at the new time level.

The trajectories are given by

$$\frac{\mathrm{d}\mathbf{x}}{\mathrm{d}t} = \mathbf{u}. \tag{3.4}$$

For a passive tracer with the advection equation given by

$$\frac{D\chi}{Dt} = 0,$$

the corresponding semi-Lagrangian advection equation is

$$\chi\left(\mathbf{x}, t + \Delta t\right) = \chi\left(\mathbf{x}_d, t\right), \tag{3.5}$$

where $\mathbf{x}_d$ denotes the departure point at the foot of the trajectory.

Trajectories

For complex problems it is not possible to calculate the exact trajectories that arrive at each grid point, and so the trajectories are approximated to find the departure points that arrive at each grid point. The departure points,

$$\mathbf{a} = \mathbf{x} - \mathbf{x}_d, \tag{3.6}$$

where $\mathbf{a}$ is the displacement, are found by solving the following implicit equation

$$\mathbf{a} = \Delta t \mathbf{u}^*\left(\mathbf{x} - \mathbf{a}/2, t + \Delta t/2\right), \tag{3.7}$$

where $\mathbf{u}^*$ is an approximation to the intermediate velocity field centred along the Lagrangian trajectory over the time-step Δt. A second-order approximation is usually used for the intermediate velocity field such as

$$\mathbf{u}^*\left(\mathbf{x}, t + \Delta t/2\right) = (3/2)\,\mathbf{u}\left(\mathbf{x}, t\right) - (1/2)\,\mathbf{u}\left(\mathbf{x}, t - \Delta t\right) + \mathcal{O}\left(\Delta t^2\right), \tag{3.8}$$

but this can suffer from instability, (Cordero et al., 2005). In the present work the following iterated implicit scheme is used

$$\mathbf{u}^*\left(\mathbf{x}, t + \Delta t/2\right) = \vartheta_T \mathbf{u}\left(\mathbf{x}, t + \Delta t\right) + \left(1 - \vartheta_T\right)\mathbf{u}\left(\mathbf{x}_d, t\right) + \mathcal{O}\left(\Delta t^2\right), \tag{3.9}$$

where ϑ_T is a time centering parameter for the advecting velocity. This is only second-order accurate when the trajectory is centred with $\vartheta_T = 1/2$ and first-order accurate otherwise. This allows for more decentering (more implicit) in the trajectory calculation, which can be beneficial from a stability point of view, see Section 4.1. In this thesis, unless otherwise stated, $\vartheta_T = \vartheta$, where ϑ is defined in Section 3.3.2, so that the advecting velocity is decentered the same as the whole system.

Interpolation

Once the departure points have been calculated it is necessary to evaluate the field there. Since there is no guarantee that the departure points will coincide with the fixed grid it is necessary to use an interpolation method.

One of the simplest methods for interpolation is to use Lagrange polynomial interpolation. For $M+1$ points it is possible to uniquely determine a polynomial of order M that exactly interpolates the function at each of the points. Examples of Lagrange interpolating polynomials in one dimension are shown in Figure 3.3 for a discontinuous and a smooth function.

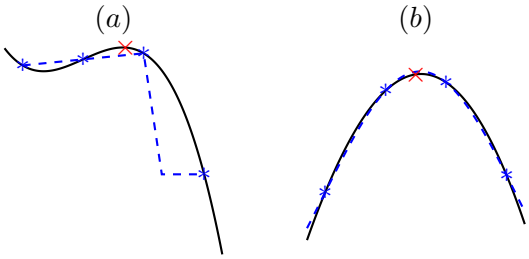

Figure 3.3: *Schematic showing one dimensional Lagrange polynomial interpolation using a piecewise cubic polynomial for (a) a discontinuous function with a sharp gradient and (b) a smooth function. In both cases the true function is the blue dashed line whilst the interpolating polynomial is the solid black line.*

Lagrange polynomials can be easily extended to higher dimensions through the Cartesian tensor product or cascade interpolation, where the full multidimensional interpolation is calculated as a series of one-dimensional interpolations. This is illustrated in two-dimensions in Figure 3.4, and the extension to three-dimensions is straightforward.

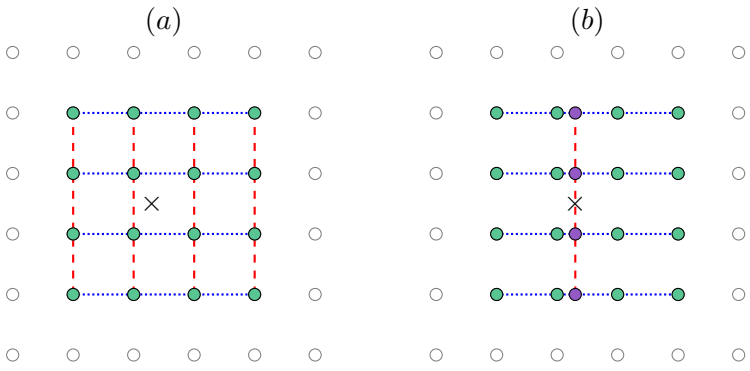

Figure 3.4: *Comparison between (a) tensor product and (b) cascade interpolation stencils.*

As well as being simple conceptually and applicable to several spatial dimensions the interpolation can be carried out efficiently for multiple tracer species. The interpolation corresponds to a weighted sum of the values of neighbouring nodes, and for multiple tracers the weights only need to be calculated once, using the efficient barycentric method of Berrut and Trefethen (2004) for example.

Accuracy

The semi-Lagrangian method approximates the material derivative, and so the spatial and temporal accuracies are intrinsically linked. In particular, the two components, trajectories and interpolation, can independently alter the accuracy.

In Xiu et al. (2005) the accuracy of the semi-Lagrangian method was noted to be of the form

$$\mathcal{O}\left(\Delta t^k + \frac{\Delta x^{P+1}}{\Delta t}\right), \tag{3.10}$$

where k is the order of the backward time integration, i.e. the trajectory calculation, and P the polynomial interpolation order. This shows that there is a need to match the spatial and temporal discretisations, since increasing either k or P independently will eventually lead to the other term dominating.

Although both the trajectories and interpolation can affect the accuracy, in practice second-order trajectories suffice so that the (spatial) error is dominated by the interpolation, (Staniforth and Côté, 1991). In operational NWP cubic interpolation generally suffices, (Davies et al., 2005).

Monotonicity

The spatial interpolation at the departure points using Lagrange polynomials is only guaranteed to be monotone for linear polynomials. In one spatial dimension, and for a Courant number

$$C = \frac{U\Delta t}{\Delta x},$$

less than unity, the semi-Lagrangian method is equivalent to the forward Euler method. For higher-order polynomials interpolation using Lagrange polynomials on equispaced points can create new extrema (Berrut and Trefethen, 2004).

The advection step should not create spurious new extrema, and so for high-order Lagrange polynomials it can be necessary to limit the interpolation to enforce monotonicity. In the present work the quasi-monotone (QM) limiter of Bermejo and Staniforth (1992) is used.

Using notation similar to Bermejo and Staniforth (1992) let $\chi^{nb} = (\chi^n_{k1}, \chi^n_{k2}, \chi^n_{k3}, \chi^n_{k4})$ be the vertices surrounding the cell in which the departure point $[\mathbf{x}]_d$ lies. The local maxmimum and minimum values are given by

$$\chi^+ = \max\left(\chi^{nb}\right); \quad \chi^- = \min\left(\chi^{nb}\right).$$

Let χ^H represent the solution using a high-order polynomial interpolation. The limited value, χ^{QM}, is given by

$$\chi^{QM} = \min\left[\chi^+, \max\left(\chi^-, \chi^H\right)\right]. \tag{3.11}$$

The QM limiter ensures that the interpolated value lies between the maximum and minimum values of the four nodes that make up the departure cell. If the interpolated value is above (below) the maximum (minimum) then the interpolated value is set to the maximum (minimum) value. The QM limiter ensures that no new extrema are created as a result of the interpolation procedure, and that spurious numerical over- and under-shoots are eliminated. This is illustrated schematically in Figure 3.5.

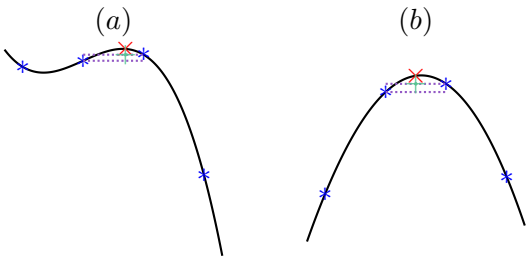

Figure 3.5: *Schematic showing the quasi-monotone limiter of Bermejo and Staniforth for the same functions as in Figure 3.3.*

Monotonicity is important not just from a stability point of view but also from an accuracy point of view; it is not physical to have negative densities, for example, and so it is desirable to avoid the generation of these spurious values. The QM limiter is scale selective. In general it will work to damp small scale oscillations but it can also potentially damp out well resolved, genuine extrema between grid points, e.g. (Zerroukat, 2010) and Figure 3.5.

A less diffusive limiter was recently proposed in Zerroukat (2010), in addition to a modification which conserved global mass properties. The proposed limiter showed an improvement over the standard (non-conservative) semi-Lagrangian scheme, whilst not being as expensive as conservative semi-Lagrangian schemes.

Conservation properties

The point-wise nature of the standard semi-Lagrangian method means that there is no guarantee of mass conservation. Although the error in mass

conservation might be small, it is systematic and made every time-step. In climate simulations, which run for several decades, this can cause the total mass to drift, eventually affecting the utility of the solution.

One option of improving mass conservation is to carry out a global "mass-fix" step after the advection; see Zerroukat (2010) for a recent comparison of these methods. The use of these mass-fixers can improve the results with relatively little extra computational effort, although the corrections need to be calculated for each field individually.

An alternative is to use *conservative* semi-Lagrangian schemes such as SLICE, (Zerroukat et al., 2002), or CSLAM, (Lauritzen et al., 2010b). These are generally more complex than their non-conservative point-wise counterparts, but can enforce local and global mass conservation.

The motivation for further improvements in transport schemes is that of closer reproduction of the continuous system. For an arbitrary passive tracer, χ, the advection equation implies conservation of any function of χ. It is clearly not possible to enforce this in a discrete model, but conservation is an important aspect to consider.

Algorithm

The algorithm for the semi-Lagrangian advection method is summarised in the following pseudo-code snippet, given in Algorithm 3.1.

```
# Initialise
a^0 ← 0
u^{*,0} ← u(x, t)
# Trajectory iteration
for k = 1, ..., m do
    # Calculate current offset
    a^k ← Δt u^{*,k-1} (x − a^{k-1}/2, Δt/2)
    # Update departure point
    x_d^k ← x − a^k
    # Calculate new advecting velocity
    u^{*,k} ← ϑ_T u(x, t + Δt) + (1 − ϑ_T) u(x_d^k, t)
# Interpolation
for all χ to be advected do
    χ(x, t + Δt) ← χ(x_d^m, t)
```

Algorithm 3.1: *Iterative semi-Lagrangian method. The trajectories are iterated for four iterations, although in practice the trajectories were generally converged after two iterations. The convergence was defined to be that the RMS norm of the difference between two successive iterations, $\mathbf{x}_d^{k+1} - \mathbf{x}_d^k$, was below a threshold of 10^{-8}.*

3.2.2 Eulerian

The Eulerian advection method solves the conservation form of the advection equation. This ensures that the transported variable is locally and globally conserved. The textbook of LeVeque (1992) provides a detailed overview of conservative methods.

Flux calculation

Starting from the conservative form of the advection equation the divergence term is expanded in each dimension as

$$\frac{\partial \chi}{\partial t} + \frac{\partial F}{\partial x} + \frac{\partial G}{\partial y} = 0, \tag{3.12}$$

where

$$F = u\chi, \quad G = v\chi.$$

This is then approximated as

$$\frac{\partial \chi_{i,j}}{\partial t} + \frac{1}{\Delta x}\left(F_{i+1/2,j} - F_{i-1/2,j}\right) + \frac{1}{\Delta y}\left(G_{i,j+1/2} - G_{i,j-1/2}\right) = 0, \tag{3.13}$$

where the temporal and spatial orders of accuracy have been decoupled using the method of lines. Equation (3.13) is now an ordinary differential equation in t for $\chi_{i,j}$ so that it can be solved using any of the well known methods for ODEs such as the Runge-Kutta method, whilst the spatial accuracy is determined by the method used to calculate the fluxes F and G (LeVeque, 1992).

The numerical fluxes can be calculated using polynomial interpolation

$$F_{i+1/2} = \sum_{l=0}^{m} w_l \left(u^* \chi\right)_{i-s+l}, \tag{3.14}$$

where m corresponds to the order of the polynomial, w_l are the interpolation weights, and s allows for the stencil to be centred or upwinded. u^* is the advecting velocity field, which maybe be explicit, $u^* = u^n$, or an approximation to the time-centred velocity field, $u^* \approx u^{n+1/2}$.

Flux limiting

For flux calculations higher than first-order it is necessary to limit the numerical flux to ensure stability. This is achieved by blending a high-order flux calculation with a low-order monotone flux calculation such as first-order upwind. The flux limiter calculates the ratio of the solution in the adjacent cells and adjusts the weighting such that in regions where the solution is smooth the high-order method is used, and in regions where the

gradients change rapidly the low-order method is used to ensure stability (LeVeque, 1992).

In Equation (3.13) the fluxes F and G are replaced by

$$F_{i+1/2,j} = F^{low}_{i+1/2,j} - \Phi\left(r^x_{i,j}\right)\left(F^{low}_{i+1/2,j} - F^{high}_{i+1/2,j}\right), \tag{3.15}$$

where Φ is the flux limiter function defined in the following paragraph, and

$$r^x_{i,j} = \frac{\chi_{i,j} - \chi_{i-1,j}}{\chi_{i+1,j} - \chi_{i,j}},$$

is the ratio of the gradient of the solution on the adjacent cells, and for the flux in the y-direction as

$$G_{i,j+1/2} = G^{low}_{i,j+1/2} - \Phi\left(r^y_{i,j}\right)\left(G^{low}_{i,j+1/2} - G^{high}_{i,j+1/2}\right), \tag{3.16}$$

with

$$r^y_{i,j} = \frac{\chi_{i,j} - \chi_{i,j-1}}{\chi_{i,j+1} - \chi_{i,j}}.$$

Two flux limiters were used in this thesis. The first was the minmod limiter given by

$$\Phi_{MM}\left(r^x_{i,j}\right) = \max\left[0, \min\left(1, r^x_{i,j}\right)\right]. \tag{3.17}$$

The second was the superbee limiter

$$\Phi_{SB}\left(r^x_{i,j}\right) = \max\left[o, \min\left(1, 2r^x_{i,j}\right), \min\left(r^x_{i,j}, 2\right)\right]. \tag{3.18}$$

Algorithm

The algorithm for the Eulerian advection method is summarised in the following pseudo-code snippet, given in Algorithm 3.2.

3.2.3 Vector invariant Eulerian

In two-dimensions it is possible to take advantage of the fact that the vorticity, as calculated from the curl of the velocity field, is a scalar field, as opposed to a vector field in three-dimensions. The vector invariant formulation is motivated by the desire to preserve vorticity in advection, whilst still retaining the use of the primitive variables (Arakawa and Lamb, 1981). The vector invariant formulation only affects the advection of momentum; for all other tracers it is still necessary to use the Eulerian scheme outlined in the previous section.

Starting from the momentum advection equation in advective form

$$\frac{\partial \mathbf{u}}{\partial t} + (\mathbf{u} \cdot \nabla)\,\mathbf{u} = 0, \tag{3.19}$$

```
# Calculate advecting velocity
u* ← ϑ_E u^{n+1} + (1 − ϑ_E) u^n
for all χ to be advected do
    # High-order flux
    F^{high}_{i+1/2,j} ← Σ_{l=0}^{m} w_l (u*χ)_{i−s+l,j}
    # Low-order flux
    F^{low}_{i+1/2,j} ← (u*χ)_{upwind}
    # Gradient ratio and limiter
    r^x_{i,j} ← (χ_{i,j} − χ_{i−1,j}) / (ε + χ_{i+1,j} − χ_{i,j})
    F_{i+1/2,j} ← F^{low}_{i+1/2,j} − Φ(r^x_{i,j}) (F^{low}_{i+1/2,j} − F^{high}_{i+1/2,j})
    Repeat for G
    # ODE solver
    χ^{n+1}_{i,j} ← χ^n_{i,j} − ∫_t^{t+Δt} (1/Δx) ΔF + (1/Δy) ΔG dt
```

Algorithm 3.2: *Eulerian advection method.*

defining the vorticity as

$$\zeta = \nabla \times \mathbf{u} = -\nabla^{\perp} \cdot \mathbf{u},$$

where the superscript $\cdot^{\perp}$ represents the perpendicular component, and using the vector identity

$$(\mathbf{u} \cdot \nabla)\,\mathbf{u} = \frac{1}{2}\nabla\,|\mathbf{u}|^2 - \mathbf{u} \times (\nabla \times \mathbf{u})\,,$$

it is possible to rewrite the momentum advection equation as

$$\frac{\partial \mathbf{u}}{\partial t} + (\mathbf{u}\zeta)^{\perp} = -\frac{1}{2}\nabla\,|\mathbf{u}|^2\,. \tag{3.20}$$

Taking the curl of Equation (3.20) the implied vorticity equation is

$$\frac{\partial \zeta}{\partial t} + \nabla \cdot (\mathbf{u}\zeta) = 0, \tag{3.21}$$

where the right hand side is zero since it is the curl of a gradient.

Momentum advection

Defining the vorticity flux vector

$$\mathbf{Z} = \mathbf{u}\zeta,$$

the momentum equation becomes

$$\frac{\partial \mathbf{u}}{\partial t} + \mathbf{Z}^{\perp} = -\frac{1}{2}\nabla\,|\mathbf{u}|^2\,. \tag{3.22}$$

The vorticity is advected on the dual grid and is then mapped onto the primal grid such that the updated momentum conserves the vorticity (Ringler et al., 2010). In the case of the nonlinear advection (two-dimensional Burgers) equation the gradient term needs to be treated separately; explicit treatment of this is not covered since when this is combined with the incompressibility condition it simply results in a modified potential in the projection step, see Section 4.3.

Algorithm

The algorithm for the vector invariant advection method is summarised in the following pseudo-code snippet, given in Algorithm 3.3.

```
# Calculate advecting velocity
u* ← ϑ_E u^{n+1} + (1 − ϑ_E) u^n
# Calculate vorticity
ζ^n ← −∇^⊥ · u^n
# High-order flux
F^{high}_{i+1/2,j} ← Σ_{l=0}^{m} w_l (u*ζ)_{i−s+l,j}
# Low-order flux
F^{low}_{i+1/2,j} ← (u*ζ)_{upwind}
r^x_{i,j} ← (ζ_{i,j} − ζ_{i−1,j}) / (ε + ζ_{i+1,j} − ζ_{i,j})
# Gradient ratio and limiter
F_{i+1/2,j} ← F^{low}_{i+1/2,j} − Φ(r^x_{i,j}) (F^{low}_{i+1/2,j} − F^{high}_{i+1/2,j})
Repeat for G
# ODE solver
(u, v)^{n+1} ← (u, v)^n − ∫_t^{t+Δt} (−G, F) + ½∇|u|² dt
For all other χ use Algorithm 3.2
```

Algorithm 3.3: *Vector invariant advection method.*

3.3 Time discretisation

In the following section the time discretisation is covered. The idealised problem is presented in Section 3.3.1, but a brief overview of operational approaches, as mentioned at the start of the chapter, is first presented.

Good forecasts require the simulation of waves, on many different space and time scales, although some, such as acoustic waves, have little impact on the large scale flow. An explicit numerical method that included acoustic waves would have a prohibitively small time-step restriction to maintain stability owing to the fast acoustic waves, whilst the time scales for the relevant atmospheric motions are much larger, such as energy spectra in Gage

and Nastrom (1986) and typical scales of various atmospheric phenomena in Smagorinsky (1974).

An *implicit* method is able to take an arbitrarily large time-step whilst still being stable for linear wave propagation. The semi-implicit method consists of a combined explicit and implicit step. This maintains the stability properties of the implicit method, as well as being second-order accurate and conserves quadratic quantities when centred in time, giving the well known Crank-Nicolson scheme (Crank and Nicolson, 1947).

The combination of a semi-implicit scheme with semi-Lagrangian treatment of advection gives a method which is stable, and where the maximum time-step is limited by accuracy requirements. It has been widely adopted in operational models, (Ritchie et al., 1995; Davies et al., 2005). With the current trend to larger number of processors, and the requirement of numerical methods to scale in parallel, it remains an open question as to whether or not the semi-implicit semi-Lagrangian scheme will still be used in the next generation of NWP models, owing to the difficulties in predicting the communication patterns in parallel implementations.

One other benefit outside of computational efficiency of the semi-implicit scheme is in the performance of the scheme in keeping solutions that remain close to geostrophic balance (Cullen, 2007a). High frequency small scale terms, such as IGWs, will not be treated accurately, but the larger scale and more slowly evolving features will be close to balance, which is improved with decentering, as shown in Section 4.6.

3.3.1 Equations

In the following section the time discretisation techniques are applied to an idealised problem. The purpose in this section is to show the important aspects of each of the methods that are used later on, whilst problem specific implementation details are covered in Chapter 4.

Idealised problem

The idealised problem will take the general form

$$\frac{\partial \mathbf{S}}{\partial t} + \mathcal{A}\left(\mathbf{u}, \mathbf{S}\right) + \mathbf{L}\left(\mathbf{S}, \mathbf{x}, t\right) + \mathbf{N}\left(\mathbf{S}, \mathbf{x}, t\right) = 0, \tag{3.23}$$

where $\mathbf{S} = \mathbf{S}\left(\mathbf{x}, t\right)$ is the state vector, $\mathcal{A}$ is the advection operator, $\mathbf{u} = \mathbf{u}\left(\mathbf{x}, t\right)$ is the advecting velocity field, $\mathbf{L}$ contains the linear forcing terms and $\mathbf{N}$ contains the nonlinear forcing terms. Equation (3.23) is solved with rigid lid boundary conditions, and a suitable initial condition representing a balanced state.

For the semi-Lagrangian methods Equation (3.23) will be expressed as

$$\frac{D\mathbf{S}}{Dt} + \mathbf{L}\left(\mathbf{S}, \mathbf{x}, t\right) + \mathbf{N}\left(\mathbf{S}, \mathbf{x}, t\right) = 0, \tag{3.24}$$

where the incompressibility of the advecting velocity field has been taken into account. The distinction of the forcing terms to linear and nonlinear allows the linear terms to be expressed as a matrix-vector product

$$\mathbf{L}(\mathbf{S}, \mathbf{x}, t) = \mathbf{L}^n = \mathsf{L}\mathbf{S}^n,$$

where L is a matrix representation of $\mathbf{L}$.

3.3.2 Semi-implicit discretisation methods

In the following section the solution of the nonlinear problem resulting from the semi-implicit discretisation method is discussed. Using the idealised problem, but combining the advection term with the nonlinear term, gives

$$\frac{\partial \mathbf{S}}{\partial t} + \mathbf{L}(\mathbf{S}, \mathbf{x}, t) + \mathbf{N}(\mathbf{S}, \mathbf{x}, t) = 0. \tag{3.25}$$

The semi-implicit discretisation of Equation (3.25) gives

$$\begin{aligned} \frac{\mathbf{S}^{n+1} - \mathbf{S}^n}{\Delta t} &+ \vartheta \mathbf{L}^{n+1} + (1-\vartheta)\mathbf{L}^n \\ &+ \vartheta \mathbf{N}^{n+1} + (1-\vartheta)\mathbf{N}^n = 0, \end{aligned} \tag{3.26}$$

where ϑ is the time centering parameter. For $\vartheta = 1/2$ this method reduces to the Crank-Nicolson method and is second-order accurate, but is first-order accurate otherwise. Rearranging for the solution at the new time level gives

$$\underbrace{(\varsigma \mathsf{I} + \vartheta \mathsf{L})\,\mathbf{S}^{n+1} + \vartheta \mathbf{N}^{n+1}}_{L^{n+1}} = \underbrace{[\varsigma \mathsf{I} - (1-\vartheta)\,\mathsf{L}]\,\mathbf{S}^n - (1-\vartheta)\,\mathbf{N}^n}_{R^n}, \tag{3.27}$$

where $\varsigma = 1/\Delta t$, and L and R refer to the left- and right-hand side terms respectively.

Fixed point iteration

One of the simplest iterative approaches to solving Equation (3.27) is to solve the linear terms implicitly but use a lagged approximation from a previous iteration for the nonlinear term. This gives

$$(\varsigma \mathsf{I} + \vartheta \mathsf{L})\,\mathbf{S}^{n+1,k+1} = R^n - \vartheta \mathbf{N}^{n+1,k}, \tag{3.28}$$

where only the evaluation of the implicit nonlinear terms need updating at every iteration. For the nonlinear Eady problem it was necessary to use up to six iterations at every time-step to ensure that the RMS norm of the residuals remained below 10^{-8} after frontal collapse.

Newton iteration

A Newton method can be derived from Equation (3.27) by first assuming that there is an estimate for the solution after k iterations as

$$L^{n+1,k} - R^n = \mathbf{r}^k, \tag{3.29}$$

where $\mathbf{r}^k$ is the residual in the k^{th} iteration. Adding a small correction to get the next iterate

$$\mathbf{S}^{n+1,k+1} = \mathbf{S}^{n+1,k} + \mathbf{S}',$$

and substituting into Equation (3.27) gives

$$(\varsigma \mathsf{I} + \vartheta \mathsf{L}) \left(\mathbf{S}^{n+1,k} + \mathbf{S}' \right) + \vartheta \mathbf{N}^{n+1,k+1} = R^n, \tag{3.30}$$

where it has been possible to separate out the linear terms but the same cannot be done for the nonlinear terms. If the nonlinear terms are instead evaluated at the current iteration

$$\mathbf{N}^{n+1,k+1} \approx \mathbf{N}^{n+1,k},$$

then

$$(\varsigma \mathsf{I} + \vartheta \mathsf{L})\, \mathbf{S}' = -\mathbf{r}^k, \tag{3.31}$$

is an approximate Newton iteration, in the sense that the Jacobian on the LHS contains only the linear terms. Note that since the RHS of Equation (3.31) is the residual of the full problem there is some flexibility in the form of the approximation of the matrix system on the LHS. For example it might be beneficial to approximate the linear forcing terms

$$\mathsf{L}\mathbf{S} \approx \tilde{\mathsf{L}}\mathbf{S},$$

so that the resulting linear problem

$$\left(\varsigma \mathsf{I} + \vartheta \tilde{\mathsf{L}} \right) \mathbf{S}' = -\mathbf{r}^k, \tag{3.32}$$

is easier to solve. A pseudo-code outline of the Newton iteration method is given in Algorithm 3.4.

3.3.3 Semi-implicit semi-Lagrangian

The semi-implicit semi-Lagrangian (SISL) discretisation of Equation (3.24) is given by

$$\frac{\mathbf{S}^{n+1} - [\mathbf{S}^n]_d}{\Delta t} + \vartheta \left(\mathbf{L} + \mathbf{N} \right)^{n+1} + (1 - \vartheta) \left[(\mathbf{L} + \mathbf{N})^n \right]_d = 0, \tag{3.33}$$

```
# Explicit RHS
R^n ← (ς I + (1 − ϑ) L) S^n + (1 − ϑ) N^n
# Initial guess
S^{n+1,1} ← S^n
for k = 1, ..., m do
    # Implicit LHS
    L^{n+1,k} ← (ς I + ϑ L) S^{n+1,k} + ϑ N^{n+1,k}
    # Residual calculation
    r^k ← R^n − L^{n+1,k}
    if ||r^k||_∞ ≤ ε then
        # Solution converged
        S^{n+1} ← S^{n+1,k}
    else
        # Solve linear system
        S' ← (ς I + ϑ L)^{−1} r^k
        S^{n+1,k+1} ← S^{n+1,k} + S'
# Maximum iterations reached
S^{n+1} ← S^{n+1,m+1}
```

Algorithm 3.4: *Iterative solution of the semi-implicit problem using Newton iteration. Convergence tolerance was set as* $\mathcal{O}\left(10^{-8}\right)$.

where ϑ is the time centering parameter and $[\cdot]_d$ indicates evaluation at the departure point. This method can be rearranged to give

$$\mathbf{S}^{n+1} + \vartheta\Delta t\left(\mathbf{L}+\mathbf{N}\right)^{n+1} = \left[\left\{\mathbf{S} - (1-\vartheta)\,\Delta t\left(\mathbf{L}+\mathbf{N}\right)\right\}^n\right]_d, \tag{3.34}$$

where there is now just a single evaluation at the departure point for the modified state

$$\mathbf{S}_{*,SL} = \mathbf{S} - (1-\vartheta)\,\Delta t\left(\mathbf{L}+\mathbf{N}\right).$$

Predictor-corrector method

One approach to solving the resulting implicit nonlinear problem is to use a predictor-corrector method, (Davies et al., 2005),

$$\mathbf{S}^1 = \left[\mathbf{S}^n_{*,SL}\right]_d - \vartheta\Delta t\left(\mathbf{L}+\mathbf{N}\right)^n, \tag{3.35}$$

$$\mathbf{S}^2 + \vartheta\Delta t\mathbf{L}^2 = \mathbf{S}^1 - \vartheta\Delta t\left[\mathbf{N}^* - \left(\mathbf{L}+\mathbf{N}\right)^n\right]. \tag{3.36}$$

In the notation above $\mathbf{S}^1$ is the predictor and $\mathbf{S}^2$ is the corrected state, which is then taken as $\mathbf{S}^{n+1} = \mathbf{S}^2$. $\mathbf{N}^* \approx \mathbf{N}^{n+1}$ is an approximation to the implicit nonlinear term, but calculated using $\mathbf{S}^n$ and $\mathbf{S}^1$.

The predictor-corrector method requires an extrapolation of the advecting velocities to the time level $t = (n + 1/2)\,\Delta t$. This can lead to stability problems, especially when using large time-steps, (Cordero et al., 2005).

Implicit iterative method

An alternative to using the predictor-corrector method is to use a fixed-point iterative method in which the evaluation of the implicit nonlinear terms is lagged by one iteration

$$(\mathbf{S} + \vartheta \Delta t \mathbf{L})^{n+1,k} = \left[\mathbf{S}^n_{*,SL}\right]_d - \vartheta \Delta t \mathbf{N}^{n+1,k-1}, \tag{3.37}$$

where

$$k = 1, 2, \ldots, m; \quad \mathbf{N}^{n+1,0} = \mathbf{N}^n; \quad \mathbf{S}^{n+1} = \mathbf{S}^{n+1,m}.$$

For $k \geq 2$ this gives second-order accuracy, and for $k = 2$ this reduces to the predictor-corrector method outlined above (Diamantakis et al., 2007).

The SISL iterative method was discussed in Diamantakis et al. (2007). Whilst the iterations were more expensive than the predictor-corrector approach the increase in forecast skill was comparable to an increase in resolution of almost 50%. The increase in cost is partly down to having to solve an elliptic Helmholtz problem at each iteration, but the number of Helmholtz iterations are reduced on each nonlinear iteration.

The iterative method can be rewritten in terms of an increment. Subtracting off the initial state from both sides gives the following form for the update

$$(\mathsf{I} + \vartheta \Delta t \mathsf{L})\, \Delta \mathbf{S}^k = \left[\mathbf{S}^n_{*,SL}\right]_d - \vartheta \Delta t \mathbf{N}^{n+1,k-1} - \mathbf{S}^n - \vartheta \Delta t \mathbf{L}^n, \tag{3.38}$$

where $\Delta \mathbf{S}^k = \mathbf{S}^{n+1,k} - \mathbf{S}^n$.

3.3.4 Semi-implicit Eulerian

The semi-implicit Eulerian (SIE) discretisation of Equation (3.23) is given by (Smolarkiewicz, 1991)

$$\frac{\mathbf{S}^{n+1} - \mathbf{S}^n}{\Delta t} + \mathcal{A}\left(\mathbf{u}^{n+1/2}, \mathbf{S}^n\right) + \vartheta \left(\mathbf{L} + \mathbf{N}\right)^{n+1} + (1 - \vartheta)\left(\mathbf{L} + \mathbf{N}\right)^n = 0, \tag{3.39}$$

where

$$\mathbf{u}^{n+1/2} = \vartheta_E \mathbf{u}^{n+1} + (1 - \vartheta_E)\, \mathbf{u}^n,$$

is an approximation to the velocity at the midpoint, with ϑ_E the Eulerian analogue of the advecting velocity time centering parameter. Note that the nonlinear and advective terms have been separated out in Equation (3.39). As with the semi-Lagrangian case, unless otherwise stated then $\vartheta_E = \vartheta$. The advection term is written in conservation form, so that for each χ in $\mathbf{S}$ the advection takes the following form

$$\frac{\chi^{n,\mathcal{A}} - \chi^n}{\Delta t} + \nabla \cdot \left(\mathbf{u}^{n+1/2} \chi^n\right) = 0, \tag{3.40}$$

which is expressed as

$$\chi^{n,\mathcal{A}} = \chi^n - \Delta t \nabla \cdot \left(\mathbf{u}^{n+1/2} \chi^n \right). \tag{3.41}$$

If the initial state is subtracted from both sides then this gives

$$\chi^{\mathcal{A}} = \chi^{n,\mathcal{A}} - \chi^n = -\Delta t \nabla \cdot \left(\mathbf{u}^{n+1/2} \chi^n \right), \tag{3.42}$$

and with

$$\mathbf{S}^{\mathcal{A}} = \mathcal{A}\left(\mathbf{u}^{n+1/2}, \mathbf{S}^n \right),$$

representing the state of advected variables, $\chi^{\mathcal{A}}$.

Implicit iterative method

As for the SISL scheme it possible to formulate the semi-implicit Eulerian method as an iterative scheme

$$\begin{aligned} \mathbf{S}^{n+1,k} + \vartheta \Delta t \mathbf{L}^{n+1,k} &= \mathbf{S}^n - \mathbf{S}^{\mathcal{A},k} - (1-\vartheta)\,\Delta t\,(\mathbf{L}+\mathbf{N})^n \\ &\quad -\vartheta \Delta t \mathbf{N}^{n+1,k-1}, \end{aligned} \tag{3.43}$$

where

$$\mathbf{u}^{n+1/2,k} = \vartheta_E \mathbf{u}^{n+1,k} + (1-\vartheta_E)\,\mathbf{u}^n,$$

and $\mathbf{S}^{\mathcal{A},k}$ is the solution of Equation (3.42) with $\mathbf{u}^{n+1/2}$ replaced by $\mathbf{u}^{n+1/2,k}$ from above. The SIE method can also be formulated for the increment as

$$\begin{aligned} (\mathsf{I} + \vartheta \Delta t \mathsf{L})\,\Delta \mathbf{S}^k &= -\mathbf{S}^{\mathcal{A},k} - (1-\vartheta)\,\Delta t\,(\mathbf{N})^n \\ &\quad -\vartheta \Delta t \mathbf{N}^{n+1,k-1} - \Delta t \mathbf{L}^n. \end{aligned} \tag{3.44}$$

3.3.5 Semi-implicit vector invariant Eulerian

The semi-implicit vector invariant Eulerian (SIVIE) formulation is almost identical to the standard semi-implicit Eulerian formulation given in the previous section, with the modified momentum equation as given in Section 3.2.3.

The advected state $\mathbf{S}^{\mathcal{A},k}$ in Equation (3.43) is simply replaced with

$$\mathbf{S}_{VI}^{\mathcal{A},k} = \begin{cases} \text{Algorithm 3.3} & \mathbf{u}, \\ \text{Algorithm 3.2} & \text{all other } \chi. \end{cases}$$

3.3.6 Advection boundary conditions

The three schemes outlined above, SISL, SIE and SIVIE, all require specific boundary conditions within the respective advection steps. Discussion of the boundary conditions is deferred to Section 4.4, since there are some simplifications that can be made with the use of the vertical slice model for frontogenesis.

3.4 Operator splitting

This section covers some of the implementation details. It would be possible to devote a chapter in itself to this topic, but attention will focus on the rationale behind the methods. The operator splitting is used for all of the SISL, SIE and SIVIE algorithms. For information on the accuracy and stability of splitting schemes the reader is referred to Durran (2010, Section 4.3) and the references contained therein.

The code is operator split, in that the full time-step is broken up into several substeps, such that the composition of all steps gives the final state at the new time level. This splitting into substeps, in particular the decoupling of the pressure and velocity equations, is a form of the SIMPLE algorithm (Patankar and Spalding, 1972). Using the implicit iterative SISL method to illustrate this, the problem is restated as

$$(\mathbf{S} + \vartheta \Delta t \mathbf{L})^{n+1,k} = \left[\mathbf{S}^n_{*,SL}\right]^k_d - \vartheta \Delta t \mathbf{N}^{n+1,k-1},$$

with

$$\mathbf{S}^n_{*,SL} = \mathbf{S}^n - (1-\vartheta)\,\Delta t\,(\mathbf{L}^n + \mathbf{N}^n)\,.$$

An iterative time-step proceeds as follows.

1. Calculate explicit linear and nonlinear forcing from

$$\mathbf{S}^n_{*,SL} = \mathbf{S}^n - (1-\vartheta)\,\Delta t\,(\mathbf{L}^n + \mathbf{N}^n)\,. \tag{3.45}$$

   Note that these terms do not change within the iterations and so they can be calculated outside the iteration loop to reduce the number of calculations per iteration.

2. Calculate advective forcing, for SISL this amounts to evaluating

$$\mathbf{S}^{1,k} = \left[\mathbf{S}^n_{*,SL}\right]^k_d\,. \tag{3.46}$$

3. Calculate lagged implicit nonlinear terms from

$$\mathbf{S}^{2,k} = \mathbf{S}^{1,k} - \vartheta \Delta t \mathbf{N}^{n+1,k-1}. \tag{3.47}$$

4. Calculate implicit linear wave forcing from

$$\mathbf{S}^{n+1,k} = (\mathsf{I} + \vartheta \Delta t \mathsf{L})^{-1}\,\mathbf{S}^{2,k}. \tag{3.48}$$

This is written in a slightly more general form than the pseudo-code snippets given for the other algorithms, and reflects the way in which one advection method can be swapped for another, without affecting the other parts of

the solution procedure. The iteration proceeds until either the difference between two successive iterations is small enough,

$$\left\| \mathbf{S}^{n+1,k} - \mathbf{S}^{n+1,k-1} \right\|_{\infty} \leq \varepsilon,$$

where $\varepsilon = \mathcal{O}\left(10^{-8}\right)$, or a maximum number of iterations has been reached.

In Section 4.3 the linear wave system is combined with incompressible mass conservation to give a single step that ensures that the velocity field at the end of the time-step is divergence-free. This single linear system will be used in the following idealised test cases, with the relevant parameters set to the appropriate values.

3.5 Idealised test cases

In this section the results of several standard simplified numerical experiments are presented to establish agreement between the program written as part of this thesis and results from published literature, using well known test cases.

3.5.1 Smooth profile advection

The first test case is that of pure advection of a smooth profile in a fixed velocity field, such that the analytic solution at $t = T$ is the same as the initial conditions.

A passive tracer field was initialised with

$$\chi\left(x, z, 0\right) = \sin\left(2\pi x\right), \tag{3.49}$$

on a domain $\Omega = [-0.5, 0.5] \times [0, 1]$ m with a constant velocity field of $\mathbf{u} = (1, 0)$ m s^{-1} and constant time-step of $\Delta t = 0.0005$ s. For this test case the tracer was located at the cell centres. This is essentially a one-dimensional transport test, but with the additional requirements of satisfactory handling of the boundaries. The boundary conditions are periodic in the horizontal and no flux in the vertical.

The spatial convergence for the SISL scheme at fixed time-step is shown in Figure 3.6. The cubic and quintic methods both seem to show the theoretical convergence rate, whilst the linear interpolation shows two slopes with only the few finest resolution points showing the convergence rate. This is likely a result of the linear interpolation being highly dissipative for small Courant numbers.

The more interesting result is that of the cubic interpolation with the QM limiter. This appears to be between the linear and cubic results, both in terms of the error but also the convergence rate. This is consistent with the known results of the QM limiter being quite dissipative, (Zerroukat,

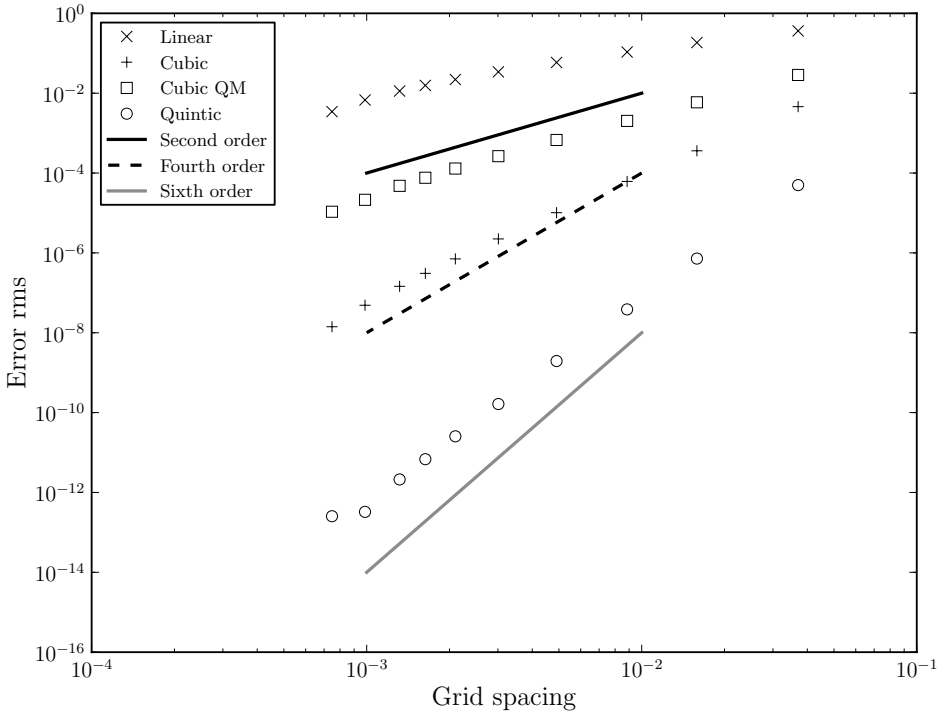

Figure 3.6: *Comparison of interpolation orders for advection of a smooth profile at $t = T$, using $\Delta t = 0.0005$* s *and the semi-Lagrangian advection method, grid spacing is given in* m. *Solid lines show the theoretical spatial convergence rates.*

2010), but is accepted in the present work since stability in the numerical integrations is important.

It should be noted that the dominant error term in a numerical method can be either dissipative or dispersive. The Eady model is representative of most geophysical problems which are concerned with the accurate treatment of waves, in which case a scheme with high dispersion error would not be acceptable. The problem of the dissipation of the scheme could be reduced by increasing resolution, whereas the same cannot be said for a dispersive scheme.

3.5.2 Slotted cylinder pure advection

This test case was originally presented in Zalesak (1979) and has been widely used to investigate the ability of a scheme to enforce monotonicity in the advected solution. A passive tracer field is initialised with a discontinuous profile of a cylinder with a slot five cells wide cut through it. It then undergoes a solid-body rotation, such that the analytic solution after one revolution at $t = T$ reproduces the initial conditions. The use of a step

function in specifying the initial cylinder challenges the ability of a transport scheme to maintain monotonicity.

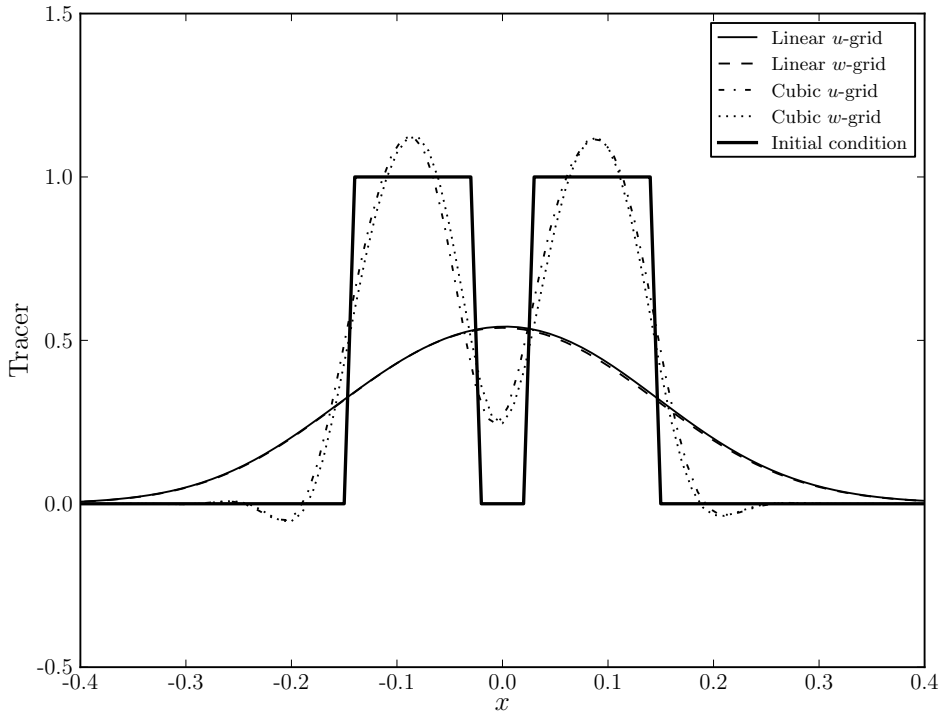

Figure 3.7: *Comparison between passive tracers advected on the u- and w-grids using the semi-Lagrangian advection method without the QM limiter.*

Figure 3.7 shows a comparison of the results after a single revolution for the semi-Lagrangian advection scheme on different grids. There is good agreement between the staggered variable locations, suggesting that the interpolation of the velocity fields to each of the variable locations appears consistent. There is a very slight shift between the two curves for the cubic interpolation; this is attributed to the initialisation being carried out on spatial coordinates, as opposed to array indices.

Figure 3.8 shows a comparison between the semi-Lagrangian and Eulerian advection schemes. With the exception of the centred flux calculation, which is known to be unstable without any flux limiting, there is good agreement between the two methods for this test case. The linear interpolation and first-order upwind method both perform poorly in terms of preserving the stepped profile, which suggests that they would not be accurate enough for modeling the sharp changes of gradients expected in the frontal region.

The third-order upwind and unlimited cubic interpolation perform very similarly, with amplification of the maxima and the creation of new minima

either side of the edge of the cylinder. The effect of the QM limiter is very pronounced, and appears to be quite beneficial in preventing the generation of the spurious extrema, but at the cost of reducing the central minima. It is clear from these results why the cubic QM interpolation is widely used; it is sufficiently accurate to capture the slotted cylinder profile, without sacrificing stability.

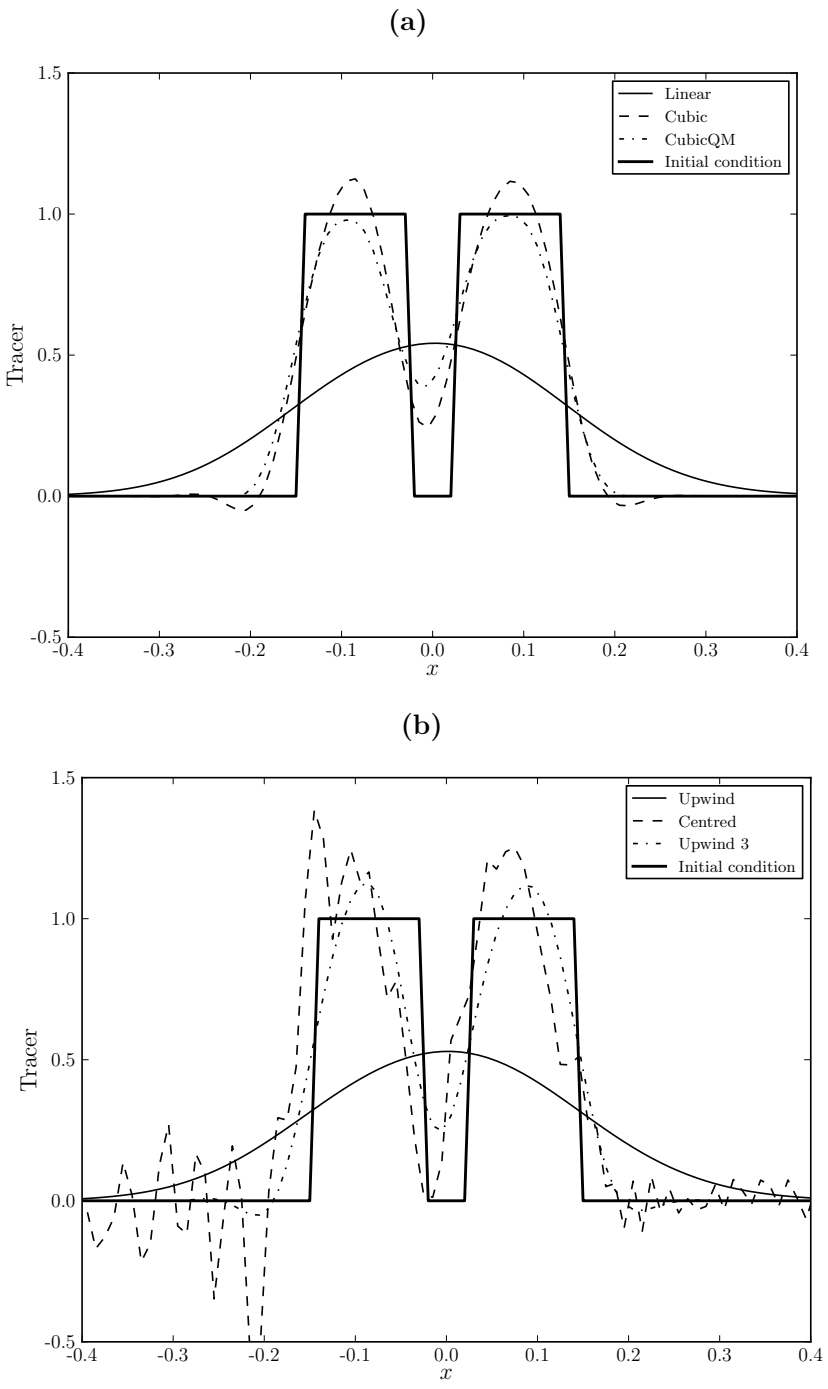

Figure 3.8: *Cross section through the slotted cylinder centreline after a single revolution using (a) the semi-Lagrangian advection scheme (SISL) and (b) the Eulerian advection scheme (SIE). The effect of the QM limiter is shown clearly in (a), in which the cubic QM results do not exceed the initial maximum and minimum values, whereas the unlimited cubic results do.*

3.5.3 Rising density current

The final test case is concerned with the modeling of buoyancy driven flows. As the Eady problem causes a strong front in the potential temperature it is vital for the correct calculation of the solution that the effects of buoyancy are handled well.

The test case is that of Robert (1993), in which a uniform perturbation is applied to the potential temperature in a stably-stratified state, causing the perturbation to rise and generating intricate roll-up features. The results of Robert (1993) are shown in Figure 3.9.

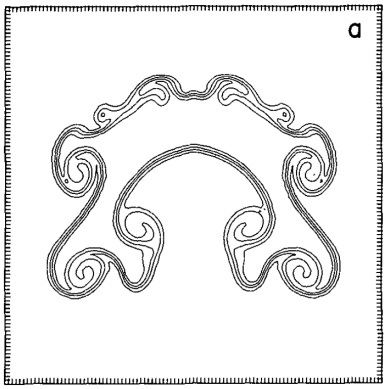

Figure 3.9: *Contours of potential temperature perturbation for the Robert (1993) test with a uniform perturbation of* 0.5 K *at day seven, over the central* 1 km *domain.*

In the present work the domain was 2 km by 1 km in the horizontal and vertical, respectively. The grid resolution was fixed at 10 m in both directions. The boundary conditions were periodic in the horizontal and rigid lids in the vertical. The initial condition corresponded to a 0.5 K circular perturbation of diameter 500 m to the potential temperature applied in the centre of the domain.

Figure 3.10 shows a comparison of the solutions at day seven for varying interpolation methods. Increasing the interpolation order results in more fine scale features, but also increases the overshoots. The cubic QM interpolation appears satisfactory in capturing sufficient details of the roll up whilst maintaining the monotonicity requirements.

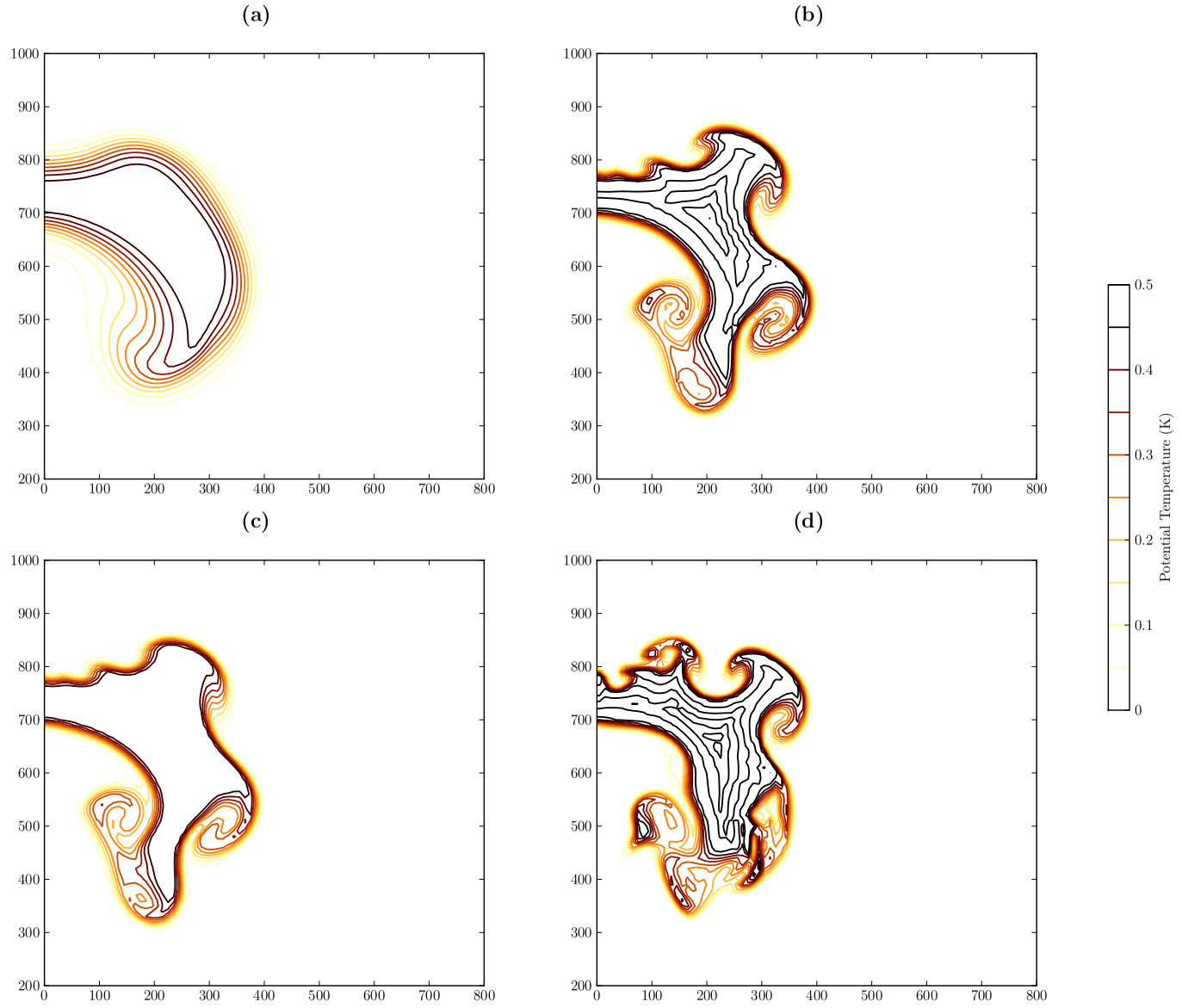

Figure 3.10: *Contours of potential temperature at day seven for the rising density current test case using the semi-Lagrangian advection method with (a) linear, (b) cubic, (c) quasi-monotone cubic and (d) quintic interpolation within the SISL algorithm. Axes are in units of* m.

3.6 Summary

In this chapter the details of the finite-difference implementation of the SISL, SIE and SIVIE schemes have been given. The use of the semi-implicit method was justified based on its use in operational models, as well as permitting large time-steps when combined with the semi-Lagrangian advection scheme. The details of the implementation, in particular the use of operator splitting to separate the full problem into smaller substeps, were shown.

Idealised test cases have been to used to verify that the methods have been implemented correctly. The theoretical convergence rates for the semi-Lagrangian advection were shown, whilst the effect of the QM limiter was shown to preserve monotonicity. Simplified wave forcing, that of buoyancy in the warm bubble test case, showed the behaviour to qualitatively agree with previous work.

The general numerical schemes outlined in this chapter will form the basis for the next chapter, in which the full details of the Eady problem specification, and the tailored numerical methods, are presented.

Chapter 4

The Eady frontogenesis model

Now that actual computation of certain aspects of the weather forecast has become a practical possibility, interest in certain simplified "models" of atmospheric motion has increased. It seems at first paradoxical that this should be so.

E. T. Eady (1952)

Contents

The previous two chapters have introduced vertical slice models to study frontogenesis, given an overview of the existing results including the properties of the semigeostrophic limit solution, and covered some of the methods used in numerical weather prediction.

This chapter presents a detailed problem definition for the Eady model of frontogenesis by building on the material presented earlier, as well as the specific considerations required in this thesis.

The chapter proceeds in a similar manner to the way in which this thesis has been ordered so far; first the equations are presented, the numerical methods and implementation details follow, and finally the asymptotic framework and initial results for the linearised problem are discussed.

4.1 Governing equations

In this section the governing equations for the Boussinesq Eady problem are shown. Solutions to the Eady model correspond to solutions to the three-dimensional Boussinesq Euler equations with the constant background profile of Equation (4.3) shown in Figure 4.1 and no meridional variation.

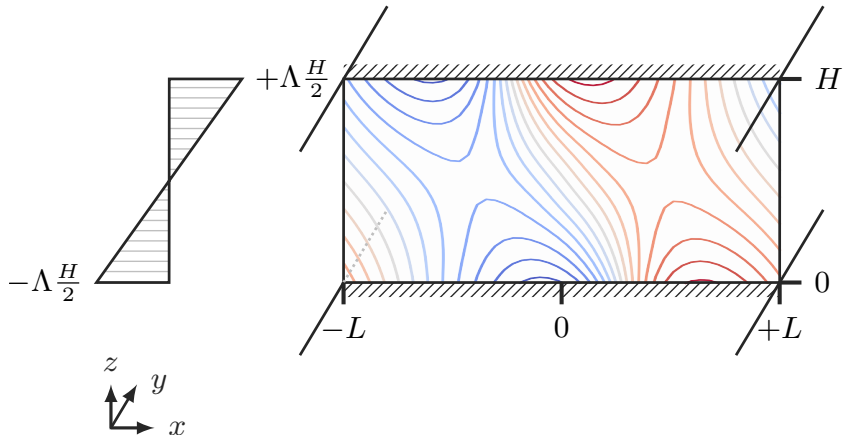

Figure 4.1: *Schematic of vertical slice domain and background shear. On the left is the background shear profile for the zonal wind, where Λ is a constant. On the right is the domain, with solid walls at $z = 0, H$, periodic boundaries at $x = -L, L$, and drawn in coloured contour lines is a representative snapshot of the meridional velocity field showing the structure of the Eady wave.*

Background profile

The shear model, as illustrated in Figure 4.1, consists of motion restricted to the (x, z) plane, so that $\partial_y = 0$ for all variables with the exception of

a background profile. The Eady background profile consists of assuming a thermally balanced profile in the meridional direction of the form

$$\begin{aligned} \phi(x,y,z,t) &= \phi_0(z) + \overline{\phi}(y,z) + \phi'(x,z,t), & (4.1)\\ \theta(x,y,z,t) &= \theta_0 + \overline{\theta}(y,z) + \theta'(x,z,t), & (4.2) \end{aligned}$$

where the primed quantities are the variables within the vertical slice. Following Snyder et al. (1993) the background potential temperature can be expressed as

$$\overline{\theta}(y,z) = \frac{\theta_0}{g}\left(-f\Lambda y + N^2 z\right), \tag{4.3}$$

where Λ is a constant vertical shear in the zonal wind

$$\overline{U} = \Lambda\left(z - \frac{H}{2}\right).$$

Using the above, and the thermal wind relation, it is then possible to write the meridional component of the geopotential as

$$\frac{\partial\overline{\phi}}{\partial y} = \frac{g}{\theta_0}\frac{\partial\overline{\theta}}{\partial y}\left(z - \frac{H}{2}\right), \tag{4.4}$$

which is a constant function of z only.

Eady model equations

Substituting in the background profile given in Equation (4.3) into Equations (2.26) to (2.28), and dropping the primes gives the (in-slice) vector form of the Eady model equations as

$$\begin{aligned} \frac{D\mathbf{u}}{Dt} &= -\nabla\phi + fv\hat{\mathbf{x}} + \frac{g}{\theta_0}\theta\hat{\mathbf{z}}, & (4.5)\\ \frac{Dv}{Dt} + fu &= -\frac{g}{\theta_0}\frac{\partial\overline{\theta}}{\partial y}\left(z - \frac{H}{2}\right), & (4.6)\\ \frac{D\theta}{Dt} + v\frac{\partial\overline{\theta}}{\partial y} &= 0, & (4.7)\\ \nabla\cdot\mathbf{u} &= 0, & (4.8) \end{aligned}$$

where

$$\mathbf{u} = (u,w), \quad \nabla = \left(\frac{\partial}{\partial x}, \frac{\partial}{\partial z}\right),$$

and all variables are now functions of (x, z, t) only. The equations can be written equivalently in component form as

$$\frac{Du}{Dt} - fv = -\frac{\partial \phi}{\partial x}, \tag{4.9}$$

$$\frac{Dv}{Dt} + fu = -\frac{g}{\theta_0}\frac{\partial \overline{\theta}}{\partial y}\left(z - \frac{H}{2}\right), \tag{4.10}$$

$$\frac{Dw}{Dt} - \frac{g}{\theta_0}\theta = -\frac{\partial \phi}{\partial z}, \tag{4.11}$$

$$\frac{D\theta}{Dt} + v\frac{\partial \overline{\theta}}{\partial y} = 0, \tag{4.12}$$

$$\frac{\partial u}{\partial x} + \frac{\partial w}{\partial z} = 0. \tag{4.13}$$

Background stratification

After some early testing it was found that it was necessary to separate off the background vertical stratification of the potential temperature in the interests of stability for the vertical velocity. Taking the background profile as

$$\frac{\partial \overline{\theta}}{\partial z} = \frac{\theta_0}{g}N^2,$$

and treating the background component explicitly modifies Equation (4.12) to give

$$\frac{D\theta}{Dt} + v\frac{\partial \overline{\theta}}{\partial y} + w\frac{\partial \overline{\theta}}{\partial z} = 0. \tag{4.14}$$

Note that the background profile modifies Equation (4.11) as

$$\frac{Dw}{Dt} - \frac{g}{\theta_0}\left(\theta + \frac{\theta_0}{g}N^2 z\right) = -\frac{\partial \phi}{\partial z}. \tag{4.15}$$

This background profile is purely hydrostatic, and so can be separated off exactly in Equation (4.15) by substituting in

$$\phi = \phi_h + \phi'; \quad \frac{\partial \phi_h}{\partial z} = \frac{\theta_0}{g}N^2,$$

such that ϕ' now refers to the perturbation from the hydrostatic geopotential.

In the present work it was sufficient to use a one-dimensional profile, but this would not be applicable in an operational model in which it it would be unrealistic to assume a constant reference profile everywhere. Other techniques to maintain stability without using a background profile include fully implicit treatment of the vertical advection of potential temperature, (Davies et al., 2005), or non-interpolating in the vertical, (Diamantakis et al., 2007).

Briefly, the non-interpolating scheme projects the departure point onto the nearest vertical level and inserts a correction to the vertical velocity in the potential temperature tendency, whilst the former approach uses the best available vertical velocity at the new time level for the transport of the potential temperature only.

Summary of equations solved numerically

The equations with the background profile separated are restated as

$$\frac{Du}{Dt} - fv = -\frac{\partial \phi'}{\partial x}, \tag{4.16}$$

$$\frac{Dv}{Dt} + fu = -\frac{g}{\theta_0}\frac{\partial \overline{\theta}}{\partial y}\left(z - \frac{H}{2}\right), \tag{4.17}$$

$$\frac{Dw}{Dt} - \frac{g}{\theta_0}\theta = -\frac{\partial \phi'}{\partial z}, \tag{4.18}$$

$$\frac{D\theta}{Dt} + v\frac{\partial \overline{\theta}}{\partial y} + \underbrace{w\frac{\partial \overline{\theta}}{\partial z}}_{\circledast} = 0, \tag{4.19}$$

$$\frac{\partial u}{\partial x} + \frac{\partial w}{\partial z} = 0, \tag{4.20}$$

where the highlighted term, $\circledast$, is present only for the *numerical* solution owing to stability requirements, in which case θ and ϕ represent the perturbations away from the hydrostatic reference state. It is these perturbations that will be shown in the results presented later.

4.1.1 Convergence to semigeostrophic equations

In this section the convergence of the standard Euler Boussinesq equations to the semigeostrophic equations is shown for the Eady model, using the nondimensional equations. The convergence is shown for the *full* potential temperature and geopotential, where the background profile has not been separated. As mentioned, the separation is for numerical stability reasons only, and does not affect the results of this section.

The nondimensional scalings are given in Section 2.3, with the addition of the background potential temperature gradient which scales as

$$\frac{\partial \overline{\theta}}{\partial y} = \epsilon\theta_0 \frac{fV}{gH}\frac{\partial \overline{\theta}'}{\partial y}.$$

This is implicitly assuming that

$$\epsilon = \frac{L}{L_y} = \frac{U}{V},$$

where L_y is a representative length scale in meridional direction. This is consistent with the continuity requirements and the assumption of cross-front geostrophic balance in HB72.

Dropping the primes for the nondimensional variables and substituting the scalings into Equations (4.9) to (4.13) gives the nondimensional Eady equations as

$$\epsilon \mathrm{Ro} \frac{Du}{Dt} - v = -\frac{\partial \phi}{\partial x}, \tag{4.21}$$

$$\mathrm{Ro} \frac{Dv}{Dt} + \epsilon u = -\epsilon \frac{\partial \overline{\theta}}{\partial y} \left(z - \frac{1}{2} \right), \tag{4.22}$$

$$\epsilon \mathrm{Ro} \delta^2 \frac{Dw}{Dt} - \theta = -\frac{\partial \phi}{\partial z}, \tag{4.23}$$

$$\frac{D\theta}{Dt} + v \frac{\partial \overline{\theta}}{\partial y} = 0, \tag{4.24}$$

$$\frac{\partial u}{\partial x} + \frac{\partial w}{\partial z} = 0. \tag{4.25}$$

For the small parameters $\epsilon, \mathrm{Ro}, \delta$ the equations can be simplified by assuming

$$\epsilon = \mathrm{Ro} \ll 1,$$

which gives

$$\mathrm{Ro}^2 \frac{Du}{Dt} - v = -\frac{\partial \phi}{\partial x}, \tag{4.26}$$

$$\frac{Dv}{Dt} + u = -\frac{\partial \overline{\theta}}{\partial y} \left(z - \frac{1}{2} \right), \tag{4.27}$$

$$(\mathrm{Ro}\delta)^2 \frac{Dw}{Dt} - \theta = -\frac{\partial \phi}{\partial z}, \tag{4.28}$$

$$\frac{D\theta}{Dt} + v \frac{\partial \overline{\theta}}{\partial y} = 0, \tag{4.29}$$

$$\frac{\partial u}{\partial x} + \frac{\partial w}{\partial z} = 0. \tag{4.30}$$

It should be noted that one of the benefits of using the vertical slice configuration is that the convergence of the full equations to the semigeostrophic equations is $\mathcal{O}\left(\mathrm{Ro}^2\right)$. For the three-dimensional case it is second-order in Rossby number under the additional restriction $\mathrm{Ro} = \mathcal{O}\left(\delta^2\right)$, and first-order otherwise. The semigeostrophic limit can more generally be obtained by taking $\epsilon \sim \mathrm{Ro}$, but setting the constant of proportionality to unity simplifies the presentation.

There are other options to relate the small parameters ϵ and Ro. If $\mathrm{Ro} < \epsilon$ then $u = \overline{U}$, which corresponds to the background steady state with no evolution. If $\epsilon < \mathrm{Ro}$ then this gives $Dv/Dt = 0$, which corresponds to unforced oscillations. Neither of these cases will be considered in this thesis.

Neglecting the terms that are quadratic in the Rossby number gives

$$v_g = \frac{\partial \phi}{\partial x}, \tag{4.31}$$

$$\frac{Dv_g}{Dt} + u = -\frac{\partial \overline{\theta}}{\partial y}\left(z - \frac{1}{2}\right), \tag{4.32}$$

$$\theta = \frac{\partial \phi}{\partial z}, \tag{4.33}$$

$$\frac{D\theta}{Dt} + v_g \frac{\partial \overline{\theta}}{\partial y} = 0, \tag{4.34}$$

$$\frac{\partial u}{\partial x} + \frac{\partial w}{\partial z} = 0, \tag{4.35}$$

which are the nondimensional semigeostrophic Eady equations, where the subscript $(\cdot)_g$ corresponds to the geostrophic value.

Whilst the momentum is approximated by the geostrophic value v_g, the trajectories, and hence the material derivative, use the unapproximated values $\mathbf{u}$. This approximation is valid assuming that the *Lagrangian* Rossby number is small, as discussed in Section 2.3.

In the semigeostrophic equations there are no longer prognostic equations for the advecting velocities u and w, since there is now exact geostrophic and hydrostatic balance. Instead, the advecting velocities must be diagnosed from the inversion of the potential vorticity. This process is outlined below.

First the geopotential is calculated from the (dimensional) semigeostrophic PV distribution (Hoskins and Bretherton, 1972; Snyder et al., 1993)

$$\left(f^2 + \frac{\partial^2 \phi_g}{\partial x^2}\right)\frac{\partial^2 \phi_g}{\partial z^2} - \left(\frac{\partial^2 \phi_g}{\partial x \partial z}\right)^2 = \rho_0 f \frac{g}{\theta_0} q_g, \tag{4.36}$$

which is a second-order nonlinear elliptic Monge-Ampère equation, and solution techniques have been given in Froese (2012); Feng et al. (2013). Once ϕ_g has been found, it is then necessary to calculate the in-slice ageostrophic circulation from

$$\left(N^2 + \frac{\partial^2 \phi_g}{\partial z^2}\right)\frac{\partial^2 \psi}{\partial x^2} - 2\frac{\partial^2 \phi_g}{\partial x \partial z}\frac{\partial^2 \psi}{\partial x \partial z} + \left(f^2 + \frac{\partial^2 \phi_g}{\partial x^2}\right)\frac{\partial^2 \psi}{\partial z^2} = -2\Lambda \frac{\partial^2 \phi_g}{\partial x^2}, \tag{4.37}$$

where

$$u = -\frac{\partial \psi}{\partial z}, \quad w = \frac{\partial \psi}{\partial x},$$

is the in-slice ageostrophic circulation. Note that Snyder et al. (1993) used the same procedure, but with q_g in Equation (4.36) replaced with q, i.e. the full potential vorticity, to diagnose the corresponding semigeostrophic fields from a given PV distribution, allowing comparisons to be made from a single model of the full equations.

4.1.2 Conserved quantities

In this section the conserved quantities for the standard and semigeostrophic Eady models are given in dimensional form.

Energy

The Eady model conserves an energy integral which is composed of kinetic and gravitational potential components. The standard model kinetic energy is given by

$$E_{ke} = \int_\Omega \frac{1}{2}\rho_0 \left(|\mathbf{u}|^2 + v^2 \right) \mathrm{d}V, \tag{4.38}$$

and for the semigeostrophic model the corresponding kinetic energy is composed of only the geostrophic velocity, i.e.

$$E^g_{ke} = \int_\Omega \frac{1}{2}\rho_0 v_g^2 \, \mathrm{d}V. \tag{4.39}$$

Both the standard and semigeostrophic models have the same potential energy

$$E_{pe} = -\int_\Omega \rho_0 \frac{g}{\theta_0}\theta \left(z - \frac{H}{2} \right) \mathrm{d}V, \tag{4.40}$$

so that the conserved total energy is

$$E_T = E_{ke} + E_{pe}, \tag{4.41}$$

and equivalently for E^g_T with E_{ke} replaced with E^g_{ke}.

Combining the terms for the standard model gives

$$\frac{E_T}{\rho_0} = \int_\Omega \frac{1}{2}\left(|\mathbf{u}|^2 + v^2 \right) - \frac{g}{\theta_0}\theta \left(z - \frac{H}{2} \right) \mathrm{d}V. \tag{4.42}$$

Taking an Eulerian time derivative gives

$$\begin{aligned} \frac{\partial}{\partial t}\left(\frac{E_T}{\rho_0} \right) = \int_\Omega \mathbf{u} \cdot \left(-\nabla\phi + fv\hat{\mathbf{x}} + \frac{g}{\theta_0}\theta\hat{\mathbf{z}} - \mathbf{u}\cdot\nabla\mathbf{u} \right) + \\ v\left(-\frac{g}{\theta_0}\frac{\partial\overline{\theta}}{\partial y}z^* - fu - \mathbf{u}\cdot\nabla v \right) - \\ \frac{g}{\theta_0}z^*\left(-v\frac{\partial\overline{\theta}}{\partial y} - \mathbf{u}\cdot\nabla\theta \right) \mathrm{d}V, \end{aligned} \tag{4.43}$$

where

$$z^* = z - \frac{H}{2}.$$

The Coriolis and meridional forcing terms cancel, which gives

$$\frac{\partial}{\partial t}\left(\frac{E_T}{\rho_0}\right) = \int_\Omega \underbrace{-\mathbf{u}\cdot\nabla\phi}_{①} \underbrace{-\mathbf{u}\cdot\nabla\left(|\mathbf{u}|^2+v^2\right)}_{②} + \underbrace{\frac{g}{\theta_0}\left(\theta\mathbf{u}\cdot\hat{\mathbf{z}}+z^*\mathbf{u}\cdot\nabla\theta\right)}_{③}\,\mathrm{d}V. \tag{4.44}$$

Looking at each of these in turn, the first of which

$$\begin{aligned} ① &= -\int_\Omega \mathbf{u}\cdot\nabla\phi\,\mathrm{d}V, \\ &= -\int_\Omega \nabla\cdot(\mathbf{u}\phi)\,\mathrm{d}V, \\ &= -\int_{\partial\Omega} \mathbf{u}\phi\cdot\hat{\mathbf{n}}\,\mathrm{d}S = 0, \end{aligned} \tag{4.45}$$

where the continuity equation, divergence theorem and boundary condition

$$\frac{\partial\phi}{\partial\hat{\mathbf{n}}} = 0,$$

have been used. Similarly it can be shown that the second term leads to

$$② = -\int_{\partial\Omega} \mathbf{u}E_{ke}\cdot\hat{\mathbf{n}}\,\mathrm{d}S, \tag{4.46}$$

which for no flux boundary conditions on the top and bottom is zero. The final term

$$\begin{aligned} ③ &= -\frac{g}{\theta_0}\int_\Omega \mathbf{u}\cdot\nabla(\theta z^*)\,\mathrm{d}V, \\ &= -\frac{g}{\theta_0}\int_{\partial\Omega} \mathbf{u}\theta z^*\cdot\hat{\mathbf{n}}\,\mathrm{d}S, \end{aligned} \tag{4.47}$$

which, again for no flux boundary conditions is zero. Note that if the background profile is explicitly accounted for above then θ in Equation (4.47) is replaced by $\theta+\overline{\theta}$ and the energy conservation is unchanged.

Ertel potential vorticity

Using Equations (2.21) with the conservation of potential temperature gives the following form for the Ertel potential vorticity as

$$q = \frac{1}{\rho_0}(\nabla\times\mathbf{v}+f\hat{\mathbf{z}})\cdot\nabla\theta, \tag{4.48}$$

where $\mathbf{v} = (u, v, w)$ is the full three-dimensional velocity vector. Expanding Equation (4.48), noting that $\partial_y = 0$ for all variables apart from θ, the potential vorticity is

$$q = \frac{1}{\rho_0}\left\{\frac{\partial\overline{\theta}}{\partial y}\zeta + \left[\frac{\partial}{\partial x}(v+fx)\frac{\partial}{\partial z}\left(\theta+\overline{\theta}\right) - \frac{\partial\theta}{\partial x}\frac{\partial v}{\partial z}\right]\right\}, \tag{4.49}$$

and

$$\zeta = \hat{\mathbf{y}}\cdot\nabla\times\mathbf{v} = \frac{\partial u}{\partial z} - \frac{\partial w}{\partial x},$$

is the in-slice component of vorticity.

The semigeostrophic potential vorticity, as discussed in Section 2.3.3, is restated here as

$$\frac{D}{Dt}\left(\zeta_g\cdot\nabla\theta\right) = 0,$$

where the geostrophic vorticity is restated

$$\zeta_g = \nabla\times\mathbf{u}_g + f\hat{\mathbf{z}} + \frac{1}{f}\left(\frac{\partial\left(u_g,v_g\right)}{\partial\left(y,z\right)}, -\frac{\partial\left(u_g,v_g\right)}{\partial\left(x,z\right)}, \frac{\partial\left(u_g,v_g\right)}{\partial\left(x,y\right)}\right).$$

Taking into account that $\partial_y = 0$ for all variables apart from the background profile, this gives the semigeostrophic PV for the Eady model as

$$\begin{aligned} q_g =& \frac{1}{f}\frac{\partial\overline{\theta}}{\partial y}\frac{\partial u_g}{\partial z}\frac{\partial}{\partial x}\left(v_g+fx\right) + \\ & \left[\frac{\partial}{\partial x}\left(v_g+fx\right)\frac{\partial}{\partial z}\left(\theta+\overline{\theta}\right) - \frac{\partial\theta}{\partial x}\frac{\partial v_g}{\partial z}\right]. \end{aligned} \tag{4.50}$$

4.2 Numerical techniques

As mentioned at the start of this chapter, the numerical techniques introduced in Chapter 3 are now discussed in more detail in terms of the implementation and the solution strategies employed. The solution of the elliptic problem that arises through the projection method, and the treatment of the initial and boundary conditions, are discussed in the following sections.

4.2.1 Vertical discretisation

The vertical staggered grid has already been covered in the start of Chapter 3, but the choice of prognostic variable locations will be briefly discussed here.

An individual primal "control volume" for the vertical slice geometry is shown in Figure 4.2. Whilst the correct representation, in the sense of the full three-dimensional system, of the horizontally staggered C-grid would be to collocate v with ϕ at the cell centres, this is avoided in this thesis and v is instead collocated with u. The benefit of this staggering is that of improved

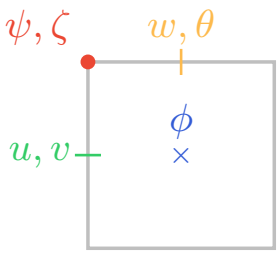

Figure 4.2: *A primal grid pseudo control volume showing the variable locations.*

Symbol	Dimension	Description
Matrices		
I	–	Identity matrix
$\mathsf{0}, \cdot$	–	Empty matrix, used interchangeably
R	$n_1 \times n_2$	Interpolation from v to θ
$\mathsf{G_x}$	$n_2 \times n_2$	Pressure gradient, x-component
$\mathsf{G_z}$	$n_1 \times n_2$	Pressure gradient, z-component
G	$(2n_1 + 2n_2) \times n_2$	Total pressure gradient
$\mathsf{D_x}$	$n_2 \times n_2$	Divergence matrix, u-component
$\mathsf{D_z}$	$n_1 \times n_2$	Divergence matrix, w-component
D	$n_2 \times (2n_1 + 2n_2)$	Total divergence
L	$(2n_1 + 2n_2) \times (2n_1 + 2n_2)$	Linear forcing components
Column vectors		
$\mathbf{0}$	–	Empty vector
$\mathbf{S}$	$(2n_1 + 2n_2)$	"State" vector, $\left[u, v, w, \theta\right]^T$
$\mathbf{p}$	n_2	"Pressure" vector, $\left[\phi\right]$
$\mathbf{F}$	$(2n_1 + 2n_2)$	Background forcing

Table 4.1: *Summary of the matrices and vectors used in this chapter.*

treatment of inertial oscillations and representation of geostrophic balance without having to average in the horizontal. This is a reasonable option in an idealised research model, although operational models using the C-grid staggering can still support intense frontogenesis, (Cullen, 2008).

The boundary conditions are covered in Section 4.4. One consequence of the rigid boundaries at the top and bottom is that there is no need to explicitly store w and θ there. For a domain $\Omega = [-L, L] \times [0, H]$ that is split into n_x by n_z control volumes in the horizontal and vertical, respectively, the fields u, v and ϕ are all of size $n_2 = n_x \times n_z$, whilst w and θ are both of size $n_1 = n_x \times (n_z - 1)$. The dimensions, for both column vectors and matrices, will be dropped in the rest of this chapter, but a summary is provided in Table 4.1.

One point to note is that where velocities are required at other variable

locations, as needed for advection, this is carried out with bilinear interpolation with the matrices created once at the start of the experiment and evaluated subsequently as matrix-vector products. No attempt was made to quantify the error resulting from this second-order accurate in space interpolation process. For interpolation of prognostic variables, as in the semi-Lagrangian method, higher order polynomial interpolation is used, as covered in Section 3.2.1.

4.2.2 Eady problem

For the standard Eady problem given by Equations (4.9) to (4.13) the non-linearity is contained entirely within the advection terms, so that $\mathbf{N} \equiv \mathbf{0}$. Writing the equations in a similar form to the idealised problem of Chapter 3, with the pressure-like variable, ϕ, separated, gives

$$\begin{aligned} \frac{\partial \mathbf{S}}{\partial t} + \mathcal{A}(\mathbf{u}, \mathbf{S}) + \mathbf{L}(\mathbf{S}, \mathbf{x}, t) + \mathcal{G}(\mathbf{p}) &= \mathbf{0}, & (4.51) \\ \mathcal{D}(\mathbf{S}) &= \mathbf{0}, & (4.52) \end{aligned}$$

where

$$\mathbf{S} = \left[u, v, w, \theta\right]^T, \quad \mathbf{p} = \left[\phi\right],$$

are the "state" and "pressure" column vectors, and

$$\mathcal{G}(\mathbf{p}) = \left[\tfrac{\partial \phi}{\partial x}, 0, \tfrac{\partial \phi}{\partial z}, 0\right]^T, \quad \mathcal{D}(\mathbf{S}) = \left[\tfrac{\partial u}{\partial x}, 0, \tfrac{\partial w}{\partial z}, 0\right],$$

are matrix representations of the gradient and divergence terms. Using the expression for the material derivative gives

$$\begin{aligned} \frac{D\mathbf{S}}{Dt} + \mathbf{L}(\mathbf{S}, \mathbf{x}, t) + \mathcal{G}(\mathbf{p}) &= \mathbf{0}, & (4.53) \\ \mathcal{D}(\mathbf{S}) &= \mathbf{0}. & (4.54) \end{aligned}$$

The forcing terms, pressure gradient and divergence terms can be written in terms of matrix-vector products as

$$\mathbf{L}(\mathbf{S}, \mathbf{x}, t) = \underbrace{\begin{bmatrix} \cdot & -f\mathsf{I} & \cdot & \cdot \\ f\mathsf{I} & \cdot & \cdot & \cdot \\ \cdot & \cdot & \cdot & -\frac{g}{\theta_0}\mathsf{I} \\ \cdot & \frac{\partial \bar{\theta}}{\partial y}\mathsf{R} & \frac{\partial \bar{\theta}}{\partial z}\mathsf{I} & \cdot \end{bmatrix}}_{\mathsf{L}} \begin{bmatrix} u \\ v \\ w \\ \theta \end{bmatrix} + \underbrace{\begin{bmatrix} 0 \\ \frac{\partial \bar{\theta}}{\partial y}\frac{g}{\theta_0}\left(z - \frac{H}{2}\right) \\ 0 \\ 0 \end{bmatrix}}_{\mathbf{F}}, \qquad (4.55)$$

$$\mathcal{G}(\mathbf{p}) = \underbrace{\begin{bmatrix} \mathsf{G}_x \\ \cdot \\ \mathsf{G}_z \\ \cdot \end{bmatrix}}_{\mathsf{G}} \left[\phi\right], \qquad (4.56)$$

and

$$\mathcal{D}(\mathbf{S}) = \underbrace{\begin{bmatrix}\mathsf{D}_\mathsf{x} & \cdot & \mathsf{D}_\mathsf{z} & \cdot\end{bmatrix}}_{\mathsf{D}} \begin{bmatrix} u \\ v \\ w \\ \theta \end{bmatrix}. \tag{4.57}$$

4.2.3 Implemented numerical schemes

In this section the specific details of the implemented schemes are presented. The first is the semi-implicit semi-Lagrangian (SISL) scheme, which is representative of operational techniques of the UK Met Office, but with the Boussinesq approximation of Section 2.2.2. The second and third are also semi-implicit schemes, but use Eulerian transport schemes in order to investigate the effects of improved conservation properties. These schemes were introduced in Section 3.3.

Unified Model – semi-implicit semi-Lagrangian

Although the lack of any explicit nonlinear terms greatly simplifies the form of the equations, there is still the requirement to iterate on the departure point calculation if an implicit method is used. The implicit iterative method applied to the standard Eady problem takes the following form

$$\begin{aligned}(\mathsf{I} + \vartheta\Delta t\mathsf{L})\,\Delta\mathbf{S}^k + \vartheta\Delta t\mathsf{G}\Delta\mathbf{p}^k &= \left[\mathbf{S}^n_{*,SL}\right]^k_d - (\mathsf{I} + \vartheta\Delta t\mathsf{L})\,\mathbf{S}^n \\ &\quad -\vartheta\Delta t\mathsf{G}\mathbf{p}^n - \vartheta\Delta t\mathbf{F}^{n+1}, \qquad (4.58)\\ \mathsf{D}\Delta\mathbf{S}^k &= -\mathsf{D}\mathbf{S}^n, \qquad (4.59)\end{aligned}$$

where

$$\mathbf{S}_{*,SL} = [\mathsf{I} - (1-\vartheta)\,\Delta t\mathsf{L}]\,\mathbf{S} - (1-\vartheta)\,\Delta t\mathsf{G}\mathbf{p} - (1-\vartheta)\,\Delta t\mathbf{F}.$$

Note that now the evaluation at the departure point has an iterative superscript; this means that the previous implicit iteration for the departure point is now contained within the outer iterations. There is also no problem with putting the additional implicit forcing term $\mathbf{F}^{n+1}$ on the right-hand side as the arrival points z^{n+1} are the fixed Eulerian grid, and so it is trivial to calculate this term.

The SISL scheme can be written as

$$\begin{aligned}\begin{bmatrix}\mathsf{I} + \vartheta\Delta t\mathsf{L} & \vartheta\Delta t\mathsf{G} \\ \mathsf{D} & 0\end{bmatrix}\begin{bmatrix}\Delta\mathbf{S} \\ \Delta\mathbf{p}\end{bmatrix}^k &= \begin{bmatrix}\left[\mathbf{S}^n_{*,SL}\right]^k_d \\ \mathbf{0}\end{bmatrix} - \begin{bmatrix}\vartheta\Delta t\mathbf{F}^{n+1} \\ \mathbf{0}\end{bmatrix} \\ &\quad - \begin{bmatrix}\mathsf{I} + \vartheta\Delta t\mathsf{L} & \vartheta\Delta t\mathsf{G} \\ \mathsf{D} & 0\end{bmatrix}\begin{bmatrix}\mathbf{S} \\ \mathbf{p}\end{bmatrix}^n. \qquad (4.60)\end{aligned}$$

The departure point evaluation is then

$$[\chi^n]_d^k = \chi\left(\mathbf{x} - \mathbf{a}^k, t\right), \tag{4.61}$$

where the iterations over $\mathbf{a}^k$ are the same as given by Algorithm 3.1 but they are now combined with the outer iterations.

For the staggered C-grid it is necessary to calculate two sets of departure points; one for u and v, and one for w and θ. The trajectory calculation also requires additional interpolation to get the velocity at the arrival points, e.g. w at u points and vice-versa, and this is calculated using bilinear interpolation, as mentioned earlier. Once the departure points have been calculated the interpolation weights can be calculated once for each field that is collocated on that particular grid, thereby saving the trajectory calculation for additional tracer species.

Semi-implicit Eulerian

Applying the semi-implicit Eulerian method to the standard Eady problem gives

$$\begin{bmatrix} \mathsf{I} + \vartheta\Delta t\mathsf{L} & \vartheta\Delta t\mathsf{G} \\ \mathsf{D} & 0 \end{bmatrix} \begin{bmatrix} \Delta\mathbf{S} \\ \Delta\mathbf{p} \end{bmatrix}^k = \begin{bmatrix} -\mathbf{S}^{\mathcal{A},k} \\ \mathbf{0} \end{bmatrix} - \begin{bmatrix} \Delta t\mathbf{F}^{n+1/2} \\ \mathbf{0} \end{bmatrix} - \begin{bmatrix} \Delta t\mathsf{L} & \Delta t\mathsf{G} \\ \mathsf{D} & 0 \end{bmatrix} \begin{bmatrix} \mathbf{S} \\ \mathbf{p} \end{bmatrix}^n, \tag{4.62}$$

where

$$\mathbf{F}^{n+1/2} = \vartheta\mathbf{F}^{n+1} + (1-\vartheta)\,\mathbf{F}^n,$$

is the semi-implicit averaging of the meridional forcing term, which is averaged over the fixed Eulerian grid, as opposed to the trajectories in the semi-implicit semi-Lagrangian scheme.

The advected state, $\mathbf{S}^{\mathcal{A},k}$, follows that defined in Section 3.3.4, which is restated here

$$\mathbf{S}^{\mathcal{A},k} = \begin{bmatrix} u^{\mathcal{A},k} \\ v^{\mathcal{A},k} \\ w^{\mathcal{A},k} \\ \theta^{\mathcal{A},k} \end{bmatrix},$$

where the individual advected variables follow

$$\chi^{\mathcal{A},k} = -\int_t^{t+\Delta t} \nabla\cdot\left(\mathbf{u}^{n+1/2,k}\chi^n\right)\mathrm{d}t,$$

with the velocity at the midpoint calculated from

$$\mathbf{u}^{n+1/2,k} = \vartheta_E\mathbf{u}^{n+1,k} + (1-\vartheta_E)\,\mathbf{u}^n,$$

which is centred for $\vartheta_E = 1/2$.

Semi-implicit vector invariant Eulerian

The semi-implicit vector invariant formulation appears the same as the semi-implicit Eulerian scheme, with the exception that the advected state is replaced with

$$\mathbf{S}_{VI}^{\mathcal{A},k} = \begin{bmatrix} u_{VI}^{\mathcal{A},k} \\ v^{\mathcal{A},k} \\ w_{VI}^{\mathcal{A},k} \\ \theta^{\mathcal{A},k} \end{bmatrix}.$$

The meridional velocity and potential temperature are transported using the same method as in the scheme above, but the in-slice velocities are now transported following a modified Algorithm 3.3. The update is calculated as

$$(u, w)_{VI}^{\mathcal{A},k} = -\int_t^{t+\Delta t} (-G, F)\,\mathrm{d}t,$$

where the gradient term has been ignored since it would be projected off after the solution of the linear system.

The matrix on the left-hand sides of all the schemes outlined above are the same. This is intentional, and means that the same solution method to solve the resulting linear problem can be reused for each of the different transport schemes. Any differences between the methods, then, will be due to the transport schemes themselves. The details of the linear solver is covered in the next section.

4.3 Linear solvers

The following section covers the solution of the linear system of equations that arises from a semi-implicit discretisation of the Eady problem, for both the Eulerian and semi-Lagrangian advection schemes. The semi-implicit discretisation is required to ensure that in the semigeostrophic limit, as $f \to \infty$ and the associated explicit timescale approaches zero, the solution of the linear system remains stable.

In the current work the fact that the problem is two-dimensional, the wave forcing terms are purely linear and stationary in time means that a direct solution method is viable. The techniques described here are specific to the current problem set-up, including grid staggering and boundary conditions.

In operational models the computational size and complexity of the resulting Helmholtz problem means that an iterative approach is used (Davies et al., 2005). Iterative schemes applied to sparse, non-symmetric matrices can be found in the textbook of Golub and Van Loan (2012).

4.3.1 Formulation of pressure correction

The linear system on the left-hand side of the semi-implicit schemes can be seen as a form of a pressure correction / projection method. This simultaneously carries out the linear wave forcing terms, i.e. inertial and buoyancy oscillations, whilst enforcing continuity through a divergence-free in-slice velocity field.

The pressure correction method results in having to solve a system of equations of the form

$$\begin{bmatrix} \mathsf{A} & \mathsf{B} \\ \mathsf{C} & \mathsf{0} \end{bmatrix} \begin{bmatrix} x_1 \\ x_2 \end{bmatrix} = \begin{bmatrix} b_1 \\ b_2 \end{bmatrix}, \tag{4.63}$$

where x_1, b_1 are column vectors of length n_1; x_2, b_2 are column vectors of length n_2; A is a non-singular square matrix of dimension n_1; $\mathsf{0}$ is the square empty matrix of dimension n_2; and B and C are non-square matrices of dimensions $n_1 \times n_2$ and $n_2 \times n_1$ respectively.

Direct solution

The direction solution can be obtained using the Schur complement (Zhang, 2005) for block matrix inversion. For a block matrix

$$\mathsf{M} = \begin{bmatrix} \mathsf{A} & \mathsf{B} \\ \mathsf{C} & \mathsf{0} \end{bmatrix}, \tag{4.64}$$

the inverse is given by

$$\mathsf{M}^{-1} = \begin{bmatrix} \mathsf{A}^{-1} + \mathsf{A}^{-1}\mathsf{B}\mathsf{S}^{-1}\mathsf{C}\mathsf{A}^{-1} & -\mathsf{A}^{-1}\mathsf{B}\mathsf{S}^{-1} \\ -\mathsf{S}^{-1}\mathsf{C}\mathsf{A}^{-1} & \mathsf{S}^{-1} \end{bmatrix}, \tag{4.65}$$

where S is the Schur complement given by $\mathsf{S} = -\mathsf{C}\mathsf{A}^{-1}\mathsf{B}$. This requires A and S to be non-singular.

In practice this requires that A^{-1} can be formed analytically. In addition A^{-1} should be block-sparse so that the Schur complement is sparse, which improves the computational efficiency. The full inverse matrix is generally not computed, and the solution method proceeds as follows:

1. x_2 is found from
$$\mathsf{S}x_2 = b_2 - \mathsf{A}^{-1}b_1, \tag{4.66}$$
2. x_1 is found from
$$x_1 = \mathsf{A}^{-1}\left(b_1 - \mathsf{B}x_2\right). \tag{4.67}$$

If A^{-1} can be formed analytically then this reduces the complexity of solving the full $(n_1 + n_2)$ system down to solving a system of n_2. The choice of the "split point", i.e. the value of n_1, and swapping rows in the full matrix can help to reduce the size of the Schur complement that needs to be inverted.

Approximate factorisation

In this section the method follows Saleri and Veneziani (2005) in using an approximate factorisation technique. The approximate factorisation technique is used in the experiments of Section 6.2, but the description of the method is given here. The exact LU factorisation of the system of Equations (4.63) is

$$\begin{bmatrix} \mathsf{A} & \mathsf{B} \\ \mathsf{C} & 0 \end{bmatrix} = \begin{bmatrix} \mathsf{A} & 0 \\ \mathsf{C} & -\mathsf{C}\mathsf{A}^{-1}\mathsf{B} \end{bmatrix} \begin{bmatrix} \mathsf{I} & \mathsf{A}^{-1}\mathsf{B} \\ 0 & \mathsf{I} \end{bmatrix}. \tag{4.68}$$

An approximate factorisation is given by

$$\mathcal{M} = \begin{bmatrix} \mathsf{A} & 0 \\ \mathsf{C} & -\mathsf{C}\mathsf{W}_1^{-1}\mathsf{B} \end{bmatrix} \begin{bmatrix} \mathsf{I} & \mathsf{W}_2^{-1}\mathsf{B} \\ 0 & \mathsf{Q} \end{bmatrix}, \tag{4.69}$$

where W_1^{-1}, W_2^{-1} are approximations to A^{-1}, and Q satisfies

$$\mathsf{Q} = \underbrace{\left(\mathsf{C}\mathsf{W}_1^{-1}\mathsf{A}\mathsf{W}_1^{-1}\mathsf{B}\right)}_{\mathsf{T}}{}^{-1}\mathsf{C}\mathsf{W}_1^{-1}\mathsf{B}. \tag{4.70}$$

It is possible to choose

$$\mathsf{W}_1^{-1} = \tilde{\mathsf{A}}^{-1}, \quad \mathsf{W}_2^{-1} = \mathsf{A}^{-1},$$

where $\tilde{\mathsf{A}}^{-1}$ is an approximation to the inverse of A. This then gives an approximate factorisation as

$$\mathcal{M} = \underbrace{\begin{bmatrix} \mathsf{A} & 0 \\ \mathsf{C} & -\mathsf{C}\tilde{\mathsf{A}}^{-1}\mathsf{B} \end{bmatrix}}_{\mathsf{L}} \underbrace{\begin{bmatrix} \mathsf{I} & \mathsf{A}^{-1}\mathsf{B} \\ 0 & \mathsf{Q} \end{bmatrix}}_{\mathsf{U}} = \begin{bmatrix} \mathsf{A} & \mathsf{B} \\ \mathsf{C} & \mathsf{C}\mathsf{A}^{-1}\mathsf{B} - \mathsf{C}\tilde{\mathsf{A}}^{-1}\mathsf{B}\mathsf{Q} \end{bmatrix}. \tag{4.71}$$

Using the previous definition of Q it is then possible to show

$$\mathcal{M} = \begin{bmatrix} \mathsf{A} & \mathsf{B} \\ \mathsf{C} & 0 \end{bmatrix}.$$

Hence, although A^{-1} is approximated *within* the factorisation, because of the choice of W_1^{-1}, W_2^{-1} and Q the approximations cancel, and the solution satisfies the full system of Equations (4.63).

The solution method then proceeds for the factorised system as:

1. y_1 is found from
$$\mathsf{A}y_1 = b_1, \tag{4.72}$$
2. y_2 is found from
$$\mathsf{C}y_1 - \mathsf{C}\tilde{\mathsf{A}}^{-1}\mathsf{B}y_2 = b_2, \tag{4.73}$$

3. x_2 is found from
$$\mathsf{C}\tilde{\mathsf{A}}^{-1}\mathsf{B}x_2 = \mathsf{T}y_2, \tag{4.74}$$

4. x_1 is found from
$$x_1 + \mathsf{A}^{-1}\mathsf{B}x_2 = y_1. \tag{4.75}$$

At first glance this might appear to be worse than the direct solution, but it allows for a solution to be calculated for situations in which it might be possible to calculate A^{-1} but the resulting linear system $\mathsf{C}\mathsf{A}^{-1}\mathsf{B}$ might be too complex to form. This can happen if there is a viscous term in the equations that is to be included as part of this single step; in doing so the diagonals in A are no longer the identity matrices but now include off diagonal terms and the resulting inverse is dense.

4.3.2 Inverse of forcing matrix

For a matrix of the form
$$\mathsf{M} = \begin{bmatrix} \mathsf{A} & 0 \\ \mathsf{C} & \mathsf{D} \end{bmatrix}, \tag{4.76}$$
the inverse, again calculated using the Schur complement, is given by
$$\mathsf{M}^{-1} = \begin{bmatrix} \mathsf{A}^{-1} & 0 \\ -\mathsf{D}^{-1}\mathsf{C}\mathsf{A}^{-1} & \mathsf{D}^{-1} \end{bmatrix}. \tag{4.77}$$

After a semi-implicit time discretisation the linear forcing terms require the inversion of
$$\mathsf{M} = \begin{bmatrix} \mathsf{I} & -\xi_1\mathsf{I} & \cdot & \cdot \\ \xi_1\mathsf{I} & \mathsf{I} & \cdot & \cdot \\ \cdot & \cdot & \mathsf{I} & -\xi_2\mathsf{I} \\ \cdot & \xi_3\mathsf{R} & \xi_4\mathsf{I} & \mathsf{I} \end{bmatrix}, \tag{4.78}$$
where
$$\xi_1 = \vartheta\Delta t f, \quad \xi_2 = \vartheta\Delta t\frac{g}{\theta_0},$$
$$\xi_3 = \vartheta\Delta t\frac{\partial\overline{\theta}}{\partial y}, \quad \xi_4 = \vartheta\Delta t\frac{\partial\overline{\theta}}{\partial z}.$$
Splitting M into 2×2 sub-matrices and calculating the inverses gives
$$\mathsf{A}^{-1} = \xi_5\begin{bmatrix} \mathsf{I} & \xi_1\mathsf{I} \\ -\xi_1\mathsf{I} & \mathsf{I} \end{bmatrix}, \tag{4.79}$$
with
$$\xi_5 = \frac{1}{1+\xi_1^2},$$
and
$$\mathsf{D}^{-1} = \begin{bmatrix} \xi_6\mathsf{I} & \xi_2\xi_6\mathsf{I} \\ -\xi_4\xi_6\mathsf{I} & \xi_7\mathsf{I} \end{bmatrix}, \tag{4.80}$$

with

$$\xi_6 = \frac{1}{1+\xi_2\xi_4}, \quad \xi_7 = 1 - \xi_2\xi_4\xi_6.$$

Finally, substituting the inverted sub-matrices into the Schur complement full matrix inversion yields

$$\mathsf{M}^{-1} = \begin{bmatrix} \xi_5\mathsf{I} & \xi_1\xi_5\mathsf{I} & \cdot & \cdot \\ -\xi_1\xi_5\mathsf{I} & \xi_5\mathsf{I} & \cdot & \cdot \\ \xi_1\xi_2\xi_3\xi_5\xi_6\mathsf{R} & -\xi_2\xi_3\xi_5\xi_6\mathsf{R} & \xi_6\mathsf{I} & \xi_2\xi_6\mathsf{I} \\ \xi_1\xi_3\xi_5\xi_7\mathsf{R} & -\xi_3\xi_5\xi_7\mathsf{R} & -\xi_4\xi_5\mathsf{I} & \xi_7\mathsf{I} \end{bmatrix}. \tag{4.81}$$

Note that both M and M^{-1} are diagonally dominant; the off-diagonal terms are multiplied by at least a factor of $\vartheta\Delta t$. In addition, for a fully explicit method the inverse correctly reduces to the identity matrix since $\xi_1 = \xi_2 = \xi_3 = \xi_4 = 0$ and $\xi_5 = \xi_6 = \xi_7 = 1$.

4.3.3 Numerical implementation

The matrices are implemented using the `scipy.sparse` module in compressed sparse row format for efficient matrix-vector multiplication. The individual matrices are formed, and then the elliptic problem for the Schur complement , given by Equation (4.65), is solved using the LU decomposition direct solver available in `scipy.sparse.linalg.dsolve`. The decomposition is calculated once only at the start of the numerical integration and the cached object is then evaluated at every time-step to reduce the cost of a full direct solve at every time-step.

The LU decomposition is not suitable for full three-dimensional models in operational use since the computational cost is too high, and so iterative methods are preferred, as mentioned at the start of this section. In the present work the direct approach is preferred since the problem size is small enough to warrant using a direct solver, and the focus is on solution accuracy rather than efficiency.

Apart from writing some interpolation routines in Fortran no profiling or optimisation of the code was carried out. The time-step was taken based on the established results and some preliminary experiments to ensure that the integrations remained stable during frontal collapse. The typical scales of the problem are linked by the Rossby number; the characteristic length is the domain half width, 1000 km; the background advective velocity, 5 m s^{-1}; the Coriolis frequency, 10^{-4} s^{-1}.

4.4 Initial and boundary conditions

Equations (4.16) to (4.20) require the specification of the initial and boundary conditions to be complete. The horizontal boundary conditions are

periodic. The vertical boundary conditions correspond to horizontal rigid lids and are given by

$$\mathbf{u} \cdot \hat{\mathbf{n}} = 0, \quad \frac{\partial \phi}{\partial \hat{\mathbf{n}}} = 0,$$

so that there is no transport across the boundaries. Note that there are no boundary conditions given for the potential temperature; no transport applies to the potential temperature, but in addition θ is not stored on the boundary, and the justification for this will be covered in Section 4.4.3.

No explicit boundary conditions are given for the horizontal velocities since the above reduces to

$$w|_{z=0,H} = 0.$$

In the inviscid case, as examined in this thesis, no further boundary conditions are required, but for viscous boundary conditions that are compatible with this thesis then Nakamura and Held (1989) provides the details.

The above boundary conditions are sufficient for the projection method, but the transport schemes require the additional constraint of monotonicity to be stable, this is discussed later in this section.

Attention is first turned towards the creation of a balanced initial condition. For the asymptotic convergence procedure to have the best chance of succeeding it is necessary to reduce, as far as possible, any initial imbalance since its presence would alter the evolution through an adjustment process. This is because any initial imbalance would mask the imbalance of the dynamics, and would not reduce as $\mathrm{Ro} \to 0$. To this end the creation of an initial perturbation corresponding to the semigeostrophic solution is discussed next.

4.4.1 Balanced initialisation

The balanced initialisation is designed to eliminate, insofar as is possible, the presence of the "fast", as compared to the balanced dynamics, inertia-gravity waves. This is achieved by initialising with a state that is in geostrophic and hydrostatic balance, so that the time derivatives of u and w are zero. First, a thermal wind balanced state is assumed of the form

$$fv = \frac{\partial \phi}{\partial x}, \tag{4.82}$$

$$\frac{g}{\theta_0}\theta = \frac{\partial \phi}{\partial z}. \tag{4.83}$$

Differentiating the above and eliminating the pressure gives

$$f\frac{\partial v}{\partial z} = \frac{g}{\theta_0}\frac{\partial \theta}{\partial x}\left(= \frac{\partial^2 \phi}{\partial x \partial z}\right). \tag{4.84}$$

Differentiating with time, and noting that this commutes with the spatial differentiation, gives

$$f\frac{\partial}{\partial z}\left(\frac{\partial v}{\partial t}\right) = \frac{g}{\theta_0}\frac{\partial}{\partial x}\left(\frac{\partial \theta}{\partial t}\right). \tag{4.85}$$

It is necessary to introduce a streamfunction, such that the velocity field will be solenoidal by construction. The streamfunction is chosen in the vertical to be

$$u = -\frac{\partial \psi}{\partial z}; \quad w = \frac{\partial \psi}{\partial x}.$$

At this point there is some flexibility in what is substituted into Equation (4.85): the full nonlinear terms from the standard Eady model, or just the linear terms where the advection terms have been discarded.

Full nonlinear equation

The time derivatives are replaced with

$$\frac{\partial v}{\partial t} = -fu - \frac{g}{\theta_0}\frac{\partial \overline{\theta}}{\partial y}\left(z - \frac{H}{2}\right) - \mathbf{u}\cdot\nabla v, \tag{4.86}$$

$$\frac{\partial \theta}{\partial t} = -v\frac{\partial \overline{\theta}}{\partial y} - w\frac{\partial \overline{\theta}}{\partial z} - \mathbf{u}\cdot\nabla\theta. \tag{4.87}$$

Using the streamfunction defined earlier, expanding the advection terms and differentiating the resulting terms gives

$$\begin{aligned} &-f\frac{g}{\theta_0}\frac{\partial \overline{\theta}}{\partial y} + f^2\psi_{zz} - f\left(\psi_{zz}v_x - \psi_z v_{xz} + \psi_{xz}v_z + \psi_x v_{zz}\right) = \\ &\frac{g}{\theta_0}\left[-v_x\frac{\partial \overline{\theta}}{\partial y} - \psi_{xx}\frac{\partial \overline{\theta}}{\partial z} - \left(-\psi_{xz}\theta_x - \psi_z\theta_{xx} + \psi_{xx}\theta_z + \psi_x\theta_{xz}\right)\right]. \end{aligned} \tag{4.88}$$

Equation (4.88) is the Sawyer-Eliassen equation, as discussed in Section 2.1. Noting that the first-order derivatives in ψ cancel, owing to the thermal wind balance, this gives the equation for the streamfunction as

$$\left(N^2 + \phi_{zz}\right)\psi_{xx} - 2\phi_{xz}\psi_{xz} + \left(f^2 + \phi_{xx}\right)\psi_{zz} = \frac{g}{\theta_0}\frac{\partial \overline{\theta}}{\partial y}\left(f - \frac{1}{f}\phi_{xx}\right). \tag{4.89}$$

Linear equation

In the linear system the time derivatives are replaced with

$$\frac{\partial v}{\partial t} = -fu - \frac{g}{\theta_0}\frac{\partial \overline{\theta}}{\partial y}\left(z - \frac{H}{2}\right), \tag{4.90}$$

$$\frac{\partial \theta}{\partial t} = -v\frac{\partial \overline{\theta}}{\partial y} - w\frac{\partial \overline{\theta}}{\partial z}. \tag{4.91}$$

Again, using the streamfunction, substituting in and simplifying leads to

$$N^2\psi_{xx} + f^2\psi_{zz} = \frac{g}{\theta_0}\frac{\partial\overline{\theta}}{\partial y}\left(f - \frac{1}{f}\phi_{xx}\right). \tag{4.92}$$

4.4.2 Breeding procedure

The initialisation process follows a "breeding" procedure to generate a balanced initialisation at the desired amplitude. First, a small perturbation is applied to the potential temperature of the form

$$\xi(x,z) = \frac{a\theta_0 N_0}{g}\left\{-\left[1 - \frac{\mathrm{Bu}}{2}\coth\left(\frac{\mathrm{Bu}}{2}\right)\right]\times \right.$$
$$\left.\sinh Z\cos\left(\frac{\pi x}{L}\right) - n\mathrm{Bu}\cosh Z\sin\left(\frac{\pi x}{L}\right)\right\}, \tag{4.93}$$

which is the structure of the (quasigeostrophic) normal mode taken from Williams (1967). The constant a corresponds to the amplitude of the perturbation, and typically a value of $|a| = 7.5$ m s^{-1} is used, which gives a perturbation in the potential temperature of approximately 0.3 K. In addition, this requires the constant

$$n = \mathrm{Bu}^{-1}\left\{\left[\frac{\mathrm{Bu}}{2} - \tanh\left(\frac{\mathrm{Bu}}{2}\right)\right]\left[\coth\left(\frac{\mathrm{Bu}}{2}\right) - \frac{\mathrm{Bu}}{2}\right]\right\}^{\frac{1}{2}},$$

and the modified vertical coordinate,

$$Z = \mathrm{Bu}\left[\left(\frac{z}{H}\right) - \frac{1}{2}\right].$$

A small perturbation of a simpler form, e.g.

$$\xi(x,z) = a\sin\left[\pi\left(\frac{x}{L} + \frac{z - H/2}{H}\right)\right],$$

could also be used (Cullen, 2006). For the parameters defining the standard model the most unstable mode (the Eady wave) very quickly dominates, and the structure of the initial perturbation rapidly loses significance. It is important to make sure that whatever the form of the perturbation the rest of the fields are balanced, so that the amount of IGWs present in the initialisation are minimised.

The hydrostatic relation is then integrated numerically in the vertical, where the geopotential reference values are set along the centreline $z = H/2$. The thermal wind relation is differentiated numerically, using the gradient matrix operator since u and v are collocated, to get the geostrophic meridional velocity field.

Once the balanced state has been generated the in-slice velocity fields are calculated using the *linear* terms given by Equation (4.92). The linear method is chosen since there is quantitatively almost no difference between the two options, whilst the linear method was found to be more robust when experimenting with larger amplitude perturbations.

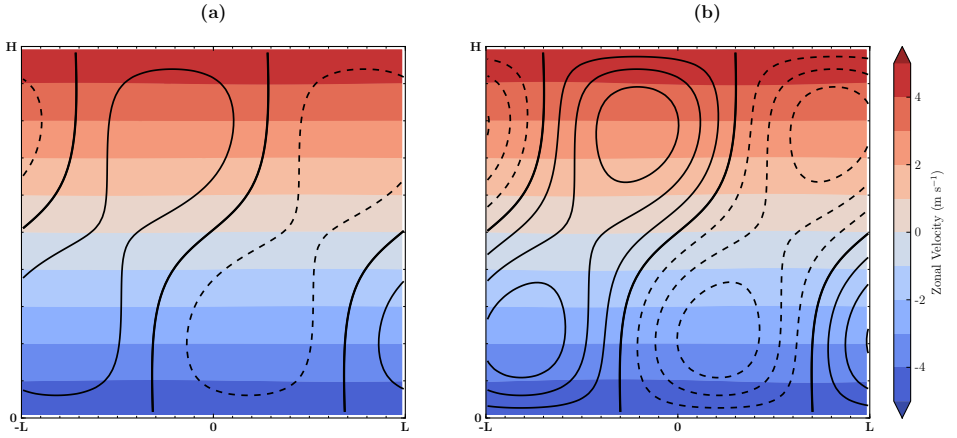

Figure 4.3: *Comparison of in-slice initial velocity fields using the linear terms (a) and the full nonlinear terms (b), zonal velocity in coloured contours and vertical velocity in contour lines with intervals at* 0.08 mm s^{-1}*, negative regions dashed and thick line at zero. The linear terms show the same structure as the nonlinear terms, but just at reduced amplitude.*

A comparison of the two velocity fields is given in Figure 4.3. The structure of the mode between the two methods is almost identical, whilst the peak amplitude of the vertical velocity in the linear case, ≈ 0.1 mm s^{-1}, is lower than the nonlinear case, ≈ 0.3 mm s^{-1}. In both cases the subsequent evolution is well balanced after the breeding process is complete. The horizontal velocity scale is $U = 5$ m s^{-1}, which, when related through the aspect ration gives a vertical velocity of $\mathcal{O}\left(1 \text{ cm } s^{-1}\right)$, which is still an order of magnitude larger than the vertical velocity perturbation amplitude.

Once the initial perturbation is applied the integrations advance in a breeding procedure, in which the solution is allowed to grow until it reaches a certain amplitude, at which point it is rescaled and the process repeated. This works since the fastest growing mode is the large scale Eady wave, which is close to balance for some finite Ro, whilst the unbalanced IGWs are purely oscillatory and not growing in time.

The breeding procedure is terminated once the meridional velocity has met the same amplitude as in NH89; RMS ≈ 1.4 m s^{-1} and $|v|_\infty \approx 3$ m s^{-1}. The time is then rescaled such that this becomes the initial condition for the rest of the integrations. The initialisation typically takes two to four days to reach the same amplitude as NH89. For $\vartheta = 0.55$, where ϑ is the

decentering parameter in the semi-implicit scheme, this is sufficient to give a well-balanced solution.

4.4.3 Potential temperature boundary conditions

In this section the appropriate boundary conditions for the potential temperature are discussed.

Figure 4.4 shows a comparison for whether or not the potential temperature is stored on the boundary, and what the implication is for the bilinear interpolation stencil from v points to θ points, which is required due to the meridional advection of the background state in the potential temperature equation.

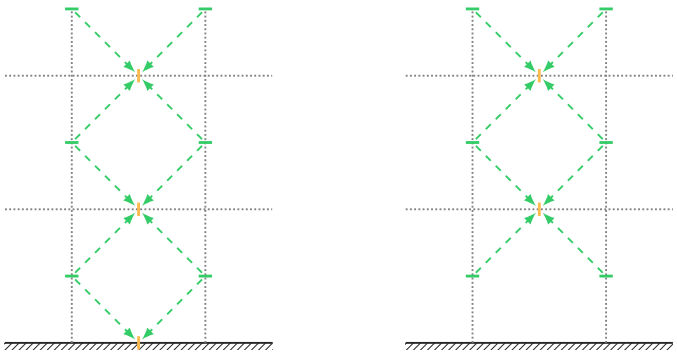

Figure 4.4: *A comparison of interpolation stencils from the meridional velocity field onto the potential temperature field for θ on the boundary (left) and not (right).*

It can be seen from Figure 4.4 (left) that the potential temperature on the boundary would require a different stencil to the rest of the domain. In particular, it is not clear what form this stencil should take, whether it should take half of the neighbouring values or a quarter. The former option implies extrapolating the meridional velocities at the boundary, whilst the latter would result in a reduced forcing component relative to the rest of the domain, neither of which is entirely satisfactory.

The alternative is to *not* store θ on the boundaries. Whilst this might seem unnatural for a problem in which a discontinuity forms on the boundary, it avoids the problems outlined above whilst trivially satisfying the boundary conditions for the vertical velocity, as well as eliminating the possibility of creating spurious values on the boundary through the numerical algorithm. Restating the vertical velocity equation

$$\frac{Dw}{Dt} - \frac{g}{\theta_0}\theta = -\frac{\partial \phi}{\partial z},$$

and now enforcing the boundary condition

$$w|_{z=0,H} = 0,$$

gives that

$$\left.\frac{Dw}{Dt}\right|_{z=0,H} = 0; \quad \frac{g}{\theta_0}\theta = \left.\frac{\partial\phi}{\partial z}\right|_{z=0,H},$$

which shows that there should be exact hydrostatic balance on the boundary.

4.4.4 Advection boundary conditions

There are two key areas that the numerical method needs to do well in to model frontogenesis successfully. The first is maintaining balance, which necessitates the use of the C-grid and Charney-Phillips grid, which are used for geostrophic and hydrostatic balance, respectively. The second is that of preserving the sharp gradients that arise, which requires minimising any operations that contain implicit numerical diffusion, such as interpolation and reconstruction. The effect that this has on the transport schemes and their respective boundary conditions will be discussed below.

Semi-Lagrangian

Whilst treatment of interpolation in the periodic horizontal direction is easily implemented, the vertical requires some consideration.

To keep the same order of interpolation throughout the vertical would require additional information outside of the domain. There are several options to account for the vertical boundaries: provide extra "ghost" points with physically compatible values; bias the stencil to achieve nominally the same order but not centred on the departure point; or to keep a centred interpolation stencil but to reduce the number of points, and hence the interpolation order.

In this thesis the final option is chosen, and is illustrated in Figure 4.5 for a nominally cubic interpolating polynomial. Early testing and comparisons between the methods showed reducing the interpolation order to be the most robust. The ghost point method was comparable to the reduced order, but showed slightly more small scale variation. The biased method was tested, but found to be unstable for realistic fields.

Eulerian

As with semi-Lagrangian the Eulerian advection term requires careful attention on a staggered C-grid. Owing to the finite-volume like formulation of the advection equation in conservation form it is necessary to choose between two options.

The first option is to advect each of the variables on their staggered grids but with the advecting velocity interpolated to the new cell edges. For a divergence-free velocity field on the staggered grid it is possible to get a divergence-free velocity field on each of the horizontally staggered, vertically

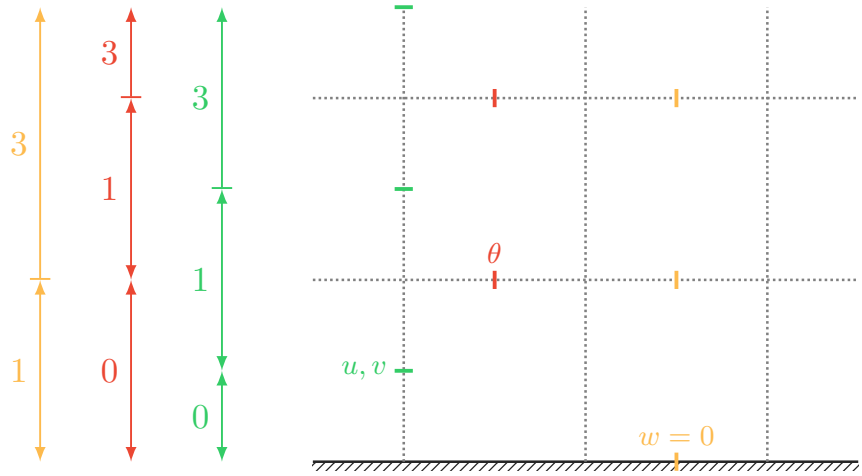

Figure 4.5: *Comparison of reduction in interpolation order in the vertical for the semi-Lagrangian method for the different prognostic variables, where the number corresponds to the interpolation order if a departure point lies in that row. The interpolation order is constant in the horizontal.*

staggered and dual grids with bilinear interpolation, but the treatment at the boundaries becomes difficult.

The second option is to reconstruct the variables to the primal cell centres, advect with the primal velocity field and then reconstruct back to the staggered variable locations. This suffers from two averaging (reconstruction) steps per advection step, which suggests that it would be difficult to preserve strong gradients and accurate representation of balance.

The first option is chosen in the current thesis. The second option was not tested since it was felt that the detrimental effects of the averaging on the sharp gradients would seriously affect the ability to support solutions with strong frontogenesis. Figure 4.6 shows an overview of the control volumes for the staggered grid at the boundary and away from it.

Potential temperature

As θ is not stored on the boundary the Eulerian advection method results in a single row of cells on the top and bottom boundaries that are $(\Delta x, {}^{3\Delta z}/_{2})$.

In practice a uniform grid of $(\Delta x, \Delta z)$ can be assumed throughout, but with a modified flux on the top and bottom boundaries, as shown in Figure 4.7. In the bottom half-cells both the horizontal and vertical fluxes are calculated using the first-order upwind scheme. The horizontal fluxes are then constrained to sum to zero, whilst the vertical flux is constrained so that the acceleration within each half cell matches that of its immediate vertical neighbour. This is then used as the vertical flux within the evolution of the

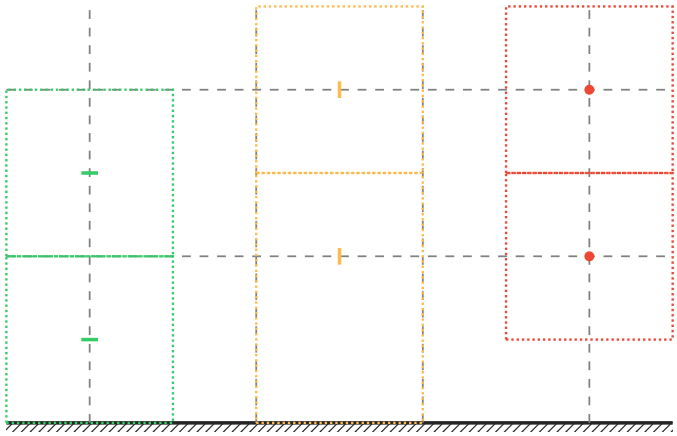

Figure 4.6: *Comparison of control volumes around the prognostic variables for the Eulerian methods.*

first row of the potential temperature cells.

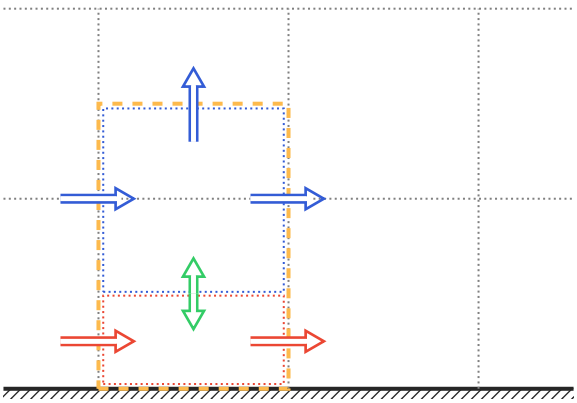

Figure 4.7: *Boundary condition and modified control volumes around the potential temperature cells, as used in the Eulerian advection schemes.*

Vector invariant

In the vector invariant formulation the vorticity is calculated on the dual grid, with the corresponding control volume. Consistent boundary conditions for the vorticity imply that it should be constant on the top and bottom. Unlike the potential temperature, though, the control volume does not extend to the boundary. The reason for this is that the fluxes on the dual grid are used as the updates for the velocity fields on the primal grid. These are linked by taking the perpendicular component, and extending to the boundary is not compatible with the boundary condition $w = 0$ there.

4.5 Asymptotic framework

In this section the effects of the rescaling of the dimensional variables in the physical domain of Cullen (2008) are shown in terms of the appropriate nondimensional parameters outlined in Section 4.1.1. Whilst the analysis will be shown in terms of the relevant nondimensional parameters, it is worth noting that the rescaling experiments are performed in dimensional variables because most operation models use dimensional units.

4.5.1 Validation framework in the Eady model

This section describes two approaches to carry out the asymptotic convergence analysis within the Eady model. Before these are discussed, the reference values of the nondimensional parameters are first considered.

The following values are used for the reference scales

$$U_0 = 5 \text{ m s}^{-1}, \quad L_0 = 1000 \text{ km}, \quad H_0 = 10 \text{ km},$$

$$f_0 = 10^{-4} \text{ s}^{-1}, \quad N_0 = 5 \times 10^{-3} \text{ s}^{-1}, \quad \Lambda_0 = 1 \times 10^{-3} \text{ s}^{-1}.$$

The reference values of the relevant parameters are

Ro	δ	Ri	Fr	Bu
U/fL	H/L	N^2/Λ^2	U/NH	Ro/Fr
0.05	0.01	25	0.1	0.5

so that

$$\text{Ro} < \text{Fr}; \quad \text{Ro}, \text{Fr} \ll 1; \quad \text{Ri} \gg 1.$$

These values are calculated for the initial conditions of the basic state. It is likely that whilst the Eady wave is growing that $\text{Ro} \approx \text{Fr}$, since this corresponds to the most efficient conversion between potential and kinetic energy. It is quite possible at later times during frontogenesis that Ro, Fr will become $\mathcal{O}(1)$ locally.

It is also possible that $\text{Ri} \leq 1/4$ in localised regions, where $\text{Ri} = 1/4$ is the critical value for shear instability (Drazin and Reid, 2004). Any shear instabilities that result will be limited only to the region in which the Richardson number is below the critical value, so that the bulk flow should still remain stable to shear instability (Hoskins, 1971; Gall et al., 1987; Koshyk and Cho, 1992). The effect, though, is that even the localised instabilities will stop a *true* discontinuity forming, (Hoskins and Bretherton, 1972).

Cullen 2008 rescaling

The C08 rescaling is equivalent to

$$U \to \beta U_0, \quad L \to \beta L_0, \quad f \to \frac{1}{\beta} f_0,$$

where the subscript $(\cdot)_0$ corresponds to the reference values above. The parameters then rescale as

Ro	δ	Ri	Fr	Bu
β	$1/\beta$	$1/\beta^2$	β	1

which corresponds to the limit of $\mathrm{Ro} \to 0$ with the semigeostrophic solution invariant through this rescaling.

This rescaling is potentially problematic in that

$$\lim_{\beta \to 0} \delta = \infty,$$

which clearly violates the assumption of hydrostatic balance in the limit. In practice this does not really pose a problem. The aspect ratio is very small to begin with, and the finite values of the rescaling parameter never even approach δ to make the nonhydrostatic term $\mathcal{O}(1)$, so that the dominant imbalance is geostrophic, (Cullen, 2008).

Extended rescaling

In order to improve the dynamical consistency by keeping the aspect ratio invariant with the rescaling it is possible to rescale in the vertical

$$W \to \beta W_0, \quad H \to \beta H_0, \quad N \to \frac{1}{\beta} N_0.$$

This rescaling results in

Ro	δ	Ri	Fr	Bu
β	1	$1/\beta^4$	β	1

in which the Richardson number is now increasing proportionally to β^{-4}. This might not be an issue, since the relevant regime is $\mathrm{Ri} \gg 1$ and the rescaling does not affect the validity of this assumption. There is still some flexibility in rescaling the potential temperature of the form

$$\theta \to \frac{1}{\beta}\theta; \quad \frac{\partial \overline{\theta}}{\partial y} \to \frac{1}{\beta}\frac{\partial \overline{\theta}}{\partial y}; \quad \left(\frac{\partial \overline{\theta}}{\partial z} \to \frac{1}{\beta^2}\frac{\partial \overline{\theta}}{\partial z}\right),$$

where the last term is not explicitly controlled but diagnosed through consistency of the buoyancy frequency. This finally gives the rescaling as

Ro	δ	Ri	Fr	Bu
β	1	$1/\beta^2$	β	1

so that the rescaling is seen as an extension of Cullen (2008) but with the aspect ratio held constant.

4.5.2 Key properties and effects of rescaling

In the following section the key properties of the invariance of the semi-geostrophic solution and the effect on the conserved properties are shown.

Cullen 2008 rescaling

The in-slice velocity equations transform as

$$\beta^2 \frac{Du}{Dt} - fv = -\frac{\partial \phi}{\partial x}, \tag{4.94}$$

$$\frac{Dw}{Dt} - \frac{g}{\theta_0}\theta = -\frac{\partial \phi}{\partial z}. \tag{4.95}$$

Note that the rescaling only affects the zonal momentum equation, so that the ageostrophic acceleration term should approach zero in the limit.

The energy will transform under the rescaling as

$$E_T \to \rho_0 \int_\Omega \frac{1}{2}\left(\beta^2 u^2 + v^2 + w^2\right) - \frac{g}{\theta_0}\theta\left(z - \frac{H}{2}\right) \mathrm{d}V, \tag{4.96}$$

so that the zonal contribution to the kinetic energy will go to zero in the limit, and the subscript for the reference values has been dropped, so that all variables can be assumed to take their values from the standard model. The Ertel potential vorticity will transform as

$$q \to \frac{1}{\rho_0}\left\{\frac{\partial \overline{\theta}}{\partial y}\left(\beta\frac{\partial u}{\partial z} - \frac{1}{\beta}\frac{\partial w}{\partial x}\right) + \frac{1}{\beta}\left[\frac{\partial}{\partial x}(v + fx)\frac{\partial}{\partial z}\left(\theta + \overline{\theta}\right) - \frac{\partial \theta}{\partial x}\frac{\partial v}{\partial z}\right]\right\}. \tag{4.97}$$

A consequence of the C08 rescaling is that one component of the in-slice vorticity, namely

$$\frac{1}{\beta}\frac{\partial w}{\partial x},$$

becomes significant, owing to the presence of the β on the denominator.

Extended rescaling

The in-slice velocity equations transform as

$$\beta^2 \frac{Du}{Dt} - fv = -\frac{\partial \phi}{\partial x}, \tag{4.98}$$

$$\beta^2 \frac{Dw}{Dt} - \frac{g}{\theta_0}\theta = -\frac{\partial \phi}{\partial z}. \tag{4.99}$$

In this case both of the ageostrophic acceleration terms should approach zero at second-order in the limit.

Comparing Equations (4.95) and (4.99) shows that the C08 rescaling does not converge to hydrostatic balance, whilst the extended rescaling does. Cullen (2008) showed that hydrostatic balance was much more closely satisfied than geostrophic balance, and the results presented in the next section support this, see Figures 4.10 and 4.11. The limitation of not converging to hydrostatic balance does not affect the results.

For the extended rescaling the energy will transform as

$$E_T \to \rho_0 \int_\Omega \frac{1}{2}\left(\beta^2 |\mathbf{u}|^2 + v^2\right) - \frac{g}{\theta_0}\theta\left(z - \frac{H}{2}\right) \mathrm{d}V, \tag{4.100}$$

so that both in-slice components of the kinetic energy will go to zero in the limit. The potential vorticity will transform as

$$q \to \frac{1}{\rho_0}\frac{1}{\beta}\left\{\frac{\partial\overline{\theta}}{\partial y}\left(\frac{\partial u}{\partial z} - \frac{\partial w}{\partial x}\right) + \frac{1}{\beta^2}\left[\frac{\partial}{\partial x}(v + fx)\frac{\partial}{\partial z}\left(\theta + \overline{\theta}\right) - \frac{\partial\theta}{\partial x}\frac{\partial v}{\partial z}\right]\right\}. \tag{4.101}$$

Note that, alongside the factor of $1/\beta$ outside the whole expression, the in-slice vorticity terms are now both of the same magnitude relative to the second term, a consequence of the vertical rescaling. This is desirable since the second term is the dominant term in the geostrophic potential vorticity.

4.6 Linear rescaling tests

This results in this section are for the asymptotic convergence test for the *linear* Eady problem; the nonlinearity within the standard Eady problem is contained entirely within the advection term. Taking a constant vertically sheared zonal velocity field of

$$\mathbf{u}^* = \left(\overline{U}, 0\right),$$

gives the advection term as

$$\mathcal{A} = \frac{\partial}{\partial x}\left[\overline{U}\,(\cdot)\right],$$

or

$$\frac{D}{Dt} = \frac{\partial}{\partial t} + \overline{U}\frac{\partial}{\partial x},$$

depending on formulation. The linearised Eady equations are

$$\frac{\partial u}{\partial t} + \overline{U}\frac{\partial u}{\partial x} - fv = -\frac{\partial \phi}{\partial x}, \tag{4.102}$$

$$\frac{\partial v}{\partial t} + \overline{U}\frac{\partial v}{\partial x} + fu = -\frac{g}{\theta_0}\frac{\partial \overline{\theta}}{\partial y}\left(z - \frac{H}{2}\right), \tag{4.103}$$

$$\frac{\partial w}{\partial t} + \overline{U}\frac{\partial w}{\partial x} - \frac{g}{\theta_0}\theta = -\frac{\partial \phi}{\partial z}, \tag{4.104}$$

$$\frac{\partial \theta}{\partial t} + \overline{U}\frac{\partial \theta}{\partial x} + v\frac{\partial \overline{\theta}}{\partial y} = 0, \tag{4.105}$$

$$\frac{\partial u}{\partial x} + \frac{\partial w}{\partial z} = 0. \tag{4.106}$$

In the Eady problem the instability is present in the linear problem (Eady, 1949), whilst the equilibration and retardation of the growth of the instability arises from the nonlinear ageostrophic motion. As such it is expected that the linear problem should grow without bound.

4.6.1 Numerical experiments

In the following section, unless otherwise explicitly stated, the numerical experiments (often just "experiments" will be written since the numerical aspect is implied) were run with the parameters given below, following Nakamura and Held (1989); Cullen (2007a).

Physical constants

The physical constants are

$$L = 1000 \text{ km}, \quad H = 10 \text{ km}, \quad f = 10^{-4} \text{ s}^{-1},$$
$$\rho_0 = 1 \text{ kg m}^{-3}, \quad g = 10 \text{ m s}^{-2}, \quad \theta_0 = 300 \text{ K},$$
$$\frac{\partial \overline{\theta}}{\partial y} = -3.0 \times 10^{-6} \text{ K m}^{-1}, \quad N_0^2 = 2.5 \times 10^{-5} \text{ s}^{-1}.$$

The standard model has the following Rossby and Froude numbers:

$$\text{Ro} = \frac{u_0}{fL} = 0.05, \quad \text{Fr} = \frac{u_0}{N_0 H} = 0.1,$$

where $u_0 = 5$ m s^{-1} is a representative velocity. Combining these two gives the Burger number, Bu $= 1/2$.

Numerical parameters

The default resolution used, for both the linear and nonlinear experiments of the next chapter, following Cullen (2008) was

$$n_x = 121, \quad n_z = 61.$$

The grid spacings are calculated as

$$\Delta x = \frac{2L}{n_x}, \quad \Delta z = \frac{H}{n_z}.$$

Upon substitution into the expression for the Burger number

$$\mathrm{Bu} = \frac{N\Delta z n_z}{f^{1}/_{2}\Delta x n_x},$$

and using $n_x \approx 2n_z$, shows that neither the horizontal nor the vertical should be under-resolved relative to the other.

In the linear experiments the default time-step and semi-implicit constant are taken as

$$\Delta t = 300 \text{ s}, \quad \vartheta = 0.55,$$

whilst for the nonlinear experiments $\Delta t = 120$ s at the control resolution, and reduces accordingly as the resolution increases.

Definition of norms

In this thesis the following norms will be used, in which the discrete scalar fields are represented as one-dimensional vectors of length n.

- Infinity norm, L_∞

$$\|\chi\|_\infty = \max\left[\mathrm{abs}\left(\chi_i\right)\right].$$

- Root mean square, RMS

$$\mathrm{RMS}\left(\chi\right) = \left(\frac{1}{n}\sum_{i=1}^{n}\chi_i^2\right)^{1/2}.$$

4.6.2 Imbalance evolution

The primary imbalance diagnostic used in both the linear and nonlinear experiments is that of the departure from geostrophic balance. The geostrophic imbalance, η_g, is given by

$$\eta_g = fv - \frac{\partial\phi}{\partial x}\left(= \frac{Du}{Dt}\right). \tag{4.107}$$

This corresponds to the instantaneous non-geostrophic acceleration for the zonal velocity. In a similar manner imbalance diagnostics for hydrostatic balance

$$\eta_h = \frac{g}{\theta_0}\theta - \frac{\partial\phi}{\partial z}\left(= \frac{Dw}{Dt}\right), \tag{4.108}$$

and the thermal wind relation

$$\eta_t = -f\frac{\partial v}{\partial z} + \frac{g}{\theta_0}\frac{\partial \theta}{\partial x}\left[= \frac{D\zeta}{Dt} - (\partial_z \mathbf{u})\cdot\nabla u + (\partial_x \mathbf{u})\cdot\nabla w\right], \tag{4.109}$$

can be defined, with the corresponding tendencies shown.

As with the standard Eady problem, the RMS norm of the geostrophic imbalance for the linear problem should converge at a rate proportional to Ro^2. This is achieved by varying the same rescaling parameter β. Figure 4.8 shows the variation of the geostrophic imbalance with β for initial and subsequent evolution of the linear problem. At day 15 it can be seen that the slope matches that of the second-order reference curve, but for earlier times this does not appear to be the case.

The discrepancy for the early stage of the evolution can be attributed to the initialisation. The experiments are being carried out at finite Rossby number, whilst the initialisation assumes an exactly balanced state. The differences are small but finite, and for the experiment shown in Figure 4.8 $\vartheta = 0.5$ and so there is no damping of any unbalanced waves. At later times the imbalance of the frontogenesis dynamics dominates any remaining initial imbalance, and so the theoretical convergence slope is recovered.

In Figure 4.9 the experiment is repeated for $\vartheta = 1$ and $\vartheta = 0.55$. The results from these experiments show the utility of adding even a very small amount of off centering in the semi-implicit discretisation in achieving a balanced solution. Increasing the implicitness of the solution clearly leads to a balanced solution faster, but even with $\vartheta = 0.55$ the solution is well balanced by day four with almost no evidence of departure from the constant slope.

The effect of the decentering leading to a more balanced solution has been investigated before, (Cullen, 2001, 2007a), with results consistent to those found here. There is inevitably a consequence of further decentering; the formal accuracy drops to first-order and energy is not necessarily conserved. Both energy conservation and balance enforcement are important for the long term evolution, and so for the present it work a value of $\vartheta = 0.55$ was deemed to be an acceptable compromise.

For all the experiments shown there is a departure from the second-order slope at large β. The second-order convergence is asymptotic, and so would not be expected to hold for $\beta = \mathcal{O}(1)$ and greater. The convergence rate appears to hold down to the smallest $\beta = \mathcal{O}\left(10^{-2}\right)$.

The evolution of the geostrophic imbalance as the solution progresses grows at a constant rate, as shown in Figure 4.10. There is a faint trace of the initialisation imbalance that can be seen from the curves for $\beta = 1$ and 8, which is damped out early on as previously stated. Although no further evolution is shown past day 10, the curves continue with constant slope, consistent with the results of the variation with β at day 15.

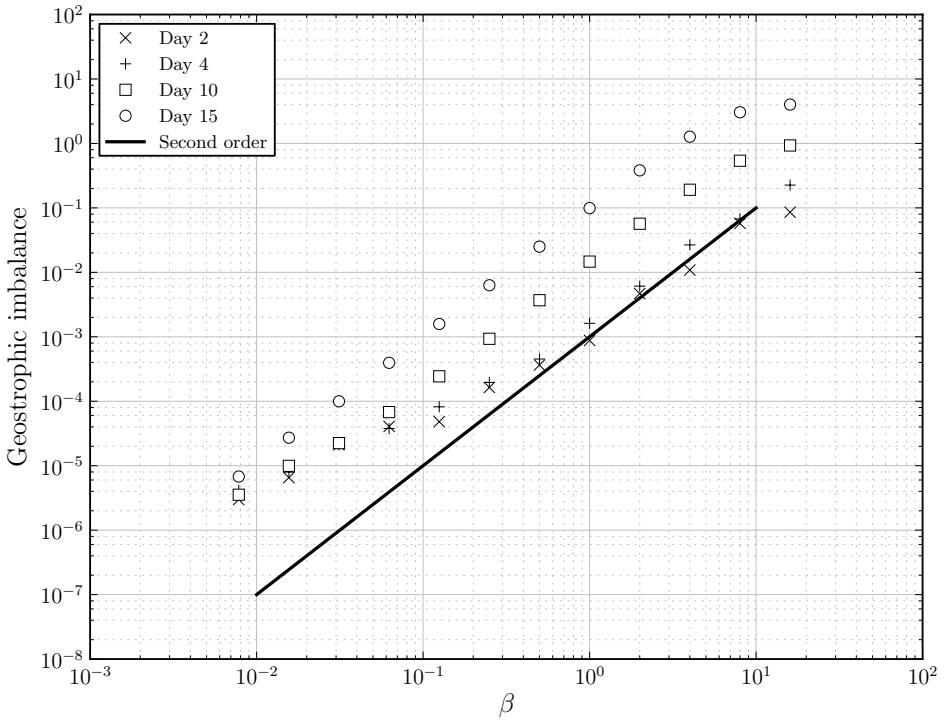

Figure 4.8: *Evolution of the RMS norm of the geostrophic imbalance for the linear problem. Experiment was carried out using a centred discretisation, $\vartheta = 0.5$.*

In the results shown so far the geostrophic imbalance continues to grow at an exponential rate. This is consistent with the linear instability growing exponentially; although the value of the imbalance might only be a small percentage of a representative value of the field, the field itself increases in amplitude and so, too, does the imbalance diagnostic.

The evolution of the hydrostatic imbalance is shown in Figure 4.11. The scale analysis shows the hydrostatic imbalance to be $\mathcal{O}\left(\mathrm{Ro}^2\delta^2\right)$, and the values of $\mathcal{O}\left(10^{-8}\right)$ shows this to be the case.

The hydrostatic imbalance also shows the exponential growth seen in the geostrophic imbalance of Figure 4.10. In this case the curves for the values of β are coincident, consistent with the dominant motion being hydrostatic and that the rescaling method does not affect the hydrostatic balance. There is a very slight departure for $\beta = 8$, but since the hydrostatic imbalance is more sensitive than the geostrophic imbalance, and the values are already much smaller, a difference of $\mathcal{O}\left(10^{-9}\right)$ is acceptable.

4.6.3 Normal mode structure

Figure 4.12 shows the normal mode structure between days nine and 10 for the linear Eady problem. Note that the contour levels intentionally change between each day, so that the same number of levels is plotted, with the new values shown.

There is a very small disagreement in the shape of the potential temperature on the bottom boundary (and corresponding minimum on the upper boundary). This is because the experiments of Figures 4.12 and 4.12 were initialised with a sinusoidal perturbation and were integrated using a centred scheme. The structure of the Eady mode clearly takes over very quickly on the large scale, irrespective of the initial conditions.

Figure 4.13 compares the normal modes from the control experiment with a rescaled experiment at $\beta = 1/8$ at day 10. The rescaling does not affect the structure of the solution, although the amplitude is clearly increasing as $\beta \to 0$. This suggests that the solutions are approaching the discontinuous solutions of the semigeostrophic equations.

Figures 4.12 and 4.13 also show the characteristics of solutions to the Eady problem. The solutions exhibit rotational antisymmetry about $(0, H/2)$; the maxima and minima are on the boundaries and decay towards the centre of the domain. The meridional velocity, and hence the geopotential (although not shown), tilts westwards with height, whilst the potential temperature tilts eastwards.

4.7 Summary

In this chapter the governing equations of the Eady model, within the vertical slice geometry, have been presented. The convergence of the Boussinesq equations to the semigeostrophic equations was shown to be $\mathcal{O}\left(\mathrm{Ro}^2\right)$ for this particular problem configuration, whilst the convergence for the three-dimensional system is $\mathcal{O}\left(\mathrm{Ro}^2\right)$ in a suitable distinguished limit, and $\mathcal{O}\left(\mathrm{Ro}\right)$ otherwise. The quantities that are preserved by both the Boussinesq and semigeostrophic equations were presented, in particular the potential vorticity and energy. An alternative derivation for slice models using the variational principle suggests that it would, in principle, be possible to extend the current work to a compressible model.

The numerical techniques of Chapter 3 were tailored to the current problem. The placement of the meridional velocity was moved from what would be the correct C-grid location to improve representation of geostrophic balance and inertial oscillations without averaging.

The details of the linear system, which arises through the use of the semi-implicit time discretisation, were presented. It was shown that through the use of the Schur complement, and an analytic inverse for part of the block matrix system, the overall complexity of the resulting problem is reduced

from $(2n_1 + 3n_2)$ down to n_2. The Schur complement approach meant that the linear forcing and pressure-correction steps could be combined. This simplification, combined with a single stored LU decomposition, produces a very efficient numerical method.

The initialisation method, which is vital for ensuring sufficiently balanced solutions for asymptotic convergence to be effective, was presented. There was little difference between solutions with and without the advective terms, and so the simpler system was selected to be used for the rest of this thesis.

The boundary conditions, in particular those for the potential temperature and the necessary treatment required within the advection step, were next presented. Since the singularity occurs on the boundary in the semigeostrophic solution careful treatment is obviously required, and so much consideration was given to the selected methods.

The effect of the asymptotic convergence framework in physical units was shown in terms of the effects on the relevant nondimensional parameters. An extended rescaling, in which that of C08 was further rescaled in the vertical, was shown to preserve the aspect ratio. The rescaled quantities were shown, with the comparison to the corresponding semigeostrophic expressions.

Finally results were presented for the linear Eady problem. The structure of this instability has been well studied in the literature, and the results presented agreed very well with the previous work. The asymptotic convergence results, and in particular the invariance of the structure of the solution as $\beta \to 0$, showed the numerical methods to be correct. These results form a strong foundation for extending the investigation into the nonlinear problem.

(a)

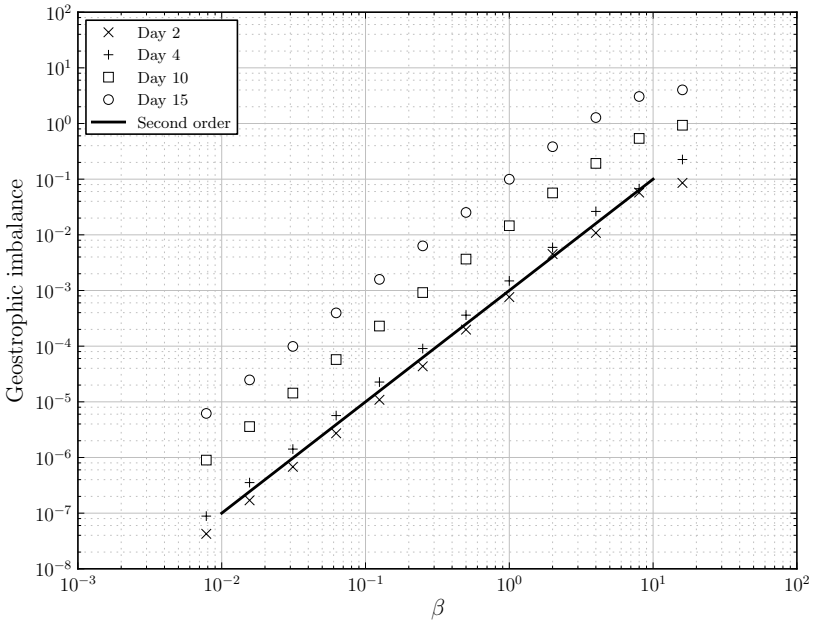

(b)

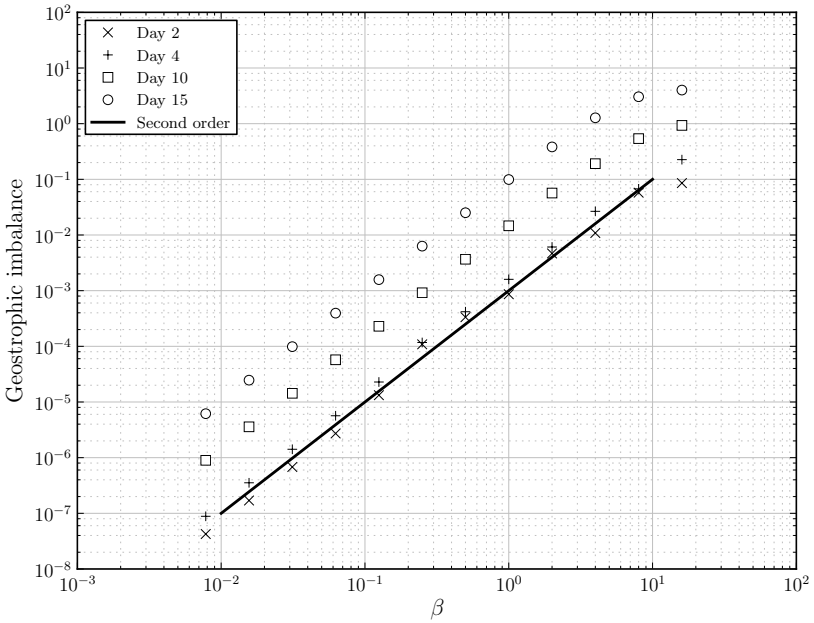

Figure 4.9: *As Figure 4.8 but for the fully implicit discretisation, $\vartheta = 1$ (a), and with a small amount of off-centering $\vartheta = 0.55$ (b).*

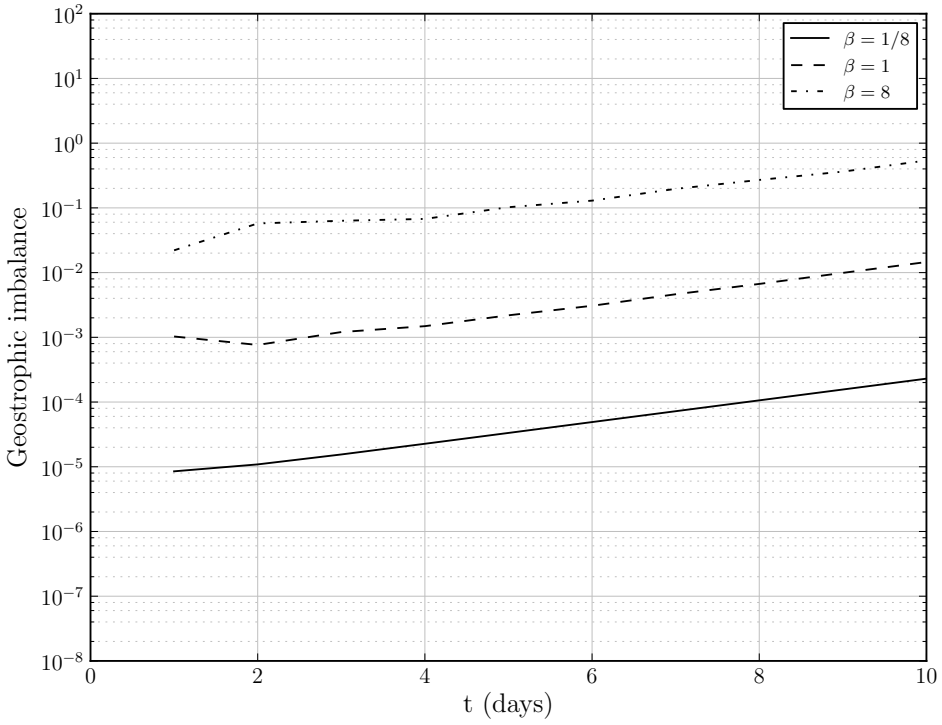

Figure 4.10: *Geostrophic imbalance growth rate for the linear problem at three different rescaling parameters. Geostrophic balance was enforced exactly through the initial conditions. Experiment was carried out using fully implicit discretisation.*

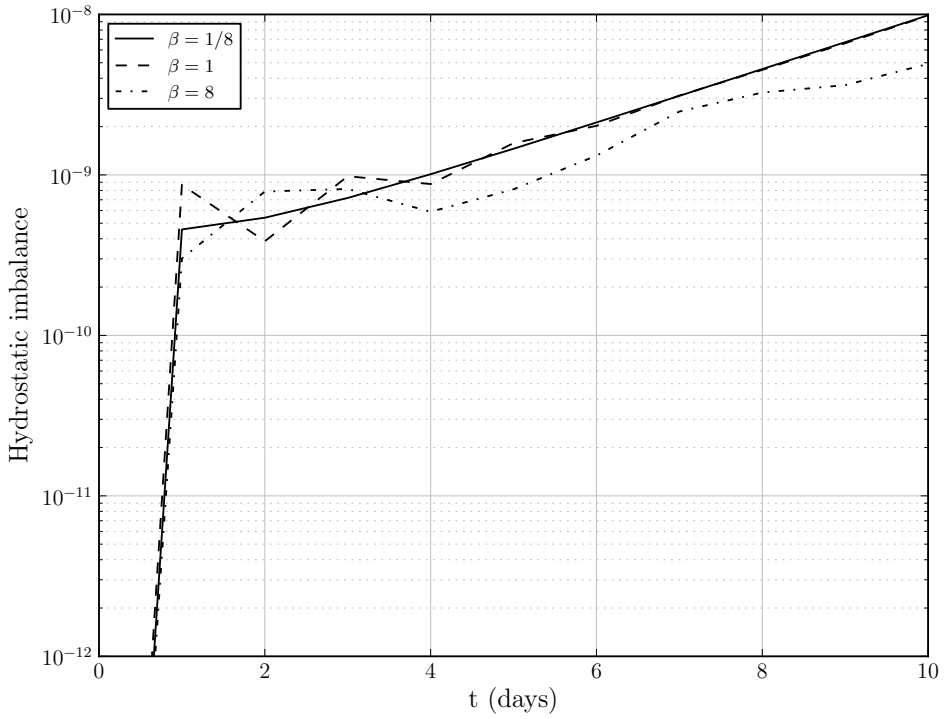

Figure 4.11: *As Figure 4.10 but for the hydrostatic imbalance. Hydrostatic balance was enforced to machine precision initially.*

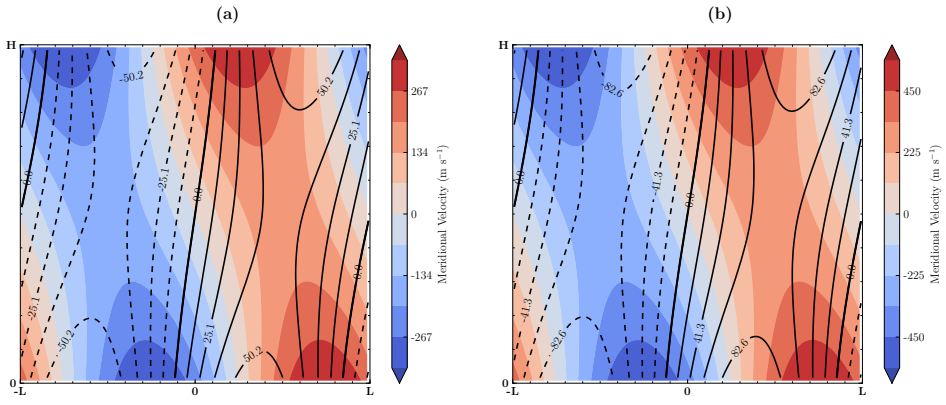

Figure 4.12: *Linear normal mode growth showing the structure of the Eady wave. Meridional velocity in filled contours and potential temperature in contour lines at (a) day nine and (b) day ten. Experiment was carried out using a centred discretisation in time and for the control rescaling.*

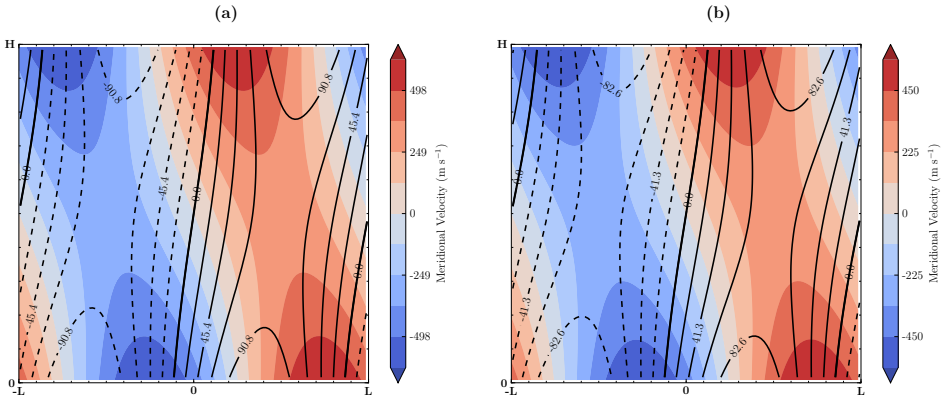

Figure 4.13: *Comparison of normal mode structure for (a) $\beta = 1/8$ and (b) $\beta = 1$, with fields as Figure 4.12 at day ten.*

Chapter 5

Asymptotic limit analysis of numerical methods in the presence of fronts

Nature laughs at the difficulties of integration.

P. Laplace

Contents

5.1 Summary of existing results

This chapter begins with recapping the features of the semigeostrophic limit solution covered in Section 2.4, so that the results from this thesis can be analysed in context, and the performance of the numerical methods assessed. A brief summary of the comparison quantitative data, and the methods used therein, is also given.

5.1.1 Properties of the limit solution

The semigeostrophic limit solution was given by the geometric model result of Cullen (2007a). The geometric model was fully Lagrangian, and the equations were solved in the isentropic coordinates given in Section 2.3.2, in which the horizontal coordinate moved with the geostrophic velocity and the vertical coordinate was a function of the potential temperature.

The numerical method was inviscid, and enforced the conservation of $v_g + fx$ and θ, as well as geostrophic and hydrostatic balance, exactly. The uniform value of the geostrophic potential vorticity was conserved exactly within the dual space, which meant that there were no regions in which the PV was negative. When mapped back to physical space the solution showed filaments of high PV, representing the contact discontinuity.

The free-boundary nature of the problem meant that the boundaries of the domain in the dual space (computational domain) were able to deform. This deformation, which was evident in the solution back in the physical domain, showed that parcels of air initially on the boundary were able to move into the domain *without* conflicting with the physical domain rigid wall boundary conditions.

The evolution of the meridional velocity field showed very intense frontogenesis, with the peak RMS value reaching almost 90 m s^{-1}. After the first peak the results showed several further quasi-periodic lifecycles which were only slightly damped.

5.1.2 Comparison results from literature

In this chapter reference data will be taken from the following sources:

C07 Cullen (2007a), Figure 4.6 solid curve, kinetic energy, inviscid semigeostrophic equations using a fully Lagrangian method.

CR93 Cullen and Roulstone (1993b), Figure 3 (a), inviscid semigeostrophic equations using a fully Lagrangian method.

NH89 Nakamura and Held (1989), Figure 1 thick curve, hydrostatic primitive equations using a viscous Eulerian method.

The results presented in this chapter extend the results first published in Visram et al. (2014).

N94 Nakamura (1994), Figure 1 solid curve, kinetic energy, semigeostrophic equations using a viscous Eulerian method.

X98 Xu et al. (1998), Figure 5 dashed curve, viscous semigeostrophic equations with free-slip boundary conditions using an Eulerian method.

These data have been obtained using an on-screen interpolation software, (Engauge Digitizer, 2013). This method does not reproduce the original results perfectly; there are sometimes very small deviations from the true results owing to artefacts in the scanning and interpolation processes, which primarily affect the results that are small in magnitude. Where noted, some of the data sets have been processed from meridional kinetic energy into representative meridional RMS values.

The "standard" model results presented in this chapter, unless otherwise stated, refer to the following numerical method and parameters: SISL with quasi-monotone cubic Lagrange interpolation and implicit midpoint velocity calculation; delta / incremental formulation with up to four fixed point iterations or a nonlinear update tolerance of 10^{-8}; uniform resolution of $n_x = 121$, $n_z = 61$; $\Delta t = 120$ s; $\vartheta = 0.55$. All other physical parameters are as stated in Section 4.6.

5.1.3 Lagrangian / Eulerian disparity

Figure 5.1 succinctly summarises the stark contrast in simulations of the standard and semigeostrophic Eady problem. As mentioned previously, there is a factor of two difference in the peak RMS values between the Lagrangian and Eulerian results. This is not due to the difference in equation sets since there is good agreement between NH89 and N94, as well as additional results in N94 that show their Eulerian solutions to the primitive and semigeostrophic equations to be very close. The differences, then, must come from the numerical methods, and the implicit diffusion contained therein.

The amplitude of the resulting quasi-periodic behaviour suggests that the Eulerian results are reaching a steady state, whilst the Lagrangian results continue to oscillate. The stronger initial frontogenesis is clearly important in the amplitude of the oscillations, but the damping suggests that the Eulerian results are failing to reproduce the inviscid motion and baroclinic lifecycles observed in the limit solution.

These results show that there is a clear dichotomy between the results for the Eady problem using Eulerian and Lagrangian numerical methods. As covered in Section 2.4 the dynamics are inherently Lagrangian, and so Eulerian methods are at a disadvantage. In reality, if the solution is only required up to frontal collapse, then Eulerian methods suffice since the solution is well resolved on the large scale.

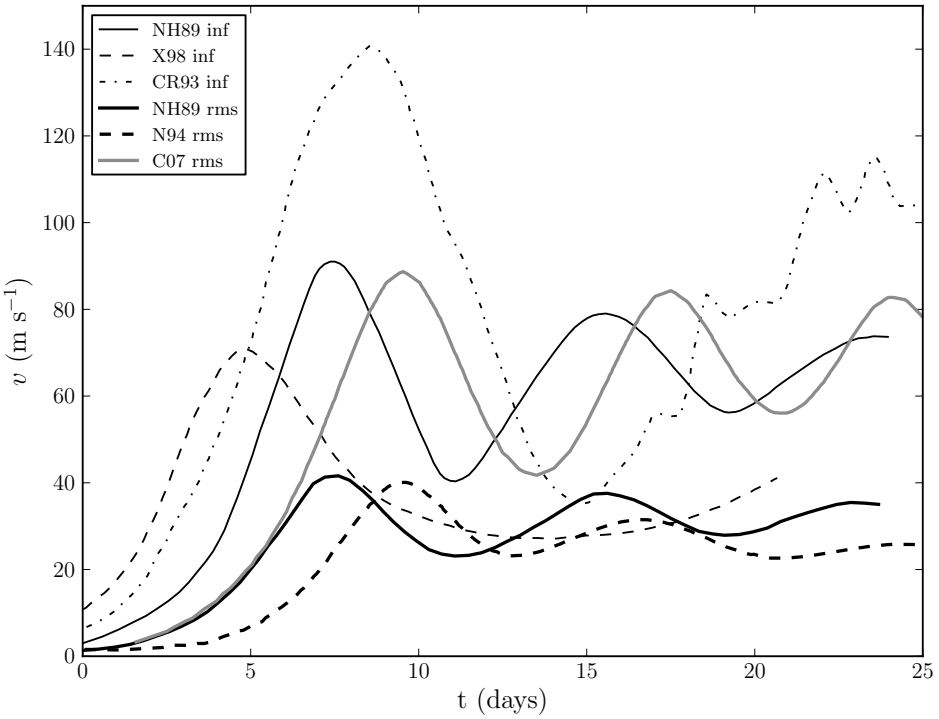

Figure 5.1: *Comparison of meridional velocity evolution for the references mentioned in the main text; thin curves show L_∞ values whilst thicker curves are for RMS values.*

Both Eulerian and Lagrangian methods should work whilst the solution is smooth and resolved, but this is not necessarily true once the solution is not fully resolved. At later times, as will be covered in Section 5.3, the Eulerian methods seem to break down. Reasons for this, as well as attempts to mitigate it, will be discussed in the following sections, but first attention is focused to the initial stage of the evolution.

5.2 Initial evolution phase

This section summarises the initial portion of the growth of the Eady wave. The growth of the wave is shown in terms of the RMS and L_∞ norms of the meridional velocity field. Up to day four the motion is well described by the linearised equations, whilst afterwards there follows a nonlinear growth regime, followed by equilibration and eventual decaying of the wave. This period, broadly covering the dynamics up to day 10, is the subject of this section.

5.2.1 Initial growth phase

Lagrangian flow characteristics

The comparison of the linear and nonlinear results in Figure 5.2 suggests that part of the reason for the Lagrangian model's success in creating several intense lifecycles is that the solution stays in the growth phase for much longer than the Eulerian results. All of the RMS results presented start to fall below the linear growth phase shortly after day five but at varying rates. Both the nonlinear results presented in this thesis and those of NH89 very quickly equilibrate by day seven, whilst the Lagrangian results of C07 suggest a nonlinear growth phase before eventually equilibrating at day nine.

One possible explanation for these differences, as touched upon earlier, is that the Lagrangian model is able to maintain the discontinuity with two cells, which are themselves able to adjust their shape and position to track the front whilst it is still growing in amplitude. The Eulerian methods, including the SISL results, are not able to distort in the same manner, and once the width of the front reduces to the grid scale the gradients are diffused and artificially damped.

A strategy that has worked very well in tackling this problem has been through mesh adaptivity. Budd et al. (2013) used a moving mesh algorithm based on a PV monitor function to simulate the Eady frontogenesis problem prior to collapse. The results with adaptivity gave an improvement, in terms of strength of gradients and reduction in spurious oscillations, better than a doubling of horizontal resolution on a fixed grid, but were not able to integrate past the point of frontal collapse as the explicit time-step went to zero. The scale collapse, in terms of both the spatial and temporal scales, suggested that there was a singularity forming in the Boussinesq equations. It is clear that being able to mimic the inviscid Lagrangian dynamics is crucial for success.

Normal mode behaviour

Figure 5.3 shows snapshots of the potential temperature, meridional velocity and the streamfunction at days 1.5 and 2. In contrast to the linear normal

mode experiments at the end of the previous chapter, see Figures 4.12 and 4.13, this experiment was initialised with the Williams (1967) perturbation. The only difference is that the lower maxima is now of the same amplitude as the lower minima, as opposed to marginally smaller with the previous initialisation strategy. The v and θ fields show the same structure as Figure 4.12, suggesting that at this early stage of the evolution the linearised equations are quite successful at reproducing the nonlinear solution.

There is a very small disagreement between the two streamfunction plots of Figure 5.3, which is shown in the positions of the third and fourth highest contour levels. This suggests that the intensity of the large scale vortex structure is increasing at a marginally faster rate than the growth in the v and θ fields. This is very much consistent with the work of HB72 in which the ageostrophic motion accelerates the convergence in the frontal zone, leading to the true discontinuity in the semigeostrophic equations. At this stage the growth is still essentially linear.

Figure 5.4 provides a snapshot into the main fields of interest; meridional velocity, potential temperature, streamfunction and Ertel potential vorticity, at day four, but now with fixed contour levels that will be used at later times for comparison. Figure 5.4 (d) is intentionally included as a uniform field, corresponding to the Eady background state.

At day four the meridional velocity and in-slice circulation fields have much the same structure as the initial perturbation, showing that the balanced initialisation has had the desired effect. The potential temperature field is starting to show some signs of nonlinearity in that the warm peak ahead of the surface front is much more compact and sharper than the trough behind. Previous results have shown this to be the correct evolution, e.g. (Budd et al., 2013), and is even captured by the quasigeostrophic model, (Williams, 1967).

All fields are well resolved at this point in the evolution. At the standard (lowest) resolution used in the experiments there are six grid points between axis tick markers, in both the horizontal and vertical. This is clearly sufficient to capture the horizontal gradients in v and θ, and shows why Eulerian models with coarser resolution have captured this stage of the evolution, e.g. NH89 used a grid of 100×20.

5.2.2 Deviation from linear growth

After the initial linear growth phase the nonlinearity in the Eady problem begins to take hold, and this starts to become noticeable from day four onwards. This is evident in the "growth rate" plot, Figure 5.2, which shows both the L_∞ and RMS norms begin to fall below the initial linear portion after day five.

Figure 5.2 shows that it is a short period of time between nonlinearity taking hold and the collapse to the grid scale. At day five there is a spike

in the L_∞ norm behaviour, deviating sharply above the path the linear growth rate would take. This is not a desirable feature, but appears to be a consequence of using the quasi-monotone limiter. The L_∞ norm is much more sensitive to isolated extrema within the field, whilst the RMS norm evolution suggests that the large-scale solution is still well behaved.

In spite of the collapse to the grid scale, and the implicit dissipation within the numerical method, the front continues to grow in intensity, albeit at a lower rate than the Lagrangian results. The numerical dissipation is quantified in Section 5.6.

The wave continues to grow because the wave is still in-phase and able to extract available potential energy from the background potential temperature gradient. The wave is advected by the background shear and eventually the phase switches and the amplitude begins to reduce, (Nakamura and Held, 1989). The equilibration and subsequent quasi-periodic behaviour is discussed in Section 5.3.

As noted the initial stage of the evolution is well resolved, and so the solution should be relatively insensitive to small changes in the spatial discretisation. Figures 5.5 and 5.6 show the pre-collapse evolution of the meridional velocity field for variations in the interpolation order and spatial resolution, respectively. As expected, these results are little altered by the changes, and in all cases the spatial discretisation looks to be sufficiently accurate for the initial stage.

There are some differences in the behaviour of the L_∞ norm. Increasing interpolation order, whilst maintaining the same spatial resolution, triggers the deviation from the linear growth rate to occur earlier with the curve generally tracking a little higher, whilst increasing spatial resolution but keeping interpolation order the same has the opposite effect. This is down to the use of Lagrange interpolating polynomials since a larger stencil is more likely to cross both sides of the discontinuity and cause spurious overshoots, as described in Section 3.2.1.

Comparison with existing Eulerian results

Figure 5.7 shows a comparison of the standard inviscid model with the results of NH89, alongside two experiments in which additional diffusion was added to match NH89. It would appear that the standard SISL scheme is only marginally less diffusive than the scheme of NH89. The combination of decentering and limiting the interpolation, necessary for stable integrations, comes at a price of high implicit diffusion within the numerical method. This is supported by the experiments with explicit diffusion showing reduced peaks in both the RMS and L_∞ norms, although the latter is not as informative about the large scale flow since isolated values can control it.

Despite the differences in the amplitudes there seems to be very good agreement in the timescales of each of the models, suggesting that the non-

linear equilibration is well resolved in each of the cases and a fundamental part of the evolution.

The introduction of viscosity appears to control the spike in the infinity norm of the inviscid experiments. At the lower resolution viscous run there is a small amount of variation once the front is at its maximum, but much reduced when compared to the inviscid results. In all cases the evolution of the RMS norm remains smooth, implying that the inviscid results are much noisier at the grid scale.

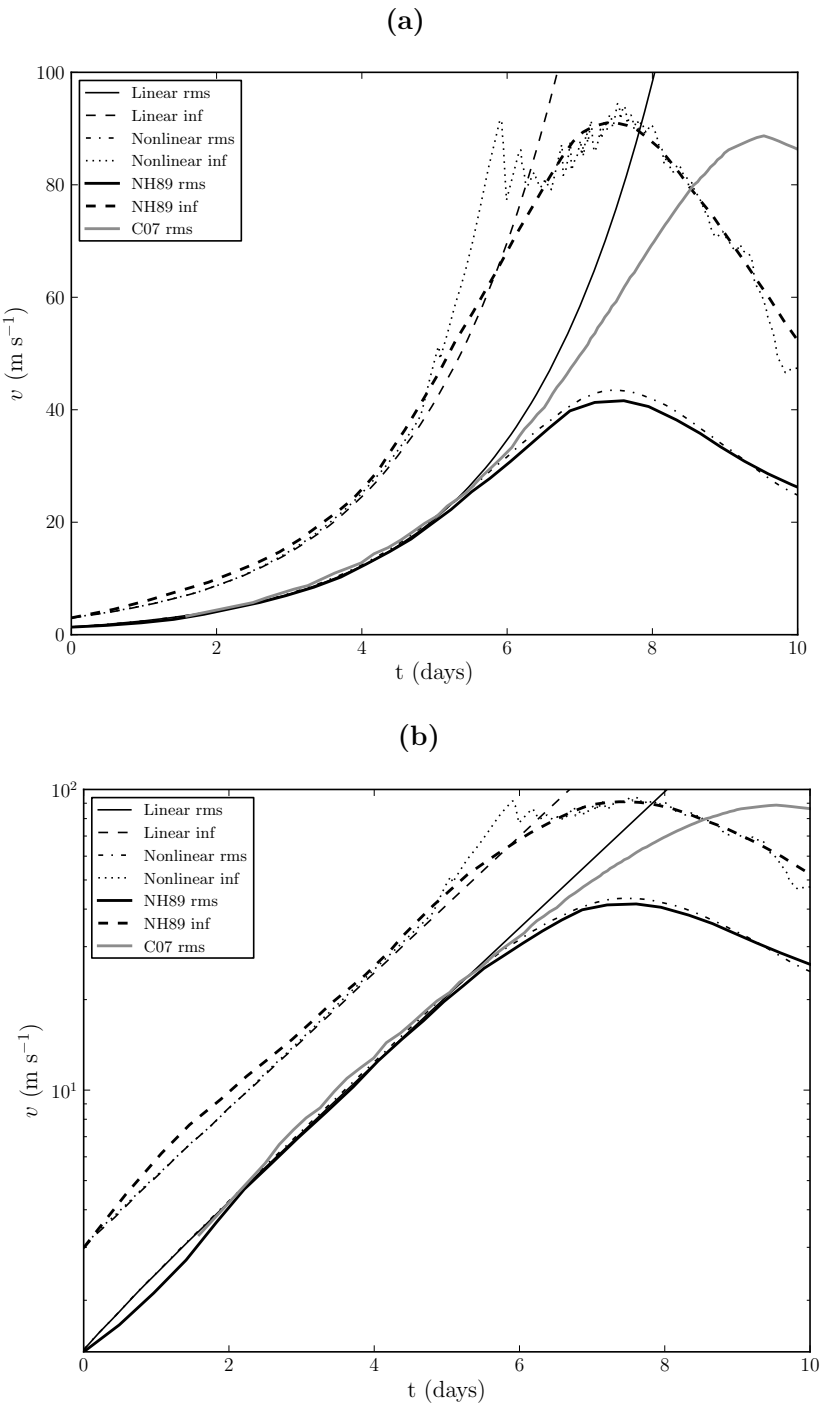

Figure 5.2: *Comparison of linear and nonlinear growth rates, both L_∞ and RMS values, for the initial evolution on (a) linear axes and (b) logarithmic y axis.*

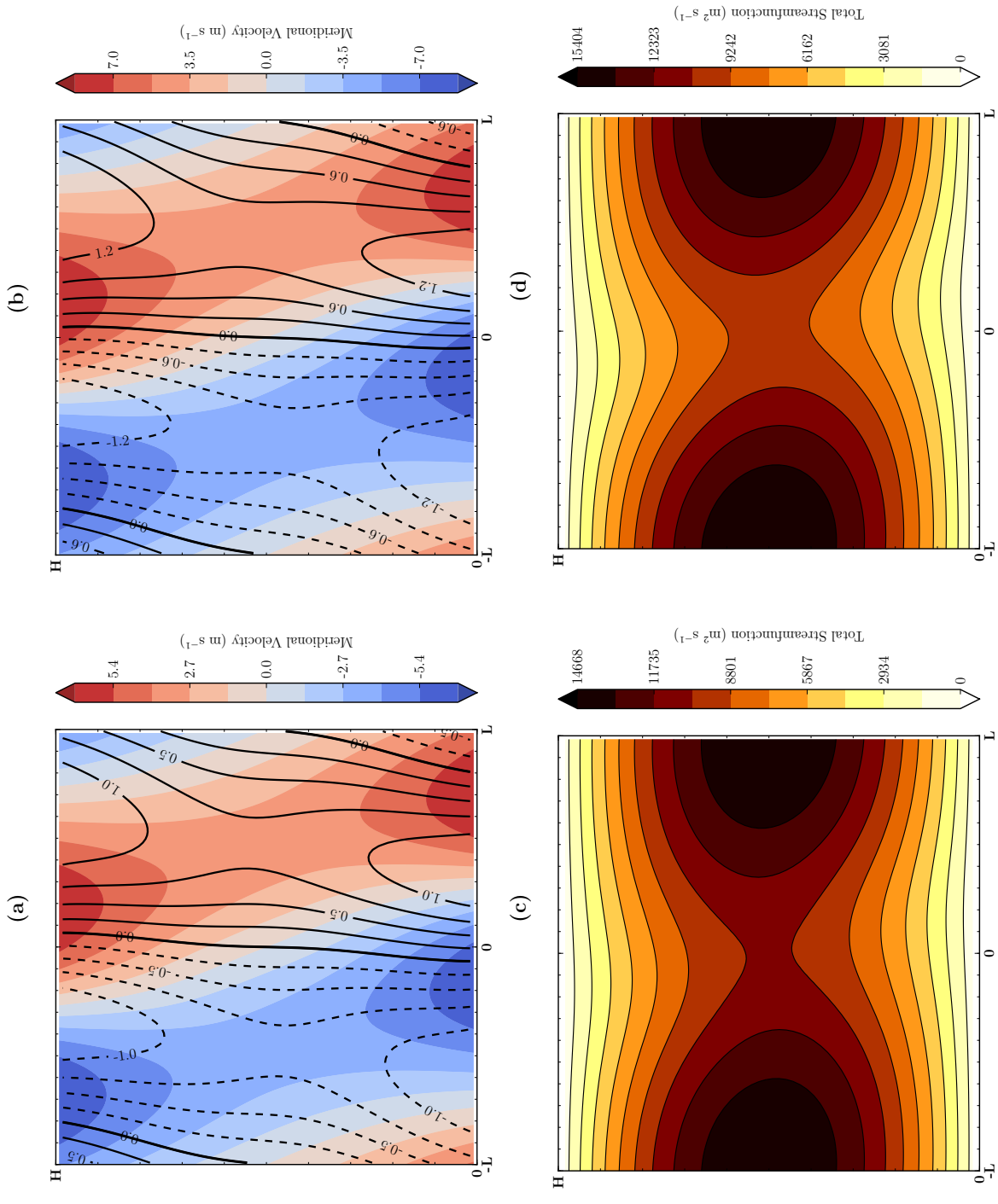

Figure 5.3: *Nonlinear normal mode growth. Top row shows meridional velocity in filled contours and potential temperature in contour lines at (a) day 1.5 and (b) day 2. Bottom row shows total streamfunction within the domain at (c) day 1.5 and (d) day 2.*

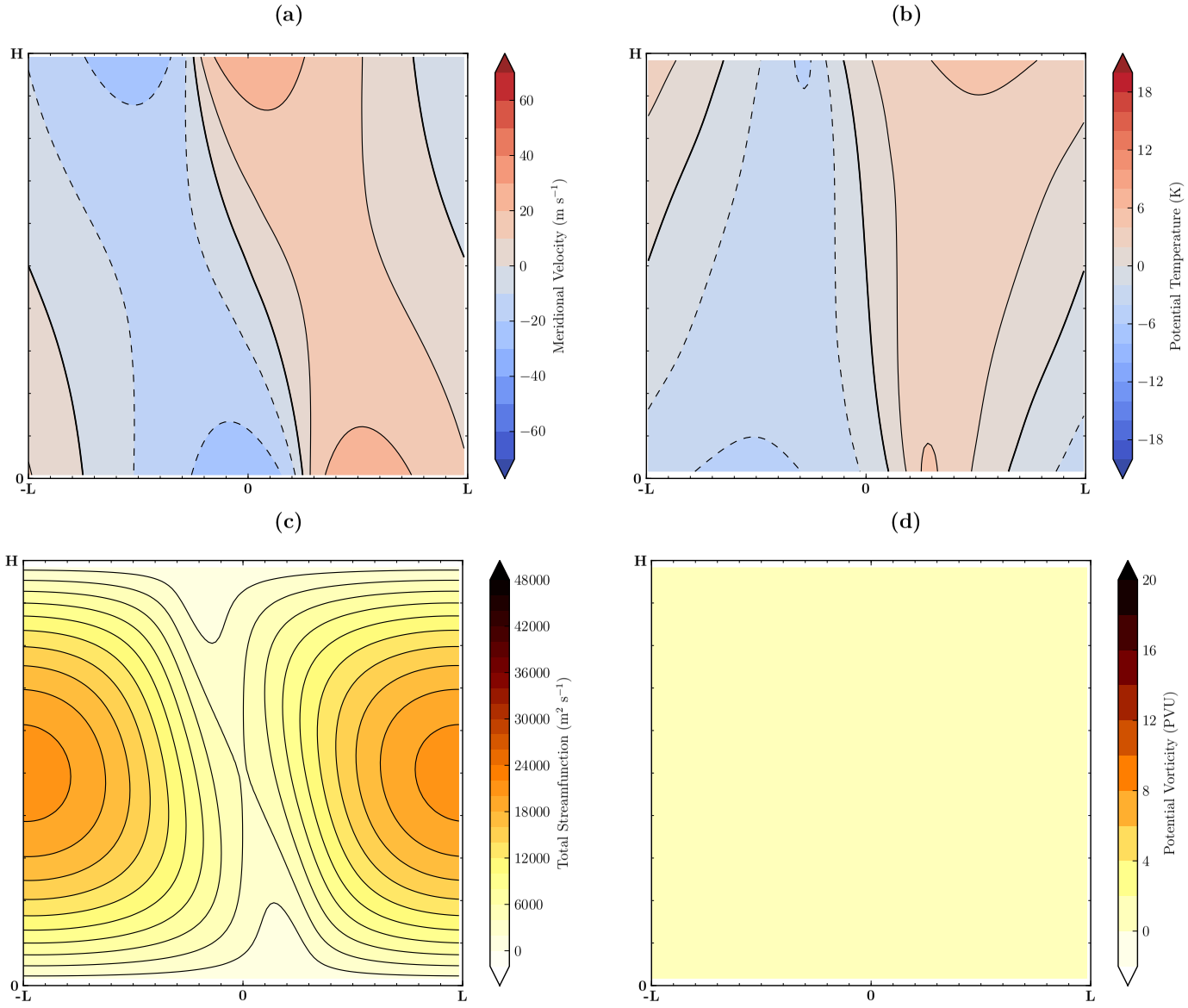

Figure 5.4: *Frontal snapshot at day four. Fields shown are (a) potential temperature, (b) meridional velocity, (c) in-slice streamfunction and (d) Ertel potential vorticity.*

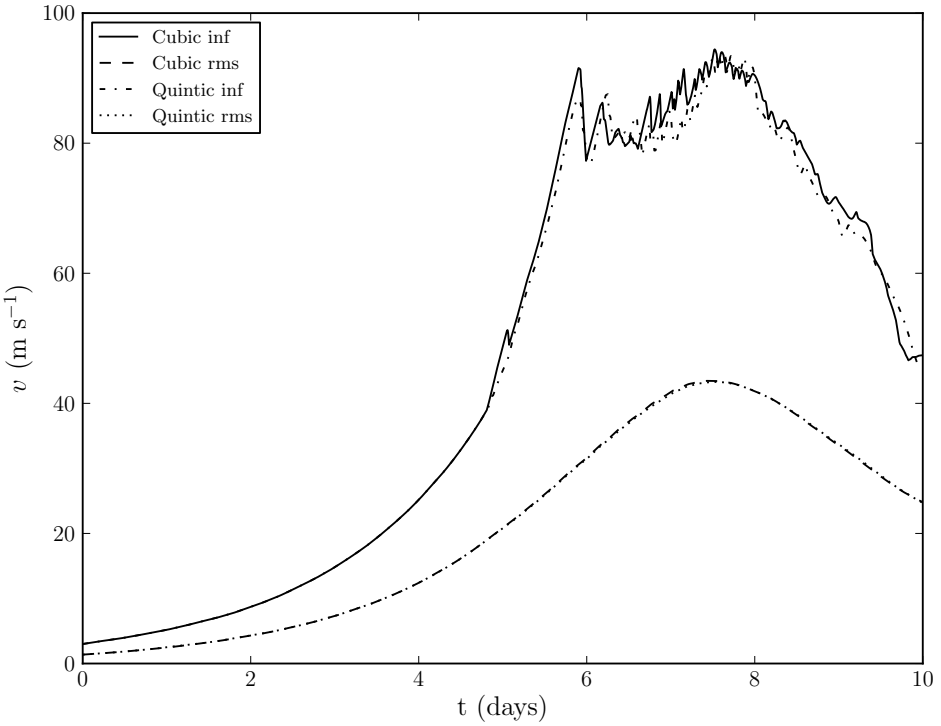

Figure 5.5: *Comparison of cubic and quintic interpolation schemes for the standard Eady model.*

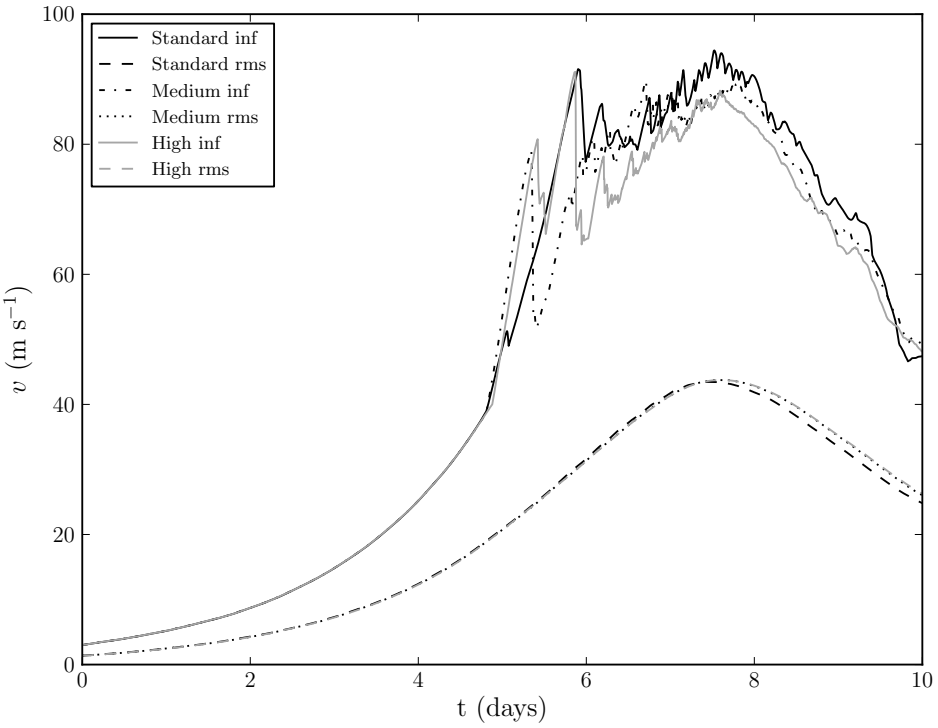

Figure 5.6: *Comparison of resolution for the standard Eady model. Resolution in* (n_x, n_z) *for standard* $(121, 61)$*, medium* $(241, 121)$ *and high* $(481, 241)$*, with* Δt *as* 120 s*,* 60 s *and* 30 s *respectively.*

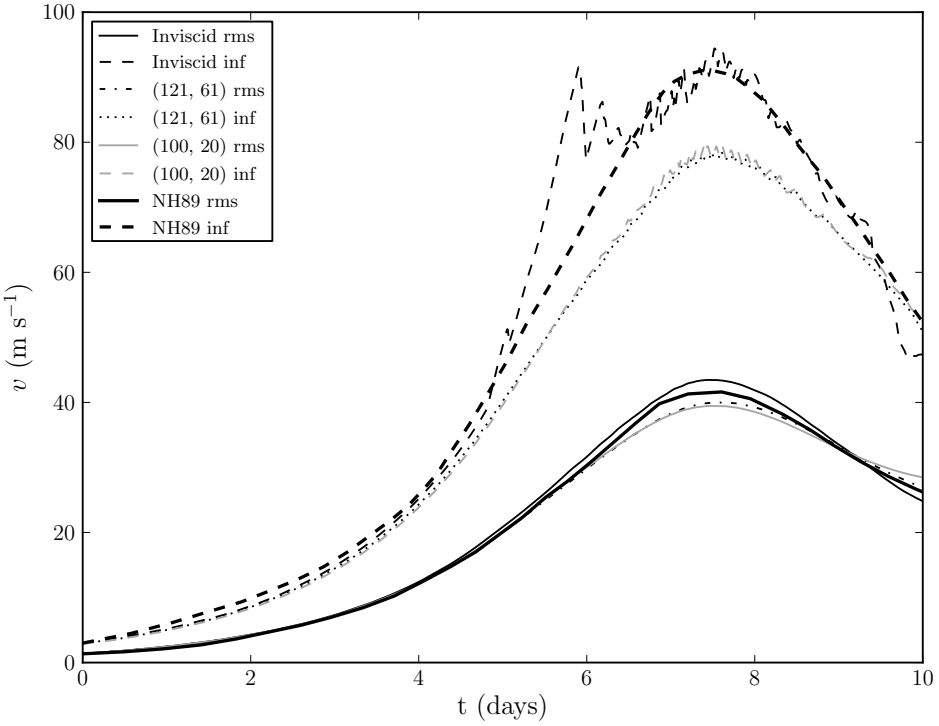

Figure 5.7: *Comparison of meridional velocity evolution for the nonlinear model using no explicit diffusion, and with the same values of diffusion as NH89 at their resolution and at the control resolution used in this thesis.*

5.3 Post-collapse evolution

In this section the solution after the front has "collapsed" is discussed. Hoskins and Bretherton (1972) found that the Eady model should produce a discontinuity after day five, which is consistent with the results presented in this thesis. Whilst the initial growth of the instability is well-studied, it is the subsequent behaviour and solution characteristics that can shed insight on long-time performance of the numerical methods.

5.3.1 Solution structure

Figures 5.8 and 5.9 show the same field snapshots as Figure 5.4, but at days seven and 11 respectively. At day seven the front is almost at peak intensity and strong gradients can be seen in all of the fields. The narrow extent of the frontal region is highlighted in the potential vorticity, which shows the characteristic filaments protruding from the boundaries.

The streamfunction plot at day seven shows the intensity of the vortex structure. Most of the structure is quite smooth, with the exception of two sharp, almost right-angled, changes in curvature corresponding to intense vertical jets away from the boundaries.

Day 11 corresponds to the first minima after the initial frontogenesis. The tilt in the meridional velocity field is now eastwards, showing the phase of the wave has changed and that there is conversion from kinetic energy back to potential energy (Nakamura and Held, 1989). The potential temperature appears to have rearranged to a low energy state, which is vertically stratified and with the extremal values at the boundaries.

The streamfunction plot suggests that the intense vertical jets are still present, but have propagated away from the initial frontal region. There is good agreement in their positions with potential temperature intrusions and, to a lesser extent, the regions of negative PV.

The initial PV filament has almost completely disappeared. Unlike NH89 and N94, in which the PV filament gets diffused along the boundaries, the primary mechanism for the reduction is that of the dynamics itself. Once the front has reduced amplitude, and gradients in v and θ are small again, the primary component of the PV is small, too.

This analysis is from a diagnostic perspective, since as discussed in Section 2.4, the conservation of PV is not sufficient in itself to determine the evolution for the Boussinesq equations. The ability of the numerical method to respect the conservation laws of the continuous system is discussed in detail in Section 5.5, whilst the next section covers the evolution for the control run.

5.3.2 Control run balance

Figure 5.10 shows the evolution of the balance metrics for the control run. The divergence, although increasing initially with the increasing intensity, never gets above a value of $\mathcal{O}\left(10^{-13}\right)$. The divergence is initially in the range of $\mathcal{O}\left(10^{-16}\right)$ to $\mathcal{O}\left(10^{-14}\right)$, but at later times the presence of the intense gradients clearly stresses the projection method in enforcing continuity.

The imbalance diagnostics, restated for convenience here as

$$\eta_g = fv - \frac{\partial \phi}{\partial x}\left(= \frac{Du}{Dt}\right),$$
$$\eta_h = \frac{g}{\theta_0}\theta - \frac{\partial \phi}{\partial z}\left(= \frac{Dw}{Dt}\right),$$
$$\eta_t = -f\frac{\partial v}{\partial z} + \frac{g}{\theta_0}\frac{\partial \theta}{\partial x}\left[= \frac{D\zeta}{Dt} - (\partial_z \mathbf{u}) \cdot \nabla u + (\partial_x \mathbf{u}) \cdot \nabla w\right],$$

are shown in Figure 5.10. All of the imbalances increase over two orders of magnitude up to day 10, at which point the values reach a plateau. There is a step change in the hydrostatic and thermal wind imbalances between days four and five. At this point there is a strong and narrow vertical jet, the accelerations of which have a small nonhydrostatic component.

It is not clear what has caused the anomalous jump in the hydrostatic imbalance at day 10. Since the values plateau and are fairly steady thereafter this could be explained by a small region of locally marginally unstable flow, which is quickly stabilised and damped out.

Figure 5.11 shows the evolution of the total and components of the kinetic energy. The spike in the hydrostatic imbalance can also be seen in the vertical component of the kinetic energy, supporting the possibility of a region of negative stratification and instability.

The evolution of the kinetic energy shows that the meridional velocity very quickly dominates the kinetic energy budget, being the major contributor even by day three. The two horizontal components oscillate after day 10, whilst the vertical component stays relatively flat.

The evolution of the total energy is shown in Figure 5.12, alongside the potential and available potential energy. The initial growth stage up to day five shows an increase in the available potential energy (APE), which then reduces and eventually approaches zero by day 25. Figure 5.12 shows the exchange from potential to kinetic energy over several lifecycles.

Over the same period the total energy is reasonably constant, but by the end the total energy has increased slightly. Although the kinetic energy is larger than the potential energy, leading to the increase, it is not apparent from this plot as to what is cause and what is effect. The numerical method is not formally energy conserving, but the fact that it remains almost constant over the initial frontogenesis is reassuring.

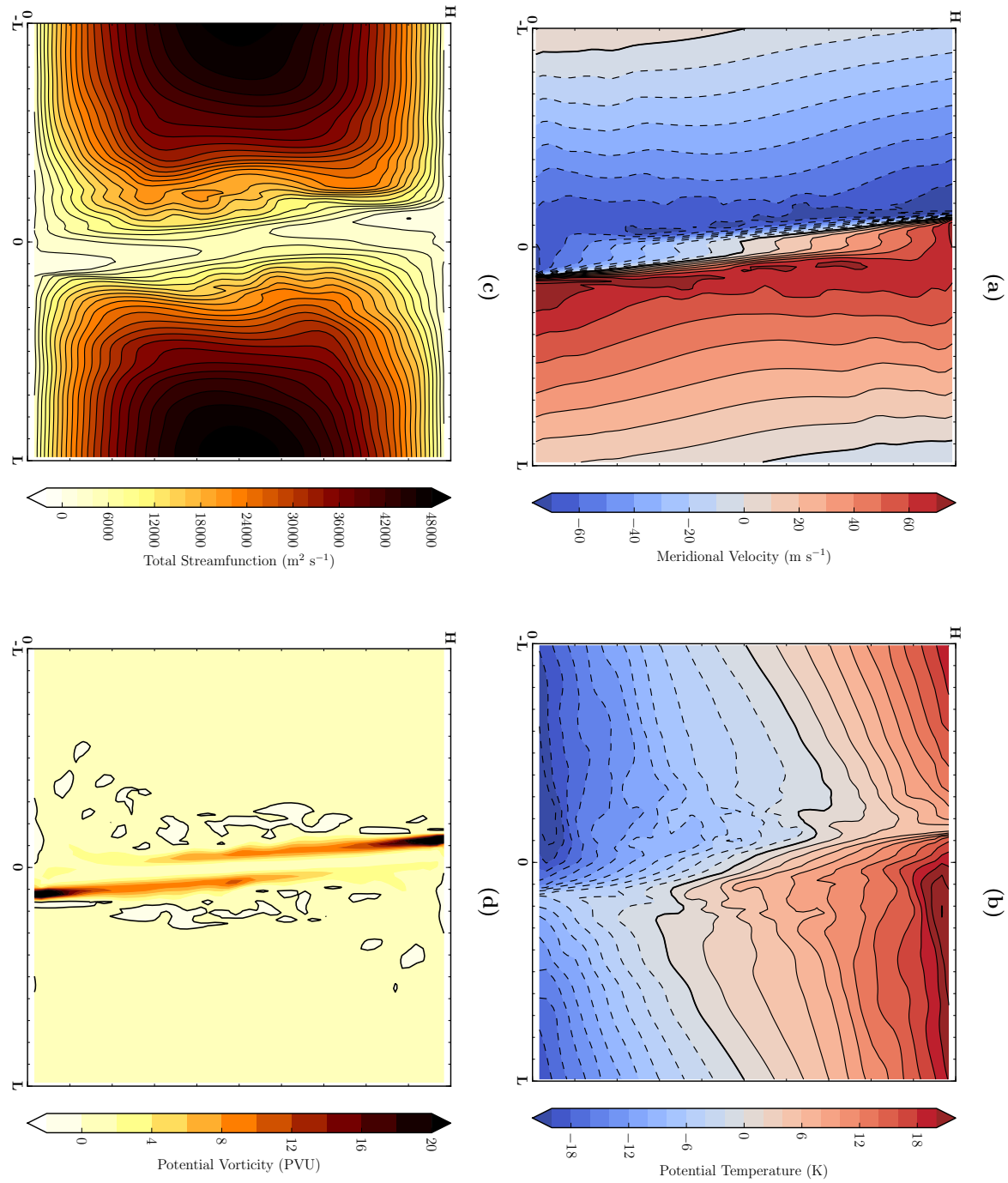

Figure 5.8: *Frontal snapshot at day seven, fields as in Figure 5.4.*

Figure 5.9: *Frontal snapshot at day 11, fields as in Figure 5.4.*

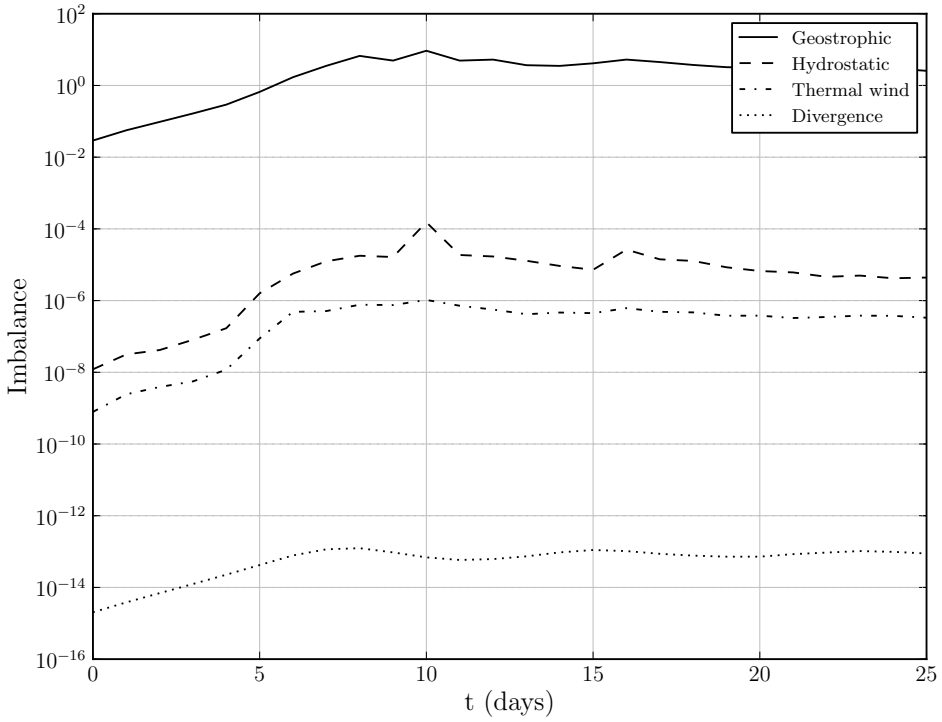

Figure 5.10: *Evolution of geostrophic and hydrostatic imbalances alongside divergence for the standard Eady model. All curves are for RMS norm values. The geostrophic and hydrostatic imbalances are in units of* $\mathrm{m\ s^{-2}}$*, thermal wind imbalance in units of* $\mathrm{s^{-2}}$ *and divergence in units of* $\mathrm{s^{-1}}$*.*

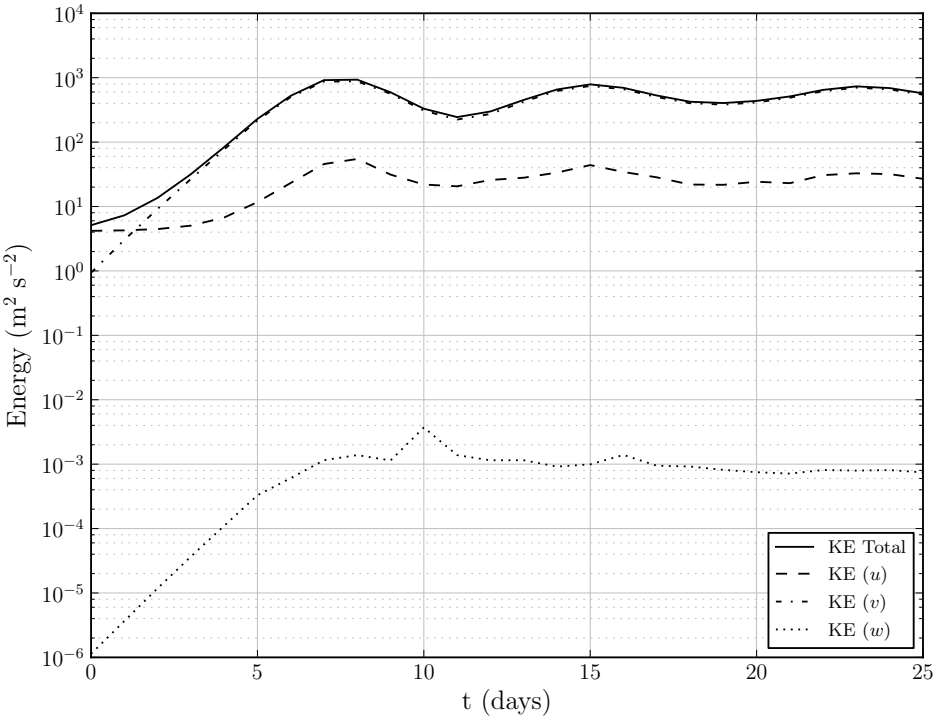

Figure 5.11: *Breakdown of kinetic energy components for control run.*

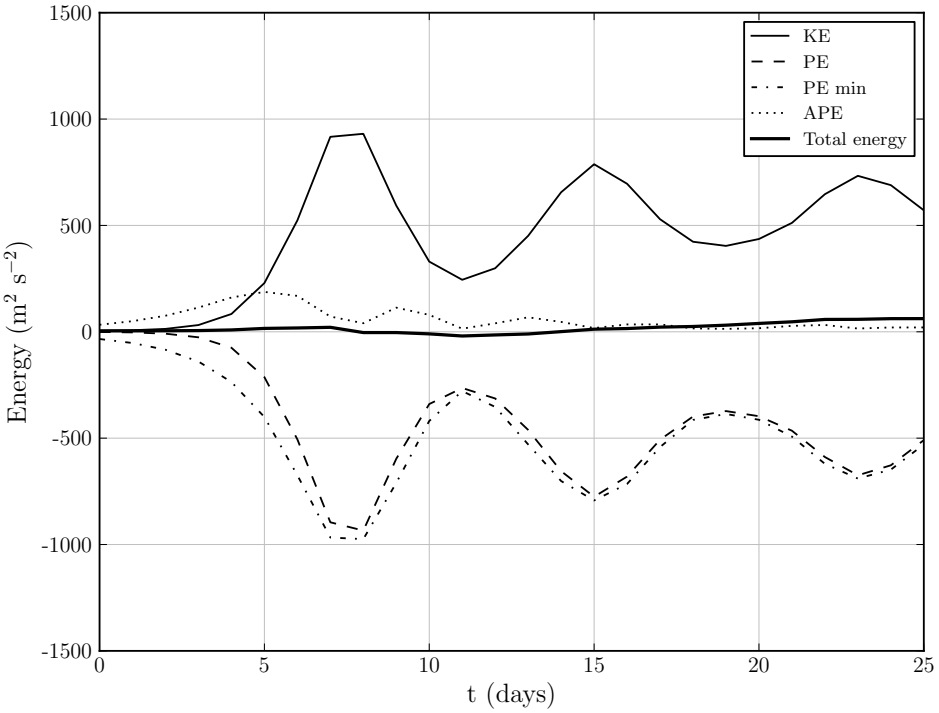

Figure 5.12: *Evolution of kinetic (KE), potential (PE), minimum potential (PE min), available potential (APE) and total energy.*

5.4 Asymptotic convergence and lifecycles

In this section the validation test of the asymptotic convergence is performed for the full nonlinear Eady model. The experimental procedure is the same as the linear model experiments of Section 4.6, but using the full SISL numerical method.

5.4.1 Asymptotic convergence validation

Figure 5.13 shows the variation of η_g from days two to ten. At days two and four the theoretical rate of convergence is achieved across the range of Rossby numbers. Note that the plots are shown for β which represents the physical rescaling but, as shown in Section 4.5, is directly proportional to the Rossby number.

At days six and eight, at which time the front is near its maximum intensity, there is a reduction in the slope, and the values at $\beta = 1/8$ are tailing off. By day 10 the imbalance is almost back to the theoretical rate, but offset from the initial values. In the subsequent evolution η_g does not increase again, even for secondary and additional intense fronts.

Figure 5.14 shows η_g, but now for experiments using the SISL algorithm alongside results using the SIE and SIVIE algorithms, with all results shown at doubled resolution. All the methods are able to reproduce the theoretical convergence rate, even at day eight, and in particular the reduction in convergence rate at low Rossby number is much reduced. These results show that it is possible to maintain balance after frontal collapse, and answers the first research objective.

Initially the SIVIE results show less imbalance than either the SISL or SIE methods at day two. At this stage the motion is essentially rearranging the near uniform PV distribution, and so the preservation of vorticity looks to be beneficial in achieving this.

There are no vector invariant results shown for $\beta > 1$ in Figure 5.14. At large β the solutions using the SIVIE algorithm very quickly diverged, often by day four. Increasing the nonlinear iterations had little effect, delaying the divergence by a day at best in some cases. At large Ro the preservation of vorticity, which is predominantly composed of unbalanced motion, is not a desirable trait in the numerical method when it is the balanced motion that is of interest.

After frontal collapse the Eulerian methods appear to perform better than the semi-Lagrangian method in maintaining balance, especially at lower Ro. This would suggest that conservation, even of the primitive fields and not the Lagrangian conserved quantities, is improving the representation of balance. This is discussed further in Section 5.5.

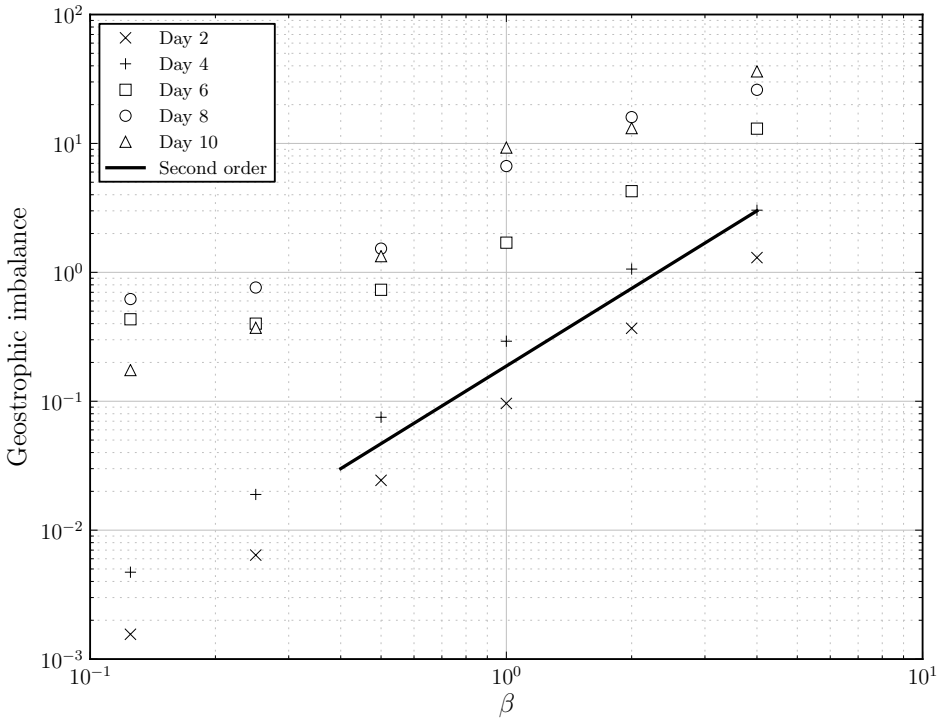

Figure 5.13: *Variation of the RMS norm of the geostrophic imbalance with rescaling at several days pre- and post-collapse, with theoretical second order slope shown, for the standard model.*

5.4.2 Extended rescaling comparison

Figure 5.15 shows one point of the extended rescaling alongside the C08 rescaling. The extended rescaling has not improved the representation of geostrophic balance after collapse, supporting previous results that have shown the motion to be essentially hydrostatic.

Figure 5.16 shows the evolution of the hydrostatic and thermal wind imbalances for the extended rescaling. There is almost no change between the two rescaling methods, showing that the simpler C08 rescaling is sufficient for the asymptotic convergence process.

Further analysis of the extended rescaling shows almost no difference between the corresponding C08 results. The meridional velocity evolution curves have not been plotted since it would not be possible to distinguish between the two methods.

The aspect ratio of the standard problem without any rescaling is $\delta = 1/200$, and the hydrostatic imbalance is $\mathcal{O}\left(\mathrm{Ro}^2\delta^2\right)$. The hydrostatic imbalance is several orders of magnitude smaller than the geostrophic imbalance. Since the extended rescaling affects the hydrostatic balance it is no surprise

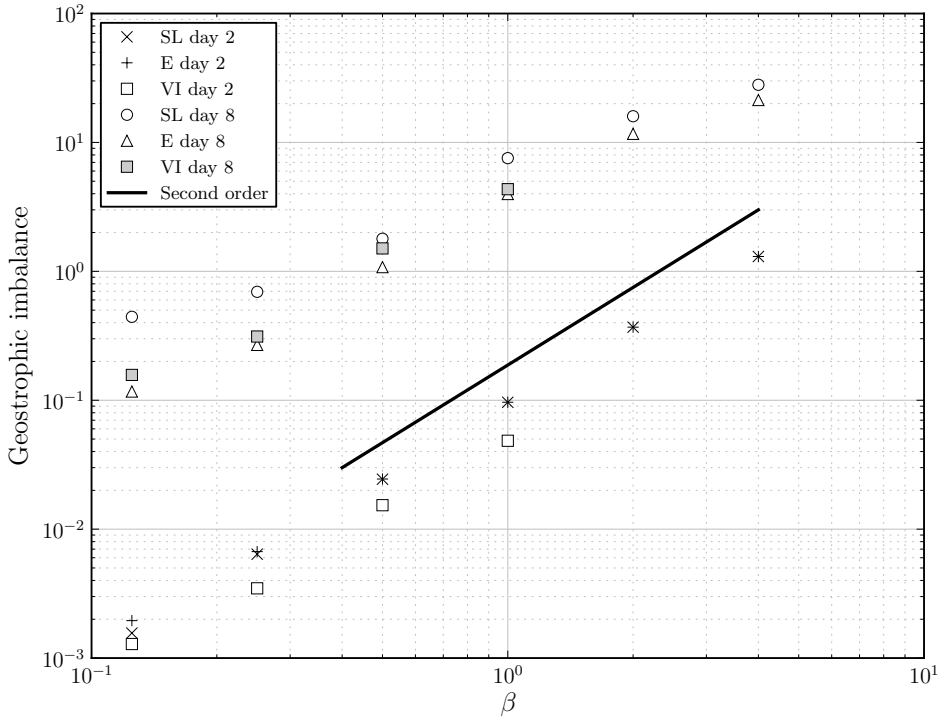

Figure 5.14: *Comparison of the RMS norm of the geostrophic imbalance at days two and eight for the various numerical methods at doubled resolution. The legend entries correspond to the advection method used; SL for semi-Lagrangian, E for Eulerian and VI for vector invariant Eulerian.*

that this does not alter the solution or convergence behaviour; at $\beta = 1/8$ the hydrostatic imbalance is still at least two orders of magnitude smaller than the geostrophic.

One might expect the extended rescaling to be necessary in situations in which $\mathrm{Ro} = \mathcal{O}(\delta)$. Continuing the rescaling down to smaller Rossby numbers such that this condition is satisfied may show the extended rescaling to be required to maintain all the balance laws, but the reduction in geostrophic imbalance slowed for $\beta < \mathcal{O}(0.1)$.

5.4.3 Baroclinic lifecycles

Figure 5.17 shows the evolution of the RMS norm of the meridional velocity field at the standard resolution for the range of rescaling parameters. As $\beta \to 0$ the peak value of the first maxima increases, but looks to be converging towards a value of around 45 m s^{-1}. This would suggest that further reducing the Rossby number would not reproduce the intensity of the C07 RMS norm results.

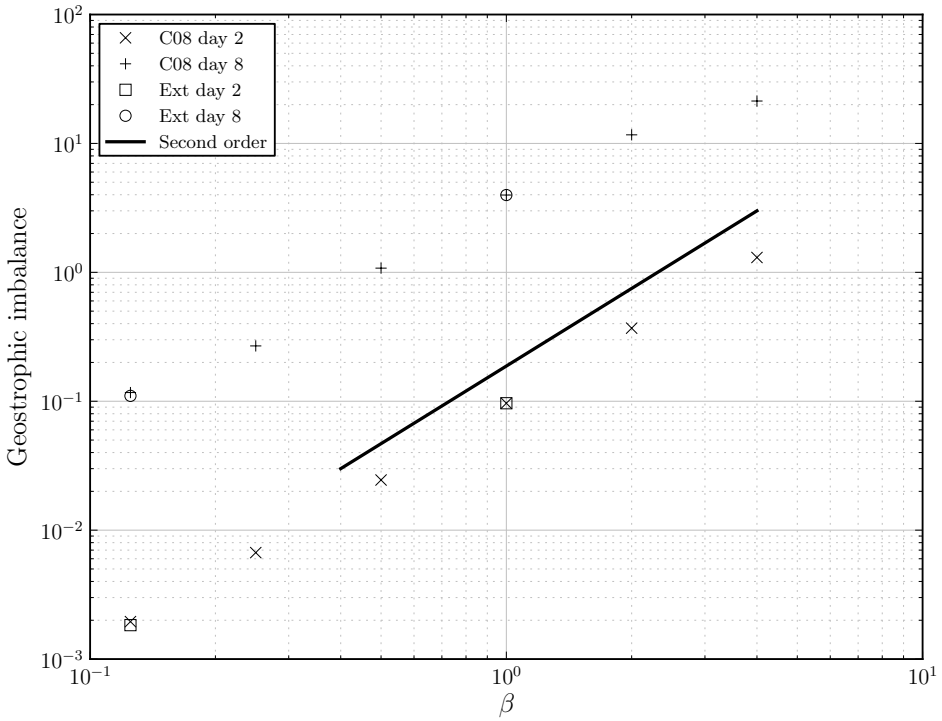

Figure 5.15: *Variation of geostrophic imbalance for the extended rescaling alongside values for the C08 rescaling. Both experiments were run at doubled resolution relative to control and used the SIE scheme.*

For $\beta < 1$ the results are similar up to the first peak, but for $\beta > 1$ this is not the case. For $\beta > 1$ the first peak reduces, and the predictability deteriorates. In addition the curves for $\beta = 2, 4$ show small amplitude secondary oscillations with a period of approximately one and two days respectively.

The results for $\beta < 1$ after the first peak do not exhibit the predictability and lifecycles of the SG results. In fact, they are much closer to the varying diffusion experiments of NH89 shown in Figure 2.7. This shows in both cases that the post collapse results are very sensitive to small changes in the model parameters. When attempting to compare against a limit solution this is troubling.

Figure 5.18 shows the RMS norm of the meridional velocity evolution, but at uniformly quadrupled resolution. The situation is now very different to the standard resolution; there is high predictability in the resulting lifecycles, with very little damping in the subsequent peaks. This strongly suggests that both the standard resolution and NH89 are insufficiently resolved to track the quasi-periodic evolution post-collapse.

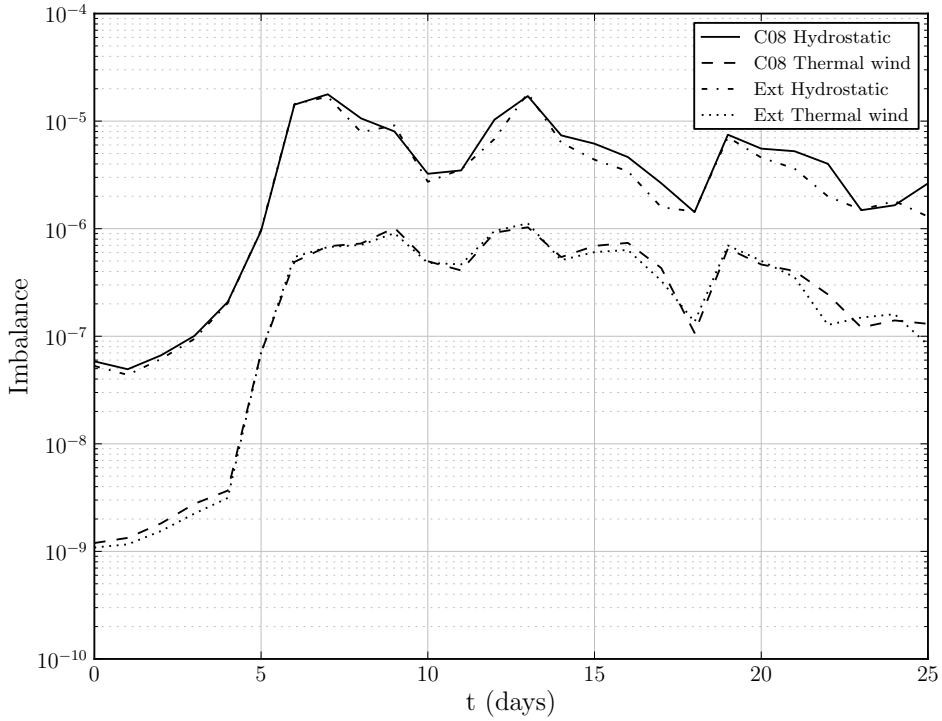

Figure 5.16: *Evolution of hydrostatic and thermal wind imbalance for the extended rescaling alongside the C08 rescaling for the SIE scheme at double resolution and* $\beta = 1/8$.

The fact that increasing resolution improves the results, in terms of the slowly damped quasi-periodic behaviour, is an informative result and answers the second research objective. Although there is no minimum scale so that the solution could be fully resolved, previous results have stated that increasing resolution has had little impact on the solution: Nakamura and Held (1989) found little effect on either the large scale solution or contour plots of the fields themselves; whilst Snyder et al. (1993) found that doubling the resolution only delayed the generation of PV, and hence the intensity of the front at the grid scale, by two hours.

Increasing resolution is continually happening in operational models, e.g. the global operational UM has gone from 90 km in 1991 to 14 km in 2014, which has generally occurred in tandem with an increase in hardware. It would be desirable to achieve a level of accuracy equivalent to a higher resolution, but at a lower resolution and reduced computational cost.

The results at high resolution are still not comparable to the limit solution. The peak RMS norm of the meridional velocity for $\beta = 1/8$ has increased from 43.5 m s^{-1} at the control resolution to 46.2 m s^{-1} and

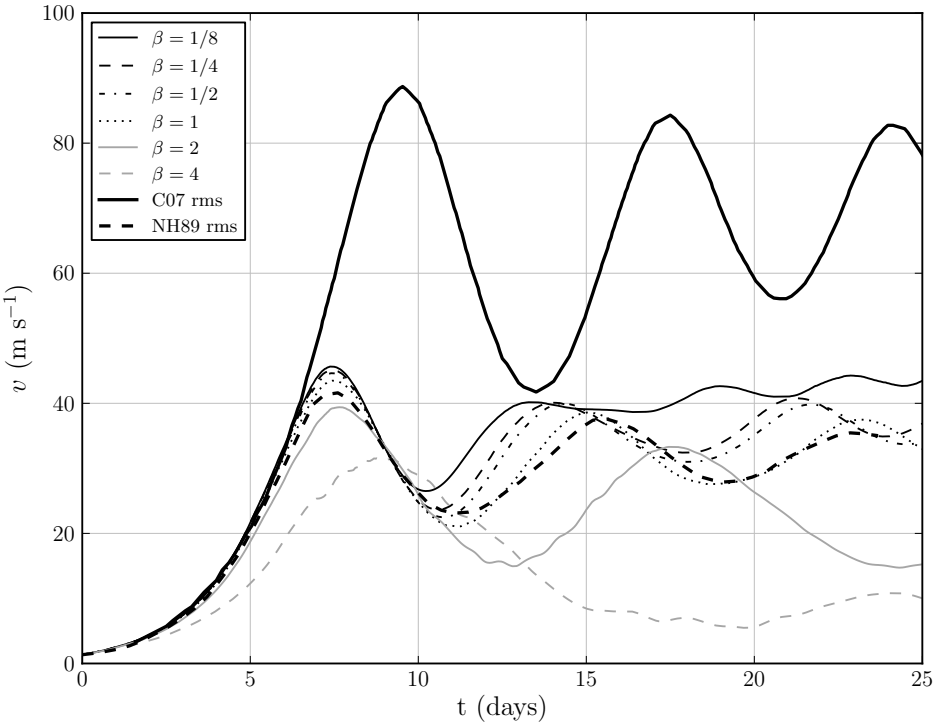

Figure 5.17: *Evolution of the meridional velocity RMS norm with rescaling for the standard model.*

46.7 m s^{-1} at doubled and quadrupled resolution, respectively. This suggests it would be prohibitively expensive, if at all possible, to reproduce the intensity of the limit solution on a fixed grid.

Figure 5.19 shows the RMS meridional velocity at uniformly doubled resolution for the three numerical methods. The most obvious result is that the doubled resolution SISL experiment at $\beta = 1/8$ cuts off the second minima, but appears to predict a reasonable third maxima. Despite the fortunate positioning of the third maxima it would be dangerous to read any more into this than pure coincidence.

It is reassuring to observe that for each β all three methods are well banded within a few m s^{-1}, with the exception noted above. As seen at the standard resolution for the SISL scheme it is not a trivial result to obtain this.

It is difficult to evaluate from Figure 5.19 alone which method performs the best. The SISL scheme attains consistently larger amplitudes, but is worrying in the behaviour around the second minima. There is little to choose between the SIE and SIVIE methods, with the former better at $\beta = 1$ and the latter better at $\beta = 1/8$.

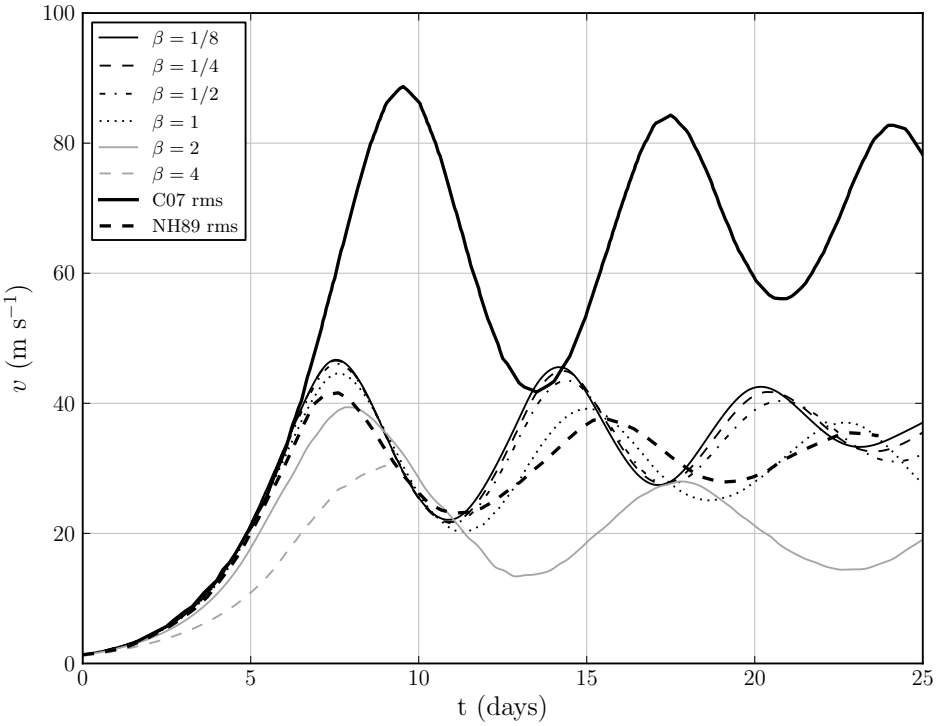

Figure 5.18: *As Figure 5.17 but with uniformly quadrupled resolution.*

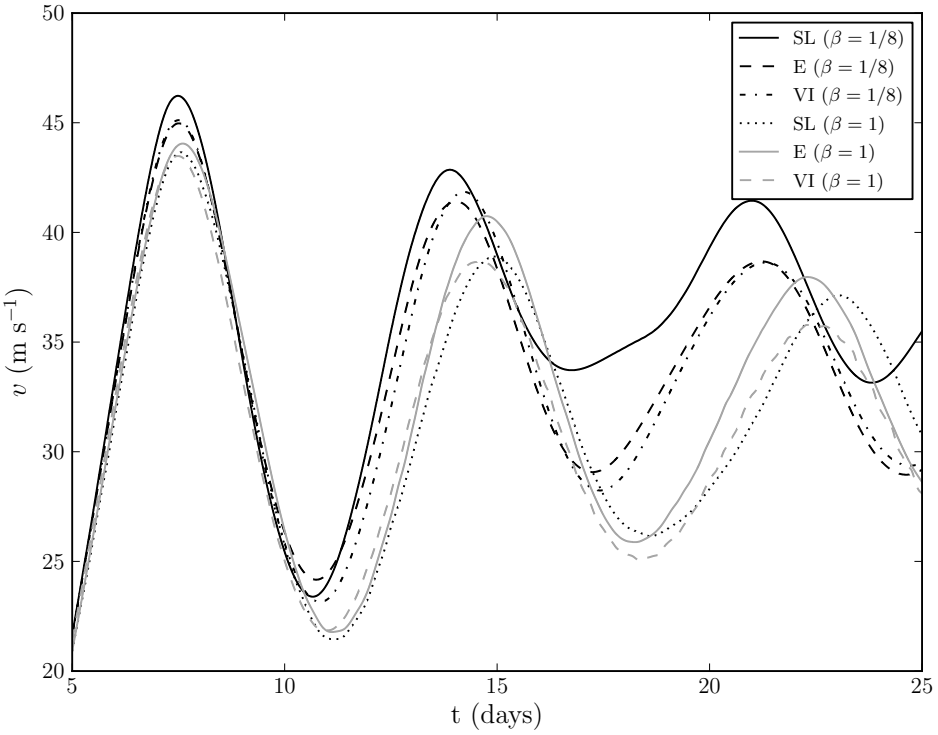

Figure 5.19: *Comparison of the meridional velocity RMS with the different numerical methods at the control and fully rescaled. Experiments were performed at uniformly doubled resolution relative to the control case.*

5.5 Quantification of balanced dynamics

This section sheds some more insight into the behaviour of the solutions by investigating the "balanced" components.

5.5.1 Potential vorticity

Figure 5.20 shows the comparison between the Ertel PV, given by Equation (4.49), and the SG PV, given by Equation (4.50), for the standard model at day seven. The fact that the Ertel and SG PV are so close, being at most $\mathcal{O}(0.1 \text{ PVU})$ different, shows that even at $\beta = 1$ the dynamics are close to balance.

There is evidence of a vertical wave pattern ahead of the fronts, which as it reaches of the opposite boundary appears to split in two and get advected away. These appear qualitatively very similar to the IGWs found in Snyder et al. (1993), see Figure 2.4, but are shown at a later stage.

The generation length scale of the gravity wave jet is very narrow, suggesting that it is strongly dependent on the width of the front, which agrees with the results found by Snyder et al.. Whilst there is significant IGW activity then locally Du/Dt must become $\mathcal{O}(1)$.

Immediately behind the fronts and almost on the boundaries are large regions in which $q > q_g$, whilst ahead of the fronts are negative regions below positive regions. These are areas in which there is strong flow turning, as discussed in the following section, and so there will be large in-slice vorticity contributions.

Figure 5.21 shows v, θ and q at day seven for $\beta = 1/8, 1$ at quadrupled resolution. The rescaling clearly reduces the unbalanced motion as the contours in Figure 5.21 (b) are much smoother than (d), in particular at approximately $H/3$ above the fronts. The rescaled solution shows much sharper gradients, including an almost horizontal region behind the front that is not observable at $\beta = 1$.

The PV plots, Figures 5.21 (a) and (c) are also noticeably different. The rescaled front is much narrower than the control case, both in terms of the intrusion itself but also the extent of the negative regions.

Figure 5.22 shows the Ertel PV alongside contours of

$$f + \frac{\partial v}{\partial x} < 0,$$

and

$$\frac{\partial}{\partial z}\left(\theta + \overline{\theta}\right) < 0.$$

The results are shown at the standard resolution, since although the analysis holds at higher resolution the contours become much harder to distinguish. It is clear that the regions of negative PV correlate closest with the meridional instability criterion.

There is a region of negative buoyancy frequency behind the fronts at $\beta = 1$, which is not present at $\beta = 1/8$. This is likely caused by the downwards vertical motion transporting warmer air parcels underneath the cooler air close to the boundary. In a real front the effects of moisture and viscosity would likely be important before these unstable regions occur.

Figure 5.23 shows the evolution of the domain averaged PV for the same β and numerical methods as Figure 5.19. Based on the contour plots one would expect the rescaled solutions to have higher PV integral values, but this is only really apparent for the second lifecycle.

The structure of the domain averaged PV curve is of interest, showing two peaks for each lifecycle. Observing the distribution of the PV shows the two filaments coalescing into a single filament in the centre of the domain, which appears to increase in intensity. Eventually a large portion of this PV gets removed, but this shows very different qualitative behaviour to the limit solution.

In the inviscid limit solution the two PV filaments never reach the opposite boundary, since this would correspond to the domain splitting in the dual space. In the Eulerian methods used in this thesis increasing resolution does not appear to prevent the coalescing happening. The PV dynamics and the Lagrangian behaviour are intertwined, and so the ability of the method to reproduce the Lagrangian behaviour is covered in the next section.

5.5.2 Lagrangian dynamics

Figure 5.24 shows normalised velocity vectors on an enlarged portion of the domain corresponding to the lower front. In both cases at day four the velocity fields are smooth, and so the fixed grid methods are able to model the advecting velocity field well. By day five, however, the velocity fields ahead of the front resemble a flow turning at a right angled wall. This is clearly a test for any numerical method, and it is unsurprising that all of the numerical methods struggle to integrate through this.

The velocity fields are not improved by increasing resolution; the same phenomena inevitably exist, but at reduced spatial scale. Whilst the overall representation of the front is improved, the same difficulties in capturing a contact discontinuity will exist on a fixed grid. In this way, viewing atmospheric motion as essentially near inviscid transport of air masses, suggests that some form of adaptive refinement could efficiently improve forecast accuracy.

Figure 5.25 shows the trajectories of passive Lagrangian particles integrated using a fourth order Runge-Kutta method with cubic quasi-monotone velocity interpolation. The strength of the vortex structure in entraining the particles is quite apparent. The trajectories are highly curved, again implying that fixed grid methods are not best suited to this problem.

Figure 5.26 shows the distribution of all the Lagrangian tracer particles

that were initially on horizontal lines alongside the PV distribution. The lowest line of particles is just offset from the boundary, and as the frontogenesis progresses these are seen to lift away from the boundary and wrap around the PV intrusion.

As mentioned in Section 2.3.2 the fact that fluid is able to lift off from the boundary is a key feature of the semigeostrophic limit solution, arising from the free boundary problem in the dual space. The numerical method appears to do a good job of resolving this phenomenon. If the top and bottom rows of particles are taken to denote a "Lagrangian boundary" then the agreement with Garner et al. (1992), see Figure 2.3, is quite striking.

By days six and seven, due to the strength of the circulation, the points behind the front look to lose coherency and are not transported as part of the large scale flow. It is likely that in this region there is grid scale motion and wave breaking, neither of which is going to be adequately captured.

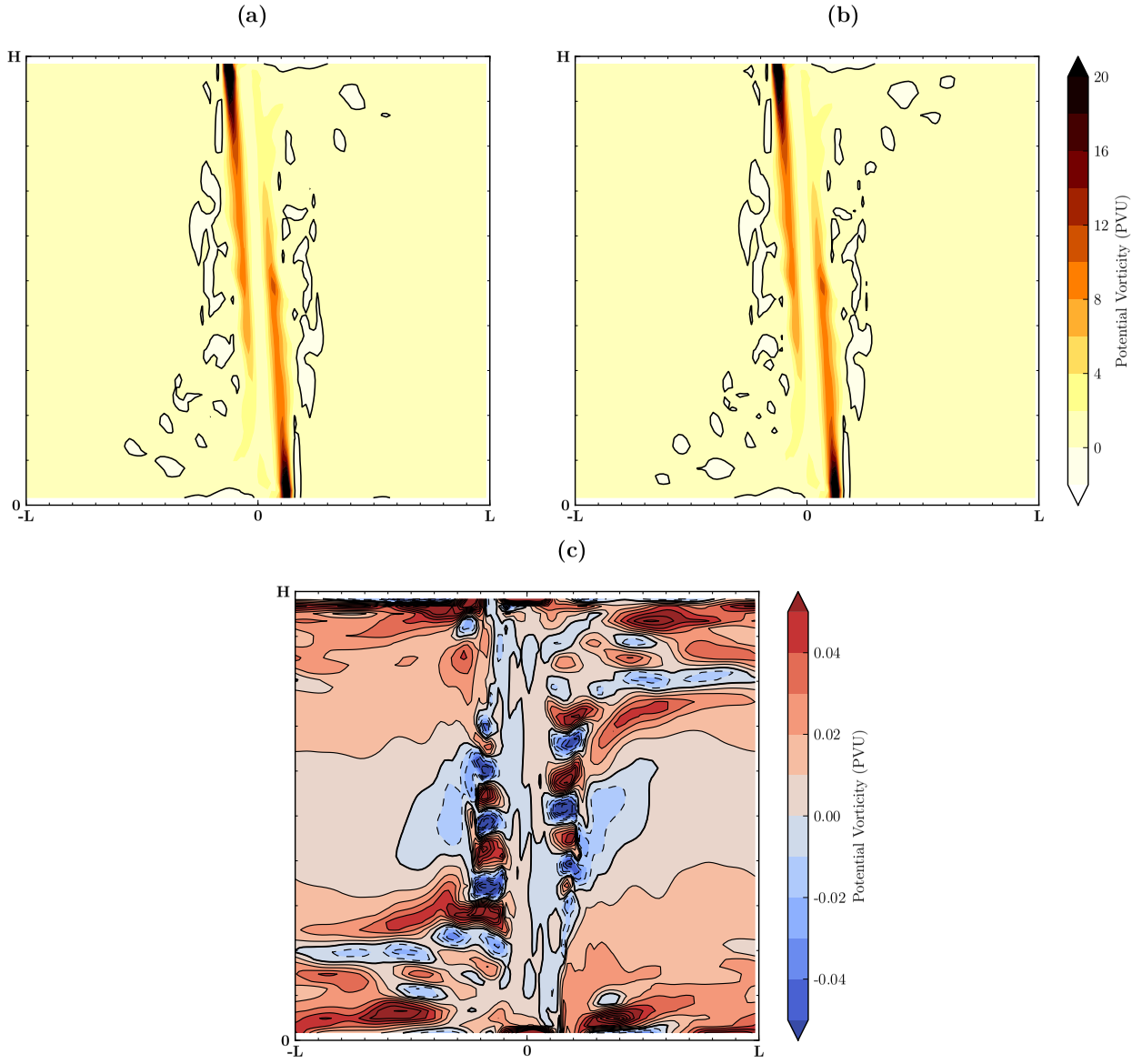

Figure 5.20: *Comparison of (a) Ertel PV, (b) semigeostrophic PV and (c) $PV_E - PV_{SG}$ at day seven. (a) and (b) are plotted on the same scale, whilst the difference plot is an order of magnitude smaller.*

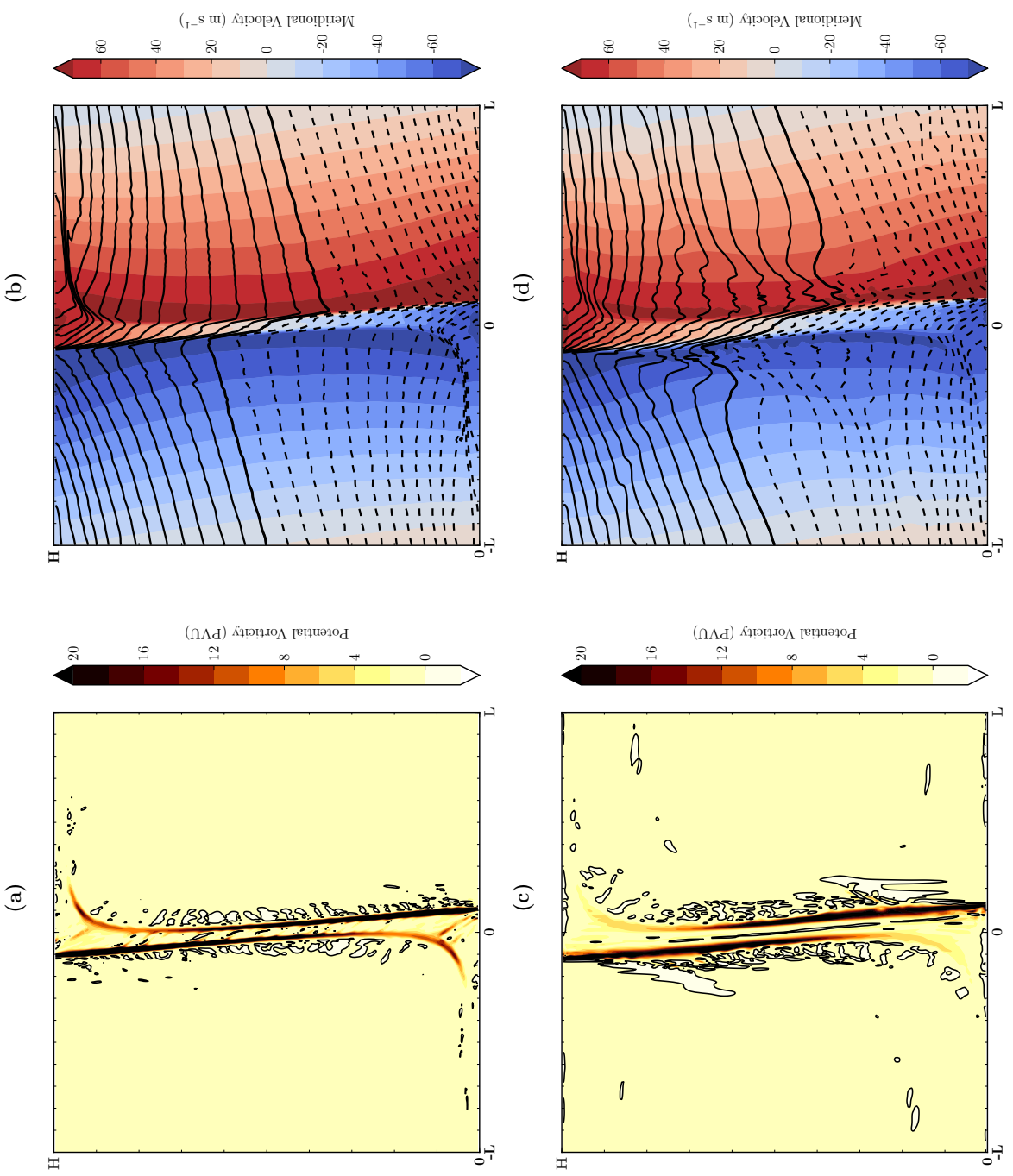

Figure 5.21: *Comparison of PV (left) and compound plots (right) of meridional velocity (coloured contours) & potential temperature (contour lines, negative dashed, interval* 2 K *and thick zero line) with rescaling parameter* $\beta = 1/8$ *(top) and* $\beta = 1$ *(bottom) at the highest resolution.*

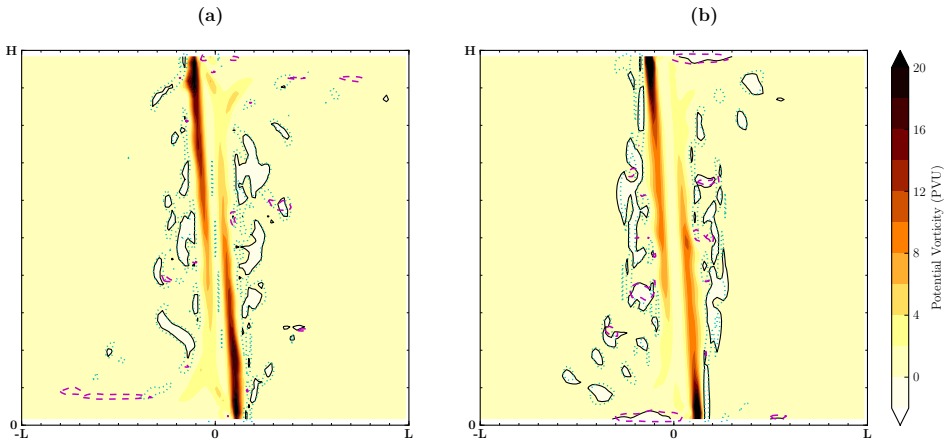

Figure 5.22: *Comparison of potential vorticity fields at day seven for (a) $\beta = 1/8$ and (b) $\beta = 1$. Dotted cyan contours show regions in which the meridional vorticity is negative and dashed magenta contours show regions in which the buoyancy frequency is negative.*

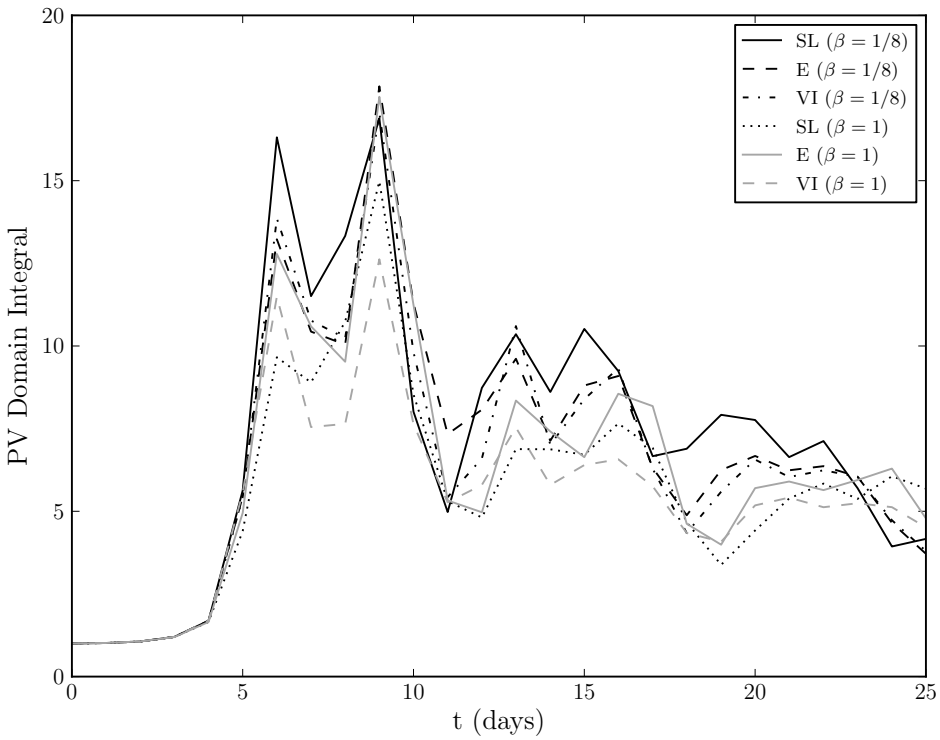

Figure 5.23: *Evolution of domain integral of potential vorticity for varying numerical methods and at different β, for a uniform resolution of $(241, 121)$ and normalised by the initial value.*

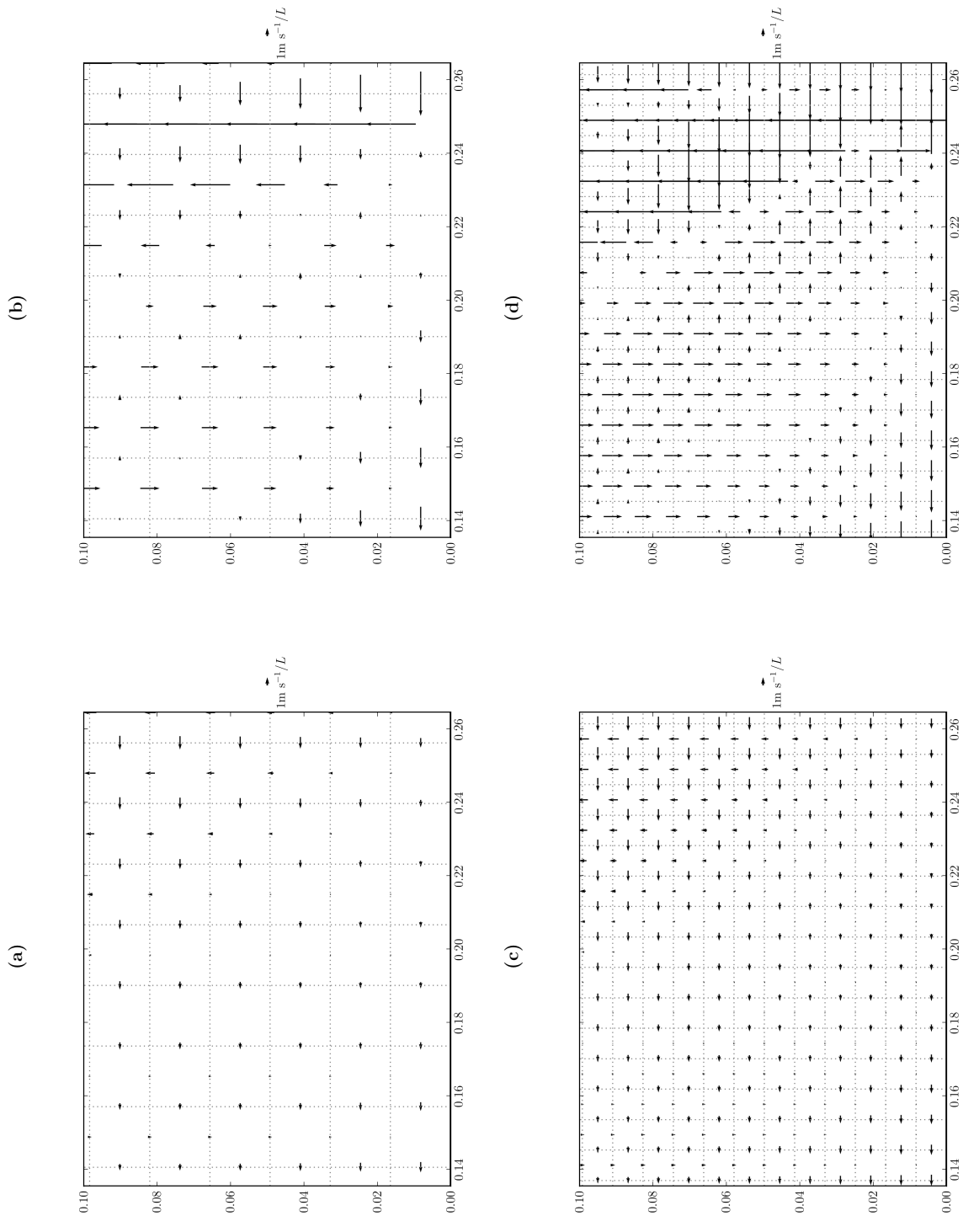

Figure 5.24: *Scaled velocity vectors, u/L and w/H, at day 4 (left) and 5 (right) for the control (top) and doubled (bottom) resolution experiments.*

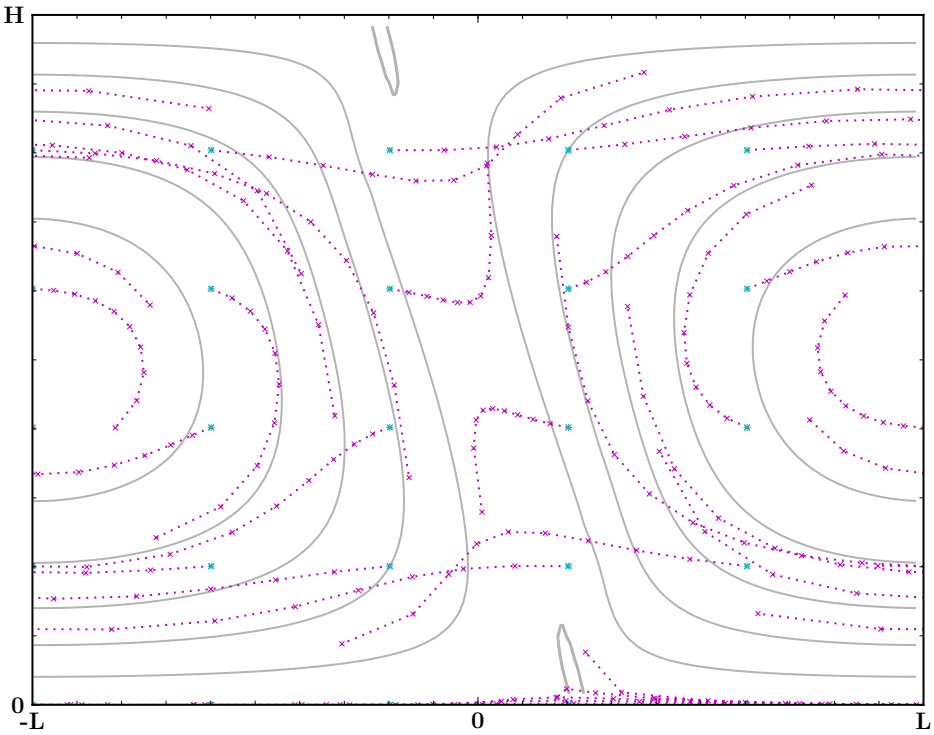

Figure 5.25: *Particle streaklines, dotted lines originating from $*$ with markers every $1/2$ day interval, and instantaneous streamlines at day five. Experiment was run at control resolution and $\beta = 1$.*

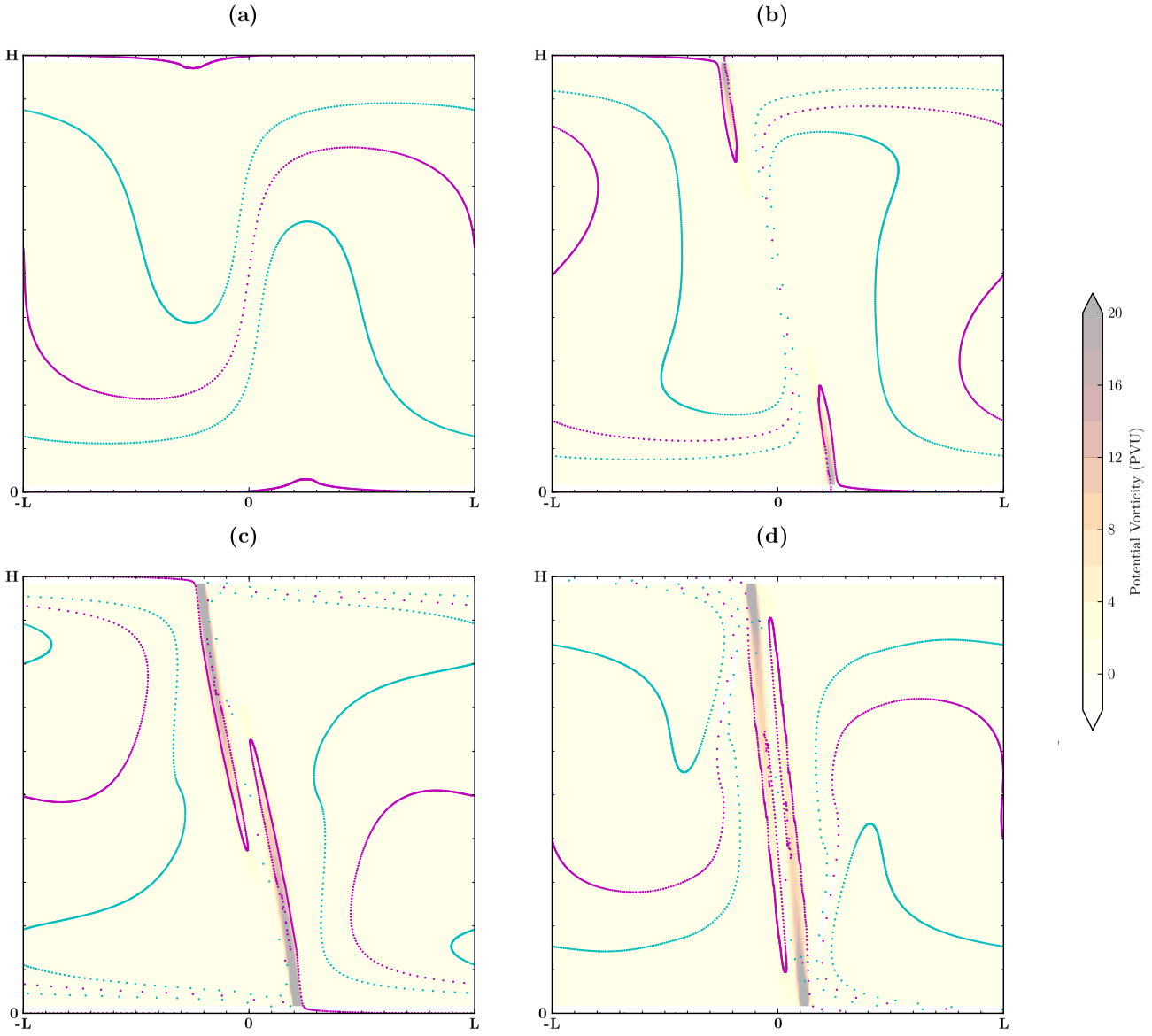

Figure 5.26: *Instantaneous particle positions at days four to seven, with PV contours. Original particle distributions were horizontal lines at* $\approx 0, H/2, \approx H$ *(magenta) and* $H/4, 3H/4$ *(cyan), where the boundary particles were offset a small distance from the top and bottom. Experiment was run at control resolution and* $\beta = 1$.

5.6 Conservation diagnostics

In this section a test case using the results of the previous sections is developed to evaluate the conservation properties of the SISL and SIE schemes. Only the SISL and SIE methods are tested, since the vector invariant advection uses the SIE advection of v and θ. The aim of this experiment is to assess how well the standard numerical methods are able to maintain the conservation properties of the continuous equations within the discontinuous flow given by the solution to the Eady model.

As touched upon earlier, a conservation law of the form

$$\frac{D\chi}{Dt} = 0,$$

implies the conservation of any function of the passive tracer χ. Whilst it is often desirable to conserve χ, either locally or globally, it is clearly not possible to achieve the conservation of any function of χ in a numerical method with a finite number of degrees of freedom.

5.6.1 Numerical method

The experiment measures the error made in the conservation of a passive tracer field over a single advection step, using velocity fields taken from solutions to the Eady problem at a given time. As the same linear solver / projection method is used for all the methods any differences in solutions should be down to differences in advection.

In the advection step all of the fields, u, v, w and θ, are treated as passive tracers, and the nonlinearity is taken care of in the outer iterations in which the advecting velocity field is updated. In this experiment the advecting velocity field is constant throughout the time-step.

There would be a small error if this advecting velocity field were to be compared with the nonlinear advecting velocity corresponding to the full numerical integration. This error is not significant since the main aim is to have a representative divergence-free velocity field for a single step.

The passive tracer field was chosen to be the potential temperature distribution at the given instant in time. Since θ should be conserved by the continuous equations using its distribution will give an accurate insight into how well the methods perform in *realistic* situations outside of idealised test cases.

As well as θ an additional field given by θ^2 was also advected. By adding in this quadratic field it is possible to get an estimate into how diffusive the numerical method is by comparing the advected θ^2 with the square of the advected θ. This would not be possible by looking at the conservation of θ alone, and sheds some insight into how well the scheme is able to preserve sharp gradients.

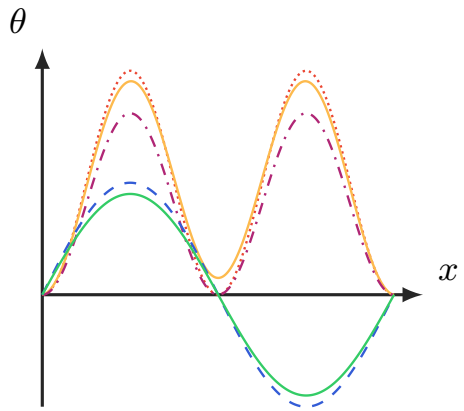

Figure 5.27: *An illustration of the advection conservation experiment for a one-dimensional profile of a sine wave. Blue dashed curve represents the analytic θ and solid green line the advected θ. Red dotted curve represents θ^2; solid orange curve the advected θ^2 and purple dot-dashed curve the advected θ then squared.*

Figure 5.27 illustrates qualitatively how the conservation experiments are performed for a sinusoidal profile. The metrics are calculated on the advected profile on the right, and shows how the additional quadratic term is used to assess the dissipation in the scheme. For a detailed account of this method applied to the first-order upwind scheme, as well as for a lock-breaking test case, see Burchard and Rennau (2008).

After the advection step the global conservation, as well as conservation of higher order moments, were calculated using the expressions below. In the following expressions the subscript now refers to the time level, and spatial indices are omitted since the conservation diagnostics are expressed as global integrals.

The conservation metrics are the conservation of θ

$$\mathcal{C}_1 = \int_V \theta_{*+\Delta t}\,\mathrm{d}V - \int_V \theta_*\,\mathrm{d}V; \tag{5.1}$$

the conservation of θ^2

$$\mathcal{C}_2 = \int_V \left(\theta^2\right)_{*+\Delta t}\,\mathrm{d}V - \int_V \left(\theta^2\right)_*\,\mathrm{d}V; \tag{5.2}$$

and a variance-like quantity

$$\mathcal{C}_V = \int_V \left(\theta_{*+\Delta t}\right)^2 - \left(\theta^2\right)_{*+\Delta t}\,\mathrm{d}V. \tag{5.3}$$

Note that the variance is given by

$$Var\left(\theta\right) = \int_V \left(\theta - \tilde{\theta}\right)^2 \mathrm{d}V,$$

Table 5.1: *Comparison of advection conservation errors over a single time-step of advection at the control resolution and day four.*

	$\mathcal{C}_1$	$\mathcal{C}_2$	$\mathcal{C}_V$
Semi-Lagrangian			
1	-7.327×10^{-09}	-2.973×10^{-06}	-1.154×10^{-04}
3	1.560×10^{-07}	2.438×10^{-06}	-1.846×10^{-07}
3QM	1.553×10^{-07}	2.604×10^{-06}	-4.712×10^{-07}
5	1.738×10^{-07}	2.070×10^{-06}	-4.741×10^{-07}
5QM	1.731×10^{-07}	2.222×10^{-06}	-7.470×10^{-07}
Eulerian			
UW	-2.321×10^{-09}	3.193×10^{-07}	-2.993×10^{-05}
UW3	-2.949×10^{-09}	2.359×10^{-07}	-1.452×10^{-07}
UW3-MM	-2.020×10^{-09}	3.189×10^{-07}	-1.001×10^{-06}
UW3-SB	1.246×10^{-08}	2.783×10^{-07}	3.784×10^{-07}

where

$$\tilde{\theta} = \int_V \theta \, \mathrm{d}V / \int_V \mathrm{d}V,$$

is the domain averaged potential temperature.

The experiments are carried out at days four and five, since these represent either side of the collapse to grid scale. The experiments are repeated at three levels of refinement, so that the convergence rates for the conservation properties can be calculated.

5.6.2 Conservation error

Table 5.1 shows the results of the conservation experiment for day four. The velocity fields are smooth at this point, and both of the methods do a reasonable job at preserving all of the conservation metrics. For the semi-Lagrangian scheme only the linear interpolation systematically reduces the conservation, whilst the others increase conservation but decrease variance. At day four for the semi-Lagrangian methods the use of the QM limiter appears to have negligible effect on the conservation properties, but roughly doubles the error in variance.

The Eulerian $\mathcal{C}_1$ results are two orders of magnitude better than the SL results, but still not at the level of numerical round-off that one would expect. Both of the limiters appear to have negative effects, with the minmod limiter degrading the variance whilst the superbee degrades the conservation.

By day five the situation has inevitably changed somewhat; all of the conservation metrics have dropped by an order of magnitude, showing the

Table 5.2: *Comparison of advection conservation errors over a single time-step of advection at the control resolution and day five. For the semi-Lagrangian methods the number corresponds to the order of the polynomial interpolation used, with QM denoting use of the quasi-monotone limiter. For the Eulerian methods UW is first-order upwind, UW3 is third-order upwind, and MM and SB correspond to the minmod and superbee limiters, respectively.*

	$\mathcal{C}_1$	$\mathcal{C}_2$	$\mathcal{C}_V$
Semi-Lagrangian			
1	-2.016×10^{-08}	6.049×10^{-05}	-1.918×10^{-04}
3	1.287×10^{-07}	2.271×10^{-05}	5.286×10^{-06}
3QM	5.974×10^{-07}	3.506×10^{-05}	-1.426×10^{-05}
5	6.970×10^{-07}	1.680×10^{-05}	6.146×10^{-06}
5QM	7.583×10^{-07}	3.724×10^{-05}	-1.975×10^{-05}
Eulerian			
UW	-1.584×10^{-08}	5.284×10^{-06}	-5.493×10^{-05}
UW3	-1.486×10^{-08}	5.145×10^{-06}	-3.520×10^{-06}
UW3-MM	-1.353×10^{-09}	5.298×10^{-06}	-1.232×10^{-05}
UW3-SB	-4.566×10^{-09}	5.257×10^{-06}	-6.932×10^{-06}

challenge the discontinuous flow presents to the numerical method.

The semi-Lagrangian results help to explain why the unlimited SISL scheme is able to integrate up to frontal collapse but not past. The unlimited Lagrange interpolation works to enhance extrema, whilst the QM limiter damps them out, albeit quite harshly. This occurs alongside an increase in the $\mathcal{C}_1$ metric, suggesting an overall increase or drift in the θ field itself.

At day five the Eulerian methods are still better than the semi-Lagrangian methods, but there is now less to choose between the methods. The application of the flux limiters improves the $\mathcal{C}_1$ metric, but, as with the QM interpolation limiter, erodes the variance. Interestingly there is very little to choose between the first- and third-order upwind methods in terms of $\mathcal{C}_1$ and $\mathcal{C}_2$. This would imply that the accuracy at this point is limited by the time-step, but checking the velocity field shows the maximum point-wise Courant number to be 0.07, which is quite low and could be unnecessarily dissipative for the non-centred semi-implicit scheme.

Using a fixed time-step method for the Eady model will always present this problem due to the reduction in scale and frontal collapse. Clearly an explicit method would not remain stable for practical values of Δt since the timescale goes to zero, so the use of semi-implicit is justified. The consequence is that not all of the dynamics of interest are being resolved, and so the evolution will be damped.

Tables 5.3 and 5.4 show the same conservation diagnostics but now at

Table 5.3: *Comparison of advection conservation errors over a single time-step of advection at the highest resolution and day four.*

	$\mathcal{C}_1$	$\mathcal{C}_2$	$\mathcal{C}_V$
Semi-Lagrangian			
1	-1.478×10^{-10}	-3.036×10^{-07}	-7.509×10^{-06}
3	8.846×10^{-10}	8.167×10^{-08}	-9.817×10^{-10}
3QM	8.828×10^{-10}	8.025×10^{-08}	-5.303×10^{-09}
5	5.458×10^{-10}	8.158×10^{-08}	-2.480×10^{-09}
5QM	5.435×10^{-10}	8.005×10^{-08}	-6.778×10^{-09}
Eulerian			
UW	-4.844×10^{-11}	1.305×10^{-08}	-1.934×10^{-06}
UW 3	-5.502×10^{-11}	1.161×10^{-08}	-1.829×10^{-09}
UW3-MM	1.466×10^{-10}	1.268×10^{-08}	-1.609×10^{-08}
UW3-SB	3.359×10^{-10}	1.248×10^{-08}	7.704×10^{-09}

the highest resolution (481×241) at days four and five, respectively. At day four the increase in resolution has greatly improved all of the conservation diagnostics for both methods.

At day five even the higher resolution experiments are struggling. The convergence rates with resolution are summarised in the following tables, but it is immediately apparent that increased resolution is not necessarily a panacea. This is because the front is close to being discontinuous for some finite Ro, and so refinement would be best carried out in an adaptive manner.

Table 5.4: *Comparison of advection conservation errors over a single time-step of advection at the highest resolution and day five.*

	$\mathcal{C}_1$	$\mathcal{C}_2$	$\mathcal{C}_V$
Semi-Lagrangian			
1	5.240×10^{-07}	1.093×10^{-05}	-2.165×10^{-05}
3	-5.501×10^{-08}	3.147×10^{-06}	-6.908×10^{-07}
3QM	-3.136×10^{-08}	2.928×10^{-06}	-1.227×10^{-06}
5	-9.404×10^{-08}	2.497×10^{-06}	-9.104×10^{-08}
5QM	-6.350×10^{-08}	1.808×10^{-06}	-9.309×10^{-07}
Eulerian			
UW	-7.368×10^{-09}	4.331×10^{-07}	-6.453×10^{-06}
UW 3	-7.192×10^{-09}	4.341×10^{-07}	-6.583×10^{-07}
UW3-MM	-5.102×10^{-09}	4.351×10^{-07}	-1.967×10^{-06}
UW3-SB	-5.250×10^{-09}	4.393×10^{-07}	-1.172×10^{-06}

Table 5.5: *Semi-Lagrangian spatial convergence of conservation properties at day four. Column headers correspond to spatial interpolation order, with QM used to denote quasi-monotone interpolation.*

	1	3	3QM	5	5QM
$\mathcal{C}_1$	2.82	3.73	3.73	4.16	4.16
$\mathcal{C}_2$	1.65	2.45	2.51	2.33	2.40
$\mathcal{C}_V$	1.97	3.78	3.24	3.79	3.39

Table 5.6: *Semi-Lagrangian spatial convergence of conservation properties at day five. See Table 5.5 for column labels.*

	1	3	3QM	5	5QM
$\mathcal{C}_1$	-2.35	0.61	2.13	1.44	1.79
$\mathcal{C}_2$	1.23	1.43	1.79	1.38	2.18
$\mathcal{C}_V$	1.57	1.47	1.77	3.04	2.20

5.6.3 Conservation rates

Tables 5.5 and 5.6 show the convergence rates for the semi-Lagrangian methods at days four and five, respectively. As could be inferred from the absolute values above there is a large change in how well the numerical method can resolve the dynamics over the two days.

The convergence rates are calculated from a linear regression curve with just three data points, so it is to be expected that there is a reasonably large error margin on these values. In spite of this it is apparent that there are diminishing returns in adding resolution at day five compared to the case when it is smooth.

Tables 5.7 and 5.8 show the convergence rates for the Eulerian methods at days four and five, respectively. Again, there is a reduction between the two days, but this time the contrast is not as large. This could partly be down to the Eulerian methods being more conservative from the start, or that the theoretical spatial orders of the Eulerian flux calculations are not as high as the semi-Lagrangian methods. At day five the $\mathcal{C}_1$ diagnostic is pretty much flat, whereas for the semi-Lagrangian methods the situation is not quite so clear.

5.6.4 Conservation analysis

It is clear from the conservation experiment results that there is a significant error being made systematically by all of the numerical methods, which is

Table 5.7: *Eulerian spatial convergence of conservation properties at day four. Columns are first-order upwind (UW), third-order upwind (UW3), third-order upwind with minmod limiter (UW3-MM) and third-order upwind with superbee limiter (UW3-SB).*

	UW	UW3	UW3-MM	UW3-SB
$\mathcal{C}_1$	2.79	2.87	1.89	2.61
$\mathcal{C}_2$	2.31	2.17	2.33	2.24
$\mathcal{C}_V$	1.98	3.16	2.98	2.81

Table 5.8: *Eulerian spatial convergence of conservation properties at day five. See Table 5.7 for column labels.*

	UW	UW3	UW3-MM	UW3-SB
$\mathcal{C}_1$	0.55	0.52	-0.96	-0.10
$\mathcal{C}_2$	1.80	1.78	1.80	1.79
$\mathcal{C}_V$	1.54	1.21	1.32	1.28

not always improved with increasing resolution.

Despite the $\mathcal{C}_2$ and $\mathcal{C}_V$ metrics showing encouraging convergence rates with resolution it is hard to avoid the fact that the lack of conservation of the θ field itself is going to be a significant source of error.

The lack of conservation motivated revisiting the original advection experiments of the slotted cylinder profile. Results for conservation in both v and θ are shown in Table 5.9 after a single revolution, i.e. the same experimental setup as in section 3.5.2.

These results clearly show that there is an error in the conservation of the θ field with the SIE algorithm, which is not evident in the advection of the v field, which is conservative down to machine precision.

The error in the conservation of θ is likely to be caused by the treatment of the boundary conditions for θ with the boundary half-cells, and/or the lack of storing θ on the boundaries, both of which are closely related.

To investigate the effects of the boundary treatment of θ further global integrals of u, v, w and θ were calculated, and are shown in Figure 5.28. Since the solutions to the Eady problem exhibit rotational antisymmetry these integrals should be zero for the continuous case, and any errors therefore represent the combined effects of lack of conservation and asymmetry in the solutions.

The results of Figure 5.28 strongly point to the lack of conservation of θ as compromising the results for the SIE algorithm, since the three velocity fields all show conservation errors of $\mathcal{O}\left(10^{-16}\right)$. It is likely that this lack of

Table 5.9: *Comparison of advection conservation errors using the pure advection test case with a slotted cylinder profile. Conservation error was calculated after a single rotation, and defined in the same way as earlier in this section, but with the sign convention such that a positive value corresponded to a reduction in mass and a negative value an increase. Two methods for calculating the global integrals were included;* ① *a single sum over all the elements,* ② *dividing the domain into sub-blocks, 10 in the horizontal and 10 in the vertical, and then summing all the sub-block contributions.*

	①		②	
	θ	v	θ	v
Semi-Lagrangian				
1	4.85×10^{-04}	2.05×10^{-04}	4.85×10^{-04}	2.05×10^{-04}
3	-1.15×10^{-05}	-1.02×10^{-06}	-1.15×10^{-05}	-1.02×10^{-06}
3 QM	1.40×10^{-03}	1.34×10^{-03}	1.40×10^{-03}	1.34×10^{-03}
Eulerian				
UW1	-1.53×10^{-03}	2.01×10^{-16}	-1.53×10^{-03}	0.00
UW3	-8.14×10^{-05}	1.04×10^{-16}	-8.14×10^{-05}	0.00
UW3-SB	4.43×10^{-06}	0.00	4.43×10^{-06}	0.00

conservation is significantly altering the background state, thereby changing the buoyancy frequency and dynamical regime with the same effect as found in Nakamura and Held (1989).

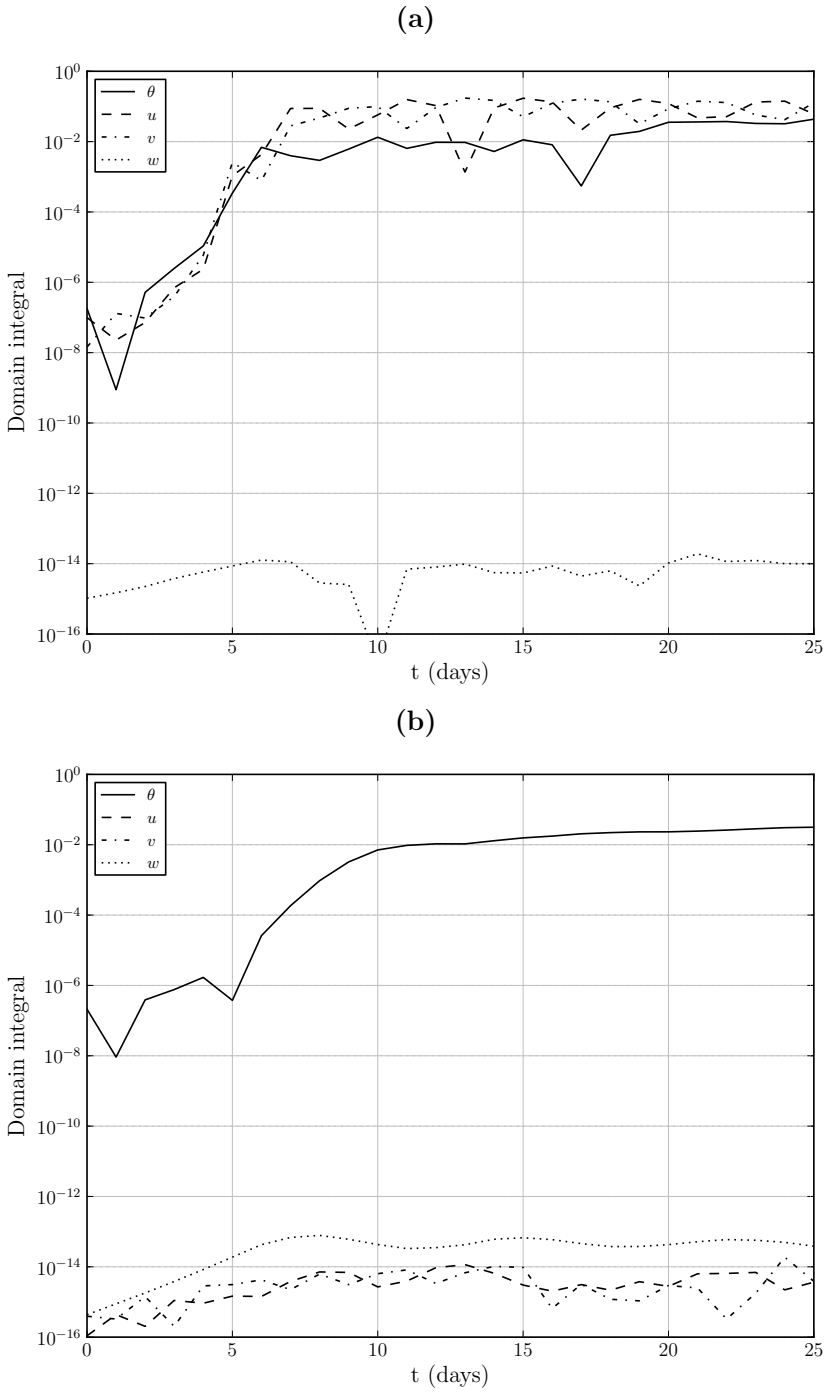

Figure 5.28: *Integrals of u, v, w and θ at doubled resolution for the SISL (a) and SIE (b) algorithms. Due to the rotational antisymmetry of the solutions these should be zero for solutions to the continuous equations. It is clear that in terms of conserving θ the Eulerian advection is no better than the semi-Lagrangian scheme. The integrals were calculated with the sub-block approach outlined in Table 5.9.*

5.7 Summary

This chapter finishes by returning to the limit solution obtained numerically using the geometric algorithm of Cullen (2007a). This solution was given by enforcing the Lagrangian conservation laws and balance laws exactly. The abilities of the various numerical methods in correctly, or, perhaps more appropriately, less wrongly, reproducing the necessary features have been presented.

The discussion first covered the initial portion of the evolution, in which the dynamics were well represented by the linear model. The SISL scheme was shown to be slightly more dissipative than the leapfrog model of NH89, but did not have the same filtering requirements in time to maintain stability.

The most striking feature of the initial evolution, which inevitably affects how the rest of the behaviour is interpreted, is that the intensity of the frontogenesis is approximately half that of the inviscid semigeostrophic limit solution. All of the Eulerian results are in a very similar range, including existing results from the works cited, suggesting that there is a limitation that is difficult to overcome.

It is an open question as to whether or not there is a minimum scale for the solution to the Euler equations, but for the solution to the Euler equations to be consistent with the semigeostrophic solution then this should rapidly approach zero. In the fixed grid methods the minimum resolvable scale, as a function of the total domain width, remained constant. This might explain part of the limitation on the amplitude, and why the rescaled solutions remain within a reasonably small window.

Increasing the grid resolution was shown to improve the amplitude, with the highest resolution case approximately 3 m s^{-1} higher than the lowest. Given that the increase in computational cost scales as $1/(\Delta x \Delta z \Delta t)$ this would appear to be prohibitively expensive for a marginal increase in intensity alone.

Carrying out several experiments with $\mathrm{Ro} \to 0$ improved the predictability and quasi-periodic nature of the solutions, but approaching the balanced limit alone was not sufficient in reproducing the limit solution.

Increased resolution, though, dramatically improved the *large-scale* predictability, showing behaviour that was similar in nature to the limit solution in spite of the scale differences. Improved conservation, either through increased resolution or more conservative numerical methods, is clearly vital in answering the second research objective.

There are numerous conflicting requirements when designing operational NWP systems, but the results presented in this chapter strongly suggest that one might reasonably see an improvement in the synoptic-scale evolution after resolving more small-scale features. This is apparent in the greatly improved predictability of the large-scale solution, as shown in Figure 5.18, and the reduction in spatial extent of regions of negative PV, as shown in

Figure 5.21.

The solution was shown to exhibit a strong positive PV intrusion whilst the front was intense, along with large patches in which the PV was negative. As the front subsided the intrusion was only partially removed, effectively changing the background PV value, and hence the expected dynamics of the evolution. Increasing resolution and carrying out the rescaling both helped to increase the intensity of the filaments whilst reducing and removing the negative patches, suggesting the solution was getting close to the non-negative PV limit solution.

The geostrophic imbalance was shown to decrease at the theoretical second-order rate, even after frontal collapse, showing that the solutions were balanced up to some finite amount proportional to the Rossby number. These results clearly answered the first research objective.

The conservative Eulerian methods performed slightly better than the semi-Lagrangian method in terms of balance, but the semi-Lagrangian method showed more energetic lifecycles. This is an interesting result when considering the difficulties in predicting semi-Lagrangian communication patterns and difficulties with scalability, and it is not possible to choose a clear winner.

Analysing the Lagrangian nature of the solution, in terms of the conservation and deformation properties, showed the fundamental challenges of simulating frontogenesis. There are strong gradients, near right-angled velocity fields at the grid scale, and narrow sloping regions, all of which occur at the boundary. Following tracer particles showed the numerical method to match the expected deformed domain shape except in the strong downdraft behind the fronts.

Calculating the conservation metrics of Section 5.6 showed all of the methods to be sufficiently conservative for smooth velocity fields, but struggled with conservation whilst the front was intense. The lack of conservation of the potential temperature was likely to be altering the background state, and so changing the dynamical regime in a similar manner to Nakamura and Held (1989).

The semigeostrophic solution is given by Lagrangian conservation laws and enforcement of balance. The results in this chapter have shown that a balanced solution can be obtained after collapse using simple numerical methods. The dominant error, supported by results from pure advection test cases, was lack of conservation. Improving conservation improved the predictability and lifecycles, but not the amplitude, which appeared to be limited by the grid-scale.

The results presented here suggest that the fixed grid solutions are either converging to the correct limit solution, as shown by the increase in amplitude, or are converging to a different solution. The fact that the limit solution has only been shown to exist in a weak Lagrangian sense (Cullen and Feldman, 2006), whereas the methods presented in this thesis

are conservative in an Eulerian sense, would imply that the methods are ill-suited and so the latter option is the more likely.

In response to the third research objective the evidence presented in this chapter suggests that the solutions are not converging to inviscid semigeostrophic solutions, but perhaps instead to *viscous* semigeostrophic solutions. One way to investigate this further could be to use the geometric model with an additional viscous term, and see what the effect on the amplitude of the wave is.

The next chapter attempts to address the stark difference in amplitude between the results in this thesis and the limit solution, as well as discussing some methods that could improve the conservation properties by regularising the advecting velocity field.

Chapter 6

Towards improving predictability for frontal dynamics

We can only see a short distance ahead, but we can see plenty there that needs to be done.

A. Turing (1950)

Contents

6.1 Motivation

In this chapter several ideas are presented to address the problems found in the results shown in the previous chapters. The main challenge is investigating the reasons behind the discrepancy in the amplitude of the front, which appears to be connected to the difficulty in enforcing conservation during collapse.

Some provisional results are presented which, unlike the previous chapters, have not been published. They should be interpreted as a proof of concept, in that the method might work but has not been developed or tuned sufficiently to the Eady problem.

The first few methods discussed in this chapter share a common theme of trying to improve conservation through regularising the advecting velocity field. The final method presented takes a somewhat different approach in developing a scheme that is PV conserving.

6.2 Filtered advection in space

The first method discussed is to use an advecting velocity field that is regularised in space. The results of Section 5.6 showed that conservation was satisfied much more closely at day four rather than day five, primarily because the advecting velocity field is discontinuous at day five. By filtering the advecting velocity field in space, thereby giving a "smoother" advecting velocity field even when the front is intense, it is hoped that the conservation would be improved.

The Lagrangian-averaged Navier-Stokes-α model (α-model) is derived using a variational principle, which means that it has a conserved energy integral and circulation theorem by design, both of which are vital for long term predictability. The α parameter represents the length at which small scales change from being active to passively swept along. The value of α is typically chosen to be a small multiple of the grid spacing, so that it prevents the cascade of energy down to the grid-scale (Hecht et al., 2008).

In Hecht et al. (2008) the α-model was implemented in an ocean model. The Lagrangian-averaged model showed results comparable to a higher resolution, as well as permitting a larger time-step which only depended on the averaging scale and not the grid resolution, (Wingate, 2004). The α-model was found to be prohibitively expensive, requiring nested linear solver iterations, but similar results were obtained when the Helmholtz problem was replaced by a simple spatial average, which was much cheaper to solve.

A common feature of results using the α-model in geophysical fluid problems is that of the solutions being more energetic at well resolved scale, (Holm and Nadiga, 2003; Hecht et al., 2008), and so potentially requiring more dissipation than their un-averaged counterparts. In Hecht et al. (2008)

this was shown through the conversion of barotropic energy to baroclinic eddies, since the α-model increased the effective Rossby radius, which produced more energetic variability consistent with higher resolution experiments.

The α-model controls small scales by making them "slaved" to the larger scales, and are swept along passively without further influencing the dynamics. This was shown by Wingate (2004) in the context of the rotating shallow water equations in which the effect of the α-model was to slow down the frequency of the high wavenumber waves.

The smoothing in the Lagrangian-averaged equations is controlled through a lengthscale α and the inverse of a Helmholtz operator, see Equation (6.7) of the following section. By choosing $\alpha > (\Delta x, \Delta z)$ it is possible to restrict the generation of the smallest gridscale motion.

It is worth remarking that as $\alpha \to 0$ the un-averaged equations are recovered. Thus, one would hope that solutions of the Lagrangian-averaged Boussinesq Euler equations would converge to solutions of the Boussinesq Euler equations as $\alpha \to 0$. One would also hope that solutions to the Lagrangian-averaged model at finite α would only be $\mathcal{O}(\alpha)$ from the un-averaged equations.

6.2.1 Lagrangian-averaged equations

An alternative derivation of the standard Eady model, as well as a regularisation based on the Lagrangian-averaged Navier-Stokes-α (LANS-α) model and a compressible model, is presented in Cotter and Holm (2013). The Eady model is derived as a special case of a family of models known as vertical slice models of the incompressible Boussinesq Euler equations, in which motion is restricted to the vertical (x, z) plane.

The models start from the Lagrangian, $\mathbb{L}$,

$$\mathbb{L} = \int_\Omega \frac{\rho}{2}\left(|\mathbf{u}|^2 + v^2\right) + \rho f v x + \rho \frac{g}{\theta_0}\left(z - \frac{H}{2}\right)\theta + \phi\,(1-\rho)\,\mathrm{d}V, \tag{6.1}$$

where ϕ acts as a Lagrange multiplier to enforce constant density. After taking variations of Equation (6.1) the standard Eady model equations are recovered. The advantage of starting the from the Lagrangian ensures that the resulting set of equations have a conserved energy and potential vorticity. This is vital for long time dynamics, as covered in Chapter 2 and in detail in the review of Cullen (2007a).

As well as providing an alternative derivation of the Eady model, Cotter and Holm also gave a LANS-α Eady model. The LANS-α formulation has been used as a turbulence model in Hecht et al. (2008) in a full ocean model, in which the filtering was shown to improve long time statistics; in large eddy simulations in Geurts and Holm (2004, 2005) both the Leray-α and LANS-α

were shown to be competitive as sub-grid models with the Leray-α model being slightly more robust, and as a hierarchy of models for GFD in Holm et al. (2002).

The compressible model presented in Cotter and Holm (2013) differed from the ones used in Cullen (2008) in one term, namely the form of the meridional forcing

$$\frac{Dv}{Dt} + fu = \begin{cases} \frac{\partial \overline{\theta}}{\partial y} c_p \Pi & \text{CH13} \\ -c_p \theta \left. \frac{\partial \overline{\Pi}}{\partial y} \right|_{t=0} & \text{C08} \end{cases}, \tag{6.2}$$

where $\overline{\Pi}$ is the background Exner pressure, which is initially in hydrostatic balance (Cullen, 2008).

It is not yet known whether these equations permit frontogenesis as in the incompressible Eady model. Whilst the fronts shown in C08 were very similar to results using the incompressible model, the lack of energy or PV conservation in the C08 system meant that baroclinic lifecycles could not be obtained post collapse (Cullen, 2008). It is hoped that the CH13 compressible system will provide a useful test case for operational models, owing to its conservation properties, but it is an open question as to whether or not the solutions will resemble those of the incompressible Eady model.

Equations summary

The Lagrangian-averaged equations for the Boussinesq incompressible Eady problem are given by Cotter and Holm (2013) as

$$\frac{D\tilde{\mathbf{u}}}{Dt} + (\nabla \mathbf{u})^T \tilde{\mathbf{u}} - fv\hat{\mathbf{x}} = -\nabla \tilde{\phi} + \frac{g}{\theta_0}\theta \hat{\mathbf{z}}, \tag{6.3}$$

$$\frac{D\tilde{v}}{Dt} + f\mathbf{u} \cdot \hat{\mathbf{x}} = -\frac{g}{\theta_0}\frac{\partial \overline{\theta}}{\partial y}\left(z - \frac{H}{2}\right), \tag{6.4}$$

$$\frac{D\theta}{Dt} + v\frac{\partial \overline{\theta}}{\partial y} + \mathbf{u} \cdot \hat{\mathbf{z}}\frac{\partial \overline{\theta}}{\partial z} = 0, \tag{6.5}$$

$$\nabla \cdot \mathbf{u} = 0, \tag{6.6}$$

$$\mathbf{u} = \left(1 - \alpha_1^2 \nabla^2\right)^{-1} \tilde{\mathbf{u}}, \tag{6.7}$$

$$v = \left(1 - \alpha_2^2 \nabla^2\right)^{-1} \tilde{v}, \tag{6.8}$$

where

$$\frac{D}{Dt} = \frac{\partial}{\partial t} + \mathbf{u} \cdot \nabla,$$

is the modified Lagrangian derivative; $\tilde{\mathbf{u}} = (\tilde{u}, \tilde{w})$ is referred to as the circulation, or "rough", velocity field; $\mathbf{u} = (u, w)$ is referred to as the advecting, or "smooth", velocity field; $\alpha_1 = (\alpha_{1,x}, \alpha_{1,z})$ & $\alpha_2 = (\alpha_{2,x}, \alpha_{2,z})$ are the filter widths; and

$$\tilde{\phi} = \phi - \frac{1}{2}\left(|\mathbf{u}|^2 + \alpha_1^2 |\nabla \mathbf{u}|^2\right),$$

is the modified geopotential.

The Lagrangian-averaged equations have a conserved energy of the form

$$\frac{E_{T,\alpha}}{\rho_0} = \int_V \frac{1}{2}\left(|\mathbf{u}|^2 + \alpha_1^2 |\nabla \mathbf{u}|^2 + v^2 + \alpha_2^2 |\nabla v|^2\right) - \frac{g}{\theta_0}\theta\left(z - \frac{H}{2}\right) \mathrm{d}V, \quad (6.9)$$

and a conserved PV of the form

$$q_\alpha = \frac{1}{\rho_0}\left[\frac{\partial \overline{\theta}}{\partial y}\nabla \times \tilde{\mathbf{u}} + \frac{\partial\left(\tilde{v}, \theta\right)}{\partial\left(x, z\right)}\right]. \quad (6.10)$$

The divergence-free condition is given for the smooth velocity, but for the Euler equations with free-slip boundary conditions the rough velocity is also divergence-free.

6.2.2 Implementation

Starting from the linear Eady wave equations for the α model as

$$\frac{\partial \tilde{u}}{\partial t} - fv = -\frac{\partial \tilde{\phi}}{\partial x}, \quad (6.11)$$

$$\frac{\partial \tilde{v}}{\partial t} + fu = F(z), \quad (6.12)$$

$$\frac{\partial \tilde{w}}{\partial t} = -\frac{\partial \tilde{\phi}}{\partial z} + \frac{g}{\theta_0}\theta, \quad (6.13)$$

$$\frac{\partial \theta}{\partial t} + v\frac{\partial \overline{\theta}}{\partial y} + w\frac{\partial \overline{\theta}}{\partial z} = 0, \quad (6.14)$$

$$\frac{\partial u}{\partial x} + \frac{\partial w}{\partial z} = 0, \quad (6.15)$$

$$\left(1 - \alpha_{1,x}^2\frac{\partial^2}{\partial x^2} - \alpha_{1,z}^2\frac{\partial^2}{\partial z^2}\right)\mathbf{u} = \tilde{\mathbf{u}} \quad (6.16)$$

$$\left(1 - \alpha_{2,x}^2\frac{\partial^2}{\partial x^2} - \alpha_{2,z}^2\frac{\partial^2}{\partial z^2}\right)v = \tilde{v}. \quad (6.17)$$

The rough velocities are eliminated from the first three equations by substituting in the Helmholtz problem directly. This gives

$$\frac{\partial}{\partial t}\left(1 - \alpha_{1,x}^2\frac{\partial^2}{\partial x^2} - \alpha_{1,z}^2\frac{\partial^2}{\partial z^2}\right)u - fv = -\frac{\partial \tilde{\phi}}{\partial x}, \quad (6.18)$$

$$\frac{\partial}{\partial t}\left(1 - \alpha_{2,x}^2\frac{\partial^2}{\partial x^2} - \alpha_{2,z}^2\frac{\partial^2}{\partial z^2}\right)v + fu = F(z), \quad (6.19)$$

$$\frac{\partial}{\partial t}\left(1 - \alpha_{1,x}^2\frac{\partial^2}{\partial x^2} - \alpha_{1,z}^2\frac{\partial^2}{\partial z^2}\right)w = -\frac{\partial \tilde{\phi}}{\partial z} + \frac{g}{\theta_0}\theta, \quad (6.20)$$

$$\frac{\partial \theta}{\partial t} + v\frac{\partial \overline{\theta}}{\partial y} + w\frac{\partial \overline{\theta}}{\partial z} = 0, \quad (6.21)$$

$$\frac{\partial u}{\partial x} + \frac{\partial w}{\partial z} = 0, \quad (6.22)$$

since the Helmholtz operator commutes with the time derivative.

Carrying out the discretisation on the staggered C-grid results in the following linear forcing matrix

$$\tilde{\mathsf{M}} = \begin{bmatrix} \mathsf{H_u} & -\xi_1\mathsf{I} & \cdot & \cdot \\ \xi_1\mathsf{I} & \mathsf{H_v} & \cdot & \cdot \\ \cdot & \cdot & \mathsf{H_w} & -\xi_2\mathsf{I} \\ \cdot & \xi_3\mathsf{R} & \xi_4\mathsf{I} & \mathsf{I} \end{bmatrix}, \tag{6.23}$$

which only differs from the standard Eady problem of Section 4.3.2 in that the first three diagonal matrices are now the Helmholtz problem matrices as opposed to the identity matrices. The Helmholtz matrices are formed as

$$\mathsf{H_u} = \mathsf{I} + \alpha_{1,x}\mathsf{G_x}\mathsf{D_x} + \alpha_{1,z}\mathsf{P_z}\mathsf{C_z}, \tag{6.24}$$

$$\mathsf{H_v} = \mathsf{I} + \alpha_{2,x}\mathsf{G_x}\mathsf{D_x} + \alpha_{2,z}\mathsf{P_z}\mathsf{C_z}, \tag{6.25}$$

$$\mathsf{H_w} = \mathsf{I} + \alpha_{1,x}\mathsf{P_x}\mathsf{C_x} + \alpha_{1,z}\mathsf{G_z}\mathsf{D_z}, \tag{6.26}$$

where $\mathsf{D_x}, \mathsf{D_z}, \mathsf{G_x}$ and $\mathsf{G_z}$ are the same divergence and gradient matrices as for the standard problem, and $\mathsf{P_x} = \mathsf{C_x}^T$ and $\mathsf{P_z} = \mathsf{C_z}^T$ are matrix representations of the gradient of the streamfunction ($\mathsf{P_x}$, $\mathsf{P_z}$) and curl operators ($\mathsf{C_x}$, $\mathsf{C_z}$), respectively.

The modified linear forcing system is solved using the approximate factorisation technique of Section 4.3. This is possible in the present work since the small problem size means calculating a direct inverse is computationally achievable, but for larger problems a more efficient method would need to be implemented, such as replacing the inversion of the Helmholtz problem with an explicit smoothing operation as in Hecht et al. (2008).

The nonlinear term $(\nabla\mathbf{u})^T\,\tilde{\mathbf{u}}$ has not been covered yet, but fortunately it can be included quite easily. Using the vector invariant scheme, and the vector identities of Section 3.2.3 but now with two distinct velocities, includes this term in the advection step without the need for any additional forcing terms.

6.2.3 Results

In the following section the experiments have been carried out at doubled resolution relative to the control. No filtering was applied to the meridional velocity field, and the in-slice velocity field was only filtered in the horizontal direction since it was not possible to formulate the correct matrices for the vertical filtering within the timescale of this research. This is summarised below as

$$\alpha_1 = \alpha = (c\Delta x, 0)\,; \quad \alpha_2 = (0, 0)\,.$$

where the experiments used a value for c of 4 or 8 as stated.

Figure 6.1 shows the RMS norm of the meridional velocity evolution for the Lagrangian-averaged equations. At $\beta = 1$ it is unclear whether the

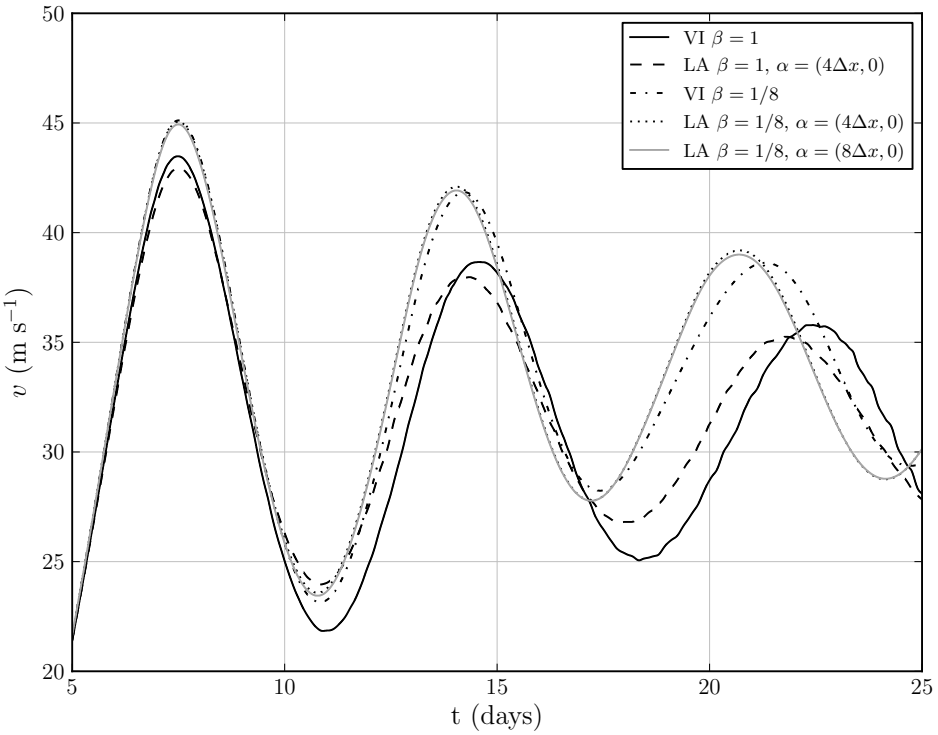

Figure 6.1: *Comparison of the evolution of the RMS norm of the meridional velocity field between the standard SIVIE scheme and the Lagrangian-averaged method. Both experiments were run at doubled resolution relative to control.*

filtering reducing the amplitude is desirable or not. There is still a trace of some unbalanced motion at later times with the filtered solution.

The results for $\beta = 1/8$ in Figure 6.1 are a bit more promising. Although the initial amplitude is slightly lower than the vector invariant control run, there is less damping and by the second maxima the filtered solution is already slightly more intense than the control. The filtered solution also appears to suffer less retardation, in that there is a third minima approximately one day ahead of the control.

Figure 6.2 shows the in-slice streamfunction for the two horizontal filter widths of $4\Delta x$ and $8\Delta x$ at days four and five. At both days shown, the smoothed advecting velocity is very similar between the filter widths. This is reassuring, and qualitatively supports the advecting velocity being determined by the PV distribution.

At day five both experiments show an intense vertical jet in the circulation velocity, but this is not present in the advecting velocity field, with the larger filtering showing a stronger jet and more wave activity propagating away from the front.

There appears to be a wave on the boundary behind the surface front which increases in amplitude and wavelength with filter length. As found in Wingate (2004) the α-model slows down the high wavenumber waves, and it is quite likely that this is the cause of the apparent dispersion occurring there.

Increasing the filter length decreases the number of high wavenumber waves which are able to couple back into the dynamics, but this does not appear to significantly change the large scale solution. This is supported by plots of the potential temperature and meridional velocity field shown in Figure 6.3.

The conservation experiments of Section 5.6 were repeated using the Lagrangian-averaged model to investigate whether the regularisation had improved conservation. The conservation metrics were found to be almost identical to the standard SIE schemes. The lack of improvement to conservation might have been because the experiment took initial fields from a solution using the standard methods. Since conservation was essentially unchanged this suggests that the improvement seen with the Lagrangian-averaged model is related to the treatment of the small scale motion.

There is one final point that is of interest. Whilst previous results have suggested that one of the effects of Lagrangian-averaging is to increase the energetics of the resolved motion, the results presented here do *not* show any significant difference as a result of using the α-model. This could be because in the experiments of (Holm and Nadiga, 2003; Hecht et al., 2008) the Rossby radius of deformation was only marginally resolved. By using the α-model the *effective* Rossby radius was increased, and so the baroclinic energy conversion was able to be better captured.

In the present work $L_{\mathrm{Ro}} = NH/f = 500$ km, and so is well resolved even without the effects of the Lagrangian-averaging. It was shown in Figure 5.12 that the baroclinic energy conversion was well resolved, and so the fact that the energetics do not alter seems very much consistent with the established results for the α-model.

Finally, it is prudent to remind the reader the preliminary nature of the results presented using the Lagrangian-averaged model, and therefore so are the conclusions. The results give a very brief insight the current problem, but further work would be required to gain more understanding in the application of Lagrangian-averaging in the context of fronts.

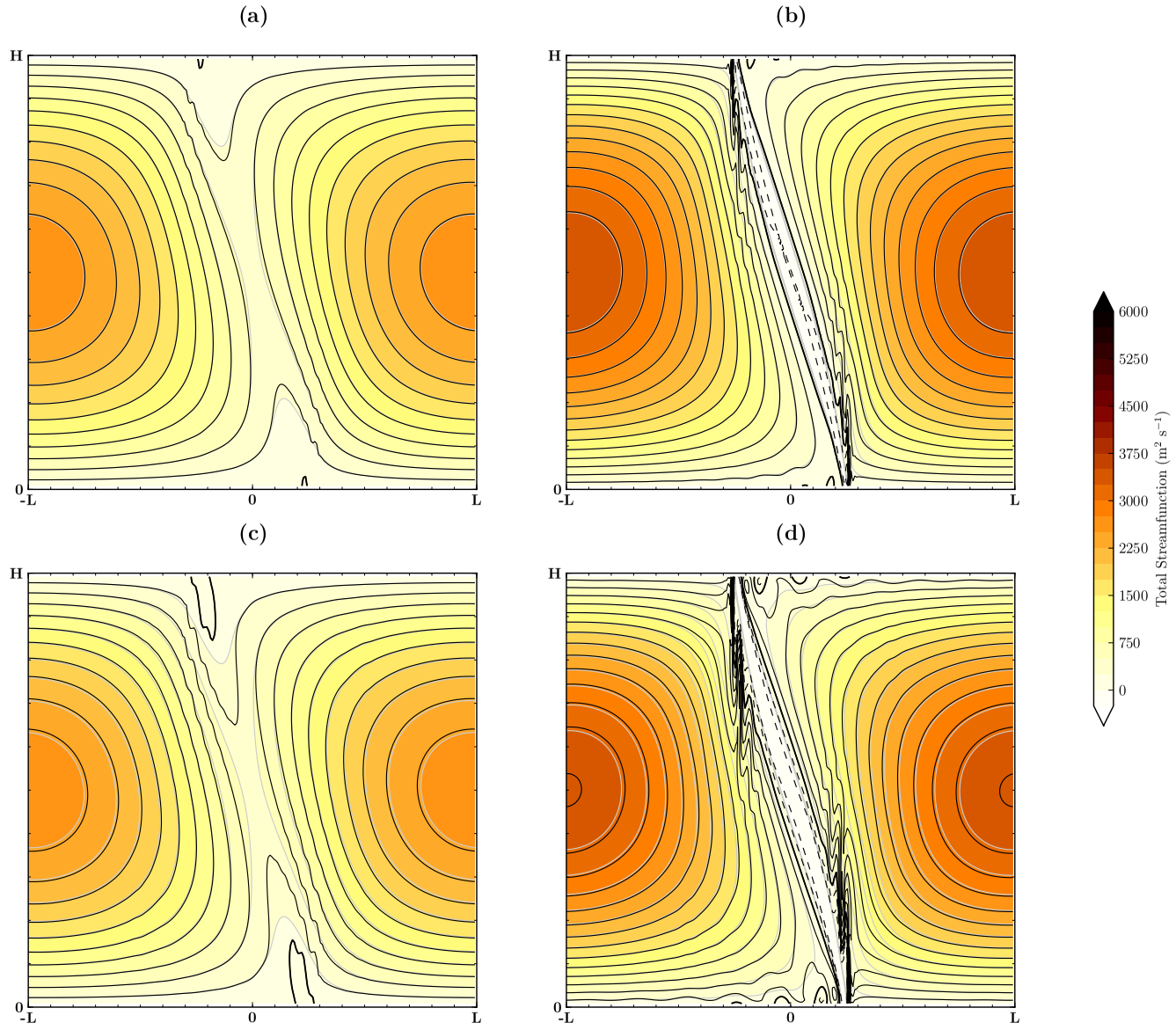

Figure 6.2: *Comparison of circulation velocity streamfunction, in black contour lines, and advecting velocity streamfunction in filled contours with grey contour lines. Top row corresponds to* $\alpha_1 = (4\Delta x, 0)$ *and bottom row* $\alpha_1 = (8\Delta x, 0)$*, whilst left column is at day four and right column at day five. Both experiments are shown at* $\beta = 1/8$ *and doubled resolution.*

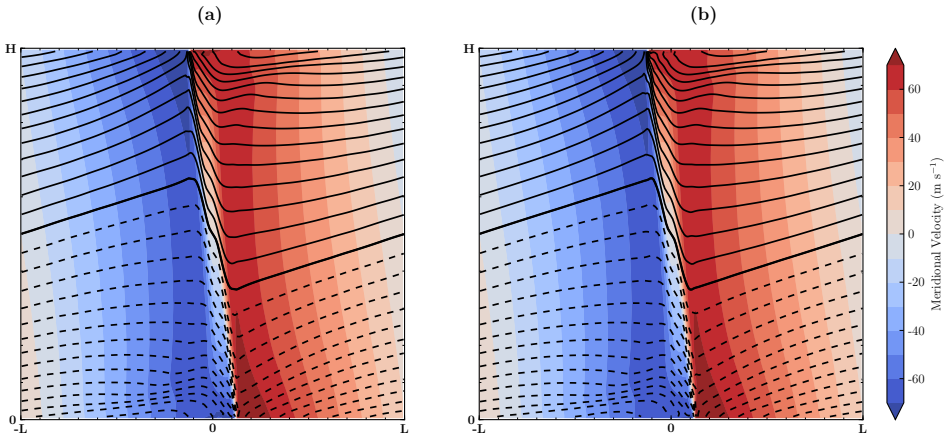

Figure 6.3: *Comparison of meridional velocity and potential temperature contour plots at day seven for* $\alpha_1 = (4\Delta x, 0)$ *(a) and* $\alpha_1 = (8\Delta x, 0)$ *(b). Both experiments are shown at* $\beta = 1/8$ *and doubled resolution.*

6.3 Filtered advection in time

The Lagrangian-averaged model of the previous section showed potential in an improved predictability of the large scale solution at long times, but the amplitude of the wave was still some way off the limit solution. In this section the possibility of filtering the advecting velocity in *time* instead of space is considered.

Filtering the advecting velocity field in time should delay the onset of the nonlinear equilibration process by keeping the advecting velocity field closer to the background shear state value, and, hence, closer to the linear solution.

6.3.1 Time-filtered equations

The time-filtered equations are given by

$$\frac{D\tilde{\mathbf{u}}}{Dt} - fv\hat{\mathbf{x}} = -\nabla\phi + \frac{g}{\theta_0}\theta\hat{\mathbf{z}}, \tag{6.27}$$

$$\frac{Dv}{Dt} + f\mathbf{u}\cdot\hat{\mathbf{x}} = -\frac{g}{\theta_0}\frac{\partial\overline{\theta}}{\partial y}\left(z - \frac{H}{2}\right), \tag{6.28}$$

$$\frac{D\theta}{Dt} + v\frac{\partial\overline{\theta}}{\partial y} + \mathbf{u}\cdot\hat{\mathbf{z}}\frac{\partial\overline{\theta}}{\partial z} = 0, \tag{6.29}$$

$$\nabla\cdot\mathbf{u} = 0, \tag{6.30}$$

$$\frac{\partial\mathbf{u}}{\partial t} = \frac{1}{\Delta}\left(\tilde{\mathbf{u}} - \mathbf{u}\right), \tag{6.31}$$

where

$$\frac{D}{Dt} = \frac{\partial}{\partial t} + \mathbf{u}\cdot\nabla,$$

is the time-filtered Lagrangian derivative; $\mathbf{u}$ is the time-filtered advecting velocity and Δ is the filtering timescale. The length of Δ determines how the advecting velocity field evolves; for long Δ the field remains close to the background state, and so the evolution is close to that given by the linear problem. As with the Lagrangian-averaged equations the continuity condition applies to the advecting velocity field, but, since the divergence term commutes with the time derivative then combining Equations (6.30) and (6.31) gives that

$$\nabla\cdot\tilde{\mathbf{u}} = 0. \tag{6.32}$$

The time-filtered equations, unlike the Lagrangian-averaged equations of the previous section, do not have a conserved potential vorticity, limiting their utility for long time solutions.

It is not immediately apparent what value to use for the filtering timescale in the model. Whilst the space filtered equations had an obvious minimum scale permitted by the grid resolution, the filtering timescale has a larger

range. Initial tests with a multiple of the time-step showed little variation, whilst having a multiple of the Coriolis frequency, such that the filtering was working to damp IGWs, showed a larger effect.

6.3.2 Implementation

The implementation of the time-filtering modification to the advecting velocity field is very simple. Equations (6.27) to (6.29) and (6.32) are the Eady problem, but with a constant advecting velocity field. These are solved using one of the standard methods described in Chapter 4 for a single iteration; the results presented in the following section use the vector invariant formulation.

Equation (6.31) is discretised in a semi-implicit manner as

$$\frac{\mathbf{u}^{n+1,k+1} - \mathbf{u}^{n}}{\Delta t} = \frac{1}{\Delta}\left[\vartheta\left(\tilde{\mathbf{u}} - \mathbf{u}\right)^{n+1,k} + (1-\vartheta)\left(\tilde{\mathbf{u}} - \mathbf{u}\right)^{n}\right]. \tag{6.33}$$

This is solved at the end of each nonlinear iteration to update the filtered advecting velocity.

6.3.3 Results

Figure 6.4 shows the evolution of the meridional velocity field for the time-filtered equations alongside the standard vector invariant results. The time-filtered solution diverged shortly after day nine.

There are two things to note about the effect of the time filtering. The first is that it does result in an extended growth period, which is particularly noticeable in the L_∞ norm showing a smooth growth instead of the abrupt change after day four of the standard model. The second, and much more worrying, is that of changing the balanced evolution after day six, which manifests itself as a secondary oscillation superposed on the Eady wave in the evolution of the RMS norm.

It is likely that the lack of conservation of PV is responsible for the incorrect evolution of the balanced solution, whilst the time filtering will also be predominantly affecting the small scale, high frequency IGWs. If these waves are being incorrectly modelled, for example being artificially slowed down through the filtering, then this will also alter the large scale solution, of which they are a part.

It is worth remarking that whilst both of the filtering methods will alter the dispersion relation, the Lagrangian-averaged model stops the coupling of the retarded waves back into the large scale solution. In contrast, and with the caveat of no dispersion analysis having been carried out, it looks likely that the time filtered model slows and damps the high wavenumber waves, without altering the coupling.

The problems encountered with the time-filtered model, in particular the instability and lack of conservation of PV, preclude it from operational

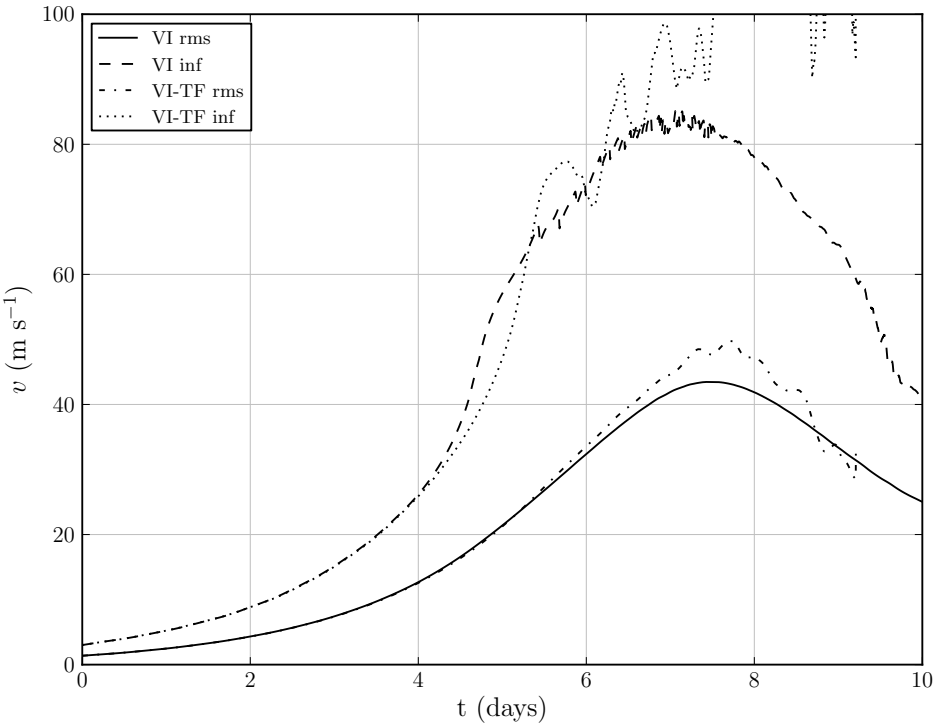

Figure 6.4: *Evolution of norms of the meridional velocity field for the standard vector invariant (VI) and the time-filtered advection vector invariant (VI-TF) at doubled resolution and* $\beta = 1$. *Time-filtered scheme used a filtering timescale of* $\Delta = 4/f$.

use. It does, though, provide some insight into the discrepancy between the amplitudes of the Eulerian and Lagrangian solutions, and supports the idea that if it possible to maintain the linear and nonlinear growth periods for longer then the Eulerian solutions could more closely match the limit solution.

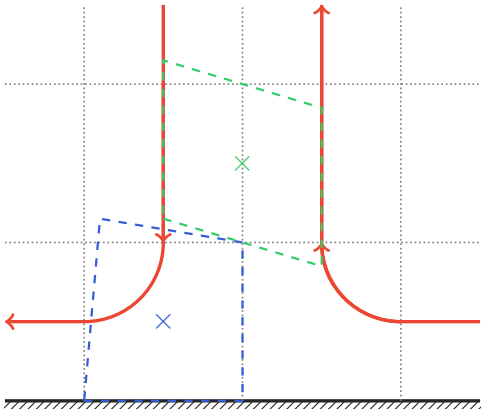

Figure 6.5: *A schematic of the streamlines in an idealised, and rather extreme, front. Two pseudo control-volumes are highlighted, showing the effect of the deformation and the difficulty in maintaining volume preservation.*

6.4 Modifications to semi-Lagrangian

As noted in Section 3.2.1 the space and time accuracy for the semi-Lagrangian method are intrinsically linked, and so any reduction in errors would likely improve the whole solution, and not just the spatial representation.

It is widely accepted that the dominant source of error within the semi-Lagrangian method is due to the spatial interpolation, (Staniforth and Côté, 1991). For the relatively benign standard suite of test cases, as touched upon in Section 3.5 when developing the models used in this thesis, it is likely that this is indeed the case. In the velocity fields presented in this thesis, though, it is likely that there are significant errors being made in the trajectories and calculation of departure points.

Figure 6.5 shows a schematic of the flow in the frontal region on a staggered grid. Even if the trajectories could be tracked exactly then it is likely that there would be large distortions in the shape of the departure cells, which would be difficult to preserve their volume.

6.4.1 Departure point modifications

Two modifications to the standard implicit centred departure point calculation are discussed below.

Monge-Ampère correction

The Monge-Ampère correction to semi-Lagrangian trajectory calculation was presented in Cossette and Smolarkiewicz (2011). The idea behind the method is conceptually quite simple; the departure points are adjusted in a global manner to enforce volume conservation. The resulting second-order

nonlinear elliptic problem is a form of Monge-Ampère equation (MAE). Methods for the solution to the MAE have been presented in Froese (2012); Feng et al. (2013).

The correction potential was solved at cell centres, and then bilinearly interpolated to the departure points for each of the fields at the staggered variable locations. This is likely to introduce an error, but keeps the computational cost low as it only requires one solve of the MAE as opposed to one per variable location.

High-order explicit trajectory calculation

Another idea for improving the departure point calculations is to use a high-order "explicit" calculation, in which the trajectories are integrated backwards in time using the latest available $\mathbf{u}^{n+1,k}$.

This method was implemented using a standard fourth-order Runge-Kutta integrator with the velocities calculated at the intermediate stages using cubic quasi-monotone interpolation.

Results

Table 6.1 shows a comparison of the suggested departure point methods alongside the implicit centred method and the Eulerian results at day four, and Table 6.2 shows the same at day five, for the conservation experiment described in Section 5.6.

The results for the two modified departure point methods are mixed. Comparing to the control neither method seems to consistently reduce the conservation errors, with RK4 being worse at day four and the MA correction being worse at day five. It is likely that the interpolation in the MA correction is costly at the levels of conservation investigated here, and so the results presented here should not completely discount it as an option to be considered.

None of the semi-Lagrangian methods, even with the modified departure points, were able to get close to the conservation values of the Eulerian methods. This is clearly disappointing, but does lead the investigation to consider alternatives to the traditional centred Lagrange polynomial interpolation.

6.4.2 Further upwinding interpolation

In addition to improving the departure point calculation a possibility might be to increase the "upwinding" in the scheme by biasing the interpolation stencil in the upwind direction. This is illustrated in Figure 6.6.

Figure 6.6 highlights some of the problems that could be occurring using the semi-Lagrangian method with centred interpolation and a low Courant number ($C < 1$). It is quite likely that close to the boundary, and where the

Table 6.1: *Comparison of conservation properties for the control (IC, implicit centred), Monge-Ampère correction (MA) and high-order explicit (RK4) departure point calculations alongside the Eulerian methods, at day four. For the semi-Lagrangian methods the number refers to the spatial interpolation order, whilst QM denotes use of the quasi-monotone limiter. For the Eulerian method the labels are first-order upwind (UW), third-order upwind (UW3), third-order upwind with min-mod limiter (UW3 MM) and third-order upwind with superbee limiter (UW3 SB). Experiment described in Section 5.6.*

	$\mathcal{C}_1$	$\mathcal{C}_2$	$\mathcal{C}_V$
IC			
1	-1.478×10^{-10}	-3.036×10^{-07}	-7.509×10^{-06}
3	8.846×10^{-10}	8.167×10^{-08}	-9.817×10^{-10}
3QM	8.828×10^{-10}	8.025×10^{-08}	-5.303×10^{-09}
5	5.458×10^{-10}	8.158×10^{-08}	-2.480×10^{-09}
5QM	5.435×10^{-10}	8.005×10^{-08}	-6.778×10^{-09}
MA			
1	-1.998×10^{-10}	-2.955×10^{-07}	-7.510×10^{-06}
3	8.319×10^{-10}	8.972×10^{-08}	-9.820×10^{-10}
3QM	8.261×10^{-10}	8.831×10^{-08}	-5.304×10^{-09}
5	4.865×10^{-10}	8.964×10^{-08}	-2.480×10^{-09}
5QM	4.898×10^{-10}	8.810×10^{-08}	-6.779×10^{-09}
RK4			
1	-3.277×10^{-09}	-3.152×10^{-07}	-7.508×10^{-06}
3	-2.336×10^{-09}	6.996×10^{-08}	-9.811×10^{-10}
3QM	-2.337×10^{-09}	6.854×10^{-08}	-5.303×10^{-09}
5	-2.674×10^{-09}	6.987×10^{-08}	-2.481×10^{-09}
5QM	-2.676×10^{-09}	6.834×10^{-08}	-6.779×10^{-09}
Eulerian			
UW	-4.844×10^{-11}	1.305×10^{-08}	-1.934×10^{-06}
UW 3	-5.502×10^{-11}	1.161×10^{-08}	-1.829×10^{-09}
UW3 MM	1.466×10^{-10}	1.268×10^{-08}	-1.609×10^{-08}
UW3 SB	3.359×10^{-10}	1.248×10^{-08}	7.704×10^{-09}

Table 6.2: *As Table 6.1 but for day five.*

	$\mathcal{C}_1$	$\mathcal{C}_2$	$\mathcal{C}_V$
IC			
1	5.240×10^{-07}	1.093×10^{-05}	-2.165×10^{-05}
3	-5.501×10^{-08}	3.147×10^{-06}	-6.908×10^{-07}
3QM	-3.136×10^{-08}	2.928×10^{-06}	-1.227×10^{-06}
5	-9.404×10^{-08}	2.497×10^{-06}	-9.104×10^{-08}
5QM	-6.350×10^{-08}	1.808×10^{-06}	-9.309×10^{-07}
MA			
1	4.304×10^{-07}	1.097×10^{-05}	-2.163×10^{-05}
3	-1.506×10^{-07}	3.200×10^{-06}	-6.944×10^{-07}
3QM	-1.273×10^{-07}	2.983×10^{-06}	-1.232×10^{-06}
5	-1.899×10^{-07}	2.552×10^{-06}	-9.591×10^{-08}
5QM	-1.605×10^{-07}	1.871×10^{-06}	-9.345×10^{-07}
RK4			
1	5.695×10^{-07}	1.066×10^{-05}	-2.165×10^{-05}
3	-4.142×10^{-08}	2.552×10^{-06}	-5.090×10^{-07}
3QM	-1.976×10^{-08}	2.319×10^{-06}	-1.073×10^{-06}
5	-8.368×10^{-08}	1.809×10^{-06}	7.516×10^{-08}
5QM	-5.392×10^{-08}	1.122×10^{-06}	-8.143×10^{-07}
Eulerian			
UW	-7.368×10^{-09}	4.331×10^{-07}	-6.453×10^{-06}
UW 3	-7.192×10^{-09}	4.341×10^{-07}	-6.583×10^{-07}
UW3 MM	-5.102×10^{-09}	4.351×10^{-07}	-1.967×10^{-06}
UW3 SB	-5.250×10^{-09}	4.393×10^{-07}	-1.172×10^{-06}

Figure 6.6: *Illustration of standard interpolation stencil centred about the departure point (a) and one which is biased in the horizontal upwind direction (b). A discontinuity is represented by the dashed red line, and cells crossing the discontinuity are highlighted in (a).*

front is most intense, the stencils are crossing both sides of the front. Numerically this leads to large oscillations, as found in Cullen (2008), and shows that the interpolation limiter must be making large changes in this area. This is also worrying from a physical perspective, in which the interpolation process is using information from both sides of the contact discontinuity.

Biasing the stencil in the upwind direction then seems appealing since it would not cross this discontinuity. Unfortunately non-centred Lagrange polynomial interpolation is unstable, and so could not be used as outlined above. One option, which has been used in the context of designing high-order finite-difference stencils close to boundaries, is to use use constrained optimisation to calculate the interpolation weights, (Desvigne et al., 2010).

6.4.3 Conservative semi-Lagrangian schemes

The final suggestion with regards to the semi-Lagrangian method would be to use a formally conservative scheme such as SLICE, (Zerroukat et al., 2002), or CSLAM, (Lauritzen et al., 2010b). A conservative semi-Lagrangian (CSL) scheme would hopefully perform as well as, if not better, than the Eulerian methods in the conservation experiments.

A comparison between conservative semi-Lagrangian and Eulerian schemes would be interesting to see if a CSL method is better at describing the Lagrangian flow characteristics. The results presented in this thesis, in that the semi-Lagrangian scheme generally gave a higher amplitude than the Eulerian schemes, would suggest that a CSL method should maintain this larger intensity and improved predictability but at lower resolution.

An improvement in conservation for the semi-Lagrangian method would

improve its performance at lower resolutions. If the conservative semi-Lagrangian schemes were comparable to, or even better than, the Eulerian methods, then there would have to be a compromise made between accuracy and efficiency. Ultimately operational requirements will dictate this, but the results of this thesis have highlighted how the accuracy can be improved, as well as the motivation for doing so in terms of the improvement on the large scale solution.

6.5 Conservation of potential vorticity

In the following section the derivation of a potential vorticity consistent scheme is shown. The scheme is termed PV consistent since it should conserve PV during advection, whilst allowing the forcing terms to control the generation and destruction.

This method is different to a formally PV conserving scheme such as the nonlinear balanced model used in the frontogenesis experiments of Ziemianski and Thorpe (2002). The PV is allowed to change from its initial value, but not through spurious diffusion within the transport scheme. Since conservation errors have been shown to be significant, it is hoped that this method could improve predictability at much lower resolution.

6.5.1 Differential geometry

Some use of differential geometry will be required in the derivation of the equations that will be used to form the PV consistent scheme. This is because it is easier to work with the equations in this form and then convert back to familiar vector calculus after the manipulations have been carried out. The commutativity of the exterior derivative with the Lie derivative is particularly useful in this regard.

Preliminaries

For a detailed treatment of differential geometry and exterior calculus the interested reader is referred to Perot and Zusi (2014) and the references contained therein.

Firstly the exterior derivative of a k-form ω is given by

$$\mathrm{d}\omega = \sigma,$$

where σ is a $(k+1)$-form. The interior product of a $(k+1)$-form σ with a vector $\mathbf{v}$ is given by

$$\iota_{\mathbf{v}}\sigma = \omega,$$

where ω is a k-form. The Lie derivative is given by

$$\mathcal{L}_{\mathbf{v}}\omega = \iota_{\mathbf{v}}\mathrm{d}\omega + \mathrm{d}\left(\iota_{\mathbf{v}}\omega\right). \tag{6.34}$$

The Lie derivative commutes with the exterior derivative such that

$$\mathrm{d}\left(\mathcal{L}_{\mathbf{v}}\omega\right) = \mathcal{L}_{\mathbf{v}}\left(\mathrm{d}\omega\right).$$

Formulation in vertical slice

Since the vertical slice is a two-dimensional model this limits the highest form permitted to two. In the two-dimensional model ω represents a zero-form, $\mathbf{u}\cdot\mathrm{d}\mathbf{x}$ a one-form and $\zeta\cdot\mathrm{d}s$ a two-form. The exterior derivative and interior product are given as

$$\mathrm{d}\omega = \nabla\omega\cdot\mathrm{d}\mathbf{x}; \quad \mathrm{d}\left(\mathbf{u}\cdot\mathrm{d}\mathbf{x}\right) = \zeta\cdot\mathrm{d}s,$$

and

$$\iota_{\mathbf{v}}\left(\mathbf{u}\cdot\mathrm{d}\mathbf{x}\right) = \left(\mathbf{v}\cdot\mathbf{u}\right); \quad \iota_{\mathbf{v}}\left(\zeta\cdot\mathrm{d}s\right) = \mathbf{v}^{\perp}\zeta\cdot\mathrm{d}\mathbf{x}.$$

6.5.2 Geometrical formulation of the Eady model

Following Cotter and Holm (2013) the Eady model can be written in geometrical form as

$$\begin{aligned}
\left(\partial_t + \mathcal{L}_{\mathbf{u}}\right)\left(\mathbf{u}\cdot\mathrm{d}\mathbf{x}\right) &= -\mathrm{d}\phi - \left(v+fx\right)\mathrm{d}v - \theta\mathrm{d}\gamma, && (6.35)\\
\left(\partial_t + \mathcal{L}_{\mathbf{u}}\right)\left(v+fx\right) &= -s\gamma, && (6.36)\\
\left(\partial_t + \mathcal{L}_{\mathbf{u}}\right)\mathrm{d}\theta &= -s\mathrm{d}v, && (6.37)\\
\nabla\cdot\mathbf{u} &= 0. && (6.38)
\end{aligned}$$

Making use of the fact that d commutes with the Lie derivative it is possible to use

$$\begin{aligned}
\left(\partial_t + \mathcal{L}_{\mathbf{u}}\right)\left[\left(v+fx\right)\mathrm{d}\theta\right] &= \mathrm{d}\theta\left(\partial_t + \mathcal{L}_{\mathbf{u}}\right)\left(v+fx\right) + \left(v+fx\right)\left(\partial_t + \mathcal{L}_{\mathbf{u}}\right)\mathrm{d}\theta,\\
&= -s\left[\gamma\mathrm{d}\theta + \left(v+fx\right)\mathrm{d}v\right], && (6.39)
\end{aligned}$$

with the momentum equation to get

$$\left(\partial_t + \mathcal{L}_{\mathbf{u}}\right)\left[\mathbf{u}\cdot\mathrm{d}\mathbf{x} - \frac{1}{s}\left(v+fx\right)\mathrm{d}\theta\right] = -\mathrm{d}\phi. \tag{6.40}$$

As shown by Cotter and Holm taking the exterior derivative of Equation (6.40) gives

$$\left(\partial_t + \mathcal{L}_{\mathbf{u}}\right)\left[\zeta\cdot\mathrm{d}s - \frac{1}{s}\mathrm{d}\left(v+fx\right)\wedge\mathrm{d}\theta\right] = 0, \tag{6.41}$$

which when written in vector calculus notation

$$\frac{\partial\tilde{q}}{\partial t} + \nabla\cdot\left(\mathbf{u}\tilde{q}\right) = 0, \tag{6.42}$$

is the equation for the evolution of the potential vorticity, where

$$\tilde{q} = \zeta - \frac{1}{s}\nabla^{\perp}\left(v+fx\right)\cdot\nabla\theta,$$

is the PV scaled by a factor of s.

6.5.3 Vector calculus formulation

Expanding out the Lie derivative in Equation (6.40) gives the following contributions. The first is from the momentum

$$\begin{aligned}\mathcal{L}_{\mathbf{u}}\left(\mathbf{u}\cdot\mathrm{d}\mathbf{x}\right) &= \mathbf{u}^{\perp}\zeta+\nabla\left|\mathbf{u}\right|^{2},\\ &= \left(\mathbf{u}\cdot\nabla\right)\mathbf{u}+\frac{1}{2}\nabla\left|\mathbf{u}\right|^{2}.\end{aligned}\tag{6.43}$$

The second is from the meridional velocity and potential temperature

$$\mathcal{L}_{\mathbf{u}}\left[\left(v+fx\right)\mathrm{d}\theta\right]=\mathbf{u}^{\perp}\left[\nabla^{\perp}\left(v+fx\right)\cdot\nabla\theta\right]+\nabla\left[\left(v+fx\right)\mathbf{u}\cdot\nabla\theta\right].\tag{6.44}$$

Substituting in the above expansions of the Lie derivative into Equation (6.40) gives

$$\begin{aligned}\frac{\partial}{\partial t}\left[\mathbf{u}-\frac{1}{s}\left(v+fx\right)\nabla\theta\right] &+ \mathbf{u}^{\perp}\left[\zeta-\frac{1}{s}\nabla^{\perp}\left(v+fx\right)\cdot\nabla\theta\right]=\\ &- \nabla\left[\phi+\left|\mathbf{u}\right|^{2}-\frac{1}{s}\left(v+fx\right)\mathbf{u}\cdot\nabla\theta\right].\end{aligned}\tag{6.45}$$

Rewriting the combined momentum equation into a clearer form gives

$$\frac{\partial\mathbf{u}}{\partial t}+\left(\mathbf{u}\tilde{q}\right)^{\perp}=-\nabla\tilde{\phi}+\frac{1}{s}\frac{\partial}{\partial t}\left[\left(v+fx\right)\nabla\theta\right],\tag{6.46}$$

where $\tilde{q}$ is the same scaled potential vorticity as conserved in Equation (6.42) and

$$\tilde{\phi}=\left[\phi+\left|\mathbf{u}\right|^{2}-\frac{1}{s}\left(v+fx\right)\mathbf{u}\cdot\nabla\theta\right],$$

is the modified geopotential variable.

6.5.4 PV consistent equations

Combining the momentum equation from the previous Section gives the PV consistent equations as

$$\frac{\partial u}{\partial t}-w\tilde{q}+\frac{\partial\tilde{\phi}}{\partial x}-\frac{1}{s}\frac{\partial}{\partial t}\left[\left(v+fx\right)\frac{\partial\theta}{\partial x}\right]=0,\tag{6.47}$$

$$\frac{\partial v}{\partial t}+\mathbf{u}\cdot\nabla v+fu+s\frac{g}{\theta_{0}}\left(z-\frac{H}{2}\right)=0,\tag{6.48}$$

$$\frac{\partial w}{\partial t}+u\tilde{q}+\frac{\partial\tilde{\phi}}{\partial z}-\frac{1}{s}\frac{\partial}{\partial t}\left[\left(v+fx\right)\frac{\partial\theta}{\partial z}\right]=0,\tag{6.49}$$

$$\frac{\partial\theta}{\partial t}+\mathbf{u}\cdot\nabla\theta+sv=0,\tag{6.50}$$

$$\frac{\partial u}{\partial x}+\frac{\partial w}{\partial z}=0.\tag{6.51}$$

Carrying out the semi-implicit discretisation gives

$$\begin{bmatrix} \varsigma\mathsf{I}+\vartheta\mathsf{L} & \vartheta\mathsf{G} \\ \mathsf{D} & 0 \end{bmatrix} \begin{bmatrix} \mathbf{S}^{n+1} \\ \mathbf{p}^{n+1} \end{bmatrix} + \begin{bmatrix} \vartheta\mathbf{N}^{n+1} \\ \mathbf{0} \end{bmatrix} = \begin{bmatrix} \varsigma\mathsf{I}-(1-\vartheta)\,\mathsf{L} & -(1-\vartheta)\,\mathsf{G} \\ 0 & 0 \end{bmatrix} \begin{bmatrix} \mathbf{S}^{n} \\ \mathbf{p}^{n} \end{bmatrix} + \begin{bmatrix} \vartheta\mathbf{N}^{n} \\ \mathbf{0} \end{bmatrix} + \begin{bmatrix} \mathbf{F}^{n+1/2} \\ \mathbf{0} \end{bmatrix}, \tag{6.52}$$

where the linear and nonlinear terms are now

$$\mathsf{L} = \begin{bmatrix} \cdot & \cdot & \cdot & \cdot \\ f\mathsf{I} & \cdot & \cdot & \cdot \\ \cdot & \cdot & \cdot & \cdot \\ \cdot & s\mathsf{R} & \cdot & \cdot \end{bmatrix},$$

and

$$\mathbf{N} = \begin{bmatrix} -w\tilde{q} & -\varsigma\,(v+fx)\,\partial_x\theta/s \\ \mathbf{u}\cdot\nabla v & \\ u\tilde{q} & -\varsigma\,(v+fx)\,\partial_z\theta/s \\ \mathbf{u}\cdot\nabla\theta & \end{bmatrix}.$$

Adopting the same notation as in the Newton iteration so that

$$L^{n+1} = \begin{bmatrix} \varsigma\mathsf{I}+\vartheta\mathsf{L} & \vartheta\mathsf{G} \\ \mathsf{D} & 0 \end{bmatrix} \begin{bmatrix} \mathbf{S}^{n+1} \\ \mathbf{p}^{n+1} \end{bmatrix} + \begin{bmatrix} \vartheta\mathbf{N}^{n+1} \\ \mathbf{0} \end{bmatrix}$$

and

$$R^{n} = \begin{bmatrix} \varsigma\mathsf{I}-(1-\vartheta)\,\mathsf{L} & -(1-\vartheta)\,\mathsf{G} \\ 0 & 0 \end{bmatrix} \begin{bmatrix} \mathbf{S}^{n} \\ \mathbf{p}^{n} \end{bmatrix} + \begin{bmatrix} \vartheta\mathbf{N}^{n} \\ \mathbf{0} \end{bmatrix} + \begin{bmatrix} \mathbf{F}^{n+1/2} \\ \mathbf{0} \end{bmatrix},$$

gives the iterative method as

$$\begin{bmatrix} \varsigma\mathsf{I}+\vartheta\mathsf{L} & \vartheta\mathsf{G} \\ \mathsf{D} & 0 \end{bmatrix} \begin{bmatrix} \mathbf{S}' \\ \mathbf{p}' \end{bmatrix} = R^{n} - L^{n+1,k}, \tag{6.53}$$

along with

$$\begin{bmatrix} \mathbf{S}^{n+1,k+1} \\ \mathbf{p}^{n+1,k+1} \end{bmatrix} = \begin{bmatrix} \mathbf{S}^{n+1,k} \\ \mathbf{p}^{n+1,k} \end{bmatrix} \begin{bmatrix} \mathbf{S}' \\ \mathbf{p}' \end{bmatrix},$$

and the residual definition as

$$R^{n} - L^{n+1,k} = -\begin{bmatrix} \mathbf{r}_{\mathbf{S}}^{k} \\ \mathbf{r}_{\mathbf{p}}^{k} \end{bmatrix}.$$

6.5.5 PV algorithm

The algorithm for the PV-consistent scheme is given in Algorithm 6.1. Whilst the scheme was not implemented owing to time constraints the proposed algorithm is still presented.

1 # Explicit contribution
2 $$\begin{bmatrix} R^n_{\mathbf{S}} \\ R^n_{\mathbf{p}} \end{bmatrix} \leftarrow \begin{bmatrix} \varsigma\mathsf{I} - (1-\vartheta)\,\mathsf{L} & -(1-\vartheta)\,\mathsf{G} \\ 0 & 0 \end{bmatrix} \begin{bmatrix} \mathbf{S}^n \\ \mathbf{p}^n \end{bmatrix} - \begin{bmatrix} (1-\vartheta)\,\mathbf{N}^n \\ \mathbf{0} \end{bmatrix} - \begin{bmatrix} \mathbf{F}^{n+1/2} \\ \mathbf{0} \end{bmatrix}$$
3 $$\begin{bmatrix} \mathbf{S}^{n+1,1} \\ \mathbf{p}^{n+1,1} \end{bmatrix} \leftarrow \begin{bmatrix} \mathbf{S}^n \\ \mathbf{p}^n \end{bmatrix}$$
4 **for** $k = 1, \ldots, m$ **do**
5 # Linear terms
6 $$\begin{bmatrix} L^k_{\mathbf{S}} \\ L^k_{\mathbf{p}} \end{bmatrix} \leftarrow \begin{bmatrix} \varsigma\mathsf{I} + \vartheta\mathsf{L} & \vartheta\mathsf{G} \\ \mathsf{D} & 0 \end{bmatrix} \begin{bmatrix} \mathbf{S}^{n+1,k} \\ \mathbf{p}^{n+1,k} \end{bmatrix}$$
7 # Advection & nonlinear terms
8 $$\begin{bmatrix} L^k_{\mathbf{S}} \\ L^k_{\mathbf{p}} \end{bmatrix} \leftarrow \begin{bmatrix} L^k_{\mathbf{S}} \\ L^k_{\mathbf{p}} \end{bmatrix} + \begin{bmatrix} \mathbf{N}^{n+1,k} \\ \mathbf{0} \end{bmatrix}$$
9 # Residual calculation
10 $$\begin{bmatrix} \mathbf{r}^k_{\mathbf{S}} \\ \mathbf{r}^k_{\mathbf{p}} \end{bmatrix} \leftarrow \begin{bmatrix} R^n_{\mathbf{S}} \\ R^n_{\mathbf{p}} \end{bmatrix} - \begin{bmatrix} L^{n+1,k}_{\mathbf{S}} \\ L^{n+1,k}_{\mathbf{p}} \end{bmatrix}$$
11 **if** $\left\|\mathbf{r}^k_{\mathbf{S}}\right\| \leq \varepsilon$ **then**
12 # Solution converged
13 $$\begin{bmatrix} \mathbf{S}^{n+1} \\ \mathbf{p}^{n+1} \end{bmatrix} \leftarrow \begin{bmatrix} \mathbf{S}^{n+1,k} \\ \mathbf{p}^{n+1,k} \end{bmatrix}$$
14 **else**
15 # Continue iterations
16 $$\begin{bmatrix} \mathbf{S}' \\ \mathbf{p}' \end{bmatrix} \leftarrow \begin{bmatrix} \varsigma\mathsf{I} + \vartheta\mathsf{L} & \vartheta\mathsf{G} \\ \mathsf{D} & 0 \end{bmatrix}^{-1} \begin{bmatrix} \mathbf{r}^k_{\mathbf{S}} \\ \mathbf{r}^k_{\mathbf{p}} \end{bmatrix}$$
17 $$\begin{bmatrix} \mathbf{S}^{n+1,k+1} \\ \mathbf{p}^{n+1,k+1} \end{bmatrix} \leftarrow \begin{bmatrix} \mathbf{S}^{n+1,k} \\ \mathbf{p}^{n+1,k} \end{bmatrix} + \begin{bmatrix} \mathbf{S}' \\ \mathbf{p}' \end{bmatrix}$$

Algorithm 6.1: *Potential vorticity conservative consistent algorithm for the Eady problem.*

It is difficult to predict *a priori* how the final scheme would behave. There are clear parallels to be made with the vector invariant form, in terms of the conservative perpendicular flux of a scalar quantity appearing in the momentum equations.

It is likely that the balance laws would be much harder to satisfy owing to the additional time derivatives in the momentum equations. For the ageostrophic and nonhydrostatic accelerations to remain small this would require the balance of three terms; perpendicular PV flux, geopotential gradient and absolute momentum time derivative.

Whilst the scheme is appealing in principle, the techniques used to obtain the final form are not applicable to the full three-dimensional system in which the background profile in potential temperature is not separable. The scheme is of limited operational use, but, as a research model, might prove insightful in modelling the PV dynamics in an Eulerian frame.

6.6 Summary

This chapter has presented several schemes of varying levels of development that have been chosen to attempt to mitigate some of the shortcomings of the results of the previous chapter. These have primarily been focused around attempting to improve conservation through regularising the advecting velocity field, so that it is easier to maintain conservation with a smoother velocity field.

The Lagrangian-averaged α-model regularises the advecting velocity field through a spatially smoothing Helmholtz problem. By having a conserved energy and PV, as well as converging to the original equations as $\alpha \to 0$, the α-model should be well suited to the Eady problem and long term predictability.

The α-model did improve the predictability at low Rossby number, in that the quasi-periodic lifecycles were not slowed down as much as in the standard model. The energetics, though, were still not improved to the level of the limit solution, and this was attributed to the fact that the baroclinic energy conversion was already well resolved in the standard model.

The advecting velocity field was then regularised by a filter in time, with the aim of preserving the growth phase for longer. This did result in an improvement in the peak amplitude, but not in a stable or robust manner. Once the front was intense the effect of the filter was to alter the treatment of the high wavenumber waves, which coupled with the lack of PV conservation, ultimately degraded the large scale solution.

Some modifications to improve conservation properties within the basic semi-Lagrangian scheme were considered, including modifying departure points and interpolation methods. Of these the most promising is likely to be a conservative semi-Lagrangian scheme, whilst modifying departure

points may still prove beneficial if implemented without interpolation.

Finally a scheme which is consistent with conservative transport of PV was presented. Although this was not implemented it would be interesting to see whether this scheme could maintain balance between three large terms, and in doing so improve the generation and removal of the PV filaments associated with the front.

Of the methods considered in this chapter the Lagrangian-averaged model looks to be the most promising. It has the desirable characteristics of conservation properties required for long time solutions, as well as limiting small scale features by removing their coupling back into the large scale solution.

Only the time-filtered model increased the amplitude of the wave noticeably, but the solution was not well behaved once the front was intense. Artificially maintaining the linear growth regime in this way is clearly not the right tactic in reproducing the limit solution.

Chapter 7

Conclusions

What satisfaction is there in being able to calculate tomorrow's weather if it takes us a year to do it?
To this I can only reply: I hardly hope to advance even so far as this... If only the calculation shall agree with the facts, the scientific victory will be won.

V. Bjerknes (1914)

Contents

7.1 Introduction

This thesis has focused on one source of model error within numerical weather prediction by looking at the effect of errors made in the idealised Eady model of frontogenesis. Fronts, despite their small spatial width, are part of the large scale solution. Any errors made in the modelling of fronts will therefore affect the large scale solution.

7.1.1 Thesis synopsis

This section gives a synopsis of the material presented in this thesis, whilst the research objectives are restated in the following section.

Chapter 2 introduced vertical slice models as a simplified setting in which to investigate atmospheric frontogenesis. Although real fronts are evidently three-dimensional, the use of the two-dimensional models was supported by excellent agreement between observations and predictions using the slice models, as demonstrated by Ogura and Portis (1982) and Blumen (1980).

Two key mechanisms, identified by Hoskins and Bretherton (1972), of deformation and vertical shear were introduced. Results common to both models were presented, which included the tendency of model fronts to reduce in scale, create intense gradients in the temperature and along-front wind, and control the in-slice circulation structure.

Results for the Eady model were divided; there was a large gap between results using Eulerian and Lagrangian methods, but also in terms of whether or not the post-collapse evolution was predictable or not. Both Eulerian and Lagrangian methods were able to capture the initial pre-collapse evolution. The inviscid fully Lagrangian method of Cullen (2006) showed a clear advantage in the post-collapse behaviour, with a much more intense front forming and showing highly predictable quasi-periodic lifecycles for several oscillations; the Eulerian methods of Nakamura and Held (1989) and Nakamura (1994) did not.

The Lagrangian model of Cullen (2006) solved the semigeostrophic equations in isentropic coordinates through enforcing balance and satisfying conservation laws exactly. In the dual space the initial geostrophic potential vorticity was conserved for all time, but the boundaries of the domain were able to deform. This deformation was vital in explaining the key solution properties of how fluid parcels can lift away from the boundary into the interior (Koshyk and Cho, 1992); the structure of the front as a contact discontinuity (Cullen and Purser, 1984); and the source of the PV filaments in the physical domain (Cullen, 2006).

The Euler equations were shown to converge to the semigeostrophic equations, and the results of Cullen (2006) represented the limit solution at $\mathrm{Ro} = 0$. For some finite Rossby number one would expect unbalanced motion in the form of inertia-gravity waves. These waves were found both

experimentally in Gall et al. (1987) and Snyder et al. (1993), but also in the observations of Sanders (1955) and Ogura and Portis (1982). This process of generating waves at a front in an otherwise balanced flow was termed "spontaneous balance adjustment" in the review of Plougonven and Zhang (2014). For the semigeostrophic limit to be valid these waves should decrease as $\mathrm{Ro} \to 0$.

The survey of the existing results presented in Chapter 2 showed two very different characteristics to solutions of the Eady frontogenesis problem. Whilst the inviscid Lagrangian semigeostrophic solutions were robust and highly predictable, the fixed grid Euler solutions were very variable. The Eady problem had been used in an asymptotic convergence study of Cullen (2008), but the lack of energy conservation and not achieving the theoretical convergence rate after collapse meant that further investigation was required. These results naturally led to the research objectives this thesis.

Chapter 3 introduced the numerical methods used in the experiments of this thesis. The details of the transport schemes and the iterative semi-implicit discretisations were covered. Code verification results for several common test cases were presented which showed the expected behaviour and showed the numerical methods to be correctly implemented.

The problem specification of the Eady model of frontogenesis was covered in Chapter 4. The Eady model was shown to correspond to a simplification of the three-dimensional Boussinesq system in which a vertically sheared background profile eliminated the meridional variation, and meant that the problem could be solved in a two-dimensional model.

The incompressible Boussinesq Eady equations were shown to converge to the semigeostrophic Eady equations at second-order in the Rossby number. The more restrictive requirement of $\mathrm{Ro} = \mathcal{O}\left(\delta^2\right)$ needed for second-order convergence of the three-dimensional system was not necessary in the vertical slice configuration. Both the incompressible Boussinesq and the semigeostrophic Eady equations were shown to have a conserved energy integral and potential vorticity, a necessary requirement for long time solutions as discussed in Cullen (2007a).

The numerical techniques introduce in Chapter 3 were tailored to the Eady model. In particular the choice of C-grid and Charney-Phillips variable staggering, primarily chosen by the need for stability (Cullen, 1989), and the relatively small problem size was fortuitous in permitting the use of a direct solution method.

Since the front forms on the boundary itself, (Hoskins and Bretherton, 1972), much consideration was given to the correct treatment of the boundary conditions under advection. The potential temperature, a Lagrangian conserved quantity for the semigeostrophic solution, was not stored on the boundary. This meant that the coupling between the meridional velocity and potential temperature was not compromised by either extrapolating values or slowing down motion along the boundary.

The effects of the rescaling in the asymptotic convergence framework of Cullen (2008) was discussed in terms of the nondimensional parameters, primarily the Rossby and Froude numbers. An extension of this method was presented in which the aspect ratio was preserved, thereby causing the hydrostatic imbalance to reduce at the same rate as the geostrophic imbalance. Both rescaling methods suggested that the energy and potential vorticity should get closer to their geostrophic counterparts.

The asymptotic convergence framework as $\beta \to 0$ (equivalently $\mathrm{Ro} \to 0$) was then used to investigate the linearised Eady model. The nonlinearity within the Eady problem is contained entirely within the advective terms, and so the advecting velocity was replaced with a stationary value given by the background shear. At very small Rossby number a small amount of decentering in the semi-implicit scheme greatly improved the representation of balance.

The main results of this thesis, and the answers to the original research questions, were presented in Chapter 5. This began with a description of the initial pre-collapse stage of the solution, and the results presented agreed well with existing Eulerian data such as Nakamura and Held (1989), although the SISL numerical method of this thesis appeared to be slightly more dissipative. None of the methods, though, were able to reproduce the intensity of the limit solution; all the results were half the amplitude of the Cullen (2006) solution.

The post-collapse evolution was discussed in terms of the balance and energetics. The results showed several baroclinic lifecycles of exchange of potential and kinetic energy. The total energy was conserved over the first of these lifecycles, although began to drift by the third. Considering that the scheme was not formally energy conserving this result was not guaranteed, especially given the discontinuous nature of the solution.

The asymptotic convergence experiments were carried out on the full nonlinear Eady problem, and the theoretical second-order convergence rate was achieved after frontal collapse. The extended rescaling method was tested, but since the motion was essentially hydrostatic no further benefit from maintaining the aspect ratio was observed.

The rescaled solutions at doubled resolution showed excellent predictability for the three different numerical methods used in this thesis. These results suggested that previous work such as Nakamura and Held (1989) and Nakamura (1994) were under-resolved, owing to the control results of this thesis showing much more variability.

The solution was discussed from a Lagrangian perspective, in which the deformation and lifting-off of fluid from the boundaries was clearly shown. The balanced component of the solution, given by the large scale potential vorticity distribution, was shown to approach what would be expected of the limit solution: the negative regions reduced, in both area and extent in to the domain, as well as there being a clear reduction in the evidence of

inertia-gravity waves.

Analysis of the transport schemes using an experiment based on a representative velocity field showed all of the methods to deteriorate in performance once the front was intense. Systematic errors made in the conservation and dissipation of transported fields were identified as being a leading cause in the inability to reproduce the limit solution given by enforcement of balance and Lagrangian conservation laws. Although balance was satisfied in this thesis, conservation was clearly not.

Attempts to improve conservation formed the theme for Chapter 6. The Lagrangian-averaged Navier-Stokes-α model, through regularising the advecting velocity field in space, showed good potential in improving the long term solution behaviour. A time-filtered model was considered, which did increase the amplitude of the wave, but ultimately the lack of a conserved potential vorticity nullified any beneficial effect. Several modifications to the existing semi-Lagrangian scheme were presented, of which using a conservative method was identified as being most likely to lead to further improvements in predictability. Finally a scheme which would conserve potential vorticity in a similar manner to the vector invariant scheme was developed but not implemented.

7.1.2 Research objectives

The original research objectives of Section 1.3 are restated here for convenience.

① Is it possible to maintain a balanced solution despite the presence of a discontinuity?

② Can the long term predictability of solutions to the Euler Eady problem be improved to show robust quasi-periodic lifecycles similar to those observed in the semigeostrophic Eady problem?

③ Do numerical solutions to the inviscid Euler Eady problem converge to inviscid semigeostrophic Eady solutions?

As mentioned at the start of this thesis, and as has been covered in the discussion throughout, the short answers to these questions are: yes, yes and, no. A detailed response to each of these questions follows in the next section.

7.2 Response to the original research objectives

This section covers the response to the original research objectives in turn, and how the results presented in this thesis have answered them.

7.2.1 Maintaining balance with intense fronts

The first research objective was concerned with the requirement of maintaining balance in numerical solutions supporting intense frontogensis, and this was investigated using the asymptotic convergence framework.

The asymptotic convergence process was first used in the context of the Eady model in Cullen (2008). The results presented in C08 showed that the theoretical convergence rate could be achieved whilst the solution was smooth, but not after collapse. The grid staggering was identified in C08 as being a likely culprit.

The grid staggering used in this thesis was a quasi-horizontal C-grid. The zonal velocity components were staggered relative to the cell centres, with the meridional velocity collocated there. As mentioned the correct C-grid requires the meridional velocity to be stored at cell centres. The approach used in this thesis permitted pure inertial oscillations without any averaging. This is likely to improve the representation of these waves when compared to the cell centred meridional velocity staggering.

The main benefit of this staggering, though, comes in the ability to calculate

$$fv = \frac{\partial \phi}{\partial x},$$

at the *zonal* velocity points using a second-order centred difference for the pressure gradient. The important aspect of this is that there is no need to average these terms, thereby effectively reducing the strength of the front. The limit solution results in a true discontinuity, and so the averaging would appear to be incompatible with representing a discontinuity in the solution.

It was suggested in C08 that a fully Lagrangian method would be required to maintain the theoretical convergence rate in the presence of a discontinuity. The results presented in Chapter 5 have shown that this is not the case, with several flavours of fixed grid Eulerian methods able to reproduce the second-order reduction in geostrophic imbalance.

The results on the representation of balance can be extended beyond the scope of the Eady model. In the real atmosphere a front is never a true discontinuity, although the width might indeed approach the grid resolution. One would reasonably expect the "intensity" of individual frontal systems to be comparable to the Eady solutions in the pre-collapse stage, in which all methods are sufficiently balanced: the Met Office's UKV model with 1.5 km resolution over the United Kingdom often generates intense fronts.

7.2.2 Improving the long term predictability

The second research objective was concerned with whether or not it was possible to improve the predictability of solutions to the Eady model using Eulerian methods.

The qualitative difference in solutions to the Eady model using Eulerian and Lagrangian methods has been a common theme in this thesis, with the Lagrangian methods showing good predictability in quasi-periodic lifecycles, and the Eulerian methods showing large variability.

The convergence of smooth solutions to the Boussinesq equations to the semigeostrophic equations for the Eady model was shown formally in Brenier and Cullen (2009). This would suggest, then, at small but finite Ro a solution to the Boussinesq equations would be qualitatively similar to the semigeostrophic solution. The convergence is discussed further in the following section, but for the present discussion this is sufficient to expect the Boussinesq solution to exhibit some predictability.

At the control resolution the SISL results were similar to the results of Nakamura and Held (1989), in that the solutions were very sensitive to a small change in a single parameter; the Rossby number and eddy viscosity, respectively. The situation was very different at quadrupled resolution, with experiments at the three smallest Ro being very predictable even up to a third frontogenesis at day 20.

The immediate piece of information learnt from these experiments was that existing results, and the control experiments of this thesis, were under-resolved to show the expected predictable behaviour after collapse. Further experiments identified the lack of conservation at lower resolution being critical in affecting the evolution. Both of these points are covered next.

The first new piece of information might at first glance appear quite trivial, but does in fact mask the complexity of solutions to the Eady problem. The semigeostrophic Eady model only supports Eady wave solutions, whilst the Boussinesq model supports Eady and inertia-gravity waves. The linearised wave solutions show the Eady wave to be large scale and unstable, and the inertia-gravity waves to be purely oscillatory and non-amplifying. It is the modelling of these inertia-gravity waves that appears to affect the predictability of the large scale solution post-collapse.

No minimum scale of these IGWs generated through fronogenesis was observed. Their length scale is likely to be closely matched to the width of the front. At the highest resolution experiments carried out there was no evidence of grid independence in these waves, but the post-collapse behaviour showed a marked improvement. This would suggest that the improved modelling of these waves, in terms of being less aliased on the finer grid and less implicit damping with a smaller time-step, was sufficient to capture their effect on the large scale solution.

The second piece of information identified that there were systematic errors being made in conservation in the advection scheme. This also helped to explain why the SISL scheme performed poorly at the control resolution. The incompressibility condition meant that a Lagrangian conservation law was compatible with an Eulerian conservation law, but even these were not being satisfied.

The isolated advection tests at the end of Chapter 5 showed that all the numerical methods struggled to maintain conservation when using a strongly deformational velocity field and near discontinuous tracer fields. All the methods reduced their conservation metrics by an order of magnitude in going from smooth to discontinuous fields.

Considering these two topics, unresolved wave activity and lack of conservation, in the wider context of atmospheric modelling it is the conservation issues that are clearly going to have a bigger impact on the large scale solution, and hence on the predictability at long times.

The point-wise nature of the basic semi-Lagrangian scheme is not conservative. Climate simulations using the Unified Model require a conservative treatment of dry density, so as to prevent the solution from artificially drifting due to generation or destruction of mass. Clearly long time solutions require that the conservation laws be satisfied, but the basic semi-Lagrangian scheme is ill-equipped for this.

The small scale and unresolved dynamics are important when they form part of the balanced solution, as found in the present work. Resolution in operational models will continue to steadily increase, but merely waiting would be a poor approach. The Lagrangian-averaged model showed clear potential in increasing the long term predictability, primarily through altering the coupling of the small scale and large scale motion. Tests on complex ocean models have shown it to have a beneficial effect, comparable to increasing resolution, but at the cost of much increased computational complexity.

7.2.3 Convergence to the limit solution

The final point addressed in this section is that of the convergence to the limit solution. The results in this thesis have been mixed in their response to this research objective, and so careful consideration is required.

The general properties of the limit solution have already been covered in the proceeding sections, but they are perhaps most easily considered as a single Lagrangian conservation law of the geostrophic potential vorticity. As covered in the earlier chapters, this is solved by inverting the PV distribution and then transporting in the dual space given by the isentropic coordinate transformation.

The previous sections have shown that some properties of the limit solution have been recovered, in particular the quasi-periodic oscillatory nature and the large scale solution being sufficiently balanced. In addition to these the results of Chapter 5 show the amount of negative potential vorticity to be decreasing with Rossby number, as well as the lifting off of fluid from the boundary and into the interior of the domain. These are all characteristics that would be expected of essentially the semigeostrophic limit solution superimposed with a small amount of inertia-gravity wave activity.

The unavoidable difference, though, comes in terms of the respective

amplitudes of the Eady wave, which differ by a factor of two. Neither increasing resolution nor further rescaling the solutions showed a drastic enough increase to suggest that the fixed grid methods would reproduce the intensity observed in the limit solution.

The explanation proposed by the author is that the solutions presented in this thesis represent *viscous* semigeostrophic solutions. The finite grid resolution provides the minimum scale permitted in the solution, thereby preventing the scale collapse to discontinuity. The solutions reproduce the characteristics of the limit solution, with the amplitude being limited by the minimum grid scale.

The results presented in Chapter 5 showed all of the numerical methods to recover the geostrophic imbalance convergence rate, even after collapse. This strongly suggests that the results are approaching a limit given by a balanced solution, which, for exact geostrophic and hydrostatic balance, is the semigeostrophic limit.

The viscous aspect of the solution is justified based on the minimum scale argument introduced by the fixed grid, as well as the maximum amplitude reached. For successive doubling of resolution the peak RMS norm of the meridional velocity only increases by 2.7 m s^{-1} and 0.5 m s^{-1}, respectively. Whilst it is dangerous to extrapolate from these three data points, it seems unlikely that, at much higher resolution, the peak amplitude would reach that of the inviscid limit.

It is for these reasons, as well as the results presented that show the fields to look qualitatively the same as the inviscid limit, that suggest the solutions are approaching a viscous semigeostrophic limit.

7.3 Limitations and future directions

In this section the limitations and considerations of the results presented in this thesis are discussed further. Several future directions are discussed, before this work is brought to a close.

7.3.1 Limitations of the methods used

In an idealised study such as the one presented in this thesis there are inevitably going to be limitations on the results presented; some will be highly restrictive, whilst others less so.

The limitations analysis begins with the use of the two-dimensional vertical slice model itself. The Eady background state allows the baroclinic instability to draw on an infinite reservoir of available potential energy, meaning that fronts and jets can reach unrealistically large values as noted in Williams (1967).

The overview of observational results showed that these slice models models were able to generate results that correlated with observations. Real

fronts are three-dimensional and often curved. The use of the rigid lid within the model is very artificial; as shown in Hoskins and Bretherton (1972) in reality the fact that the tropopause is able to deform prevents it from forming a true discontinuity.

The limitations of the results are also highly dependent on the validity of the assumptions made in Chapter 2, and these will be discussed in turn.

The first assumption made was that of inviscid flow. This has been a topic throughout this work, in particular in response to the third research objective. The limit solution of Cullen (2006) appeared to satisfy this property, but it is worth considering how this relates to the real atmosphere. The effect of diffusion has been shown to lift the jet away from the surface, (Xu et al., 1998; Beare and Cullen, 2013).

The next assumption was that of constant rotation. For large-scale flow at low Rossby number this is going to be problematic, but for modelling the effect of frontogenesis on the large-scale flow it greatly simplified the dynamics. If extending the work to three-dimensions then it would be necessary to use at least the β-plane approximation, $f = f_0 + \beta y$, to account for this variation with latitude.

The motion was considered to be adiabatic, but it was already noted in Chapter 1 that fronts were associated with regions of extreme weather. Moisture (Knight and Hobbs, 1988) and latent heat release (Ross and Orlanski, 1978) are among the neglected processes occurring in real fronts.

Finally, the incompressible Boussinesq assumption is covered. The fully compressible equations are solved for operational models, but as found in Cullen (2008) the lack of energy conservation in the slice model configuration meant that they were not suited to the dynamics study of this thesis. A compressible model with the required conservation properties was derived from a variational principle in Cotter and Holm (2013), but it is not clear if the solutions from that model resemble the traditional Eady wave.

7.3.2 Future research directions

Several future research directions were touched upon in Chapter 6. Of those implemented the use of Lagrangian-averaging offered the most potential. Further investigation would be required to confirm whether there was an improvement in long term predictability, and in particular on the computational side to make it much more affordable.

The lack of conservation has been reiterated throughout this thesis, and it is likely that the conservative semi-Lagrangian schemes mentioned would improve the results at lower resolution.

7.3.3 Final thoughts

This work is but a small part in the collective attempt to do the seemingly impossible and predict the future. This is ever improving, and the author feels privileged to have been a part of it.

Bibliography

S. Acharya, B. R. Baliga, K. Karki, J. Y. Murthy, C. Prakash, and S. P. Vanka. Pressure-based finite-volume methods in computational fluid dynamics. *Journal of Heat Transfer*, 129(4):407–424, 2007.

L. Ambrosio, M. Colombo, G. De Phillippis, and A. Figalli. A global existence result for the semigeostrophic equations in three dimensional convex domains. *arXiv preprint arXiv:1205.5435*, 2012.

A. Arakawa and V. R. Lamb. Computational design of the basic dynamical processes of the UCLA general circulation model. *Methods in Computational Physics*, 17:173–265, 1977.

Akio Arakawa and Vivian R Lamb. A potential enstrophy and energy conserving scheme for the shallow water equations. *Monthly Weather Review*, 109(1):18–36, 1981.

G. K. Batchelor. *An introduction to fluid mechanics*. Cambridge University Press, 1967.

R. J. Beare and M. J. P. Cullen. Diagnosis of boundary-layer circulations. *Philosophical Transactions of the Royal Society A: Mathematical, Physical and Engineering Sciences*, 371(1991), 2013.

J.-D. Benamou and Y. Brenier. Weak existence for the semigeostrophic equations formulated as a coupled Monge–Ampère/transport problem. *SIAM Journal on Applied Mathematics*, 58(5):1450–1461, 1998.

R. Bermejo and A. Staniforth. The conversion of semi-Lagrangian advection schemes to quasi-monotone schemes. *Monthly Weather Review*, 120(11): 2622–2632, 1992.

J. P. Berrut and L. N. Trefethen. Barycentric Lagrange interpolation. *SIAM Review*, 46(3):501–517, 2004.

W. Blumen. Unstable nonlinear evolution of an Eady wave in time-dependent basic flows and frontogenesis. *Journal of the Atmospheric Sciences*, 36:3–11, 1979.

W. Blumen. A Comparison between the Hoskins-Bretherton model of frontogenesis and the analysis of an intense surface frontal zone. *Journal of the Atmospheric Sciences*, 37:64–77, 1980.

W. Blumen. The geostrophic coordinate transformation. *Journal of the Atmospheric Sciences*, 38:1100–1105, 1981.

W. Blumen. A semigeostrophic Eady-wave frontal model incorporating momentum diffusion. Part I: Model and solutions. *Journal of the Atmospheric Sciences*, 47:2890–2902, 1990a.

W. Blumen. A semigeostrophic Eady-wave frontal model incorporating momentum diffusion. Part II: Kinetic energy and enstrophy Dissipation. *Journal of the Atmospheric Sciences*, 47:2903–2908, 1990b.

Y. Brenier and M. J. P. Cullen. Rigorous derivation of the $x - z$ semigeostrophic equations. *Communications in Mathematical Sciences*, 7:779–784, 2009.

F. P. Bretherton. Critical layer instability in baroclinic flows. *Quarterly Journal of the Royal Meteorological Society*, 92(393):325–334, 1966.

C. J. Budd, M. J. P. Cullen, and E. J. Walsh. Monge-Ampère based moving mesh methods for numerical weather prediction, with applications to the Eady problem. *Journal of Computational Physics*, 236:247–270, March 2013.

H. Burchard and H. Rennau. Comparative quantification of physically and numerically induced mixing in ocean models. *Ocean Modelling*, 20(3): 293–311, 2008.

S. Chandrasekhar. Hydrodynamic and hydromagnetic stability. *International Series of Monographs on Physics, Oxford: Clarendon*, 1, 1961.

E. Cordero, N. Wood, and A. Staniforth. Impact of semi-Lagrangian trajectories on the discrete normal modes of a non-hydrostatic vertical-column model. *Quarterly Journal of the Royal Meteorological Society*, 131(605): 93–108, 2005.

J. F. Cossette and P. K. Smolarkiewicz. A Monge-Ampère enhancement for semi-Lagrangian methods. *Computers & Fluids*, 46(1):180–185, 2011.

C. J. Cotter and D. D. Holm. A variational formulation of vertical slice models. *Proceedings of the Royal Society A: Mathematical, Physical and Engineering Science*, 469(2155), 2013.

J. Crank and P. Nicolson. A practical method for numerical evaluation of solutions of partial differential equations of the heat-conduction type.

In *Mathematical Proceedings of the Cambridge Philosophical Society*, volume 43, pages 50–67. Cambridge Univ Press, 1947.

M. J. P. Cullen. Implicit finite difference methods for modelling discontinuous atmospheric flows. *Journal of Computational Physics*, 81(2):319–348, 1989.

M. J. P. Cullen. On the accuracy of the semi-geostrophic approximation. *Quarterly Journal of the Royal Meteorological Society*, 126(564):1099–1115, 2000.

M. J. P. Cullen. Alternative implementations of the semi-Lagrangian semi-implicit schemes in the ECMWF model. *Quarterly Journal of the Royal Meteorological Society*, 127(578):2787–2802, 2001.

M. J. P. Cullen. *A mathematical theory of large-scale atmosphere/ocean flow*. Imperial College Press, 2006.

M. J. P. Cullen. Modelling atmospheric flows. *Acta Numerica*, 16:67–154, 2007a.

M. J. P. Cullen. Semi-geostrophic solutions for flow over a ridge. *Quarterly Journal of the Royal Meteorological Society*, 133(623):491–501, 2007b.

M. J. P. Cullen. A comparison of numerical solutions to the Eady frontogenesis problem. *Quarterly Journal of the Royal Meteorological Society*, 134 (637):2143–2155, 2008.

M. J. P. Cullen and A. R. Brown. Large eddy simulation of the atmosphere on various scales. *Philosophical Transactions of the Royal Society A: Mathematical, Physical and Engineering Sciences*, 367(1899):2947–2956, 2009.

M. J. P. Cullen and M. Feldman. Lagrangian solutions of semigeostrophic equations in physical space. *SIAM journal on Mathematical Analysis*, 37 (5):1371–1395, 2006.

M. J. P. Cullen and R. J. Purser. An extended Lagrangian theory of semi-geostrophic frontogenesis. *Journal of the Atmospheric Sciences*, 41:1477–1497, 1984.

M. J. P. Cullen and I. Roulstone. A geometric model of the nonlinear equilibration of two-dimensional eady waves. *Journal of the atmospheric sciences*, 50(2):328–332, 1993a.

M. J. P. Cullen and I. Roulstone. A geometric model of the nonlinear equilibration of two-dimensional Eady waves. *Journal of the Atmospheric Sciences*, 50(2):328–332, 1993b.

M. J. P. Cullen, T. Davies, M. H. Mawson, J. A. James, S. C. Coulter, and A. Malcolm. An overview of numerical methods for the next generation UK NWP and climate model. *Atmosphere-Ocean*, 35(sup1):425–444, 1997.

M. J. P. Cullen, W. Gangbo, and G. Pisante. The semigeostrophic equations discretized in reference and dual variables. *Archive for rational mechanics and analysis*, 185(2):341–363, 2007.

B. Cushman-Roisin and J. Beckers. *Introduction to geophysical fluid dynamics: Physical and numerical aspects*. Academic Press, 2011.

H. C. Davies and C. H. Bishop. Eady edge waves and rapid development. *Journal of the Atmospheric Sciences*, 51(13):1930–1946, 1994.

H. C. Davies and J. C. Muller. Detailed description of deformation-induced semi-geostrophic frontogenesis. *Quarterly Journal of the Royal Meteorological Society*, 114(483):1201–1219, 1988.

T. Davies, M. J. P. Cullen, A. J. Malcolm, M. H. Mawson, A. Staniforth, A. A. White, and N. Wood. A new dynamical core for the Met Office's global and regional modelling of the atmosphere. *Quarterly Journal of the Royal Meteorological Society*, 131(608):1759–1782, 2005.

D. Desvigne, O. Marsden, C. Bogey, and C. Bailly. Development of noncentered wavenumber-based optimized interpolation schemes with amplification control for overlapping grids. *SIAM Journal on Scientific Computing*, 32(4):2074–2098, 2010.

M. Diamantakis, T. Davies, and N. Wood. An iterative time-stepping scheme for the Met Office's semi-implicit semi-Lagrangian non-hydrostatic model. *Quarterly Journal of the Royal Meteorological Society*, 133(625):997–1011, 2007.

P. G. Drazin and W. H. Reid. *Hydrodynamic stability*. Cambridge University Press, 2004.

D. R. Durran. *Numerical Methods for Fluid Dynamics: With Applications to Geophysics*, volume 32. Springer Verlag, second edition, 2010.

E. T. Eady. Long waves and cyclone waves. *Tellus*, 1(3):33–52, 1949.

J. Egger. Baroclinic instability in the Eady model: Interpretations. *Journal of the Atmospheric Sciences*, 66(6):1856–1859, 2009.

A. Eliassen. *On the formation of fronts in the atmosphere*. Oxford University Press, 1959.

A. Eliassen. On the vertical circulation in frontal zones. *Geofysiske Publikasjoner*, 24(4):147–160, 1962.

Engauge Digitizer. Engauge digitizer, 2013. URL `http://digitizer.sourceforge.net/`.

X. Feng, R. Glowinski, and M. Neilan. Recent developments in numerical methods for fully nonlinear second order partial differential equations. *SIAM Review*, 55(2):205–267, 2013.

R. Ferrari. A frontal challenge for climate models. *Science*, 332(6027):316–317, 2011.

D. C. Fritts and G. D. Nastrom. Sources of mesoscale variability of gravity waves. Part II: Frontal, convective, and jet stream excitation. *Journal of the Atmospheric Sciences*, 49(2):111–127, 1992.

B. D. Froese. *Numerical methods for the elliptic Monge-Ampère equation and optimal transport*. PhD thesis, Simon Fraser University, 2012.

K. S. Gage and G. D. Nastrom. Theoretical interpretation of atmospheric wavenumber spectra of wind and temperature observed by commercial aircraft during gasp. *Journal of the Atmospheric Sciences*, 43(7):729–740, 1986.

R. L. Gall, R. T. Williams, and T. L. Clark. On the minimum scale of surface fronts. *Journal of the Atmospheric Sciences*, 44(18):2562–2574, 1987.

R. L. Gall, R. T. Williams, and T. L. Clark. Gravity waves generated during frontogenesis. *Journal of the Atmospheric Sciences*, 45:2204–2220, 1988.

S. T. Garner, N. Nakamura, and I. M. Held. Nonlinear equilibration of two-dimensional Eady waves: A new perspective. *Journal of the Atmospheric Sciences*, 49(21):1984–1996, 1992.

S. T. Garner, D. M. W. Frierson, I. M. Held, O. Pauluis, and G. K. Vallis. Resolving convection in a global hypohydrostatic model. *Journal of the Atmospheric Sciences*, 64(6):2061–2075, 2007.

B. J. Geurts and D. D. Holm. Alpha-modeling strategy for LES of turbulent mixing. *Turbulent flow computation*, pages 237–278, 2004.

B. J. Geurts and D. D. Holm. Leray and LANS-α modeling of turbulent mixing. *Arxiv preprint nlin/0504038*, 2005.

A. E. Gill. *Atmosphere-ocean dynamics*, volume 30. Academic press, 1982.

G. H. Golub and C. F. Van Loan. *Matrix computations*, volume 3. Jon Hopkins University Press, 2012.

W. Gu and Q. Xu. Baroclinic Eady wave and fronts. Part III: unbalanced dynamics-departures from viscous semigeostrophy. *Journal of the Atmospheric Sciences*, 57(20):3414–3425, 2000.

M. W. Hecht, D. . Holm, M. R. Petersen, and B. A. Wingate. Implementation of the LANS-α turbulence model in a primitive equation ocean model. *Journal of Computational Physics*, 227(11):5691–5716, 2008.

D. D. Holm and B. T. Nadiga. Modeling mesoscale turbulence in the barotropic double-gyre circulation. *Journal of Physical Oceanography*, 33 (11):2355–2365, 2003.

D. D. Holm, J. E. Marsden, and T. S. Ratiu. The Euler–Poincaré equations in geophysical fluid dynamics. *Large-scale Atmosphere-ocean Dynamics: Geometric methods and models*, 2:251–300, 2002.

B. J. Hoskins. Atmospheric frontogenesis models: Some solutions. *Quarterly Journal of the Royal Meteorological Society*, 97(412):139–153, 1971.

B. J. Hoskins. The geostrophic momentum approximation and the semi-geostrophic equations. *Journal of the Atmospheric Sciences*, 32(2):233–242, 1975.

B. J. Hoskins. Baroclinic waves and frontogenesis Part I: Introduction and Eady waves. *Quarterly Journal of the Royal Meteorological Society*, 102 (431):103–122, 1976.

B. J. Hoskins. The mathematical theory of frontogenesis. *Annual Review of Fluid Mechanics*, 14(1):131–151, 1982.

B. J. Hoskins and F. P. Bretherton. Atmospheric frontogenesis models: Mathematical formulation and solution. *Journal of the Atmospheric Sciences*, 29(11):11–37, 1972.

B. J. Hoskins and W. A. J. Heckley. Cold and warm fronts in baroclinic waves. *Quarterly Journal of the Royal Meteorological Society*, 107(451): 79–90, 1981.

B. J. Hoskins and N. V. West. Baroclinic waves and frontogenesis. Part II: Uniform potential vorticity jet flows-Cold and warm fronts. *Journal of the Atmospheric Sciences*, 36:1663–1680, 1979.

B. J. Hoskins, E. C. Neto, and H. R. Cho. The formation of multiple fronts. *Quarterly Journal of the Royal Meteorological Society*, 110(466):881–896, 1984.

J. T. Houghton. *The Physics of Atmospheres*. Cambridge University Press, third edition, 2002.

C. Jablonowski and D. L. Williamson. A baroclinic instability test case for atmospheric model dynamical cores. *Quarterly Journal of the Royal Meteorological Society*, 132(621C):2943–2975, 2006.

E. Kalnay. *Atmospheric modeling, data assimilation, and predictability.* Cambridge University Press, 2003.

D. Keyser and R. A. Anthes. The influence of planetary boundary layer physics on frontal structure in the Hoskins-Bretherton horizontal shear model. *Journal of the Atmospheric Sciences*, 39:1783–1802, 1982.

D. J. Knight and P. V. Hobbs. The mesoscale and microscale structure and organization of clouds and precipitation in midlatitude cyclones. Part XV: A numerical modeling study of frontogenesis and cold-frontal rainbands. *Journal of the Atmospheric Sciences*, 45(6):915–931, 1988.

P. Knippertz, J. M. Chagnon, A. Foster, L. Lathouwers, J. H. Marsham, J. Methven, and D. J. Parker. Research flight observations of a prefrontal gravity wave near the southwestern UK. *Weather*, 65(11):293–297, 2010.

J. N. Koshyk and H.-R. Cho. Dynamics of a mature front in a uniform potential vorticity semigeostrophic model. *Journal of Atmospheric Sciences*, 49:497–510, 1992.

P. H. Lauritzen, C. Jablonowski, M. A. Taylor, and R. D. Nair. Rotated versions of the jablonowski steady-state and baroclinic wave test cases: A dynamical core intercomparison. *Journal of Advances in Modeling Earth Systems*, 2(4):15, 2010a.

P. H. Lauritzen, R. D. Nair, and P. A. Ullrich. A conservative semi-Lagrangian multi-tracer transport scheme (CSLAM) on the cubed-sphere grid. *Journal of Computational Physics*, 229(5):1401–1424, 2010b.

P. D. Lax and R. D. Richtmyer. Survey of the stability of linear finite difference equations. *Communications on Pure and Applied Mathematics*, 9(2):267–293, 1956.

R. J. LeVeque. *Numerical methods for conservation laws.* Birkhäuser, 1992.

B. E. Ley and W. R. Peltier. Wave generation and frontal collapse. *Journal of the Atmospheric Sciences*, 35:3–17, 1978.

E. N. Lorenz. Deterministic Nonperiodic Flow1. *Journal of the Atmospheric Sciences*, 20:130–141, 1963.

E. N. Lorenz. A study of the predictability of a 28-variable atmospheric model. *Tellus*, 17(3):321–333, 1965.

E. N. Lorenz. The predictability of a flow which possesses many scales of motion. *Tellus*, 21(3):289–307, 1969.

E. N. Lorenz. Predictability: Does the flap of a butterfly's wings in brazil set off a tornado in texas? *American Association for the Advancement of Science, Washington, DC*, 1972.

D. Majewski, D. Liermann, P. Prohl, B. Ritter, M. Buchhold, T. Hanisch, G. Paul, W. Wergen, and J. Baumgardner. The operational global icosahedral-hexagonal gridpoint model gme: Description and high-resolution tests. *Monthly Weather Review*, 130(2):319–338, 2002.

J. Michalakes, J. Dudhia, D. Gill, T. Henderson, J. Klemp, W. Skamarock, and W. Wang. The weather research and forecast model: software architecture and performance. In *Proceedings of the 11th ECMWF Workshop on the Use of High Performance Computing In Meteorology*, volume 25, page 29. World Scientific, 2004.

N. Nakamura. Nonlinear equilibration of two-dimensional Eady waves: Simulations with viscous geostrophic momentum equations. *Journal of the Atmospheric Sciences*, 51(7):1023–1035, 1994.

N. Nakamura and I. M. Held. Nonlinear equilibration of two-dimensional Eady waves. *Journal of the Atmospheric Sciences*, 46:3055–3064, 1989.

Y. Ogura and D. Portis. Structure of the cold front observed in sesame-ave iii and its comparison with the Hoskins-Bretherton frontogenesis model. *Journal of Atmospheric Sciences*, 39:2773–2792, 1982.

I. Orlanski and B. B. Ross. The circulation associated with a cold front. Part I: Dry case. *Journal of the Atmospheric Sciences*, 34:1619–1633, 1977.

T. N. Palmer, G. J. Shutts, R. Hagedorn, F. J. Doblas-Reyes, T. Jung, and M. Leutbecher. Representing model uncertainty in weather and climate prediction. *Annual Review of Earth and Planetary Sciences*, 33:163–193, 2005.

S. V. Patankar and D. B. Spalding. A calculation procedure for heat, mass and momentum transfer in three-dimensional parabolic flows. *International Journal of Heat and Mass Transfer*, 15(10):1787–1806, 1972.

O. Pauluis, D. M. W. Frierson, S. T. Garner, I. M. Held, and G. K. Vallis. The hypohydrostatic rescaling and its impacts on modeling of atmospheric convection. *Theoretical and Computational Fluid Dynamics*, 20(5-6):485–499, 2006.

J. Pedlosky. *Geophysical fluid dynamics*. Springer, 1987.

J. B. Perot and C. J. Zusi. Differential forms for scientists and engineers. *Journal of Computational Physics*, 257(B):1373–1393, 2014.

R. Plougonven and F. Zhang. Internal gravity waves from atmospheric jets and fronts. *Reviews of Geophysics*, 52(1):33–76, 2014.

R. Plougonven, D. J. Muraki, and C. Snyder. A baroclinic instability that couples balanced motions and gravity waves. *Journal of the Atmospheric Sciences*, 62(5):1545–1559, 2005.

T. D. Ringler, J. Thuburn, J. B. Klemp, and W. C. Skamarock. A unified approach to energy conservation and potential vorticity dynamics for arbitrarily-structured c-grids. *Journal of Computational Physics*, 229(9): 3065–3090, 2010.

H. Ritchie, C. Temperton, A. Simmons, M. Hortal, T. Davies, D. Dent, and M. Hamrud. Implementation of the semi-lagrangian method in a high-resolution version of the ecmwf forecast model. *Monthly Weather Review*, 123(2):489–514, 1995.

A. Robert. A stable numerical integration scheme for the primitive meteorological equations. *Atmosphere-Ocean*, 19(1):35–46, 1981.

A. Robert. Bubble convection experiments with a semi-implicit formulation of the Euler equations. *Journal of the Atmospheric Sciences*, 50(13):1865–1873, 1993.

B. B. Ross and I. Orlanski. The circulation associated with a cold front. Part II: Moist case. *Journal of the Atmospheric Sciences*, 35:445–65, 1978.

F. Saleri and A. Veneziani. Pressure correction algebraic splitting methods for the incompressible Navier–Stokes equations. *SIAM Journal on Numerical Analysis*, 43(1):174–194, 2005.

F. Sanders. A Investigation of the Structure and Dynamics of an Intense Surface Frontal Zone. *Journal of the Atmospheric Sciences*, 12:542–552, 1955.

J. S. Sawyer. The vertical circulation at meteorological fronts and its relation to frontogenesis. *Proceedings of the Royal Society of London. Series A. Mathematical and Physical Sciences*, 234(1198):346, 1956.

M. A. Shapiro and A. J. Thorpe. THORPEX international science plan. *WMO/TD*, 2004.

J. Smagorinsky. Global atmospheric modeling and the numerical simulation of climate. *Weather and Climate modification*, pages 633–686, 1974.

Piotr K Smolarkiewicz. On forward-in-time differencing for fluids. *Monthly weather review*, 119(10):2505–2510, 1991.

C. Snyder, W. C. Skamarock, and R. Rotunno. Frontal dynamics near and following frontal collapse. *Journal of the Atmospheric Sciences*, 50(18): 3194–3211, 1993.

A. Staniforth and J. Côté. Semi-Lagrangian integration schemes for atmospheric models: A review. *Monthly Weather Review*, 119(9):2206–2223, 1991.

A. Staniforth and J. Thuburn. Horizontal grids for global weather and climate prediction models: a review. *Quarterly Journal of the Royal Meteorological Society*, 138:1–26, 2012.

I. Szunyogh, H. Wernli, J. Barkmeijer, C. H. Bishop, E. Chang, P. Harr, S. Jones, T. Jung, N. Kitabatake, P. Knippertz, et al. Recent Developments in Predictability and Dynamical Processes (PDP) Research: A Report by the THORPEX PDP Working Group. *Bulletin of the American Meteorological Society*, 2008.

THORPEX. Workshop report: "diagnosis of model errors". World Metereological Society, 2010.

J. Vanneste. Balance and spontaneous wave generation in geophysical flows. *Annual Review of Fluid Mechanics*, 45(1):147–172, 2013.

A. R. Visram, C. J. Cotter, and M. J. P. Cullen. A framework for evaluating model error using asymptotic convergence in the Eady model. *Quarterly Journal of the Royal Meteorological Society*, 140(682):1629–1639, 2014. doi: 10.1002/qj.2244.

H. Volkert and C. H. Bishop. The semi-geostrophic Eady problem as a testbed for numerical simulations of frontogenesis. *Tellus A*, 42(1):202–207, 1990.

A. A. White and R. J. Beare. Flavours of pseudo-height. *Quarterly Journal of the Royal Meteorological Society*, 131(606):759–764, 2005.

R. T. Williams. Nonlinear, non-geostrophic effects in a baroclinic atmosphere. *Journal of the Atmospheric Sciences*, 22:388–401, 1965.

R. T. Williams. Atmospheric frontogenesis: A numerical experiment. *Journal of the Atmospheric Sciences*, 24:627–641, 1967.

R. T. Williams. Quasi-geostrophic versus non-geostrophic frontogenesis. *Journal of the Atmospheric Sciences*, 29:3–10, 1972.

R. T. Williams and J. Plotkin. Quasi-geostrophic frontogenesis. *Journal of the Atmospheric Sciences*, 25:201–206, 1968.

B. A. Wingate. The maximum allowable time step for the shallow water α model and its relation to time-implicit differencing. *Monthly Weather Review*, 132(12):2719–2731, 2004.

D. Xiu, S. J. Sherwin, S. Dong, and G. E. Karniadakis. Strong and auxiliary forms of the semi-Lagrangian method for incompressible flows. *Journal of Scientific Computing*, 25(1):323–346, 2005.

Q. Xu and W. Gu. Baroclinic Eady wave and fronts. Part II: Geostrophic potential vorticity dynamics in semigeostrophic space. *Journal of the Atmospheric Sciences*, 57(6):861–872, 2000.

Q. Xu, W. Gu, and J. Gao. Baroclinic Eady wave and fronts. Part I: Viscous semigeostrophy and the impact of boundary condition. *Journal of the Atmospheric Sciences*, 55(24):3598–3615, 1998.

S. T. Zalesak. Fully multidimensional flux-corrected transport algorithms for fluids. *Journal of Computational Physics*, 31(3):335–362, 1979.

M. Zerroukat. A simple mass conserving semi-Lagrangian scheme for transport problems. *Journal of Computational Physics*, 229(24):9011–9019, 2010.

M. Zerroukat, N. Wood, and A. Staniforth. SLICE: A semi-Lagrangian inherently conserving and efficient scheme for transport problems. *Quarterly Journal of the Royal Meteorological Society*, 128(586):2801–2820, 2002.

F. Zhang. *The Schur complement and its applications*, volume 4. Springer Verlag, 2005.

M. Z. Ziemianski and A. J. Thorpe. Nonlinear balanced simulation of a baroclinic wave. *Quarterly Journal of the Royal Meteorological Society*, 128(584):1879–1897, 2002.